



Heidelinde Trimmel, Dipl. Ing. 00025807

Surface Energy Balance
and Thermal Conditions during Heat Waves
for Riparian and Urban Systems

Dissertation

to achieve the university degree of
Doctor rerum naturalium technicarum (Dr. nat. techn. / Ph.D.)

submitted to

University of Natural Resources and Life Sciences, Vienna

Supervisor

Ao. Prof. Mag. Dr. Philipp Weihs

Department of Water, Atmosphere and Environment
Institute of Meteorology and Climatology
Head: Univ.-Prof. Mag. Dr. Harald Rieder

Vienna, September 2020

AFFIDAVIT

I declare that I have authored this thesis independently, that I have not used other than the declared sources/resources, and that I have explicitly indicated all material which has been quoted either literally or by content from the sources used. The text document uploaded to BOKUonline is identical to the present doctoral thesis dissertation.

Vienna, _____
Date

Signature

Acknowledgment

I want especially to thank my home institution, the Institute of Meteorology and Climatology at BOKU, along with the Oregon Department of Environmental Quality (DEQ), the Groupe de Météorologie à Moyenne Echelle (GMME)/Ville et Climat urbain (VILLE) at the Centre National de Recherches Météorologiques and Météo-France in Toulouse, the Norsk institutt for luftforskning (NILU) in Kjeller, Norway and all co-authors and reviewers for their help, feedback and criticism.

Furthermore, I want to thank the Austrian Climate Research Programme (ACRP), who funded the BIO_CLIC, LOWFLOW and URBANIA projects; the Marietta Blau scholarship of the OEAD; the Zentralanstalt für Meteorologie und Geodynamik, who created the INCA data set; the European Commission's Sixth Framework Programme, who produced regional climate model data within the ENSEMBLE project; the World Climate Research Programme (WCRP) who initiated EURO-CORDEX as the European branch of the CORDEX initiative; the federal state governmental geoinformation service authorities of Burgenland, Styria, Lower Austria and Vienna; and the Austrian Hydrographic Service.

Last but not least, I would like to thank my family and friends for their patience and support.

Abstract

The energy balance of the Earth's surface fundamentally defines the magnitude and amplitude of different ecosystem' state variables. Ecosystems are sensitive to present climate extremes, such as heat waves. Moreover, such systems are at risk due to amplifications caused by climate change. Inland waters are vulnerable systems with limited migration potentials. Likewise vulnerable are urban areas, already home to the majority of the global human population trending upwards. In this thesis, the energy fluxes and state variables within a pre-alpine river and the Viennese urban canopy layer are analysed using numerical modelling to address the following key issues: How do surface properties and vegetation affect selected state variables? Will the behaviour of the systems change due to changes in climate? How are the living conditions of organisms affected? Long-term meteorological measurements and campaigns were performed to collect data used to force and evaluate the numerical models applied to the studied systems. Land cover and urban parameters were calculated, land use scenarios developed to feed the models and simulate and analyse present and future heat waves. Both environments are facing serious health threats. A shift of one fish zone in Eastern Austrian rivers will pose a mortal threat to cold-water species. All energy fluxes apart from the latent heat flux add energy to the water surface. Stream temperature minima increase stronger than the maxima for all vegetation scenarios. Stream temperature maxima are best reduced by dense shade, but the expected increase in air temperature cannot be compensated. In urban systems, an increase in maximum urban canopy air temperature by 6.7 K is noted under heat wave conditions. The radiation balance and sensible heat flux dominate the energy balance. At night, heat stress can be reduced by up to 1 K using higher albedo and low thermal conductance of urban materials. During daytime, shade is the most effective measure.

Zusammenfassung

Die Energiebilanz der Erdoberfläche definiert grundlegend die Magnitude und Amplitude der Zustandsvariablen verschiedener Ökosysteme. Diese reagieren empfindlich auf aktuelle Klimaextreme wie Hitzewellen sowie Klimaänderungen. Binnengewässer reagieren empfindlich sowie haben begrenzten Migrationspotentialen. Ebenso anfällig sind städtische Gebiete, in denen bereits die Mehrheit der Weltbevölkerung wohnt - mit steigender Tendenz. In dieser Arbeit werden die Energieflüsse und Zustandsvariablen eines voralpinen Flusses und der Wiener Stadthindernisschicht mittels numerischer Modelle analysiert, um die folgenden Fragen zu beantworten: Wie beeinflussen Oberflächeneigenschaften und Vegetation ausgewählte Zustandsvariablen? Wird sich das Verhalten der Systeme aufgrund von Klimaveränderungen ändern? Wie sind die Lebensbedingungen betroffen? Es wurden meteorologische Langzeitmessungen und Messkampagnen durchgeführt um Daten zu sammeln, die zum Erzwingen und Bewerten der auf die untersuchten Systeme angewendeten numerischen Modelle verwendet wurden. Landbedeckung und städtische Parameter wurden berechnet sowie Landnutzungsszenarien entwickelt und als Eingabeparameter verwendet um gegenwärtige und zukünftige Hitzewellen zu simulieren und analysieren. Beide Systeme sind ernsthaft bedroht. In Gewässern kann eine Verschiebung um eine Fischzone Kaltwasserarten in Ostösterreich verdrängen. Die Wassertemperaturminima steigen für alle Vegetationsszenarien stärker als die Maxima an. Jene Maxima werden am besten durch dichten Schatten verringert, aber der erwartete Anstieg der Lufttemperatur kann dadurch nicht kompensiert werden. Im städtischen System wird ein Anstieg der maximalen bodennahen Lufttemperatur um 6,7 K festgestellt. Die Energiebilanz wird von Strahlung und fühlbaren Wärmefluss dominiert. Nachts kann die Wärmebelastung durch höhere Albedo und niedrige Wärmeleitfähigkeit städtischer Materialien um bis zu 1 K reduziert werden. Tagsüber ist Schatten die effektivste Maßnahme.

Contents

1. Introduction and Motivation	1
1.1. The Earth’s surface – the structure of the atmospheric boundary layer	1
1.2. Energy and mass exchanges, and balances	1
1.3. Heat waves as a threat to organisms	3
1.4. Research questions	5
2. Methods	7
2.1. Measurements and evaluation	7
2.2. Numerical models	8
2.3. Initial and boundary conditions	11
3. Results and Discussion	15
3.1. Surface energy fluxes during heat wave conditions	15
3.2. Influence of surface properties	16
3.3. The effect of vegetation on energy balance during heat waves	19
3.4. Expected changes due to climatic changes	21
3.5. Influence on living conditions	24
4. Summary and Outlook	27
A. Annex: Publications	31
A.1. Overview of dissertation publications	31
A.1.1. riverine spaces	31
A.1.2. urban spaces	31
A.2. Additional studies contributing and informing work listed in Annex 1	33
A.3. Dissertation publications, full texts:	34
Bibliography	137
B. Abbreviations	149

1. Introduction and Motivation

1.1. The Earth's surface – the structure of the atmospheric boundary layer

The influence of the Earth's surface on the Earth's atmosphere is restricted to the lowest 10 km of the atmosphere (the troposphere) (Oke, 1987). Within periods of about one day, the surface influence is limited to the (planetary or atmospheric) boundary layer, which is spread much less vertically and is well mixed through the process of turbulence. During daytime, sun-driven thermal mixing (convection) results in an expansion of the boundary layer of up to 2 km. At night, the surface cools faster than the atmosphere, causing the boundary layer to shrink in extent to sometimes less than 100 m. The (turbulent) surface layer is subject to the most intense turbulence, dependent on the surface roughness and convection. It can extend to about 50 m during the day, but it shrinks to only a few metres at night. The roughness sublayer is dependent on the roughness of the surface, and its height lies in the range of one to three times the height or spacing of ground objects such as trees or buildings. The laminar boundary layer is non-turbulent and only a few millimetres thick. It covers all surfaces and acts as a buffer between the actual surface and its surrounding diffusive air.

Internal boundary layers can form between areas of distinct surface properties, whether this be uniform vegetation stands or a homogeneous urban surface (the urban boundary layer). Between adjacent objects where the distance is less than or roughly equal to their height, a canopy layer forms which is dominated by the immediate surroundings. Canopy layers can be found within tree stands as well as in urban areas (the urban canopy layer or “canyons”). Finally, the boundary layer includes “the uppermost layer of the underlying material (soil, water, building material etc.) extending to a depth where diurnal changes of water and heat become negligible” (Oke, 1987).

1.2. Energy and mass exchanges, and balances

Energy in the Earth-atmosphere system mainly exists as radiant, thermal, kinetic or potential energy and is continuously being transformed from one of these four forms into another (Oke, 1987). The exchange of energy between the Earth's surface and the overlying atmospheric layers

occurs through conduction, convection and radiation, which are described in more detail below. For most natural systems, energy input and output can be only considered as balanced when aggregated over long time periods, such as a year. For shorter periods, there is a significant difference between the incoming and outgoing energy, which causes a change in the system's energy storage. This change can be an accumulation or a depletion. An accumulation in a soil-vegetation-atmosphere system will most likely result in an increase in soil and/or air temperature (Oke, 1987). Besides energy, mass is exchanged in the Earth-atmosphere system. Masses such as water, carbon, nitrogen and other substances (including pollutants) are conserved at all times but can be found in different states. For example, water can be present in gaseous, liquid or solid form. Transport occurs via convection, precipitation, percolation and runoff, and the system's mass storage can be measured as changes of water content (air humidity, soil moisture) (Oke, 1987).

The surface energy balance is the balance between incoming and outgoing energy fluxes plus energy storage changes in the upper ground layer with respect to the Earth's surface. The major energy fluxes are the radiation balance (absorption and emission of "natural" electromagnetic radiation by the surface), the conduction heat flux (thermal conduction of heat energy from the surface towards the ground), the sensible heat flux (turbulent transfer of heat energy towards or away from the surface within the atmosphere) and the latent heat flux (turbulent transfer of energy used for condensation of atmospheric water vapour onto the surface or the evaporation of water stored in the soil). There can be additional sources, such as the waste heat of engines (anthropogenic heat flux) or sinks and the metabolic heat produced by biological organisms. Analogous to the mass balance is the balance between the incoming and outgoing mass fluxes plus the mass storage changes.

Both the surface energy and mass balance vary with the magnitude of the input variables and the surface properties, which determine the magnitude of the storage and output terms. The main cycles are the cycles of solar energy (heat) and water (mass). This work focuses on the energy rather than the mass fluxes. The surface heat and moisture fluxes modify the boundary layer (Stull, 1988). The better the energy balance is known, the more precisely the state of the atmosphere close to the surface (i.e. the 2-m air temperature) can be estimated. The state of the near-surface atmosphere is of utmost importance because it directly influences chemical and biological processes and thus surface life conditions at the microscale for plants (Larcher, 2001), animals and humans (Fanger, 1970; Oke, 1987; Jendritzky, et al., 1990; Hoppe, 1993). These conditions even affect the lifetime of pathogens, which increases with temperature, and thus the spread of vector-borne and other infectious diseases (Cook, 1992).

The primary energy source for the whole atmosphere – solar radiation – is mostly transformed at the surface; the energy that is transformed into latent heat stored in water vapour drives atmospheric motions. Other particles which may subsequently act as cloud condensation nuclei originate mainly in the boundary layer. However, around half of the kinetic energy of the atmosphere is dissipated in the boundary layer (Stull, 1988). These and other processes in the

boundary layer contribute to atmospheric processes at a synoptic scale and consequently also indirectly influence life conditions. Therefore, the correct calculation of the surface energy balance is an important feature of all weather forecasting systems (LeMoigne, 2018).

1.3. Heat waves as a threat to organisms

Heat waves present a specific meteorological situation. Heat waves mostly coincide with high-pressure situations, undisturbed radiation and low wind speeds, and they further result in elevated stream temperatures and low soil humidity. There are many ways to characterize a heat wave. The method used in this thesis is by the number of Kysely days, defined as the days of a heat-wave period, which is specified as a period of at least three subsequent days with a daily maximum air temperature greater than 30 °C that continues until the daily maximum air temperature drops below 25 °C (Kysely et al., 2000).

Global warming causes a rapid warming in the Arctic regions (Arctic amplification), which reduces the temperature gradients between the Arctic and mid-latitudes. This effect is expected to result in a wavier jet stream, which would allow weather systems to remain at the same location for a longer period, thereby increasing the likelihood for extreme events such as floods, droughts and heat waves globally (Petoukhov et al., 2013; Francis and Vavrus, 2015; Mann et al., 2017). This process might also be supported by an increase in soil moisture forcing (Teng et al., 2019). Moreover, the decline of the temperature gradient from mid-latitudes to the tropics would result in an increasing height of the tropopause, which could foster a poleward shift of subtropical regimes (Terzy et al., 2020). All these processes indicate a future increase in heat wave length and intensity in Europe, in both rural (Gobiet et al., 2014) and urban areas (e.g. for Paris [Lemonsu et al., 2013] and Vienna [Formayer et al., 2007]). For the 2015 heat wave, which is analysed in this thesis, the resonance of the planetary waves may provide an explanation for the development of this extreme event (Duchez et al., 2016; Kornhuber et al., 2017).

The living conditions and thermal comfort of both aquatic organisms and humans are highly dependent on their own energy balance, which is the result of all incoming and outgoing energy fluxes towards and from the organism's skin. This energy balance causes different organisms' bodies to heat or cool. Because water is highly conductive, the water temperature itself is the main parameter that influences the body temperature of aquatic organisms. Consequently, for the river system the stream water temperature was taken as an indicator for the quality of living conditions and for any potentially lethal conditions for aquatic organisms (Melcher et al., 2015). Stream temperature - an important factor influencing the physical, chemical and biological properties of rivers and thus the habitat of aquatic organisms - is linked to climate. Consequently, freshwater biodiversity is highly vulnerable to climate change, with extinction rates exceeding those of terrestrial taxa (Heino et al., 2009). Stream temperature is highly correlated with the assemblages

of fish and benthic invertebrates along the river course (Melcher et al., 2015). In particular, the duration and magnitude of the maximum summer stream temperatures are the key limiting factors for the occurrence of many fish species. High temperatures may produce high physiological demands and stress while simultaneously reducing the oxygen saturation in the water column. Together with the decreased oxygen availability, the increased metabolic requirements pose a severe environmental challenge, which in the worst case produces lethal effects; the average optimum temperature for cold water species is below 16 °C (Matulla et al., 2007; Pletterbauer et al., 2015).

In recent decades, heat waves have also been recognized as a lethal threat to humans around the world (McMichael et al., 2003; Valleron and Boumendil, 2004; Kim and Kyselý, 2009; Hutter et al., 2007; Grimmond et al., 2010). Additionally, the combination of the elevated air temperature during heat waves with high irradiation (Schreier et al., 2013; Otani et al., 2017), humidity (Steadman, 1979a, b) or air pollution (Schnell and Prather, 2017) poses a threat to human health. Air is less conductive, so in urban canopy systems, apart from air temperature, the radiation balance and water vapour content of the air also play an important role in determining the organism's energy balance. Wind speed acts on the laminar boundary layer and helps to transfer warmed air away from the skin. In practice, air temperature, air humidity, the mean radiant temperature (MRT), which is a quantity that describes the short-wave and long-wave radiation balance of the human body, and wind speed are the main indicators for the quality of living conditions in urban systems. The Universal Thermal Climate Index (UTCI [°C]; Fiala et al., 2001; Broede et al., 2012) is a metric frequently used to summarize the effects of these four parameters. For example, the UTCI is used by meteorological services to quantify outdoor human thermal comfort. It takes into account whole-body thermal effects by utilizing a multi-node thermophysiological model. The UTCI is derived from the air temperature, the water vapour pressure, the MRT at pedestrian level and wind speed at 10-m height (Jendritzky et al., 2012; Weihs et al., 2012).

Generally, vegetation has different strategies to adapt during heat stress (Larcher, 1987). Plants can change their optical properties (albedo) to reduce absorbance and increase reflection, thereby altering the short-wave energy balance (Ehleringer, 1976). Furthermore, the thermal properties of the plants' environment can change due to dried surface soil layers and dry leaves, which serve as an isolation layer. Another strategy is to change the geometric properties of vegetation by alterations in leaf inclination and loss of leaves to reduce the received solar radiation. Some plants react with increased evapotranspiration during heat episodes, while evaporation tends to be limited during extreme heat due to saturated air or lack of available soil moisture (Hagen et al., 2014; Trimmel et al., 2018a). High temperatures, high solar radiation and low soil humidity can cause heat stress for trees, which can subsequently force them to modify their interaction with the atmosphere (Penuelas et al., 2009). Increases in short-wave radiation caused by higher reflections can also increase thermal stress for vegetation (Hillinger, 2017). Many species alter their optical and thermal properties by changing their leaf colour and water content. In extreme cases, they

radically change their canopy geometry by losing leaves (Teskey et al., 2015). Apart from their biophysical properties, their biogeochemical properties can also change, that is, transpiration rates adapt to the situation (Teskey et al., 2015). Extreme conditions can be lethal for many plants if their adaptation possibilities are exhausted (Niu et al., 2015). In cases where no migration or adaptation is possible because the changes occur too rapidly or more favourable climate zones cannot be reached, the affected species can become extinct (Dullinger et al., 2012). These changes directly affect the energy fluxes. Under such conditions, vegetation tries to negatively feedback the temperature increase. However, during extreme stress the feedback stops, which further increases temperatures. During such high temperatures, the emission of biogenic volatile organic compounds (BVOC) can peak (Guenther et al., 1991). BVOCs can react with NO_x and consequently facilitate the formation of tropospheric ozone, which is toxic to both humans (WHO, 2006) and vegetation (Fishman et al., 2010) and contributes to global warming because it acts as a greenhouse gas (IPCC, 2013). An additional effect is that vegetation suffering from water deficit results in a significant decrease in ozone dry deposition (Emberson et al., 2000; Lin et al., 2020). Thus, tree stress can seriously affect air quality and human wellbeing (Vautard et al., 2005).

1.4. Research questions

The energy balance fundamentally defines the magnitude and amplitude of the ecosystems' state variables. According to IPCC (2007) ecosystems are vulnerable to these changes in state variables depending on their level of exposure (e.g. location in an area of rapid climate change and an intense urban heat island [UHI]), their sensitivity (degree to which the system is affected by atmospheric changes) and their adaptive capacity (ability to adjust or cope with the impact). Ecosystems are sensitive to existing environmental conditions such as heat waves or UHIs. Moreover, such systems are at risk due to their amplification by climate change, which increases their exposure. Inland waters are sensitive ecosystems, which react very directly to changes in air temperature, with only limited adaptive capacity for the resident fauna due to restricted migration potentials. Urban areas are already the home to a majority of the global human population, and this trend continues to grow. This fact makes urban areas next to their high exposure also very sensitive.

This thesis focuses on the effect of surface energy balance changes during present and future heat waves on riparian and urban ecosystems. The analysis is guided by following research questions:

1. What are the surface energy balance and the surface energy heat fluxes of riparian and urban systems during heat wave conditions?
2. How do changes in surface properties affect the energy balance and the selected state variables of riparian and urban systems?
3. How does vegetation affect riparian and urban systems?
4. How is the behaviour of riparian and urban systems expected to change due to climatic changes?
5. How are the living conditions of organisms affected?

To answer these overarching research questions, two case studies have been performed combining measurements and numerical modelling. Both studies analyse the surface energy balance changes caused by human planning measures and their effects on the state of the following surface parameters: ground/water temperature, near-surface air temperature, humidity and the radiation balance. Extreme heat wave events for present and future climates are chosen as the time periods for both studies. Finally, numerical models have been validated with measurements and further used for model simulations in both studies.

In the first study, the key analysed system is the water body in a pre-alpine Eastern Austrian river, which in forested sections is highly influenced by the canopy layer and its state variable water temperature. In the second study, the key analysed system is the urban canopy layer of the Viennese urban agglomeration and its state variables canyon air temperature, radiant temperatures, air humidity and wind speed. In addition, the energy fluxes and the energy balance of the urban canopy layer, which determines which values are fed back to the atmospheric model, are charted. In both studies, the effect of heat waves on organisms are investigated. For the riparian system, aquatic organisms are identified as the most affected targets. For the urban system, the effect of different urban configurations on the human population in the Viennese urban agglomeration is analysed.

Within the dissertation period, a total of four first-author and nine co-author journal articles were produced. In addition, six first-author posters and three oral contributions to national and international conferences that address the research topics were presented. From this pool of work, three first-author and three co-author journal articles were selected to be included in this thesis, which focuses on the main research questions outlined above. The selected articles and my own contributions to them are listed in Annex 1. These documents will be referred to as [Ax] hereinafter.

2. Methods

This section summarises the methods used in the scientific work of the dissertation. In addition to literature research, the following steps were performed: the measurements needed for model validation were taken, gridded static data (e.g. land cover, vegetation zone or soil classification) and dynamic observational data (e.g. soil moisture, lateral boundary conditions of air/water temperature) were prepared, land cover scenarios were developed and numerical simulations were conducted.

2.1. Measurements and evaluation

For this thesis, the data necessary for site-level analysis and model evaluation was collected at 64 sites between 2012 and 2014 (Trimmel et al., 2017a). In the pre-alpine riparian systems studied, the air temperature, air humidity and solar radiation were measured in vertical and cross-sectional profiles in the riparian zone. Water temperature and light received by the river bed were measured along the river covering 51 km. [A1] analyses a subset of these measurements: the hourly water temperature for the medium-sized river Pinka during a heat wave at low flow conditions. The effect of riparian shading on stream water temperature is also analysed in this study. The measurements were subsequently utilized for evaluating the model Heat Source (see [A2]) . This deterministic model includes, for example, the shading processes from topography, river bank and vegetation and the reflections on the river surface and bed. Heat Source was updated, improved and tested for application to Eastern Austrian lowland rivers. The Heat Source model is used to assess the influence of meteorological components on stream temperature and simulation accuracy under heat wave conditions. The forward propagation of measurement imprecision on simulated water temperature was calculated. The total model imprecision caused by measurement errors of sky obstructing elements (+1.24/-1.40 K) was found to exceed the error caused by measurement errors of meteorological input parameters (+0.66/-0.70 K). The most important sky obstructing elements are vegetation height and density. For the urban systems studied, the TEB (Town and Energy Balance) model and the modelling platform SURFEX (Surface Externalisée), which are described in Section 2.2 below, were used. The UTCI has been included in the TEB model to provide standardized information about human thermal comfort for grid resolutions >100 m and with highly parameterized building morphology.

Both models have been validated by the model developers (e.g. Masson et al., 2002), and the model errors are found to be relatively small. The study of the urban system was focused on the city of Vienna. Vertical irradiance and reflections (see [A4]), surface temperature and wind speed (see [A5]) within one urban canyon were measured. To this end, eight air temperature and humidity sensors were distributed in multiple street canyons to represent the different urban climate zones of Vienna (see [A6] – Supplement A). In [A4], the potential increase of solar irradiation and its influence on PV facades inside an urban canyon facilitated by increasing the ground albedo was measured and simulated. Similar to riverine spaces, in urban spaces solar radiation fundamentally affects living conditions of organisms. Apart from solar radiation, the long-wave radiation emitted from urban surfaces plays an important role for human living conditions in urban areas. In [A5], the surface temperatures of typical surfaces were measured to determine the absolute values and spatial differentiation within an urban canyon.

2.2. Numerical models

The river and urban systems are both exposed to similar atmospheric conditions but have distinct surface characteristics, which are caused by geometric, optical and thermal properties, along with water availability and additional factors that differ between surfaces (Figure 2.1). To calculate the effect of land cover changes and obtain reliable estimates of the surface energy fluxes and the state of the atmosphere close to the surface, deterministic numerical models were utilised to resolve the surface energy balance. In this thesis, specific models were used for each system studied.

The models can be applied in different configurations to answer different questions. For example, they can be run stand-alone, in coupled modes and using different scales. Point, longitudinal, 2D and 3D microscale and 3D atmospheric models can be distinguished, and each type needs different meteorological forcing. The point, 2D and 3D microscale models well resolve microscale processes (1–100 m) and were used to capture the effect that the meteorological forcing and changes in surface properties have on the near-surface conditions such as in the urban canopy layer. The longitudinal stream temperature model captured the changes in energy balance caused by meteorological forcing and changed surface properties, but also the advection of stream water (500–100,000 m) and thus the influence of the upstream on the downstream. The 3D atmospheric model includes the advection of air parcels and vertical mixing within the boundary layer to take account of interactions between the surface conditions and the atmospheric layers above. In coupled mode, the processes captured in both models are linked to improve the results.

Heat Source (Longitudinal)

For the river system, the 1-D energy balance and hydraulic model Heat Source (Boyd and Kasper, 2003), which was developed and is maintained by the Oregon Department of Environmental

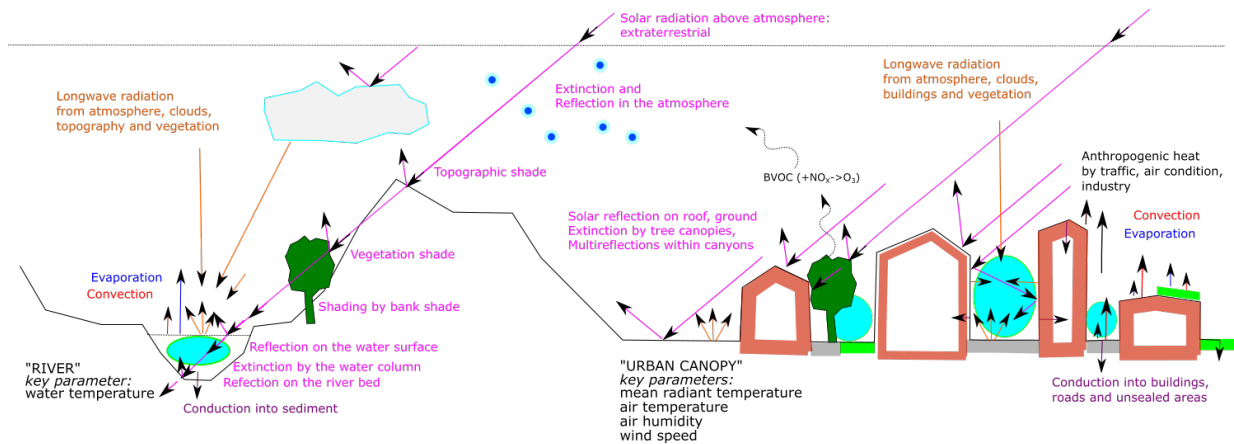


Figure 2.1.: Overview of the main energy fluxes and processes in two analysed systems

Quality (DEQ), was used to solve the energy balance equations for the water surface and determine the stream water temperature. The short-wave energy balance was determined as the balance between the incoming direct and diffuse short-wave solar radiation and the part of it that is reflected from the Earth's surface. The long-wave energy balance was determined as the balance between the radiant temperature of the sky, clouds, surrounding objects and surface. All parts of the radiation balance are found to be greatly altered by horizontal obstruction or shading, whether these effects are due to topography, buildings or vegetation. The conduction heat flux in this case was dependent on the heat gradient between the water temperature and the sediment. The latent heat flux was determined using the Penman method (Penman, 1948) by taking into account the difference between the saturated vapour pressure and the vapour pressure of the ambient air, the wind speed, the horizontal obstructions, the radiation balance, the slope of the saturation vapour versus air temperature curve, the density of water, the latent heat of vaporization and the psychrometric constant. The sensible heat flux was determined via the Bowen ratio approach by multiplying the gradient between the temperature of the ambient air and surface temperature with the psychrometric constant and dividing it by the saturation-ambient vapour pressure difference. The calculation of stream water temperature is dependent on not only the specific heat capacity and mass of the medium water and the energy balance but also the advection defined by flow velocity and river morphology. Heat Source was used in this thesis to calculate the energy balance along the river surface and the stream temperature from near the source to the lower reaches.

Solar long-wave environmental irradiance geometry (SOLWEIG) model (3D microscale)

The solar long-wave environmental irradiance geometry model (SOLWEIG; Lindberg et al., 2008 2018) estimates the spatial variations of 3D radiation fluxes and MRT in complex urban settings. The SOLWEIG model calculates the short-wave and long-wave radiation fluxes from six directions and was used in this thesis to derive the MRT. The model ingests direct, diffuse and global short-

2. Methods

wave incoming radiation, air temperature, relative humidity, urban geometry and geographical information. Additional vegetation and ground cover information was utilized to improve the estimation of MRT. In [A5], an improved prediction of wall and ground surface temperatures for SOLWEIG is presented. For vertical surfaces, a parameterization based on global radiation instead of solar elevation was implemented. For ground surfaces, a two-layer force-restore method to calculate ground temperature for different soil conditions was included. As demonstrated in [A5], the canyon air temperature was calculated using TEB methods, and a good agreement was found between modelled and measured air temperature.

Surface Externalisée (SURFEX) model (2D)

For the urban system, different models have been used. In [A6], the complex land surface model SURFEX (Boone, et al., 2017) was applied. SURFEX is a surface modelling platform developed by Météo-France in cooperation with the scientific community. It is composed of various physical models for natural land surfaces, urbanized areas, lakes and oceans. For each gridpoint, the energy and mass fluxes for all occurring land surfaces are calculated and aggregated depending on their spatial share. SURFEX was used in this thesis to jointly use below mentioned schemes together with others on a two dimensional domain.

Interactions between soil-biosphere-atmosphere (ISBA) model (Point)

The interactions between soil-biosphere-atmosphere scheme (ISBA; Noilhan and Planton, 1989; Mahfouf and Noilhan, 1996) computes the exchanges of energy and water between the soil-vegetation-snow continuum and the atmosphere above. The force-restore method with three layers for hydrology was employed (Bhumralkar, 1975; Blackadar, 1976) to obtain the prognostic equations for the surface temperature and its mean value over one day. One energy balance is considered for the ground-vegetation system. Heat and mass transfers between the surface and the atmosphere are related to the mean values of surface temperature and liquid water, respectively. The net radiation at the surface is the sum of the absorbed fractions of the incoming solar radiation and of the atmospheric infrared radiation, reduced by the emitted infrared radiation. The turbulent fluxes are calculated using the classical aerodynamic formulas. The sensible heat flux is dependent on the difference between surface temperature and temperature at the lowest atmospheric level, specific heat, air density, wind speed, and the drag coefficient depending on the thermal stability of the atmosphere. The water vapour flux E is the sum of the evaporation of liquid water from the soil surface and from the vegetation. Soil heat flux is characterized as the heat flow along the thermal gradient. The soil thermal conductivity and heat capacity are functions of soil properties and moisture. ISBA was used within this thesis to determine soil moisture and water vapour flux on natural surfaces as precise as possible. Additionally, vegetation parameters derived from ISBA

such as LAI were used.

Town and Energy Balance (TEB) model (Point)

The TEB model was specially designed by Masson (2000) to represent the exchanges between an idealized urban canyon and the atmosphere. This model is based on the canyon concept, where a town is represented with a roof, a road and two facing walls, which play a key role in the town energy budget by trapping a fraction of the incoming solar and infrared radiation. All heat and moisture fluxes over urban areas are calculated using an aerodynamic resistance (or conductance) network approach. This approach utilizes the difference between the surface temperature of the considered surface (roof, road, wall) and the air temperature (either above the roof or in the canyon) and an exchange coefficient term. For horizontal surfaces, formulations that take into account the vertical atmospheric stability effects are used. Heat conduction from the building surface towards the inside is calculated using a finite difference method for the roof, wall and floor surfaces separately. The building energy model (BEM; Bueno et al., 2012), which is coupled to the TEB model, considers a single thermal zone, one thermal mass to represent the thermal inertia of the materials indoors, the heat gains from solar radiation transmitted through glazing and internal heat sources, infiltration and ventilation. TEB was used in this thesis to estimate air temperature, MRT, wind speed and humidity varying with urban surface parameters within the urban canyon as precise as possible.

Model of Emissions of Gases and Aerosols from Nature (Point)

The Model of Emissions of Gases and Aerosols from Nature (MEGAN; Guenther et al., 2012) is a framework of mechanistic algorithms accounting for the main known processes controlling the BVOC of vegetation. Its purpose is to estimate the fluxes of biogenic compounds between terrestrial ecosystems and the atmosphere. Biogenic emissions are strongly dependent on the state variables within the tree canopy, especially the incoming photosynthetically active radiation, air temperature and soil humidity. MEGAN was used forced by SURFEX results in this thesis and used to estimate whether during heat waves the emission of BVOC and potential interactions with ozone formation can play a crucial role to deteriorate living conditions in the urban system.

2.3. Initial and boundary conditions

Generally, the performance and output precision of these models is mainly dependent on (1) the initialization values and (2) the precision and correctness of the surface properties, which are also frequently referred to as background estimates (Lahoz, 2010). The initialization values (i.e. soil temperature, soil moisture) are derived from previous forecasts or observations. From this starting

2. Methods

point, the air, water, wall or soil temperature is calculated for each consecutive time step.

Representation of surface properties

Each model requires information about the composition and texture of the simulated surface. In this thesis, a basic parameter used for this purpose was the distribution of land cover types. The available data sources were scoped, but an individual analysis was performed for the riparian system to identify forests, agricultural surfaces and urban areas in great detail. Combining information about future urban development new data sets were created to define the future land cover distribution. Depending on the model employed, the surface can be described using different properties, including optical (e.g. albedo, type of reflectance, emissivity), geometric (geographic position and orographic height, inclination, river width, surface roughness, openness to sky: sky view factor [SVF] or leaf area index [LAI], ratio of wall to horizontal surfaces) and thermal properties (thermal conductivity and heat capacity), as well as water availability for evaporation or transpiration. Additional information such as data on anthropogenic heat sources, parameters for heating, ventilation and cooling (HVAC) systems, window fractions and more were collected. This information was compiled from different raw data sources, the author's own measurements and relevant literature. Next, these data were processed, with any spatial or temporal gaps filled if necessary, and then patched and corrected to derive continuous data. Finally, the data were converted to the input format required by the model. For the SURFEX, TEB and MEGAN models, different geoinformation (GIS) systems and custom scripts were developed to pre-process the necessary geodata.

Meteorological forcing for present and future heat wave conditions

The objective of this section is to define the meteorological conditions for representative heat wave events in the present and future climate.

River system: Here, stand-alone longitudinal simulations along the river centreline during present and future heat waves were performed. To obtain data for present heat wave conditions, the INCA (Integrated Nowcasting through Comprehensive Analysis; Haiden et al., 2011) data set, which is based on observations, was used. Comparison with our on-site reference station indicated an r^2 of 0.99 and an RMSE of 0.67 K for consecutive hourly measurements during the summer half year of 2013.

To obtain future meteorological conditions at the reference station, data were extracted from 25 km resolution runs of the regional climate model ALADIN (<http://ensembles-eu.metoffice.com/>), driven by the global climate model ARPEGE; Déqué et al., 1994). The RCM runs were bias corrected using the quantile mapping technique (Déqué, 2007) based on the E-OBS data set (Haylock et al., 2008) and scaled. In a second step, the data were spatially localized to a 1 km \times 1 km grid encompassing the area under investigation utilizing the INCA data set. In a third

step, the data were temporally disaggregated from a resolution of 1 day to 1 h. Temperature was disaggregated based on the daily maximum and minimum temperatures using three piecewise continuous cosine curves (Koutsoyiannis, 2003; Goler and Formayer, 2012). The temperature data were elevation corrected with a lapse rate of 0.65 °C per 100 m.

Urban system: Here, different model configurations were used for both present and future heat waves. First, the point model TEB and the 3D microscale models SOLWEIG were employed. For the main analysis, the high-resolution 3D atmospheric WRF model was used in coupled mode with TEB. Finally, TEB was integrated into the modelling platform SURFEX as a 2D model for the inner WRF-TEB domain and used in stand-alone mode using WRF and WRF-TEB data as meteorological forcing. For the heat wave with a 15-year return period for present climate conditions (see [P6]), the atmospheric WRF model was utilized to downscale the ECMWF analysis data set for present-day conditions (temporal resolution of 6 h, horizontal resolution of 9 km; <https://www.ecmwf.int/en/forecasts/datasets/set-i>) via two intermediate nests (3 km and 1 km resolution) using one-way grid nesting to a 333-m resolution domain covering the city of Vienna. For the future heat wave, the lateral boundary conditions for a heat wave that fulfils the air temperature criteria (41.3 °C average 5-day daily maximum air temperature) were taken from a high-resolution regional climate scenario simulation. This simulation was based on the global model GFDL-CM3 (Donner et al., 2011), which was forced with the RCP8.5 emission scenario and downscaled with the WRF model (Michalakes et al., 2001) with an optimized set-up for the Alpine region (Arnold et al., 2011).

3. Results and Discussion

This chapter contains the synthesis of the main results of the selected research articles which comprise this cumulative thesis.

3.1. Surface energy fluxes during heat wave conditions

1. What are the surface energy balance and the surface energy heat fluxes of riparian and urban systems during heat wave conditions?

River system: In [A2], it is shown that both net short-wave radiation and evaporation are the most influential components in the evolution of stream water temperature under heat wave conditions and that both are subject to shading by topography and vegetation. During heat waves, long-wave radiation and sensible heat flux are mostly positive, so evaporation is the main energy flux that causes cooling of the surface. Typically, the primary input into the system is solar radiation, which is transformed into the other energy fluxes. It was demonstrated that during heat wave conditions the short-wave radiation balance contributed 64% of the total input, while the long-wave radiation balance and sensible heat flux accounted for 11% and 25% of the total energy input, respectively. Latent heat flux was responsible for 100% of heat loss from river water (Figure 3.1). This process is caused by the high air temperatures in relation to the stream water temperature. In riparian systems, where water is not a limiting factor, evaporative cooling can reach its maximum (see [A2, A3]).

Urban system: In urban systems, due to the high sealing levels, evaporation capacity and thus latent heat flux are very low. The main daytime heat fluxes considered in this thesis are the long-wave and short-wave radiation fluxes (sum of fluxes in the order of 800 W/m^2), the sensible heat flux (in the order of $100\text{--}200 \text{ W/m}^2$) and the conduction heat flux. The radiation balance is increased during heat waves because of the high irradiation levels which are typically observed due to clear-sky conditions under the prevalence of stable high-pressure areas. Over natural or artificial soil surfaces, soil humidity and vegetation transpiration rates determine the latent heat flux. The results indicate that the lower the latent heat flux is, the higher the sensible heat flux becomes. Thus, when low surface soil humidity occurs during heat stress, it reduces the cooling ability of the surface and can cause a further increase in air temperature close to the ground (see

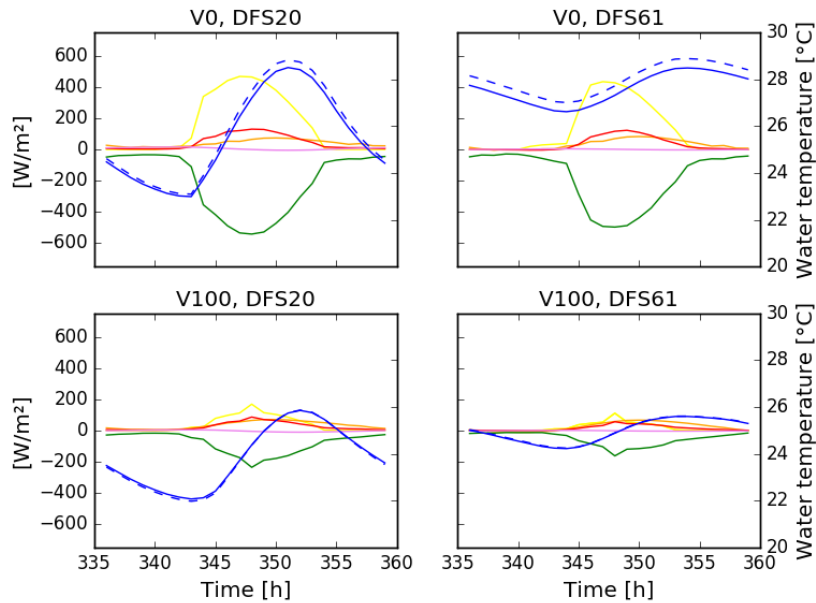


Figure 3.1.: Diurnal amplitude of all energy fluxes (green: latent heat flux, yellow: radiation balance, red: sensible heat flux, purple: conduction heat flux) for an upstream (DFS 20 km) location and a downstream location (DFS 61 km) for no vegetation (V0) and maximum vegetation (V100) blue: stream water temperature for mean low flow, blue dashed: mean low flow minus 15% (Figure 6, [A3])

[A6]). If high conduction heat flux is facilitated due to heat absorptive materials (e.g. traditional massive brick buildings), this can cause a reduction of air temperatures at the beginning of the heat wave, especially during daytime. At night, the building material radiates this energy back into the canyons and urban boundary layer, which results in elevated minimum canyon air and radiant temperatures. As the heat wave proceeds, the daytime benefits of these absorptive materials diminish.

3.2. Influence of surface properties

2. How do changes in surface properties affect the energy balance and the selected state variables of riparian and urban systems?

The energy balance of a surface is significantly determined by its optical properties, especially the albedo, which alters the reflected portion of incoming radiation and thus the radiation balance (see [A4]). This finding is in agreement with Trimmel et al. (2012). Furthermore, the energy balance of a surface is substantially altered by its thermal properties, especially thermal conductivity and thus conduction heat flux (see [A5]). This result is in agreement with earlier findings regarding green roofs (Scharf et al., 2012) and buildings (Trimmel et al., 2018c). The energy balance of a surface can be significantly altered by latent heat flux. The amount of latent heat flux depends on

water availability, radiation balance, wind speed and air temperature. For water surfaces, water availability is not a limiting factor, and the influence of the other energy fluxes could be studied (see [A2, P3]). Primarily, water temperature was found to be highly sensitive to the presence, density and height of riparian vegetation (see [A2]), so these parameters were determined as precisely as possible (see [A2, A3]). For land surfaces, the soil moisture availability plays an important role (Trimmel et al., 2012 2018c; [A6]). Urban thermal comfort was found to be very sensitive to the surface properties dominant in an urban open space (see [A5]). This result is in agreement with earlier findings from Trimmel et al. (2012) and Hagen et al. (2014). Therefore, for [A4, A5 and A6], the parameters were also defined as precisely as possible.

River system: In riverine systems, geometric aspects such as riparian shading by topography and trees are of great importance (Figure 3.1, 3.2). They influence the radiation balance by limiting the amount of incoming solar radiation and also reduce the long-wave radiation loss. Moreover, shading obstacles reduce the turbulent exchange with the air above the canopy, which leads not only to a reduced heating of the canopy air temperatures during the day but also a reduced cooling of the canopy air temperatures at night, in comparison to the conditions outside the canopy. This canopy thermal environment is propagated to the stream temperature. In the case of missing shade, the diurnal amplitude is more pronounced during heat waves. This effect was evident in the analysed system, where the water temperature differs by about 3 K between shaded and non-shaded rivers.

Urban system: In the urban canopy system, the main state variables affecting living conditions are MRT, air temperature, humidity and wind speed. All these variables are highly dependent on the surface properties of an urban structure. Wind speed is influenced by the geometry (orientation, SVF), humidity by the available moisture and turbulent exchange facilitated by urban geometry, MRT within the canyon by the thermal and optical properties of the ground and wall, and the urban geometry and air temperature by all the above-mentioned parameters.

Changes in sealed and built area

The most effective human actions that can change the energy balance by altering surface properties in the urban canopy system are the sealing of unsealed surfaces and the construction of buildings. Strongly sealed but sparsely and low-built areas, such as the industrial areas in the south-east of Vienna, heat up as strongly as the centre during daytime, but cool down more than the centre at night. Thus, the centre stays warmest at night. Compared to the dry rural surroundings during heat wave conditions, the daily amplitude is damped for all subregions (see [A6]). The larger the urban area, the higher the difference in near-surface air temperature between the urban centre and rural surroundings (UHI intensity), both during the day and at night (Table 1). To study this effect, three scenarios were analysed. First, a reference scenario (“R”), which assumes a present-day

urban area. Second, an urban sprawl scenario (“S”), where the urban area is spread beyond the current extent towards a potential maximum level driven by population growth without any change in urban materials. Third, an optimized (“O”) scenario, which indicates the minimum extent achievable assuming the same population growth combined with increases in albedo and reductions in the thermal conductivity of urban materials. “R” exhibits a smaller UHI intensity than “S”. The denser the building structure, the more the daily amplitude is dampened, similar to a low-pass filter. For a densification of the building fraction of the “industrial” and “low-density residential” urban areas from 16% and 22% respectively to 24.2% without a change in building height (11 m on average), a mean increase in minimum air temperature of 0.1 K and 0.6 K in minimum MRT was simulated during an extreme heat wave (see [A6]). Assuming a higher increase in fraction of the built area (+25%) for the category “compact low rise”, which is a subcategory of “low-density residential”, next to the increase of the minima, a reduction of canyon air temperature of up to 1 K was simulated (Trimmel et al., 2017b).

Changes in material properties

In [A4], the effect of albedo changes in a 15-m wide street canyon were measured and simulated. The results demonstrated an increase of about 0.13% vertical irradiance for local albedo changes from 0.13 to 0.77. In [A6], local street and facade albedo increases of 0.14 and 0.2 respectively to 0.3 and a roof albedo increase from 0.15 to 0.68 indicated a reduction in the maximum canyon air temperature during heat wave conditions of 0.2 K. The maximum MRT, however, was increased by 2.3 K due to the higher reflection. At night, both air temperature and MRT were reduced. Other studies have found that albedo can reduce the air temperature during daytime by around 1 K (Weihs et al., 2018; Žuvela-Aloise et al., 2018). In [A5], it is shown that using different surface wall and ground configurations a decrease of about 1.5 K in both the maximum canyon air temperature and the human thermal comfort index UTCI can be achieved.

In this regard, changes in thermal conductivity showed the greatest effect. If the thermal conductivity of buildings was reduced, as demanded by the zero-energy standard in the Energy Performance of Buildings Directive (<http://data.europa.eu/eli/dir/2018/844/oj>), the canyon air temperature increased during the day (up to 1.5 K compared to the current standard construction), but it was also reduced at night [A6]. This result is in line with the pre-study by Trimmel et al. (2017b). This effect reduces the UHI at night, but increases it during the day. During the course of the heat wave, the canyon air temperature decreased more strongly each night compared to the reference scenario (see [A6 – Figure 9]).

	MIN		delta	MAX		delta
	1988-2017	2036 - 2065		1988-2017	2036 - 2065	
	ur/ru(ur-ru)	ur/ru(ur-ru)	ur(ur-ru)	ur/ru(ur-ru)	ur/ru(ur-ru)	ur(ur-ru)
R	24.8/21.8(3.0)	28.0/23.4(4.6)	3.2(+1.6)	34.2/34.5(-0.4)	40.9/42.5(-1.6)	6.7 (-1.3)
S	25.2/22.0(3.2)	28.2/23.4(4.8)	3.4(+1.6)	34.2/34.6(-0.4)	40.9/42.5(-1.6)	6.7 (-1.2)
O	24.0/21.5(2.5)	27.4/23.5(3.9)	2.6(+1.4)	33.9/34.5(-0.6)	40.6/42.4(-1.7)	6.5 (-1.1)

Table 1: 2 m air temperature minima/maxima °C for statistically selected heat waves with a 15 year return period for present and future mid century climate conditions for Viennese central districts (ur) and an rural reference area (ru) of 9 km² for actual urban configuration (R), an urban sprawl scenario (S) and an optimized scenario with increased building density, higher albedo and improved insulation (O).

3.3. The effect of vegetation on energy balance during heat waves

3. How does vegetation affect riparian and urban systems?

River system: In [A3], tree stands considerably alter the surface energy fluxes depending on their height and density (Figure 3.2). Thus, vegetation can strongly reduce the short-wave but also long-wave radiation balance received by the ground or water surface by reflection on different height levels above the ground. Furthermore, forests impede the long-wave radiation loss during the night. The sheltering from trees reduces the turbulent air exchange and turbulent heat fluxes (see [A2, A3]). Thus, the trees effectively dampen temperature extremes within their canopy. Measurements in [A1] indicated that stream temperature directly responded to air temperature, cloudiness and riparian shade. A downstream warming of 3.9 K was observed in unshaded areas, whereas a 3.5 K downstream cooling was recorded in shaded areas.

Urban system: The ratio of vegetated surfaces versus sealed and built areas is very important for the energy balance of urban systems and is a key factor to understand the change of 2-m air temperature in urban agglomerations (see [A6]).

Effects of Evaporation

Evaporative cooling is strongly dependent on available soil moisture. In the studies conducted in this dissertation, the changes caused by local extensive green roofs to the canyon air temperature are marginal (see [A6]), which is consistent with prior research (e.g. Hagen et al., 2014). Moreover, the cooling effects decline when the available water in the roof substrate is fully consumed towards

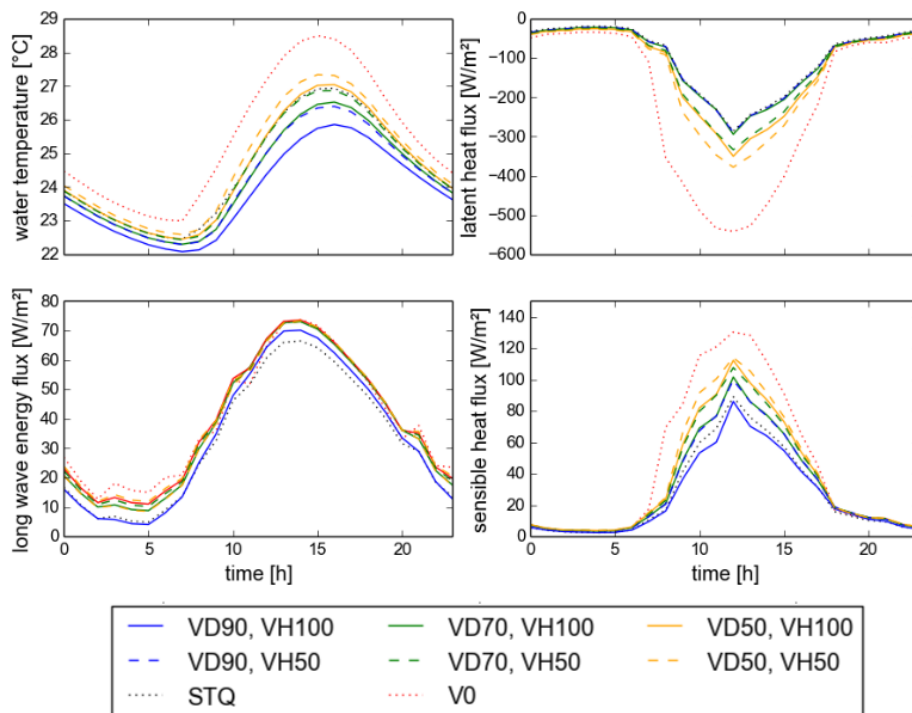


Figure 3.2.: The effect of the vegetation scenarios of maximum vegetation height (VH100) and 50% vegetation height (VH50), natural dense vegetation (VD90), natural light vegetation (VD70), sparse vegetation (VD50), V0 (no vegetation) and STQ (actual vegetation) on the diurnal amplitude of water temperature and the air-temperature-dependent energy fluxes long-wave radiation, sensible and latent heat fluxes for the 20-year return period events of the final day of the climate periods centred on 2085 for mean low flow conditions (MLF) for an upstream location (DFS 20 km) (Figure 7, [A3])

the end of the heat wave and the latent heat flux seizes (see [A6]). The literature indicates that within the street canyon, evapotranspiration has a more notable effect. Especially the maximum air temperatures at street level can be reduced by the unsealing of urban surfaces and the associated evaporative cooling (Hagen et al., 2014). The maximum cooling generated during heat wave conditions caused by the evapotranspiration of city-wide vegetation (not shading) within the city modelled by deMunck et al. (2018) varied between 0.5 and 2 K. This range lies far above the 0–0.2 K simulated local effects of green roofs established by [A6].

Effects of Shading

Trees within urban canyons help to reflect the major part of short-wave radiation at the top of the canyon instead of allowing it to enter and heat the canyon surfaces. Thus, (tree) shade is a fundamental method to reduce MRT and thus improve human thermal comfort during the clear-sky conditions throughout heat wave periods. In two pre-studies (Trimmel et al., 2012; Hagen et al., 2014), tree plantations showed the greatest effect for urban spaces (compared to lawn and water surfaces), especially in areas shaded by the trees. Moreover, the relative position of the green/water areas and the trees was not irrelevant for their microclimatic influence (Trimmel et al., 2012). Although the influence of tree shade on wall, road and canyon temperatures is not considered in [A6], the main influence of tree shade is demonstrated, namely the reduction of direct radiation, by presenting the MRT in the sun and shade. By using this tree shade proxy, a difference of 25 K between sun and shade was simulated. Wang et al. (2018) simulated the effect of radiative cooling (not evapotranspiration) of trees in the built environment of urban areas in the contiguous United States and found an average decrease in near-surface air temperatures of 3.1 K. The authors demonstrate that trees not only reduce incoming solar radiation during daytime but also increase radiative cooling at night. The conduction heat flux is reduced in intensity in the shaded areas. The evaporative and shading effects of urban trees simulated together on confined open spaces at a local scale led to a reduction of up to 3–9 K in air temperature in the pre-study by Loibl et al. (2014).

3.4. Expected changes due to climatic changes

4. How is the behaviour of riparian and urban systems expected to change due to climatic changes?

River system: For an air temperature change of 2 K, we modelled a 1.3 K change in water temperature for unshaded reaches, but lower effects for shaded reaches (see [A1]). Daily variations were also (up to 4 K) lower in shaded reaches (see [A1]). In the analysed riparian system, the minimum temperatures are expected to increase more than the maximum temperatures (see [A2]). Shading measures have the greatest effect on the maximum temperatures (Figure 3.3). This

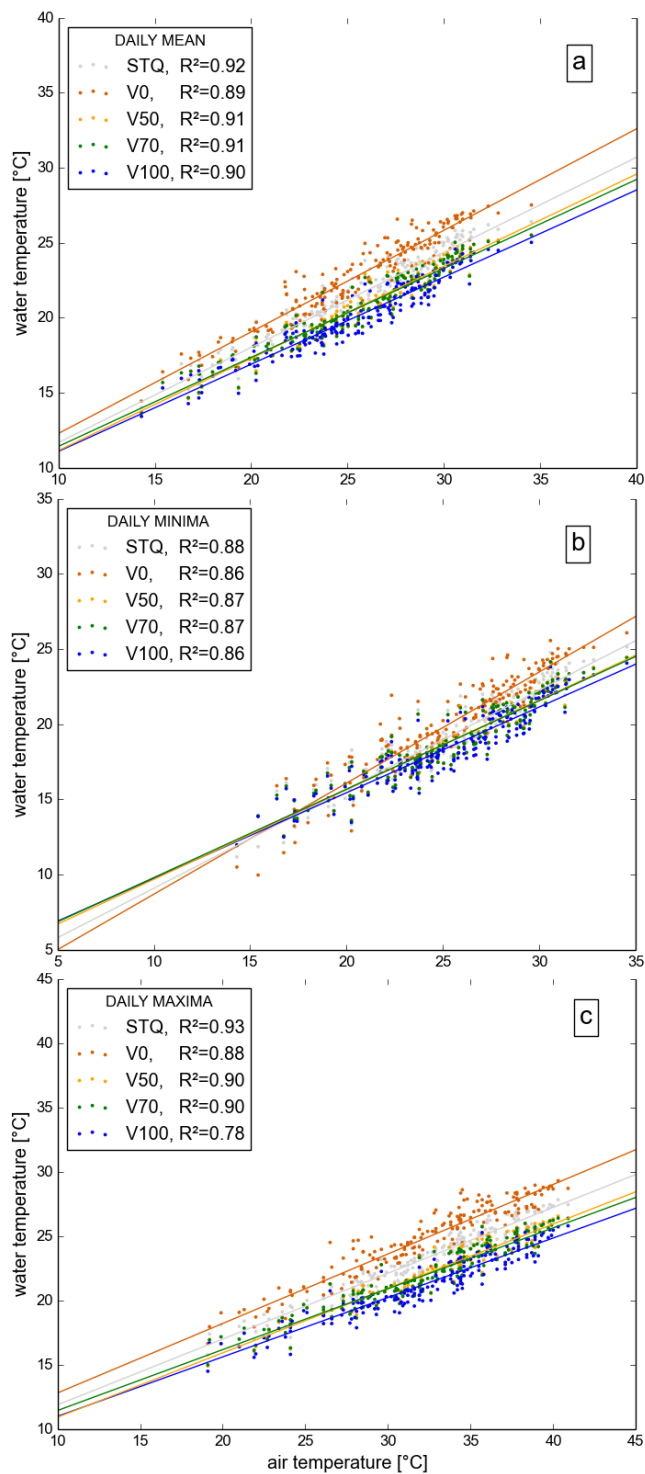


Figure 3.3.: Correlations between water temperature and the daily (a) mean, (b) minima and (c) maxima air temperatures for the 1a, 5a, 20a and Max episodes of the climate periods centred at 2030, 2050 and 2085 for existing vegetation (STQ), no vegetation (V0), vegetation height of 50% (V50), vegetation of 70% density (V70) and full vegetation (V100) reported with the squared Spearman rank correlation coefficient. ANCOVA showed significant interactions between vegetation and air temperature ($p < 0.001$) (Figure 8, [A3])

outcome indicates the following dilemma: even if the shading is effective at present, elevated temperatures in a warmer world could cause river warming to levels lethal to the many occurring fauna. Vegetation could reduce stream temperature during heat waves when conditions of high solar radiation predominate. Even when the maximum vegetation extent with the maximum height and density including plantations and replacement plantings was assumed, the additional riparian vegetation was found to be unable to fully mitigate the expected temperature rise caused by climate change. However, during extreme heat waves, maximum stream temperatures could be reduced by 2.2 K and mean temperatures by 1.6 K. The removal of existing vegetation amplified stream temperature increases and could cause an increase of maximum and mean stream temperatures by 1.8 and 1.3 K, respectively, in comparison with the status quo vegetation scenario. With complete vegetation removal, maximum stream temperatures in annual heat events at the end of the century could increase by more than 4 K compared to present levels. Daily amplitudes were found to be reduced by riparian vegetation, and the timing of the peak temperature was delayed by about 1 h. A reduction of vegetation density by 20% was found to cause a similar effect to a 50% reduction of vegetation height. Vegetation was able to reduce maximum temperatures more effectively on an absolute scale but also reduced the trends significantly compared to the no-vegetation scenario. The minimum temperatures were found to increase most.

Urban system: The air temperature calculated for selected subregions of Vienna increases by up to 7 K for the maximum canyon air temperature and by 2 to 4 K for the minimum canyon air temperature for the actual and future heat waves (see [A6]). Both heat waves are characterized by multiple Kysely days (Kysely et al., 2000) and tropical nights ($T_{min} > 20\text{ °C}$). Both cases exhibit a strong increase in maximum canyon air temperature during extreme heat waves compared to the mean annual air temperature increase of 3.5 K published by Gobiet et al. (2014), which also refers to the A1B instead of the more extreme RCP8.5 emission scenario (IPCC, 2013). It is interesting to note that the projected up to 7 K increase in maximum canyon air temperature (Figure 5, [A6]) is twice as large as the increase projected for the mean annual temperature in Austria (3.5 K), while the minimum canyon air temperature was projected to increase by the same magnitude as the mean annual temperature. As a result, the daily temperature range is projected to increase. Such an increase in daily temperature range was also found by Cattiaux et al. (2015), and it could also be partly attributed to the decreasing surface evaporation due to soil moisture depletion predicted for future European summers (Jasper et al., 2006). This process disproportionately affects rural regions, which are even more severely affected by reduced soil moisture than urban areas with high sealing fractions. Moreover, a decrease of soil moisture was also simulated in this thesis. Drier soils have a lower heat capacity and can cool more strongly than wetter soils. This effect relates to the high values of maximum air temperature in the rural subregion during the day as well as the low values of minimum air temperature during the night. Furthermore, this explains the increase in nocturnal canopy UHI, which is expected to increase from 3 to 4.6 K by

mid-century and is caused by the smaller increase of minimum temperatures in the rural areas than within the city. The nocturnal UHI for an urban sprawl (S) scenario was slightly increased by 0.2 K compared to the reference scenario. The nocturnal UHI of an optimized material usage scenario (O) was reduced by 0.7 K (Table 1). The actual and future UHI was dominated by the mesoscale thermal regime. The future UHI was affected by high temperature reinforced by dry fields in the surroundings, a process known to occur during heat waves (Fischer and Seneviratne, 2007; Hartmann, 1994). Fischer and Seneviratne (2007) analysed soil-atmosphere interactions for the 2003 summer heat wave in Europe and found that the precipitation deficits, early vegetation growth and positive radiation anomalies preceding the heat wave contributed to the rapid loss of soil moisture. Zampieri et al. (2009) demonstrated that drought in the Mediterranean region can favour heat wave conditions in Europe at a continental scale due to changes in atmospheric circulation and hot air mass advection. This finding suggests that soil moisture deficits ought to be reduced by suitable methods on a continental scale rather than only at a regional scale. Duchez et al. (2016) and Kornhuber et al. (2017) identify a stationary jet stream position, caused by global-scale circulation patterns, that coincides with observed European temperature extremes, including the 2015 heat wave event.

3.5. Influence on living conditions

5. How are the living conditions of organisms affected?

River system: Global warming has already affected European rivers and their aquatic biota, and climate models predict an increase of temperature in central Europe across all seasons. In [A3], the impact of expected changes in heat wave intensity during the twenty-first century was simulated for a pre-alpine river. The modelled stream water temperature increased less than 1.5 K within the first half of the century. During the second half of the century modelled here, a more significant increase of around 3 K in minimum, maximum and mean stream temperatures was predicted for a 20-year return period heat event. Riparian vegetation would be able to mitigate 1 to 2 K of this increase, while the removal of such vegetation could lead to an increase of more than 4 K for maximum stream temperatures in annual heat events. Such a dramatic water temperature shift, especially in summer, would indicate a total shift in aquatic biodiversity. The result indicates clearly that in a highly altered river system, riparian vegetation cannot fully mitigate the predicted temperature rise caused by climate change but would be able to reduce the water temperature by 1 to 2 K. Conversely, the removal of riparian vegetation amplifies stream temperatures. The results demonstrate that effective river restoration and mitigation require re-establishing riparian vegetation. These findings also emphasize the importance of land-water interfaces and their ecological functioning in aquatic environments.

As [A3] shows, it is highly likely that during extreme events a stream temperature increase

of 2 K will be exceeded during this century. Such an increase corresponds to the magnitude of the temperature differentiation of fish zones, particularly for the occurrence of native cold-water-preferring and warm-water-preferring fish species ((Pletterbauer et al., 2015). At a stream temperature of 20 °C, cold-water-adapted species begin to experience temperature-induced mortality (Melcher et al., 2014; Schaufler, 2015). During a simulated annual heat wave event in the period 2016–2035, this threshold was never exceeded in the uppermost stream region (DFS 13 km), which is currently populated by the cold-adapted species brown trout (Guldenschuh, 2015). At the end of the century, during a heat wave event of a 20-year return period, the threshold would likely be exceeded for 72 of 120 h. At the lower boundary of the trout zone (DFS 20 km), the 20 °C mark was exceeded for 70 of the 120 h during heat waves at the beginning of the century. However, riparian vegetation shade could reduce this period to 9 h. Nonetheless, the mitigation possibilities of vegetation are limited and cannot fully compensate for the whole predicted temperature rise. At the end of the century, in heat waves of a 5-year or shorter return period, even if maximum vegetation was assumed, it was found that the 20 °C mark is likely to be exceeded during the whole heat wave event.

Urban System: [A6] concludes that rising air temperatures will represent an unprecedented heat burden for the Viennese inhabitants, which cannot easily be reduced by measures concerning buildings within the city itself. This heat burden is mainly caused by the expected increase in the maximum canyon and minimum air temperature, which is directly related to the corresponding increases simulated by the global and regional models. Comparing the periods 1988–2017 and 2036–2065, the expected absolute increases of the minimum and maximum air temperature in the central districts of Vienna lie at 2.6–3.4 K and 6.5–6.7 K, respectively. The study results indicate that the most effective measure to reduce maximum air temperature spikes is to increase the albedo of urban roofs. Within the canyon, the already high radiation balance during heat waves is further elevated to critical values. The albedo within the urban canyon should not exceed 0.2/0.3 because additional solar reflections can lead to negative effects on thermal comfort, which is consistent with the findings of Weihs et al. (2018). The most effective measure identified to reduce the minimum air temperature was to decrease thermal insulation. However, this action shows negative effects during daytime as the conduction heat flux is suppressed, while surface temperatures, long-wave radiation and the sensible heat flux all rise, which negatively affects living conditions within the canyon. [A6] showed that by changing both the above-mentioned surface parameters, the minimum canyon air temperature can be reduced by up to 0.9 K and the maximum canyon air temperature by 0.2 K. Wall temperatures can be increased by up to 10 K and MRT by 5 K. The maximum UTCI is expected to change during the extreme heat waves projected for the climate period 2036-2065, from strong (32–38 °C UTCI) to very strong (38–46 °C UTCI) heat stress. This finding is in agreement with other studies regarding future human thermal comfort. For example, Muthers et al. (2010) projected that heat-related mortality could

3. Results and Discussion

increase by up to 129% in Vienna by the end of the century if no adaptation occurs. In addition, Matzarakis and Endler (2010) demonstrated an increase of days with heat stress in the order of 5% per year.

4. Summary and Outlook

The main findings regarding the research questions addressed in this thesis are summarized below.

What are the surface energy balance and the surface energy heat fluxes of riparian and urban systems during heat wave conditions? Within this thesis, it was found for both riparian and urban systems that during heat waves the sensible heat flux contributes to a larger extent to the surface energy balance than during non-heat wave conditions. While the riparian system dissipated heat via the latent heat flux, the urban canopy system dissipated heat via reflected radiation and the sensible heat flux.

How do changes in surface properties affect selected state variables of riparian and urban systems? Changes in horizontal obstruction by topography, buildings or vegetation dampen the diurnal amplitude in both systems, which is critical because the daily minima are increased. Changes in albedo can decrease the air temperature but also increase MRT during the day. Changes in thermal conductivity reduce the conduction heat flux and increase the sensible heat flux during the day, which leads to higher air temperatures. At night, the reduced heat storage results in lower air temperatures in the canyon.

How does vegetation affect riparian and urban systems? In riparian systems, vegetation mainly affects air temperature via its geometry by providing shade from solar radiation as well as shelter. Consequently, long-wave radiation cooling by night and turbulent exchanges are impeded. Trees can help to reduce the solar radiation entering the street canyon and are thus a very important measure to reduce both MRT and air temperatures within the urban canyon. Green roofs can help to reduce the air temperatures via evaporation and albedo increases at roof levels, which are eventually advected and mixed with the canopy air.

How is the behaviour of riparian and urban systems expected to change due to climatic changes? Climatic changes are expected to aggravate the situation in both systems. For the analysed riparian system, it was found that the stream temperature minima will rise faster than the daily maxima. This increase is strongest for the no-vegetation river scenario. For the analysed urban canopy system, it was determined that the benefit of optimized urban materials compared to regular materials is tending to decline. In addition, the nocturnal difference between urban and rural

regions is increasing due to the expected dry conditions in rural areas, resulting in stronger cooling.

How are the living conditions of organisms affected? In both studies, a shift in climatic zones is predicted. In the riparian system, a 2 K shift and the exceedance of the 20 °C mark in stream temperature will drive out cold-water-adapted species from the river Pinka. The urban canopy systems will experience an increase in air temperature by 7 K during day and up to 4 K at night, which will pose a critical threat to the inhabitants not adapted to these increases. It is also possible that heat waves and their corresponding effects on tree stress and BVOC emission might impair human health due to elevated ozone concentrations.

The key methods to reduce the strain on living organisms during heat waves in both river and urban systems are to prevent solar radiation from entering the respective system and to prevent heat being stored within the system. A common method to reduce the temperatures in both systems is to provide shade. For the riparian system, not only shade directly on the water body but also increased shading of the ground within the catchment area can reduce the ground water temperature, increase soil moisture content and decrease near-ground air temperatures, which affect the water body. For urban areas, shading within the canyons provides direct reduction of MRT, which is the dominant factor of thermal discomfort during summer days. Furthermore, shading, like albedo and insulation increases, reduces the heat uptake of building material. In addition, shading in the rural and suburban areas surrounding the city can help decrease the temperature of the advected air. Vegetation shade generates all the benefits that shading by buildings would yield, but without the negative effects of either heat storage in the system and subsequent higher minimum temperatures or heat rejection within the system and subsequent increases in sensible heat flux and air temperatures. The magnitude of a vegetation stand's effect on the energy balance directly relates to its height and density. One measure of the height and density of the forest is the leaf area index (LAI), defined as the total leaf area [m²] per ground area [m²]. It is an essential climate variable (ECV), as defined by the Global Observing System for Climate (GCOS). While we can use LAI to estimate the provided shade and the consequences for the energy balance, we can also estimate the available biomass and the potential BVOCs emitted (Trimmel et al., 2020), which can aid in assessing air pollution potential. Initial simulations regarding emissions of BVOCs within Vienna indicate that reduced soil moisture during heat waves tends to reduce the BVOC isoprene, which is expected to reduce the ozone potential (Trimmel et al., 2020). When sufficient water is available, the isoprene emissions are expected to increase, especially by the *Populus* sp., which are abundantly planted along the Viennese waterways and can be found south-east of Vienna in the floodplain forests. During heat wave situations, the dominant wind speed is south-east. High emitter species can also be found close to the centre along the main traffic routes following the Danube. Furthermore, the forests north and west of Vienna have considerable portions of *Fagus sylvatica* stands, which are known to emit monoterpene. Apart from its potential to contribute to ozone formation during heat waves, drought-stressed vegetation

reduces stomatal ozone uptake, which can exacerbate ozone pollution extremes (Lin et al., 2020).

In general in this thesis it was found that, after soil moisture, the spatial distribution and absolute values of vegetation density, which can also be indicated by the LAI or information regarding the vegetation's water status greatly increase the information about vegetation stands needed to make responsible choices for future spatial and environmental planning. Presently in land surface models key surface properties, such as LAI, can be set constant, be set to follow a climatology or be resolved by supplementary vegetation models. Future research based on these findings could be to include more accurate and timely information in the models based on observations. By including updated information, the modelled values used to provide a more precise estimate of the actual state of the simulated system can be corrected. By including updated and potentially highly spatially resolved LAI values from satellite data, a more realistic representation of vegetation in the models could be provided.

A. Annex: Publications

A.1. Overview of dissertation publications

The dissertation is based on six publications, three SCI articles as first author and three SCI publications as coauthor.

A.1.1. riverine spaces

A1 "The influence of riparian vegetation shading on water temperature during low flow conditions in a medium sized river", (Kalny et al. 2017)

<http://dx.doi.org/10.1051/kmae/2016037>

Own contribution: planning, installation, maintenance, repair, read-out and sanity check of all meteorological and water temperature measurements, preparation of manuscript.

A2 "Application of the model 'Heat Source' to assess the influence of meteorological components on stream temperature and simulation accuracy under heat wave conditions", (Trimmel et al. 2016)

https://www.schweizerbart.de/papers/metz/detail/25/85498/Application_of_the_model_Heat_Source_to_assess_the?af=crossref

Own contribution: preparation of input data, setup of model, improvement of model, simulation runs, validation and analysis, preparation of manuscript.

A3 "Can riparian vegetation shade mitigate the expected rise in stream temperatures due to climate change during heat waves in a human-impacted pre-alpine river?", (Trimmel et al. 2018a)

<https://www.hydrol-earth-syst-sci.net/22/437/2018/>

Own contribution: preparation of input data, simulation of stream temperature, analysis of results, preparation of manuscript.

A.1.2. urban spaces

A4 "Potential increase of Solar Irradiation and its influence on PV-Facades inside an Urban Canyon by increasing the Ground Albedo", (Revesz et al. 2018)

<https://doi.org/10.1016/j.solener.2018.08.037>

Own contribution: technical discussion regarding model, scientific discussion, correction of manuscript.

- A5 "Coupling of urban energy balance model with 3-D radiation model to derive human thermal (dis)comfort", (Oswald et al. 2018)

<https://doi.org/10.1007/s00484-018-1642-z>

Own contribution: preparation of land cover and physical input data, technical discussion and cooperation regarding models (TEB and SOLWEIG), scientific discussion, correction of manuscript.

- A6 "Thermal conditions during heat waves of a mid-European metropolis under consideration of climate change, urban development scenarios and resilience measures for the mid-21st century", (Trimmel et al. 2019b)

https://www.schweizerbart.de/papers/metz/detail/prepub/91938/Thermal_conditions_during_heat_waves_of_a_mid_Euro?af=crossref

Own contribution: planning and help with maintenance of measurements, calculation and processing of urban parameters for usage with all models, development of future urban scenarios, offline TEB and SURFEX/TEB simulations, analysis of all simulations, preparation of manuscript.

A.2. Additional studies contributing and informing work listed in Annex 1

Apart from the dissertation publications many additional prestudies have been performed and publications have been presented and published during the Dissertation period as first author and peer reviewed articles as coauthor (Table 2). Below the publications are listed with full title and corresponding link.

analyzed system		keywords		publication
riverine spaces	methods	simulation	P	Trimmel et al. 2013
	results	stream temperature measurements	A	Trimmel et al. 2017a
		effects on aquatic fauna	A	Melcher et al. 2016
urban spaces	prestudies	green roofs and urban spaces	P	Trimmel et al. 2012
		(green) roofs: thermal performance	A	Scharf et al. 2012
		urban fabric types: microclimate response	A	Hagen et al. 2014
		open space design and UHI effects	A	Loibl et al. 2014
		open space design and microclimate	O	Trimmel et al. 2014
	methods	land use and urban morphology	P	Trimmel et al. 2017b
		albedo and radiation II	A	Revesz et al. 2020
		surface temperature of PV	A	Zsiboracs et al. 2018
	results	vegetation fraction	O	Trimmel et al. 2018b
		UHI and urban growth	P	Trimmel et al. 2018c
		mitigation strategies	O	Trimmel et al. 2018d
		urban growth and thermal comfort	P	Trimmel et al. 2019a
consequences on atmospheric pollution		P	Trimmel et al. 2020	

Table 2: List of peer reviewed and first author publication within the Dissertation period

A.3. Dissertation publications, full texts:

The influence of riparian vegetation shading on water temperature during low flow conditions in a medium sized river

Gerda Kalny^{1,*}, Gregor Laaha⁴, Andreas Melcher³, Heidelinde Trimmel², Philipp Weihs² and Hans Peter Rauch¹

¹ Institute of Soil Bioengineering and Landscape Construction, Department of Civil Engineering and Natural Hazards, University of Natural Resources and Life Sciences Vienna, Peter Jordan-Strasse 82, Vienna 1190, Austria

² Institute of Meteorology, Department of Water, Atmosphere and Environment, University of Natural Resources and Life Sciences Vienna, Gregor Mendel Strasse 33, Vienna 1180, Austria

³ Institute of Hydrobiology and Aquatic Ecosystem Management, Department of Water, Atmosphere and Environment, University of Natural Resources and Life Sciences Vienna, Gregor Mendel Strasse 33, Vienna 1180, Austria

⁴ Institute of Applied Statistics and Computing, Department of Landscape, Spatial and Infrastructure Science, University of Natural Resources and Life Sciences Vienna, Peter Jordan-Strasse 82, Vienna 1190, Austria

Abstract – Stream water temperature limits the growth and survival of aquatic organisms; whereby riparian shading plays a key role in inhibiting river warming. This study explains the effects of riparian shading on summer water temperatures at a pre-alpine Austrian river, during heatwave and non-heatwave periods at low flow conditions. A vegetation-shading index was introduced for the quantification of riparian vegetation effects on water temperature. For maximum water temperatures, a downstream warming of 3.9°C was observed in unshaded areas, followed by a downstream cooling of 3.5°C in shaded reaches. Water temperature directly responded to air temperature and cloudiness. For an air temperature change of 2°C we modelled a water temperature change of 1.3°C for unshaded reaches, but lower changes for intensively shaded reaches. Similar daily variations at shaded reaches were up to 4°C lower than unshaded ones. This study gives clear evidence that for a medium-sized pre-alpine river, restoration practices should consider that discontinuity of riparian vegetation should be less than 6000 m; with more than 40% dense vegetation in order to minimize water temperature increases due to unshaded conditions.

Keywords: riparian vegetation / vegetation-shading index / water temperature / river vegetation management / restoration

Résumé – L'influence de la végétation rivulaire sur la température de l'eau pendant les conditions de faible débit dans une rivière de taille moyenne. La température de l'eau d'une rivière limite la croissance et la survie des organismes aquatiques ; de ce fait l'ombrage rivulaire joue un rôle clé dans la limitation du réchauffement des rivières. Cette étude analyse les effets de l'ombrage rivulaire sur les températures estivales de l'eau dans une rivière autrichienne préalpine, pendant les périodes de canicule et de non-canicule à faible débit. Un indice d'ombrage de la végétation a été introduit pour la quantification des effets de la végétation rivulaire sur la température de l'eau. Pour les températures maximales de l'eau, un réchauffement en aval de 3,9°C a été observé dans les zones non ombragées, suivi d'un refroidissement en aval de 3,5°C dans les zones ombragées. La température de l'eau a répondu directement à la température de l'air et à la nébulosité. Pour un changement de température de l'air de 2°C, nous avons modélisé un changement de température de l'eau de 1,3°C pour les zones non ombragées, mais des changements plus faibles pour les niveaux intensivement ombragés. Des variations quotidiennes semblables dans des zones ombragées étaient jusqu'à 4°C inférieures à celles non ombragées. Cette étude montre clairement que pour une rivière préalpine de taille moyenne, les pratiques de restauration devraient considérer que la discontinuité de la végétation riveraine doit être

* Corresponding author: gerda.kalny@boku.ac.at

inférieure à 6 000 m, avec plus de 40 % de végétation dense afin de minimiser les augmentations de température de l'eau dues aux conditions non ombragées.

Mots clés : végétation riveraine / indice d'ombrage de la végétation / température de l'eau / gestion de la végétation des rivières / restauration

1 Introduction

Stream water temperature is an important and limiting parameter for a number of organisms such as fish or aquatic invertebrates (Broadmeadow and Nisbet, 2004; Matulla *et al.*, 2007; Rahel and Olden, 2008; Logez and Pont, 2013; Pletterbauer *et al.*, 2014). It results from the multiple processes, which influence the gains and losses of thermal energy in streambeds, depending on the amount of stream discharge, topography and atmospheric conditions along the river course (Caissie, 2006). Upstream water temperature and discharge, hyporheic exchange, ground water inflow, bed heat conduction, tributary inflow and its water temperature, turbulent exchange (sensible and latent heat), solar radiation (incident, reflected), and long wave radiation are components of these processes (Moore *et al.*, 2005; Caissie, 2006). Taking into consideration atmospheric conditions, air temperature and incoming short-wave radiation are mentioned as major influencing factors on water temperatures by Evans *et al.* (1998). They recorded total energy gains dominated by a net short-wave radiation of 97.6%. Solar radiation reaching the stream is influenced by different topographic factors, including the prevailing riparian vegetation buffer, which can decrease incoming energy by up to 95% (Rutherford *et al.*, 1997; Moore *et al.*, 2005; DeWalle, 2010). During summer heatwave periods in particular, solar energy plays a key role in influencing stream energy heat budget, and consequently stream water temperature (Johnson, 2004; Leach and Moore, 2010; Groom *et al.*, 2011). Hence shading through riparian vegetation, primarily in small to medium sized and slowly flowing lowland rivers, is often most relevant to avoid excessive heating in order to mitigate adverse effects on the ecosystem (Ghermandi *et al.*, 2009; He *et al.*, 2011; Holzapfel *et al.*, 2013).

Some studies were undertaken to quantify the influence of riparian vegetation on river water temperature, however, they have mainly explored small rivers, with a discharge of up to only 30 l/s (Story *et al.*, 2003; Johnson, 2004; Rutherford *et al.*, 2004; Moore *et al.*, 2005; Gomi *et al.*, 2006). The most widely discussed vegetation parameters of these studies are buffer width, vegetation height and its density. For instance DeWalle (2010) specifies varying minimum buffer widths for sufficient shading, and corresponding water temperature influence, depending on stream orientation. Buffer widths for east–west oriented rivers necessitate a minimum buffer width of 6–7 m, whereas for north–south orientated rivers the buffer width needs to be 18–20 m, and for meandering rivers no more than 12 m. According to Sridhar *et al.* (2004), vegetation width exceeding 30 m distance has hardly any further influence on stream water temperature. However, the height and density of the riparian vegetation have an equal or even higher impact on water temperature (Sridhar *et al.*, 2004; DeWalle, 2010). Davies-Colley *et al.* (2009) and DeWalle (2008) showed that the ratio of canopy height to stream width has particular high influence on stream light exposure and is therefore notably relevant.

Apart from riparian vegetation structures, also the temperature conditions of river and atmosphere determine the cooling effect of vegetation. Cooling occurs when energy gains are reduced by riparian vegetation, which minimizes water temperature increase, so that the influence of cooler water is prevalent (Garner *et al.*, 2014). The cooling effect is greater at high water temperatures, typically occurring during heatwaves and at daily temperature peaks (Moore *et al.*, 2005) whereas there is only a minor effect of vegetation shading on daily temperature minima (Rutherford *et al.*, 2004).

However, these findings primarily apply to smaller rivers, which are usually shallow, so they adjust quickly to incoming solar radiation. Consequently, water temperature changes are rather fast (Moore *et al.*, 2005), and riparian vegetation influence can be high (Poole and Berman, 2001). The effect of shading might be different for larger rivers where water temperature fluctuations are normally lower (Poole and Berman, 2001) and solar radiation may play a different role, but these effects are not fully explored yet. Moreover, studies investigating riparian shade and its impact on stream water temperatures have been carried out in most temperate regions of the world, but up to date only a few studies have been conducted in Europe (Ghermandi *et al.*, 2009; Broadmeadow *et al.*, 2011; Garner *et al.*, 2014; Johnson and Wilby, 2015). So far, studies, focusing on effects of riparian vegetation on water temperature of medium sized rivers are missing, especially for Central European climates where climate change impacts are predicted to be high (Kovats *et al.*, 2014; Laaha *et al.*, 2016).

The aim of this study is to analyse the effects and mitigation evidence of different river type specific riparian vegetation on summer river water temperature, under heatwave and non-heatwave conditions at a medium sized river in Central Europe. The specific objectives are (i) to describe the summer temperature regime during heatwave and non-heatwave periods (ii) to better understand longitudinal riparian vegetation shading impacts on water temperature by introducing a new vegetation-shading index (VSI), (iii) to explore the sensitivity of VSI to the section length used in its calculation and (iv) to validate the effects of shaded and unshaded river reaches on water temperature variations. The findings will be discussed in the light of riparian vegetation management.

2 Materials and methods

2.1 Study site

The study was conducted at the river Pinka, located in the south-east of Austria (Fig. 1). In this area, in particular, climate change impacts are predicted to be high, in terms of an increase of heatwaves and exacerbation of low flow conditions (Kovats *et al.*, 2014; Laaha *et al.*, 2016). The river source is at an altitude of about 1480 m.a.s.l, and it discharges into the river Raab at about 200 m.a.s.l. Along the river, mean discharge increases up to 2.0 m³/s. The study area belongs to the trout,

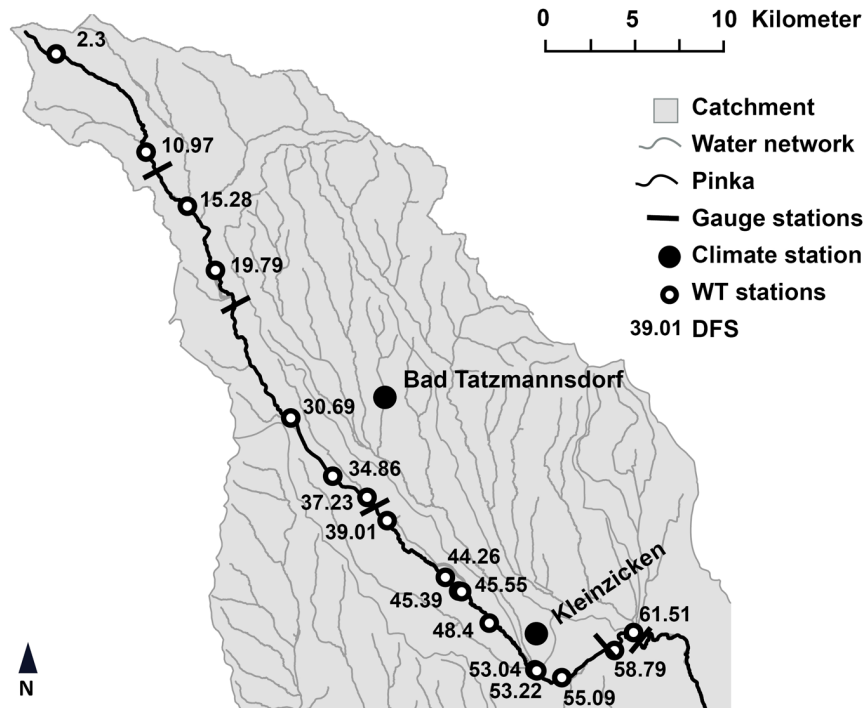


Fig. 1. Study site—the river Pinka from distance from source (DFS) 0–DFS 62 including river course, tributaries, gauge stations, water temperature (WT) measuring stations and climate stations.

grayling and barbel fishzone, bearing 24 fish species and 140 benthic taxa (Melcher *et al.*, 2016).

The catchment is situated at a transition zone of alpine, illyric and continental climate. It is characterised by a mean annual rainfall of about 800 mm, frequent thunderstorms, heavy rainfalls (Cejka *et al.*, 2005) and high temperature amplitudes between summer and winter (Fink *et al.*, 2000). The river Pinka exhibits sound hydro-morphological sections with near natural riparian vegetation and minor land use, as well as highly impacted sections in terms of vegetation cover, in total twelve urban/settlement areas, river geometry and continuity. Substrates are dominated by late tertiary sedimentary rocks and, to a lesser extent, by volcanic rocks (Wimmer *et al.*, 2012). The main hydrological characteristics are summarized in Table 1.

While the entire Austrian river stretch (source to distance from source 62.55 km (DFS 62.55)) was the object of investigations, the river stretch between DFS 30.00 and DFS 50.00 was chosen for detailed analysis. This river stretch has no remarkable tributaries and a rather uniform flow direction. Discharge records were available at four gauges situated at DFS 12.45, 37.75, 58.65 and 62.55 (Fig. 1). For describing the meteorological situation, records of air temperature (AT), hours of sunshine, global radiation and precipitation at two near-by stations Kleinzicken (1.5 km to DFS 52.00) and Bad Tatzmannsdorf (3 km to DFS 38.00) were used.

2.2 Vegetation-shading index (VSI)

Vegetation mapping was performed based on aerial photographs and field measurements. Following DeWalle (2010), Moore *et al.* (2005) and Sridhar *et al.* (2004) we

considered a buffer zone of 50 m from the centreline of the river as being relevant for stream temperature. From aerial photographs we delineated polygons that were homogeneous in terms of land use, vegetation cover and vegetation composition. The polygons were refined by evidence from intensive site visits, where also vegetation height in the form of Koch classes (<5, -10, -20, >20 m), and vegetation density clustered as Braun Blanquet (<5, -25, -50, -5, -100%), see (Traxler, 1997), were recorded. In a following step, the results were transferred from area to point information, using the Arc View sampling extension “TTools” (Kasper and Boyd, 2002). During the process, the information was assigned to cross-sections, every 50 m along the river, perpendicular to the river axis. Ten points were generated every 5 m orographically left and right from the centerline, with vegetation parameters being assigned at each of these cross-sections.

For each 50 m cross-section, VSI was calculated that integrates the parameters vegetation height (h_R), vegetation width (w), and vegetation density (d), as these parameters were found to influence water temperature (WT) most (DeWalle, 2010; Holzapfel *et al.*, 2013). For the VSI of a northwards or southwards flowing river, all vegetation parameters were calculated as mean values of the orographic left and right river bank. When the river was flowing eastwards, the orographically right bank was used for calculations, and when it was flowing westwards the orographically left bank was used. Based on this guideline the VSI is computed as:

$$VSI = \left(\frac{h_R}{h_{\max}} + \frac{w}{w_{\max}} + \frac{d}{d_{\max}} \right) \div 3, \quad (1)$$

Table 1. Hydrological data describing different sites along the river Pinka. Abbreviations: DFS = distance from source, MQ = mean discharge; WT = water temperature measuring point.

DFS (km)	MQ (m ³ /s)	Flow direction (→)	Catchment (km ²)	Strahler order number (→)	Altitude (m.a.s.l.)	Gradient (‰)	River width (m)	Distance from last WT (km)	Minutes from last WT (min)	Average time 500 m (min)
2.3		East		2			2			
10.97	0.4	South	36	3	559	0.036	5			
15.28	1.0	South		4	515	0.014	8	4.49	116	12
19.79	1.0	South	134	5	414	0.008	10	4.51	140	14
30.69	1.0	North		5	342	0.004	13	10.9	336	15
34.86	1.2	East		5	319	0.006	7	4.17	132	13
37.23	1.2	East	172	5	306	0.004	7	2.37	60	12
39.01	1.2	South		5	299	0.004	7	1.78	47	9
44.26	1.2	East		5	279	0.002	10	5.25	235	21
45.39	1.2	East		5	276	0.003	10	1.13	55	14
45.55	1.2	East		5	275	0.003	10	0.16	8	8
48.4	1.2	South		5	266	0.004	10	2.85	125	18
53.04	1.2	North		5	257	0.001	8	4.64	224	22
53.22	2.0	East		6	256	0.001	8	0.18	11	11
55.09	2.0	East		6	249	0.002	6	1.87	76	15
58.79	2.0	East	417	6	244	0.001	6	3.7	139	17
61.51	2.0	North	664	6	240	0.002	5	2.72	119	17

where h_R (%), relative vegetation height, weighted ratio of vegetation height and river width, which is calculated as:

$$\text{if } \frac{\text{vegetation height} * 100}{\text{river width} * 1.5} \leq 100; \text{ then } h_R = \frac{\text{vegetation height} * 100}{\text{river width} * 1.5}; \text{ else } h_R = 100. \quad (2)$$

Note: That multiplication of the river width with 1.5 is due to the fact that a tree height of 15 m generates, at this geographic position, a shade length of 10 m, from 10 a.m. to 2 p.m., and can fully shade the present river width. h_{\max} (%) – maximum vegetation height (=100 %); w (m) – width of the woody riparian vegetation buffer; w_{\max} (m) – maximum vegetation width, (=50 m, as this is defined as maximum width influencing the WT); d (%) – vegetation density = vegetation cover related to ground area; d_{\max} (%) – maximum vegetation density (=100%).

The obtained VSI values range between 0 (no vegetation) and 1 (full vegetation). Because of river flow, WT at a river site will depend on the upstream situation but it is unclear at what section length vegetation will have most influence. We therefore calculated mean VSI values for upstream sections of WT measurement points of various lengths, ranging between 50 m and 10000 m (VSI₅₀ to VSI₁₀₀₀₀). For validating these VSI indices we used the Global Site Factor (GSF), computed from hemispherical photographs (Rich *et al.*, 1999) that were taken at 43 sites between DSF 0.05 and DFS 62.81.

2.3 Selection of the study period

Heatwave events were of particular interest in this project. Hence, the analysis was carried out for the summer of 2013

(1 June–31 August) when record temperatures of 40.5 °C were measured by public meteorological stations in this region. The days were classified into non-heatwave periods (NK), heatwave periods (K) and extreme heatwave days (K+) following Kyselý *et al.* (2000). According to this definition, a heatwave period (K) is characterised by at least three subsequent days with maximum air temperatures (AT_{\max}) ≥ 30 °C and continues until the AT_{\max} drops below 25 °C or the mean AT_{\max} of the period is below 30 °C. Extreme heatwave days (K+) additionally have clear sky conditions ($\geq 80\%$ of possible sun hours – defined by (MeteoSchweiz)), precipitations below 1 mm/day and discharges of a maximum of 75% of the mean discharge (used as a threshold for low flow conditions).

For comparison of sunny and cloudy days additionally, single consecutive days with clear sky conditions ($\geq 80\%$ of possible sun hours) and cloudy conditions ($\leq 50\%$ of possible sun hours), with no intermediate rain, were selected (Tab. 2).

2.4 Measurement and analysis of water temperature

Data sets concerning river WT were collected at a spatially distributed network of 17 HOBO Pendant Temperature Data Loggers 8K*UA-002-08 along the river Pinka (Tab. 1 and Fig. 1). Data was sampled hourly, from June 2013 until August 2013. We analyse the relationships between water temperature along the river with meteorological variables and with the VSI by means of Spearman's rank correlation (r_s). In addition, we analysed the relationships between impotent parameters by linear regression.

2.5 Numerical water temperature model

In order to gain a better understanding of the influence of riparian shading on the change in WT_{\max} the energy balance

Φ_{total} along the river was calculated using the model HEAT SOURCE version 9 (Boyd and Kasper, 2003). The model is based on the following energy balance equation:

$$\Phi_{\text{Total}} = \Phi_{\text{Evaporation}} + \Phi_{\text{Convection}} + \Phi_{\text{Longwave}} + \Phi_{\text{Solar}} + \Phi_{\text{Conduction}}, \quad (3)$$

where Φ_{Total} is the energy balance, $\Phi_{\text{Evaporation}}$ the evaporation flux, $\Phi_{\text{Convection}}$ the convection flux, Φ_{Longwave} the long wave radiation balance (all referring to the stream surface), Φ_{Solar} is the short wave energy, which is absorbed by the water column,

Table 2. Two 5-day periods with consecutive days of clear sky and cloudy conditions and the according maximum air temperatures (AT_{max}). Abbreviations: DFS=distance from source; NK=non-heatwave period; K=heat wave period.

Date	% possible sun	Discharge (DFS 37.75)	AT_{max} (°C)	Period
13.07.2013	58	0.69	24.8	NK
14.07.2013	72	0.68	26.4	NK
15.07.2013	28	0.68	25.5	NK
16.07.2013	92	0.6	26	NK
17.07.2013	92	0.63	28.6	NK
29.07.2013	86	0.44	36.9	K
30.07.2013	48	0.43	27.9	K
31.07.2013	36	0.43	28.7	K
01.08.2013	82	0.42	30.6	K
02.08.2013	92	0.41	34.3	K

and $\Phi_{\text{Conduction}}$ the conduction flux. The model was validated for use in the research area in a study by Trimmel *et al.* (2016).

WT increase (ΔT) caused by energy gains was calculated by using the following formula:

$$\Delta T = \frac{Q}{c \cdot m}, \quad (4)$$

where Q is the heat energy input (W/m^2) into the river, m the water mass (kg) and c the specific heating capacity of water.

Possible ground water (GW) influences were analysed in the area between DFS 37.75 (38) to DFS 58.65, by considering the discharge volume (WV) of the tributaries Zickenbach (Zick), Teichbach (Teich) and Gerentbach (Ger). The WT of these assumed inflows was then incorporated, and the resulting WT (WT_R) of the river Pinka was estimated using the formula as follows:

$$WT_R = \%WV_{38} * WT_{38} + \%WV_{Zick} * WT_{Zick} + \%WV_{Teich} * WT_{Teich} + \%WV_{Ger} * WT_{Ger} + \%WV_{GW} * WT_{GW}, \quad (5)$$

where $\%WV_{38}$ = percentage of the water volume at DFS 37.75.

3 Results

3.1 Riparian vegetation

In the upper reaches of the river Pinka (from source to DFS 20.00), the mean VSI_{50} was 0.69, which reveals a high level of shading, and points to areas of rather high, wide and dense riparian vegetation, often featured by commercial forests (Fig. 2a). Downstream of DFS 20.00, the river flows through

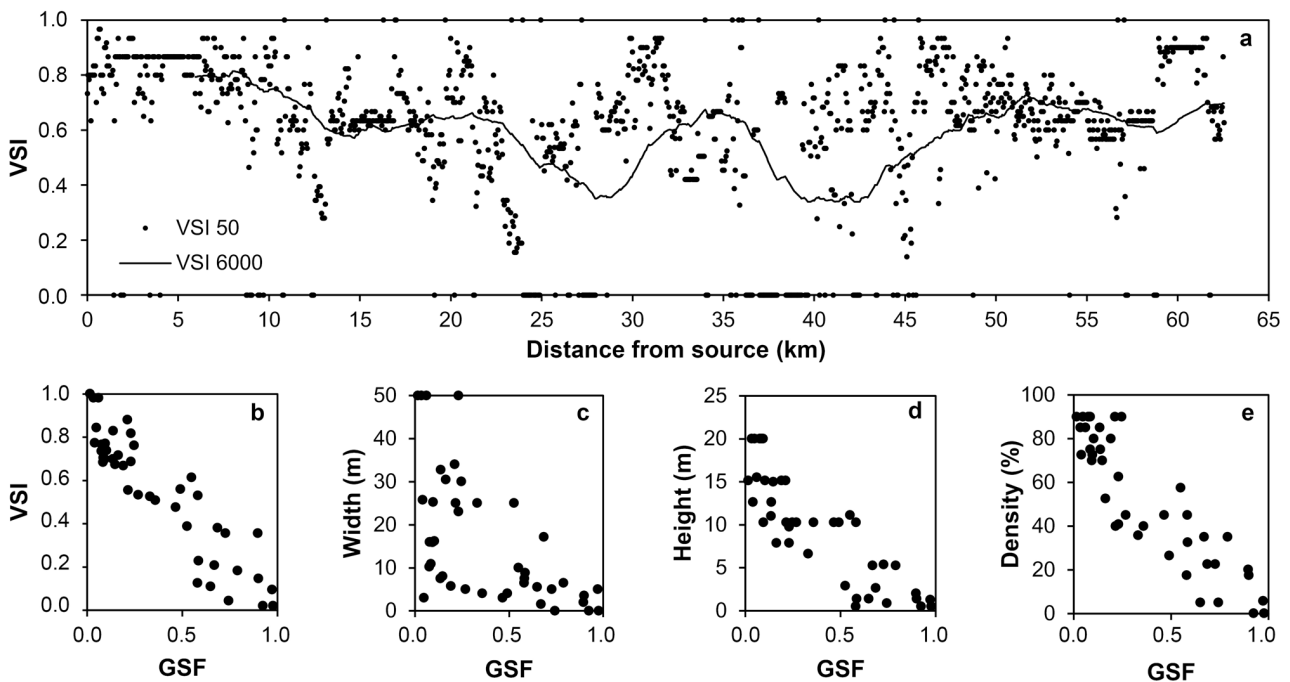


Fig. 2. (a) Distribution of the longitudinal vegetation-shading index (VSI) values of the river Pinka, referring 50 m sections upstream of the water temperature measuring points, as well as 6000 m sections. The scatter plots show the ratio of Global Site Factors (GSF) and VSI_{50} (b), as well as the vegetation parameters width (c), height (d) and density (e).

settlement areas and agricultural lands. The VSIs for these middle and lower reaches were more diverse, 16% of the river stretch showed a VSI_{50} below 0.2 and 62% had a VSI_{50} above 0.6. Particularly notable was the very low mean VSI_{50} of 0.15 from DFS 37.00 to DFS 39.65. This section had almost no riparian vegetation and consequently no vegetation shading effect (Fig. 2). In terms of longer stretches, the VSI_{6000} showed two deep depressions between DFS 20.00 and DFS 50.00, dropping down to 0.35 and 0.34.

The VSI values were compared with GSF values from the hemispherical photographs. The correlation coefficient (r_s) between GSF and VSI (Fig. 2b) was 0.8 during times of highest sun elevation, and 0.9 for the GSF over the whole day ($p < 0.01$). The high correlation coefficients underline the appropriateness of the newly proposed VSI for characterising vegetation shading. Vegetation parameters height, width and density (Fig. 2c–e) cannot reach higher correlations.

3.2 Hydro-meteorological conditions

Figure 3 shows the hydro-meteorological conditions of summer 2013 for the study area. According to the Kysely classification the summer of 2013 is characterised by two heatwave periods (K): from 17th June 2013 to 23rd June 2013, and from 23rd July 2013 to 9th August 2013, which amounted, in total, to 25 days (Fig. 3a). These two periods included 16 clear sky days and 20 days without any precipitation. Extreme heatwave days (K+) were defined on 2nd, 3rd, 6th, 7th and 8th August 2013 additionally taking into account days with a discharge of less than 75% of the mean flow.

The temporal patterns of precipitation and discharges at DSF 12.45 and 37.75 km are presented in Figure 3b. There were only few and mostly minor precipitation events during the summer of 2013. Consequently, the discharges steadily decreased and reached a minimum at 3rd August 2013, corresponding to a low flow event. WT shows temporal development that is reverse to the discharge (Fig. 3c) as would be expected.

Figure 4 shows the distribution of WT along the river. On average, daily mean water temperatures (WT_{mean}) increased, from about 9.4 °C to 18.7 °C, WT_{max} increased from 10.4 °C to 20.4 °C. During heatwave periods (K), average WT_{max} increased much stronger, up to 24.4 °C at DFS 62.55, and even to 26 °C during the extreme heatwave days (K+). However, there was no steady increase in WT from source to DFS 62.55. Especially noticeable is the decrease of WT_{max} in the extreme heatwave days (K+) of 4.7 °C, from DFS 39.01 to DFS 53.22. This decrease was much lower during the non-heatwave period (NK) it was only 3 °C. Such increases and decreases were mainly observed for WT_{max} and daily water temperature range (WT_{range}), whereas variations were small in WT_{mean} (Fig. 4c,d). The highest WT values in all periods were measured at DFS 39.01; a low shaded area, where at extreme heatwave days (K+), on average, values of $WT_{range} = 6.9$ °C and $WT_{max} = 28.2$ °C, were reached. This issue will further be explored in a later section.

For the middle reaches (DFS 30.00 to DFS 50.00), which represent conditions without considerable inflows, we assessed the dependence of WT on meteorological parameters. Spearman correlations coefficients (r_s) point to a strong

relationship between WT_{max} and AT_{max} , with values between 0.85 and 0.94 ($p < 0.01$). In addition, we observed significant, but lower correlations (about 0.5) with global radiation, and with sun hours as well.

3.3 Effects of VSI section length on water temperature

Figure 5 illustrates the VSI as a function of WT_{max} , WT_{range} , WT_{mean} and daily minimum water temperatures (WT_{min}), during the extreme heatwave days (K+) in the middle reaches (DFS 30.00 to DFS 50.00), for the different river section lengths from 50 m and up to 10000 m upstream of the WT measuring points. Mostly negative correlations are observed, illustrating that a higher VSI is related with lower WT. The strengths of the correlation strongly depended on the section lengths and the WT parameters. WT_{max} and WT_{range} were the most highly correlated parameters (Fig. 5). Correlations for these parameters increased when increasing the considered river section length for VSI calculation from 50 m to 6000 m, from -0.34 to -0.73 for WT_{range} , and from -0.5 to -0.82 for WT_{max} . However, larger river section lengths again led to a decrease of the correlations. The calculated VSIs for river section lengths from 4000 m to 7000 m, showed the highest correlations with values of about -0.7 . The statistically best performing VSI value was calculated for a section length of 6000 m with -0.82 for WT_{max} and -0.73 for WT_{range} . Consequently, VSI_{6000} were considered as most representative in this study. In contrast, much lower correlations were observed for WT_{min} and WT_{mean} with a correlation coefficient of -0.05 (WT_{min}) and -0.42 (WT_{mean}) for VSI_{6000} . They represent more the night conditions; hence, they do not depend so much on radiation and shading effects. We will therefore focus on WT_{max} and WT_{range} in the subsequent analyses.

Similar relationships were also observed between WT_{max} and selected vegetation parameters with correlations coefficients (r_s) between -0.77 (vegetation width) to -0.84 (vegetation density). Vegetation height showed a lower correlation with a coefficient of -0.55 .

3.4 Impact of shading and cloudiness on water temperature

Observing successive days with differing cloud cover conditions (Tab. 2), but same discharges, WT_{max} reacted in different ways. During the heatwave period (K) greatest increases and decreases in WT could be seen from DFS 34.86 to DFS 53.22 (Fig. 6a). On the 29th July 2013, a clear day, WT_{max} rose from DFS 34.86 to DFS 39.01, by 3.9 °C to WT_{max} values of 28.8 °C. The river morphology of this stretch is heavily impacted by river regulations and low amount of riparian vegetation which results in a mean VSI_{50} of 0.31. The 14.21 km long river stretch downstream of DFS 39.01, has a more natural appearance with dense riparian vegetation buffers (mean $VSI_{50} = 0.61$). Henceforth, WT_{max} decreased from 28.8 °C down to 23.8 °C. On the 30th July 2013, a mean cloudy day, WT_{max} at DFS 39.01 had a lower peak of 25.1 °C with lower warming (1.1 °C) and cooling (2.6 °C) gradients. These gradients decreased even more on the 31st July 2013, a cloudy

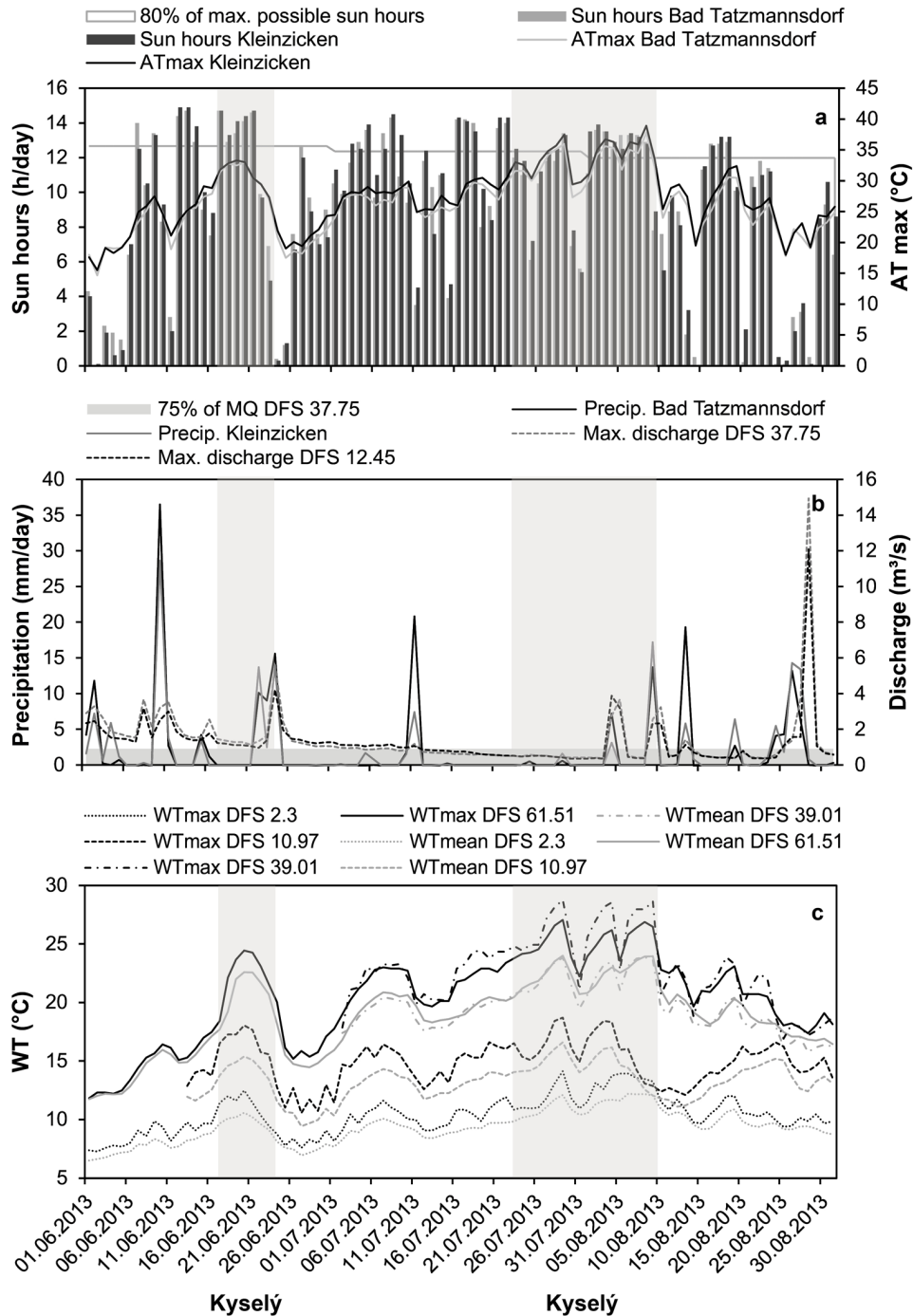


Fig. 3. Hydro-meteorological characteristics of the summer of 2013 at the Pinka region: (a) daily maximum air temperature (AT_{max}), and sun hours per day measured at the climate stations Kleinzicken and Bad Tatzmannsdorf, (b) daily precipitation (precip.) at the same climate stations, and the resulting discharges at two gauges (DFS 12.45 and 37.75), and (c) daily maximum and mean water temperatures (WT max and WT mean) at selected sites along the river Pinka (DFS = distance from source). The heat wave periods (Kysely) are shaded in grey.

day. On 1st August 2013, and 2nd August 2013, two clear days, WT_{max} rose back to precloud conditions. Figure 6b shows the same tendencies in the non-heatwave periods (NK). Daily WT_{min} remained stable during both periods. Since no precipitation occurred during these periods, and discharge volume remained at the same level, we anticipated that the influence of ground water on WT is similar on all days. Consequently the key element for changing WTs is the

incident solar radiation influenced by the appearance of riparian vegetation.

3.5 Daily variations of water temperature

Considering the VSI_{6000} of the river sections, there was a clear difference in WT behaviour. In the extreme heatwave

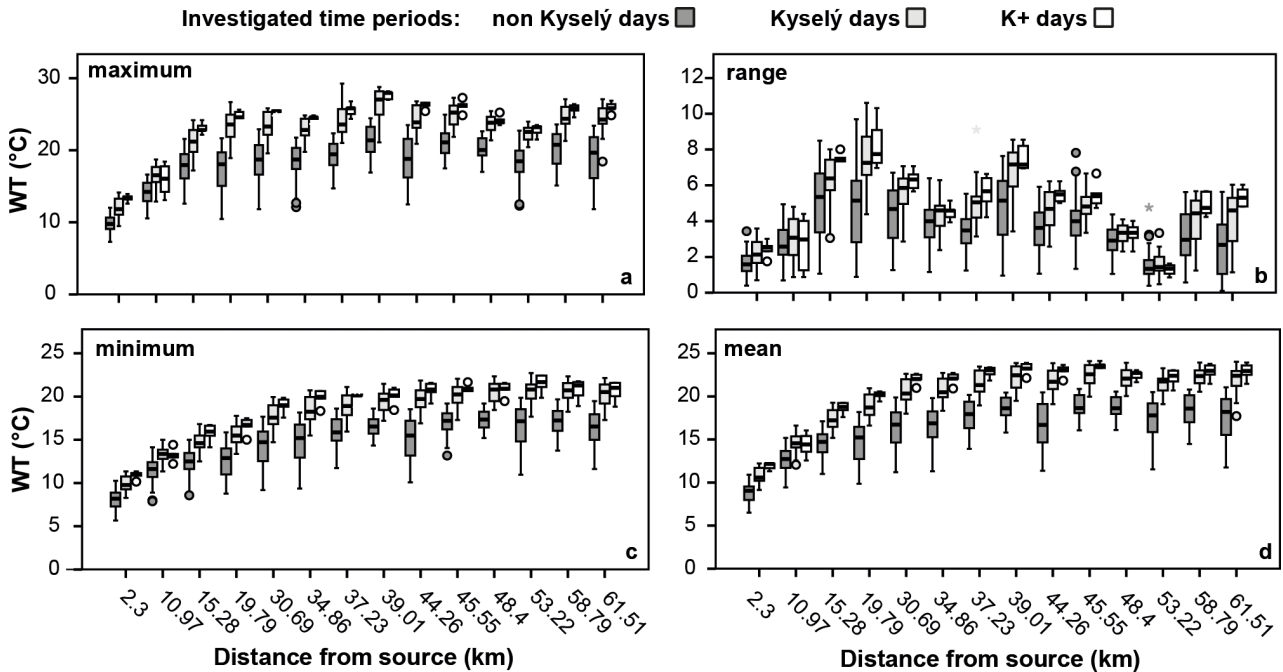


Fig. 4. Distribution of water temperature (WT) at the different WT stations along the river Pinka during summer 2013, for periods of non-heatwave periods (non-Kyselý), heatwave periods (Kyselý) and extreme heatwave days (Kyselý+) respectively. With (a) WT maximum, (b) WT ranges, (c) WT minimum and (d) WT mean.

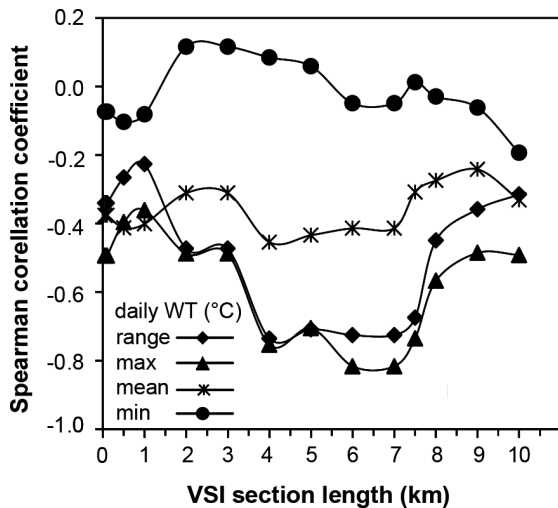


Fig. 5. Absolute spearman correlation coefficients of the vegetation-shading index (VSI) to the daily water temperature (WT) parameters, related to the specific VSI section lengths. The data from WT stations is related to distance from source (DFS) 30.00 and DFS 50.00 on extreme heatwave (K+) days.

days (K+) a WT_{max} of $28.1^{\circ}C$ was reached earliest at 1 p.m. at DFS 39.01, a very sparsely shaded section (VSI_{6000} 0.37). Opposed the most shaded areas (VSI_{6000} above 0.6) reached mean WT_{max} of $23.6^{\circ}C$ from 6 p.m. to 9 p.m. (Fig. 7). The WT_{range} amounted to $7.6^{\circ}C$ for the unshaded, to an average of $5.3^{\circ}C$ for medium shaded and to an average of $3.6^{\circ}C$ for highly shaded upstream conditions. In the heatwave and non-heatwave periods, the temporal curve progression was quite

similar, except that the entire curve had a temperature offset. In the extreme heatwave days (K+) mean WT_{max} was $6.7^{\circ}C$ higher than in non-heatwave periods (NK).

3.6 Correlation of water and air temperature

WT_{max} and AT_{max} are highly correlated. Figure 8a shows scatter-plots for selected WT stations. The slopes of the $WT_{max}-AT_{max}$ regression line is low in the upstream reaches, whereas the slopes much higher at locations between DFS 30.69 and DFS 61.51. However, the slopes of the regression lines also depend on the VSI value (Fig. 8b). The analysis of the interrelationship between different slopes of the $WT_{max}-AT_{max}$ regression line and the riparian vegetation (Fig. 8c-f) revealed that steeper slopes indicate a lower VSI and therewith a higher impact of the AT on the WT. Considering these correlations, Table 3 shows the calculated WT changes due to an AT increase of $2^{\circ}C$.

3.7 Field data validation by a numerical river temperature model

The energy balance of two sites with different vegetation structures (full vegetation DFS 46.00/no vegetation DFS 39.01), was simulated by HEAT SOURCE, using formula (3). Energy balance never dropped below $0W/m^2$ during the daytime in both cases, independent of cloudiness (Fig. 9). At the time of highest sun elevation on a clear day, the maximum values of the energy balance varied from $194W/m^2$ (Fig. 9a), for areas without vegetation, to $35W/m^2$ (Fig. 9b) for fully vegetated areas. Vegetation structures had less impact during cloudy conditions with a difference of just $39W/m^2$.

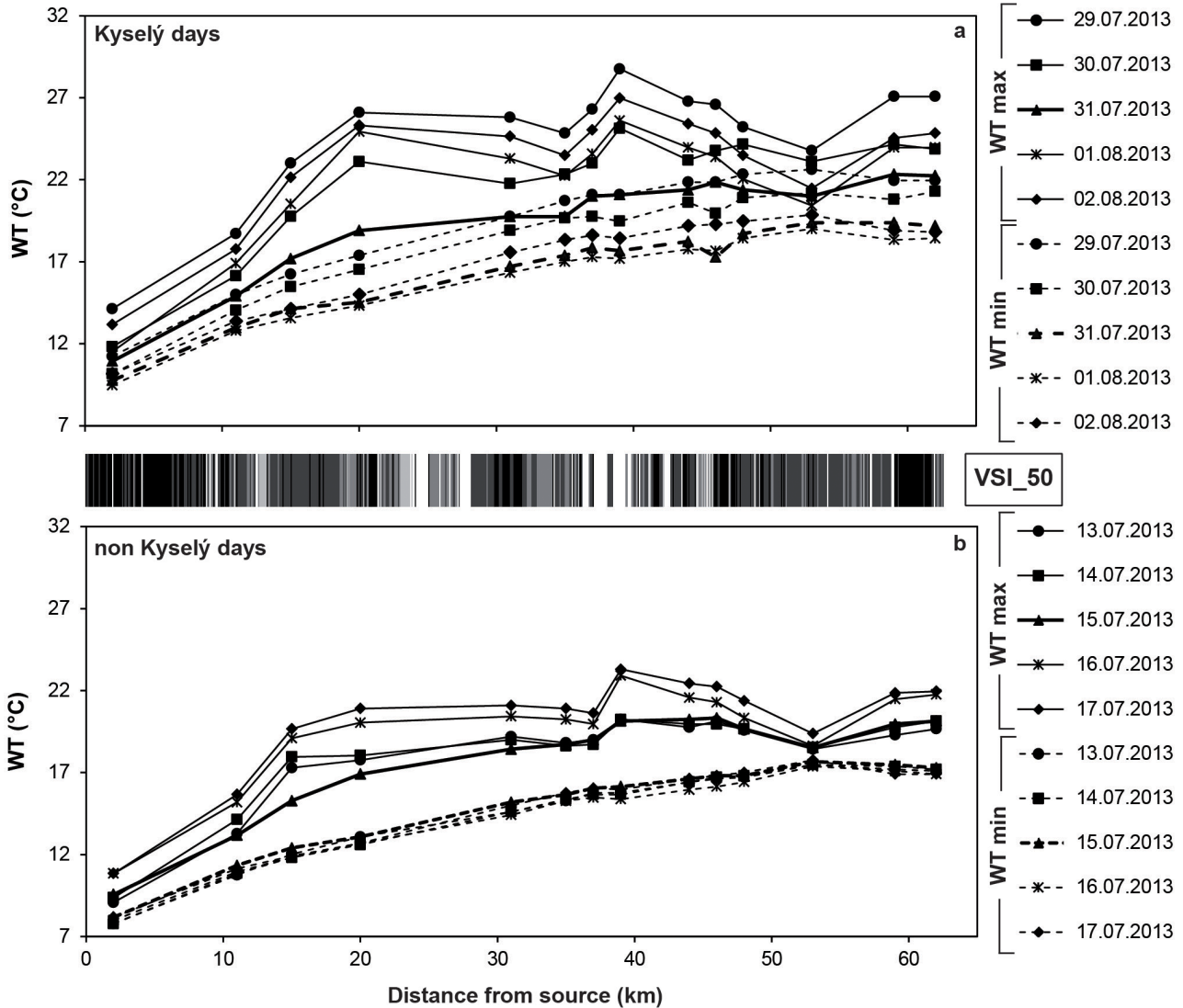


Fig. 6. Distribution of the longitudinal vegetation-shading index (VSI 50) and water temperature (WT) values of two 5-day periods with differing cloudiness conditions. Periods describe (a) heatwave (Kysely) and (b) non-heatwave (non-Kysely) conditions.

The calculated energy gains on a 1 km long river stretch, with dimensions such as DFS 39.01, and no riparian vegetation, increased river WT by 0.4 °C (Formula (4)). This results in an increase of 3.3 °C for a river section of 9 km. Under the same conditions, but with less energy due to dense vegetation, the WT increased just by 0.1 °C. Consequently, other cooling influences could have a stronger impact in shaded areas.

Observing the time period with the lowest discharge values, DFS 39.01 amounted to 60% of the water mass achieved on DFS 58.79. Above ground tributaries added another 24% of water mass. The WT of the Zickenbach, the biggest tributary showed no significant differences in WT in comparison to the river Pinka. Therefore, 16% of the water mass was ground water and assumed to be the reason for the WT decrease. Ground water temperatures from nearby stations showed mean values of 12 °C. Formula (5) was used to calculate the WT of 1 m³ water along the 19.78 km long river

stretch. WT decreases of 3.6 °C were calculated whereas the observed reduction of WT_{max} was 5 °C.

4 Discussion

4.1 VSI and its spatial scale in terms of water temperature

In the present study, VSI was calculated as an integral parameter, taking into account vegetation height, width and density, whereby all three have a verifiable impact on the solar radiation situation input on a stream surface. These are the parameters most commonly studied concerning global radiation reduction (Zwieniecki and Newton, 1999; DeWalle, 2010; Sridhar *et al.*, 2004) but there are no clear results concerning the ranked importance of these. The VSI results in a significant correlation which had the same or even better correlation coefficients with WT as the

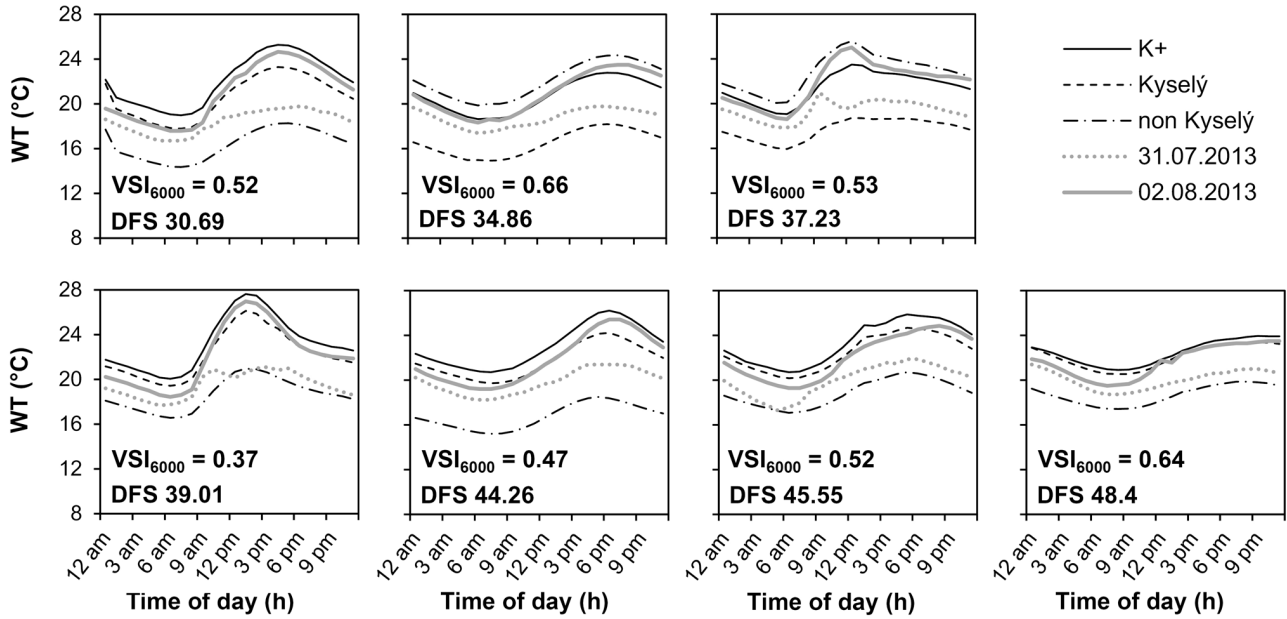


Fig. 7. Overview of the mean daily water temperature (WT) variations from non-heat wave (non-Kyselý), heat wave (Kyselý) and extreme heat days (K+), as well as mean WT variations for a cloudy day (31.7.2013) and a clear sky day (2.8.2013) at seven selected WT stations between distance from source (DFS) 30.00 and DFS 50.00.

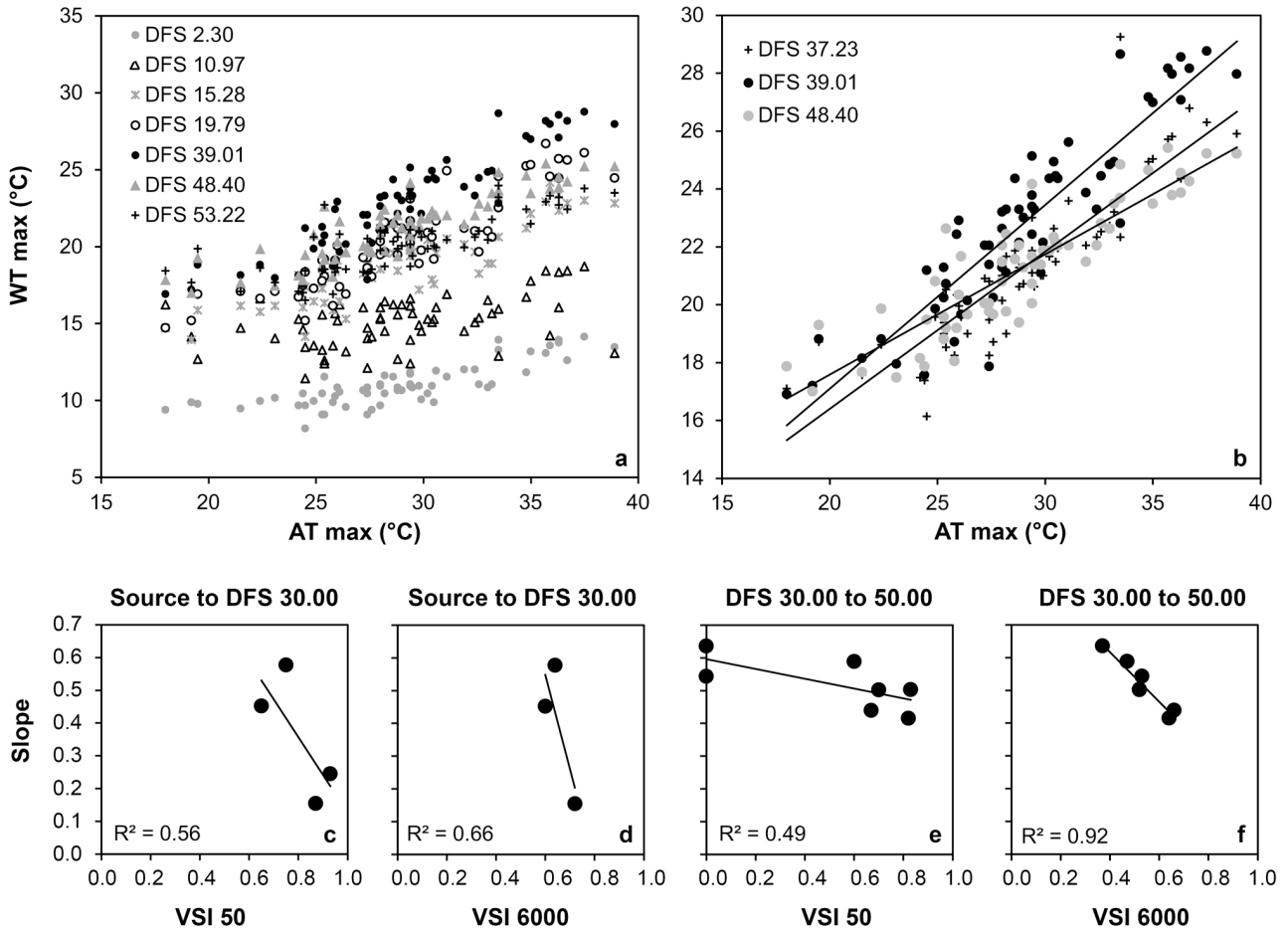


Fig. 8. Maximum water temperatures (WT_{max}) shown as a function of air temperature (AT) at selected WT stations along the whole river stretch (a), and for selected WT stations between distance from source (DSF) 30.00 and DFS 50.00 (b) for summer 2013. (c–f) Show the regressions of vegetation-shading indexes (VSI) to the slopes of the AT to WT regression lines.

Table 3. Water temperature (WT) change according to an air temperature (AT) change of 2 °C. Abbreviations: DFS = distance from source, VSI = vegetation shading index.

DFS (km)	VSI ₆₀₀₀	Slope	R ² AT/WT	AT change (°C)	AT from (°C)	AT to (°C)	WT from (°C)	WT to (°C)	WT change (°C)
2.3		0.245	0.66	2	30	32	11.3	11.8	0.5
10.97	0.72	0.155	0.19	2	30	32	15.3	15.6	0.3
15.28	0.6	0.452	0.72	2	30	32	19.5	20.4	0.9
19.79	0.64	0.577	0.8	2	30	32	20.9	22.1	1.2
30.69	0.52	0.503	0.81	2	30	32	21.7	22.7	1
34.86	0.66	0.439	0.84	2	30	32	21.3	22.2	0.9
37.23	0.53	0.543	0.8	2	30	32	21.8	22.9	1.1
39.01	0.37	0.635	0.83	2	30	32	23.5	24.7	1.3
44.26	0.47	0.589	0.88	2	30	32	22.6	23.8	1.2
45.55	0.52	0.502	0.87	2	30	32	22.7	23.7	1
48.4	0.64	0.416	0.78	2	30	32	21.7	22.6	0.8
53.22	0.69	0.325	0.61	2	30	32	20.5	21.2	0.6
58.79	0.69	0.512	0.82	2	30	32	22.6	23.6	1
61.51	0.68	0.511	0.84	2	30	32	22.7	23.8	1

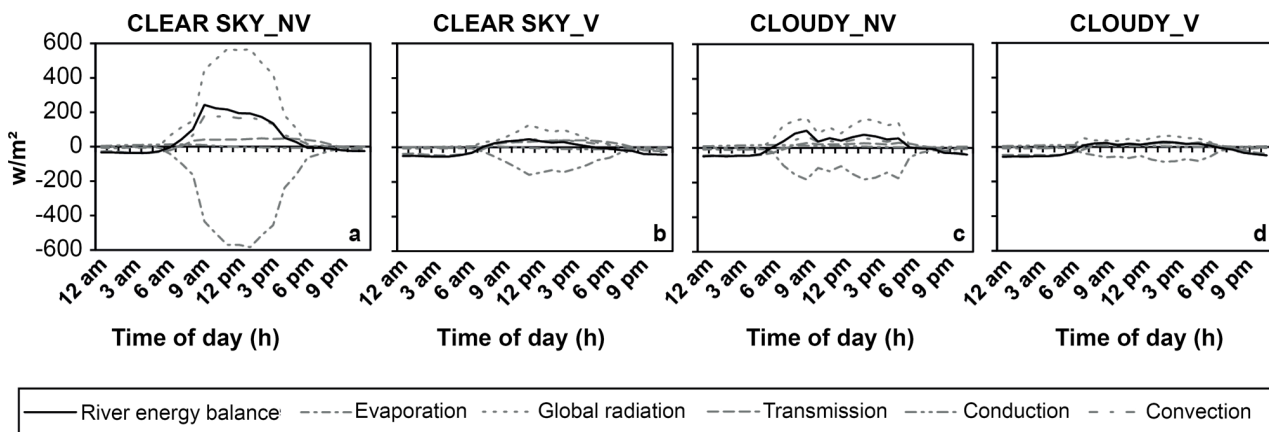


Fig. 9. Daily variations of energy balances for a cloudy (31.7.2016) and a clear sky day (2.8.2016), without vegetation (NV) and with vegetation (V).

individual vegetation parameters. Additionally, it was highly correlated to the GSF with a coefficient of 0.9 ($p < 0.01$). Depending on river size, different lengths are of relevance, in order to heat the water to a specific temperature. In the present study, the influence of the mean VSIs of different lengths on WT was tested for a stream with 1–1.2 m³/s discharge and points to 4–7 km (peak correlation coefficient for WT_{max} of –0.82 at 6 km VSI length) as being an appropriate length. The results are not directly comparable to those of most existing studies which deal with smaller streams with a discharge of up to 0.03 m³/s (Story *et al.*, 2003; Johnson, 2004; Rutherford *et al.*, 2004; Moore *et al.*, 2005; Gomi *et al.*, 2006). Rutherford *et al.* (1997) mentioned 1st order streams need 250 m to 500 m; 2nd order 500 m to 1.5 km and 3rd order 1.5 km to 5 km unshaded sections in order to heat the water by 5 °C. Johnson and Wilby (2015) stated that around 0.5 km of complete shade is necessary to decrease WT by 1 °C in July at a headwater site; whereas 1.1 km shade is needed 25 km downstream. Accordingly,

larger rivers need a longer distance to reach the same WT changes than smaller ones.

In the present study, WT_{min} and WT_{mean} showed a steadily increasing curve from source to DFS 62.55, unaffected by riparian vegetation conditions. However, WT_{max} and WT_{range} had peaks at unshaded reaches, of up to approximately 4 °C difference to shaded ones, which followed a steadily increasing curve. These findings correlates well with the findings of Bowler *et al.* (2012), Johnson (2004) and Webb *et al.* (2008) which show that if a riverine reach is fully clear cut, the daily WT_{max} and WT_{range} are particularly affected.

4.2 Heatwave periods, VSI and their impact on water temperature

We focused on the comparison between non-heatwave periods (NK) and extreme heatwave days (K+), as well as clear sky and cloudy days. Only considering AT to divide the

summer into non-heatwave (NK) and heatwave (K) days, differences in WT_{max} of 4.3 °C were found at all WT stations. Additionally, taking into account cloudiness and discharge conditions, extreme heatwave days (K+) were selected. Differences in WT_{max} to the non-heatwave periods (NK) increased by another 1.2 °C. Many other studies have analysed WT behaviour after clear cut, especially on clear sky and hot days (*i.e.*, Story *et al.*, 2003; Moore *et al.*, 2005; Quinn and Wright-Stow, 2008). Increases of daily WT_{max} , on non-vegetated sites, of up to 13 °C were found (Moore *et al.*, 2005).

Additionally, we also analysed the differences between consecutive clear sky and cloudy days to have the same hydrological boundary conditions. The only changing parameter was the radiation input through different cloudiness conditions. On a clear day, the maximum values of the energy balance differed by 159 W/m² between areas without vegetation and fully vegetated areas, whereas on cloudy days differences decreased to 39 W/m². Garner *et al.* (2014) also recorded the dramatically reduced energy gains of the river at vegetated sites compared to open sites.

These differing energy inputs to the river were reflected in the different WT_{max} during the clear sky days. Open sites with hardly any vegetation showed a WT_{max} of up to 27.8 °C, while densely shaded ones showed, on the same day, a WT_{max} of 24.9 °C. The lowest WT_{max} with 22.7 °C occurred on a heavily shaded river stretch (mean VSI_{50} = 0.61). The shading effects of the vegetation have caused a reduction of incoming solar radiation, resulting in a reduction of the increase of WT. Ground water and other potential inflows are acting as cooling factors. Story *et al.* (2003) concluded from their study that ground water inflow in a shaded reach caused 40% of the 3 °C cooling effect in daily WT_{max} , whereas bed heat conduction and hyporheic exchange caused 60% of this effect. In our study, ground water influence for a 19.78 km long river stretch was numerically modelled with a WT_{max} decrease of 3.6 °C, neglecting energy exchange with the atmosphere or soil.

4.3 Water temperature variations

When considering daily WT variations, the most relevant parameters were daily WT_{max} and WT_{range} . The results of the present study showed differences between shaded and unshaded sites of up to 4.2 °C for daily WT_{max} . The correlation between VSIs and WT changes is high. It is specifically most apparent up to VSI_{6000} of 0.4, when the vegetation cover is generally very low. The unshaded areas showed up to 2.6 °C higher daily WT_{max} in the extreme heatwave days (K+) than fully or patchy shaded ones (VSI_{6000} above 0.4) in the processed area did. This is consistent with Bowler *et al.* (2012) who concluded that mean WT_{max} are up to 4.9 °C lower at forested riversides than at pasture riversides.

Disregarding all these different conditions and parameters, DFS 39.01, the WT measuring point with the lowest vegetation density (VSI_{50} = 0; VSI_{6000} = 0.37) showed the highest WT_{max} in all periods. This highlights the importance and possibilities of riparian vegetation management and the need for at least a degree of riparian vegetation as previously stated in Holzapfel *et al.* (2013). Rutherford *et al.* (1997) also emphasizes that a natural shading of 95–99% radiation reduction is not necessary and 70% is sufficient. In the present study, sites with VSI_{6000} of about 0.4 (40% density) had a significant effect on preventing

WT increase in pre-alpine conditions. Similarly, Correll (2005) stated that from an ecological point of view continuous buffers are more important than wider but fragmented ones.

4.4 Water temperature influenced by air temperature dependent on VSI

We found a relationship between WT_{max} and AT_{max} with an R^2 of 0.8–0.9 in summer. Based on this correlation an increase of 2 °C AT_{max} , results in an increase of WT_{max} of 1.3 °C for an unshaded reach and 0.8 °C for a shaded reach. Following a WT increase at an AT change is always dependent on the riparian vegetation situation. Webb and Nobilis (1997) recorded a R^2 of 0.97 between AT and WT for monthly mean values over the entire year. In the summer, between June and August, R^2 was only between 0.47 and 0.7.

5 Conclusion

WT is a very important and limiting parameter for the development of riverine life, which is driven by meteorological variables, but also influenced by riparian vegetation stands and many other abiotic factors. This paper focuses explicitly on the impact of different riparian vegetation stands on WT. Most sensitive to changes caused by riparian vegetation is the daily WT_{max} followed by the daily WT_{range} .

In particular, during extreme meteorological events such as heatwave periods, when the river system suffers from highest WTs, vegetation has an impact on WT. In this case, our study has shown that sparse riparian vegetation is sufficient, in order to avoid a WT increase in pre-alpine conditions. VSIs of above 0.4 already achieved good results. On cloudy days the existence of riparian vegetation has no further effects due to solar radiation decrease.

The VSI is a representative parameter which characterises the shading effects of riparian vegetation by its height, width and density. The most relevant considered VSI section length is dependent on specific local boundary conditions. Since the highest correlation between WT and VSI was registered for vegetation stretches of 6000 m, we conclude that for a medium-sized pre-alpine river, restoration practices should consider that discontinuity of riparian vegetation should be less than 6000 m, with more than 40% dense vegetation in order to minimise WT increases due to unshaded conditions.

The cooling of WT directly by riparian vegetation was not possible, as the energy balance on a clear sky day never dropped below 0. The findings have shown that riparian vegetation can prevent the WT from an additional increase, and therefore effects such as ground water inflow can have higher impacts. WT directly reacted to changes in AT, riparian vegetation significantly influenced this relationship.

The present study confirmed findings of other studies regarding the influence of riparian vegetation on WT. Each river, however, is a unique system and highly dependent on size, predominant meteorological situations and geographical position. Climate change effects, in particular, put an additional pressure on river ecosystems and its inhabitants, such as fish and benthic invertebrates. To ensure the preservation of habitats for aquatic organisms, riparian vegetation management should be a not dispensable sector in future river planning and management,

particularly at low water conditions to buffer extreme WT peaks in heatwave periods.

Acknowledgements. This paper was part of the projects BIO_CLIC and LOWFLOW+. The funding for these projects was provided by the Austrian Climate and Energy Fonds (Programm ACRP). Thanks to Viktoria Jachs, Valeria Ledochowski, Wolfgang Bartel and Christoph Hlousek for their assistance in the fieldwork throughout these projects. Statistical analysis was supported by Erwin Lautsch. Hydrological data, meteorological data and aerial photographs were provided by the Legal Water Authorities of Styria and Burgenland and the West Transdanubian Water Direction.

References

- Bowler D, Mant R, Orr H, Hannah D, Pullin A. 2012. What are the effects of wooded riparian zones on stream temperature? *Environ Evid* 1: 3.
- Boyd M, Kasper B. 2003. Analytical Methods for Dynamic Open Channel Heat and Mass Transfer: Methodology for the Heat Source Model Version 7.0.
- Broadmeadow S, Nisbet TR. 2004. The effects of riparian forest management on the freshwater environment: a literature review of best management practice. *Hydrol Earth Syst Sci* 8: 286–305.
- Broadmeadow SB, Jones JG, Langford TEL, Shaw PJ, Nisbet TR. 2011. The influence of riparian shade on lowland stream water temperatures in southern England and their viability for brown trout. *River Res Appl* 27: 226–237.
- Caissie D. 2006. The thermal regime of rivers: a review. *Freshw Biol* 51: 1389–1406.
- Cejka A, Dvorak M, Fortman I, *et al.* 2005. Das Lafnitztal – Flusslandschaft im Herzen Europas. Wien: Neuer Wissenschaftlicher Verlag, p. 233.
- Correll DL. 2005. Principles of planning and establishment of buffer zones. *Ecol Eng* 24: 433–439.
- Davies-Colley RJ, Meleason MA, Hall RMJ, Rutherford JC. 2009. Modelling the time course of shade, temperature, and wood recovery in streams with riparian forest restoration. *N Z J Mar Freshw Res* 43: 673–688.
- DeWalle DR. 2008. Guidelines for riparian vegetative shade restoration based upon a theoretical shaded-stream model. *J Am Water Resour Assoc* 44: 1373–1387.
- DeWalle DR. 2010. Modeling stream shade: riparian buffer height and density as important as buffer width. *J Am Water Resour Assoc* 46: 323–333.
- Evans EC, McGregor GR, Petts GE. 1998. River energy budgets with special reference to river bed processes. *Hydrolog Process* 12: 575–595.
- Fink M, Moog O, Wimmer R. 2000. Fließgewässer – Naturräume Österreichs. Wien: Umweltbundesamt.
- Garner G, Malcolm IA, Sadler JP, Hannah DM. 2014. What causes cooling water temperature gradients in a forested stream reach? *Hydrol Earth Syst Sci* 18: 5361–5376.
- Ghermandi A, Vandenberghe V, Benedetti L, Bauwens W, Vanrolleghem PA. 2009. Model-based assessment of shading effect by riparian vegetation on river water quality. *Ecol Eng* 35: 92–104.
- Gomi T, Moore RD, Dhakal AS. 2006. Headwater stream temperature response to clear-cut harvesting with different riparian treatments, coastal British Columbia, Canada. *Water Resour Res* 42: W08437.
- Groom JD, Dent L, Madsen LJ, Fleuret J. 2011. Response of western Oregon (USA) stream temperatures to contemporary forest management. *Forest Ecol Manag* 262: 1618–1629.
- He J, Chu A, Ryan MC, Valeo C, Zaitlin B. 2011. Abiotic influences on dissolved oxygen in a riverine environment. *Ecol Eng* 37: 1804–1814.
- Holzzapfel G, Weihs P, Rauch HP. 2013. Use of the Shade-a-lator 6.2 model to assess the shading potential of riparian purple willow (*Salix purpurea*) coppices on small to medium sized rivers. *Ecol Eng* 61: 697–705.
- Johnson MF, Wilby RL. 2015. Seeing the landscape for the trees: metrics to guide riparian shade management in river catchments. *Water Resour Res* 51: 3754–3769.
- Johnson SL. 2004. Factors influencing stream temperatures in small streams: substrate effects and a shading experiment. *Can J Fish Aquat Sci* 61: 913–923.
- Johnson MF, Wilby RL. 2015. Seeing the landscape for the trees: metrics to guide riparian shade management in river catchments. *Water Resour Res* 51: 3754–3769.
- Kasper B, Boyd M. 2002. TTools 7.0 User Manual. Portland: Oregon Department of Environmental Quality.
- Kovats RS, Valentini R, Bouwer LM, *et al.* 2014. Europe. In: Climate Change 2014: Impacts, Adaptation, and Vulnerability. Part B: Regional Aspects. Contribution of Working Group II to the Fifth Assessment Report of the Intergovernmental Panel on Climate Change. Cambridge, United Kingdom and New York, USA: Cambridge University Press, pp. 1267–1326.
- Kyselý J, Kalvová J, Květon V. 2000. Heat waves in the South Moravian region during the period 1961–1995. *Studia Geophys Geodaet* 44: 57–72.
- Laaha G, Parajka J, Viglione A, *et al.* 2016. A three-pillar approach to assessing climate impacts on low flows. *Hydrol Earth Syst Sci* 20: 3967–3985.
- Leach JA, Moore RD. 2010. Above-stream microclimate and stream surface energy exchanges in a wildfire-disturbed riparian zone. *Hydrolog Process* 24: 2369–2381.
- Logez M, Pont D. 2013. Global warming and potential shift in reference conditions: the case of functional fish-based metrics. *Hydrobiologia* 704: 417–436.
- Matulla C, Schmutz S, Melcher A, Gerersdorfer T, Haas P. 2007. Assessing the impact of a downscaled climate change simulation on the fish fauna in an Inner-Alpine River. *Int J Biometeorol* 52: 127–137.
- Melcher A, Kalny G, Dossi F, *et al.* 2016. Der Einfluss der Ufervegetation auf die Wassertemperatur unter gewässerspezifischer Berücksichtigung von Fischen und benthischen Evertebraten am Beispiel von Lafnitz und Pinka. Österreichische Wasser- und Abfallwirtschaft.
- MeteoSchweiz, B.f.M.u.K., Definition Schönwettertage. <http://www.meteoschweiz.admin.ch/home/klima/vergangenheit/klimader-schweiz/berichte-rund-ums-jahr/altweibersommer.html>.
- Moore RD, Spittlehouse DL, Story A. 2005. Riparian microclimate and stream temperature response to forest harvesting: a review. *J Am Water Resour Assoc* 41: 813–834.
- Pletterbauer F, Melcher A, Ferreira T, Schmutz S. 2014. Impact of climate change on the structure of fish assemblages in European rivers. *Hydrobiologia* 744: 235–254.
- Poole GC, Berman CH. 2001. An ecological perspective on in-stream temperature: natural heat dynamics and mechanisms of human-caused thermal degradation. *Environ Manag* 27: 787–802.
- Quinn JM, Wright-Stow AE. 2008. Stream size influences stream temperature impacts and recovery rates after clearfell logging. *Forest Ecol Manag* 256: 2101–2109.

- Rahel FJ, Olden JD. 2008. Assessing the effects of climate change on aquatic invasive species. Evaluación de los Efectos del Cambio Climático sobre Especies Acuáticas Invasoras. *Conserv Biol* 22: 521–533.
- Rich PM, Wood J, Vieglais DA, Burek K, Webb N. 1999. User Manual for HemiView-Version 2.1. Oregon: Delta-T Devices Ltd, p. 79.
- Rutherford JC, Blackett S, Blackett C, Saito L, Davies-Colley RJ. 1997. Predicting the effects of shade on water temperature in small streams. *N Z J Mar Freshw Res* 31: 707–721.
- Rutherford JC, Marsh NA, Davies PM, Bunn SE. 2004. Effects of patchy shade on stream water temperature: how quickly do small streams heat and cool? *Mar Freshw Res* 55: 737–748.
- Sridhar V, Sansone AL, LaMarche J, Dubin T, Lettenmaier DP. 2004. Prediction of stream temperature in forested watersheds. *J Am Water Resour Assoc* 40: 197–213.
- Story A, Moore RD, Macdonald JS. 2003. Stream temperatures in two shaded reaches below cutblocks and logging roads: downstream cooling linked to subsurface hydrology. *Can J For Res* 33: 1383–1396.
- Traxler A. 1997. Handbuch des Vegetationsökologischen Monitorings - Methoden, Praxis, angewandte Projekte - Teil A: Methoden. Wien: Umweltbundesamt Österreich, p. 391.
- Trimmel H, Gangneux C, Kalny G, Weihs P. 2016. Application of the model 'Heat Source' to assess the influence of meteorological components on stream temperature and simulation accuracy under heat wave conditions. *Meteorolog Z* 25: 389–406.
- Webb BW, Nobilis F. 1997. Long-term perspective on the nature of the air-water temperature relationship: a case study. *Hydrolog Process* 11: 137–147.
- Webb BW, Hannah DM, Moore RD, Brown LE, Nobilis F. 2008. Recent advances in stream and river temperature research. *Hydrolog Process* 22: 902–918.
- Wimmer R, Wintersberger H, Parthl N. 2012. Fließgewässertypisierung in Österreich – Hydromorphologische Leitbilder Band 2: Naturraumbeschreibungen, Bioregionen und Typologie. Vienna: Bundesministerium für Land- und Forstwirtschaft, Umwelt und Wasserwirtschaft – Abt. VII / 1.
- Zwieniecki MA, Newton M. 1999. Influence of streamside cover and stream features on temperature trends in forested streams of Western Oregon. *Soc Am For West J Appl For* 108: 106–113.

Cite this article as: Kalny G, Laaha G, Melcher A, Trimmel H, Weihs P, Rauch HP. 2017. The influence of riparian vegetation shading on water temperature during low flow conditions in a medium sized river. *Knowl. Manag. Aquat. Ecosyst.*, 418, 5.



Application of the model ‘Heat Source’ to assess the influence of meteorological components on stream temperature and simulation accuracy under heat wave conditions

HEIDELINDE TRIMMEL^{1*}, CLEMENT GANGNEUX², GERDA KALNY³ and PHILIPP WEIHS¹

¹Institute of Meteorology, University of Natural Resources and Life Science (BOKU), Vienna, Austria

²Institut National des Sciences Appliquées de Lyon (INSA), Villeurbanne, France

³Institute of Soil Bioengineering and Landscape Construction, University of Natural Resources and Life Science (BOKU), Vienna, Austria

(Manuscript received April 29, 2015; in revised form October 27, 2015; accepted November 20, 2015)

Abstract

Stream temperature is one of the most important factors for aquatic organism, but also regulates drinking water quality, which are both threatened by temperature rises. Atmospheric heat fluxes are primary drivers of stream temperature changes, all of them dependent on the rivers’ openness to sky.

To be able to simulate stream temperature in rivers of complex terrain and shaded by riparian vegetation a deterministic model including all shading processes was used and validated for the application for Eastern Austrian lowland rivers during summer and the heat wave 2–8 August 2013. The global radiation was included as direct input, which lead to an improvement. It is shown, that both net short wave radiation and evaporation are the most influential components under heat wave conditions and that both are subject to the influence of shading by topography and vegetation. The forward propagation of measurement imprecisions of atmospheric input parameters on simulated water temperature was calculated. The total model imprecision caused by measurement errors of sky obstructing elements (+1.24/–1.40 °C) exceeds the error caused by measurement errors of meteorological input parameters (+0.66/–0.70 °C). The most important sky obstructing elements are vegetation height and vegetation density. A total model imprecision caused by measurement errors of meteorological and shading input parameters is calculated with +1.90/–2.10 °C. While the errors caused by meteorological input are expected much smaller under normal conditions, sky view reducing errors are realistic or even underestimated.

Keywords: stream temperature simulation, energy balance, sensitivity, shade, vegetation, heat wave

1 Introduction

Water temperature influences the physical, chemical and biological properties of rivers and therefore the habitat of aquatic organisms (DAVIES-COLLEY and QUINN, 1998). Exposure to high water temperatures pose a threat to aquatic life (KALNY et al., 2015; MATULLA et al., 2007; MELCHER et al., 2014). To protect biological diversity but also the ability of rivers to provide drinking water, food and allow industrial use, it is important to understand how stream temperature can be maintained within the range of biological needs (HAAG and LUCE, 2008).

1.1 Stream temperature influences

Stream temperature is controlled by a multitude of factors. These factors include heat mass transfer such as the addition or loss of water volume from surface and sub-surface in- and outflows. Further the stream is warmed

or cooled by the magnitude of the net heat fluxes acting on the water volume, both on the air-water and water-substrate interface (CAISSIE 2006; GARNER et al., 2014; WEBB and ZHANG, 1997). Channel morphology and channel roughness also play a major role by influencing flow velocity and therefore defines the time which is available for the energy changes to take effect, the area which is exposed to these changes and also whether stratification or dispersion plays a role (MOORE et al. 2005).

In this paper the focus is on the atmospheric fluxes acting on the energy balance at the river surface and the influence of topography and riparian vegetation.

Net short wave radiation is a dominant energy flux influencing river water temperature (CAISSIE, 2006; CAISSIE et al., 2007; HANNAH et al., 2008; JOHNSON, 2004). Increased incoming radiation can increase water temperature and be caused by clear sky conditions, high solar zenith angles, flat topography or vegetation removal (THEURER et al. 1984, 1985; JOHNSON and WILBY, 2015).

Evaporation flux is the most significant factor in dissipation of stream heat (PARKER and KRENKEL, 1969). It is dependent on the difference between water and air

*Corresponding author: Heidelinde Trimmel, Institute of Meteorology, University of Natural Resources and Life Science (BOKU), Peter-Jordanstrasse 82, 1190 Vienna, Austria, e-mail: heidelinde.trimmel@boku.ac.at

Table 1: Relative percentage of input (in) and output (out) and absolute magnitudes of energy flux components: comparison literature, own simulations.

	Hannah et al. 2008 forest reach, Scottish Cairngorms Aug 2008 %	Benyaha et al. 2012 Catamaran brook, New Brunswick, Canada 22 May–6 Jun 2008 7–23 Jun 2008 % %		Maheu et al. 2014 2–11 Jul 2012 %	in this study Pinka, Eastern Austria 2–8 Aug 2013 % W/m²	
Sw	85 in	98 in	73 in	70–100 in	69 in	114.4
Lw	58 out	75–79 out	25 in	36–54 out	6 in	9.39
Ev	42 out	21–25 out	100 out	31–46 out	100 out	130.8
Cv	0.3 in	2 in	3 in	15 out–23 in	21 % in	34.53
Cd	15 in	–	–	32 out–19 in	4 % in	6.56

temperature, wind speed – which is governed by the roughness of the environment – and net radiation. Riparian vegetation has an influence on many microclimatic parameters close to the river (wind speed, air humidity, air temperature) and therefore also affects evaporation (RUTHERFORD et al., 1997). In particular a change in the evaporative heat flux affects the cooling of rivers during warmer summers (CAISSIE et al., 2007).

The sensible heat flux is related to evaporation, and as long as evaporation is occurring, which is mostly the case over water surfaces, this term stays small. CAISSIE et al. (2007) found sensible heat flux represents between 6 % of output and 20 % of heat input. According to WEBB and ZHANG (1997, 1999) the net value is 10 % of the magnitude of evaporation. BROWN and BARNWELL (1987) felt that the sensible heat term is negligible for most stream temperature modelling applications.

Long wave radiation flux consists of the long wave radiation emitted by atmosphere and land cover towards the stream (positive) and the back radiation from the stream (negative). The atmospheric component is mainly dependent on air humidity, air temperature and the height of cloud cover (TAESLER and ANDERSON, 1984; ANDERSON et al., 1984). The land cover component is dependent on the radiating surface area (BOYD and KASPER, 2003). The emitted long wave radiation is the second largest component in dissipating heat energy from a stream (PARKER and KRENKEL, 1969). It is influenced mainly by water temperature, but also by the openness to the sky. Riparian vegetation reduces the sky view and thereby impedes radiation loss during cloudless nights leading to an increase of minimum stream temperatures.

Generally atmospheric heat fluxes are known to be significant in small lowland rivers (ŁASZEWSKI, 2013).

Conduction is estimated by (MOORE et al., 2005) to be 10 % of net radiation. EVANS et al. (1998) suggests conduction flux to be 15 % of total energy exchange.

An overview of the magnitudes of heat fluxes in comparable studies is given in Table 1. While short wave radiation is always the largest input and evaporation always the largest output, the magnitude and direction of long wave radiation and convection varies depending on the season and period (BENYAHYA et al., 2012).

1.2 Modelling stream temperature

There are several approaches to simulate water temperature. Water temperature can be predicted using statistical functions and be correlated to independent variables (e.g. air temperature, water temperature of the previous days, or streamflow). These models are called regression and stochastic models. According to (ERICKSON and STEFAN 2000) 88 % to 95 % of the variations in stream temperature can be predicted using air temperature data if the watershed is large enough to enable air-water interaction and there are no major subsurface influences. GROOM et al. (2011) found that stream temperature is most strongly correlated to shade levels, followed by reach length, stream gradient and changes in upstream water temperature. ARISMENDI et al., (2014) used 11–44 years of stream temperature data and found that linear and non-linear regression models based on air temperatures predict stream temperature well during the periods used to develop them, but not during other years. Correlations might be helpful to predict patterns but do not implicate their causation. For example air temperature and stream temperature are often closely correlated but air temperature is not the primary driver of stream temperature (JOHNSON, 2003; WEBB and NOBILIS, 1997).

On smaller rivers it is preferable to use a deterministic model to better understand the physical forcing parameters that explain river temperature changes because it quantifies the influencing energy components (CAISSIE et al., 2007).

Sources of model prediction error can be related to (1) parameter uncertainty, (2) parametric variability of model input, (3) discrepancy or simplifications between model and true physics, (4) measurement observation errors, (5) interpolation uncertainties and (6) numerical uncertainties caused by approximation (KENNEDY and O’HAGAN, 2001). In this study we quantified prediction errors associated with points (2), (3) and (4).

Sensitivity analysis evaluates how sensitive model outputs are to changes in model input values. This can provide an estimate of prediction uncertainty associated with the chosen input parameters and their ranges.

Another method is inverse assessment of model uncertainty and parameter uncertainty. The discrepancy between the experiment and the mathematical model is

estimated by finding more precise values of known parameters or the values of unknown parameters in the model (calibration). This can be done manually or more efficiently with newly available regularization software, which is able to find unique solutions to ill-posed inverse problems, as river systems are (PEST 2015).

Because imprecise parameterization is known to be a major source of error for deterministic models, (BOYD and KASPER, 2003) tried to achieve maximum robustness when developing Heat Source by: (1) avoiding parametrization in favor of an analytical methodology that included all complex processes that affect riverine dynamic thermal regimes – and (2) a high resolution of input data to match the dynamic nature of stream temperature.

Therefore the acknowledged limitations of the model rather lie in the difficulty to obtain the precise input according to BOYD and KASPER (2003).

To quantify these errors already the INDEPENDENT MULTIDISCIPLINARY SCIENCE TEAM (IMST) (2004) recommended a sensitivity analysis of the major input variables included in Heat Source. Also their report advised to publish the validity of Heat Source using independently observed water temperature data.

Within the scope of the present study, the validity of Heat Source will be tested using meteorological data and stream water temperatures measured within this study in summer 2013. The atmospheric heat fluxes of the Eastern Austrian lowland river Pinka during heat wave conditions will be simulated and analyzed. The sensitivity of the model Heat Source towards meteorological inputs will be tested and model inputs that cause significant uncertainty in the output identified that should therefore be the focus of attention if the robustness is to be increased by further research.

2 Methods

2.1 Study period and region

For the validation of the model all available measurement data between July and August 2013 was used. As the focus of this study was to analyze the change in summer water temperatures caused by meteorological parameters the main temporal focus is on the 2–8 August 2013 (“study period”), a heat wave period in which a new air temperature maximum for Austria was reached. Also this corresponds to the time of main interest of HOLZAPFEL et al. (2015). The short time span and also the time of year assures, that there are no significant changes in vegetation cover, as it is the case in other studies performed earlier in the season (BENYAHYA et al., 2012).

The river Pinka, flows about 100 kilometers from the Alps in Eastern Austria at 1480 meters above sea level to the Hungarian plain, where it discharges into the river Raab at 200 meters above sea level. The land-use ranges from coniferous forest close to the source,

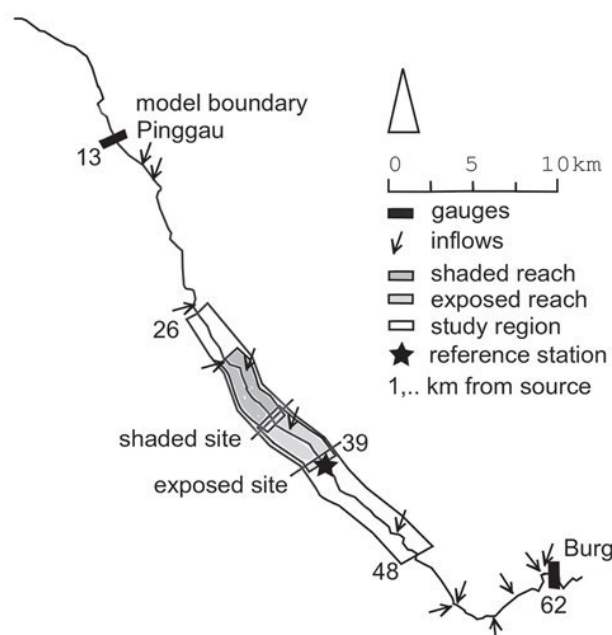


Figure 1: Study region: the river Pinka in Eastern Austria between the two gauges Pinggau (federal state Styria) and Burg (federal state Burgenland).

different agricultural and horticultural regions, as well as housing areas. The “study region”, measured as the kilometer distance of the river from the source (DFS) is at DFS 26–48 km. This section has no major tributaries (see Fig. 1) and a low slope (0.005 m m^{-1}) and is the region of main interest where the interrelation between the riparian vegetation cover and water temperature has been analyzed KALNY et al. (2015) and in more detail by HOLZAPFEL and RAUCH (2015).

Here the river has an average wetted width of 7.60 m, a maximum depth of 0.44 m, an average flow volume of $0.55 \text{ m}^3/\text{s}$ and the average flow velocity is 0.40 m/s, which represents a travel time of 15.69 hours through the reach. A temporal, local influence of ground water is possible (PAHR, 1984), but was not quantified within this study, because the ground water level was not above average within the study period.

KALNY et al. (2015) studied the relationship between the riparian vegetation cover and water temperature in this reach and introduced the Vegetation Shading Index VSI, which describes the riparian vegetation as an integral shading parameter, including vegetation height, width and density as these are the incoming radiation most influencing parameters (HOLZAPFEL et al. 2013). The VSI ranges between 0 to 1. Full vegetation (VSI = 1) is defined as vegetation height more than 1.5 times river width and a dense vegetation width of 50 m left and right of the river bank, which is enough to shade a river of this size at this latitude completely during summer.

Shading varies within few meters significantly but pattern of vegetation intensities can be differentiated when looking at larger scales. KALNY et al. (2015) found

that 3–8 km is the best spatial magnitude to explain the influence of vegetation on water temperature at this river size and 5 km is subsequently used for further analysis. In this paper two 5 km reaches of minimum and maximum VSI will be compared. The reach of minimal shading, called “exposed reach”, is upstream of DFS 39 km, and has a VSI of 0.35. The average view to sky (VTS) is 0.58. The reach with the most shade, called “shaded reach”, lies upstream DFS 35 km. The VSI here is 0.64. The mean VTS is 0.49.

Also two sites – referring to one sampling point or simulation node – who are situated in those reaches will be compared. The “shaded site” at DFS 35 km, has the minimum VTS within the shaded reach (0.24), while the “exposed site” at DFS 38 km has maximum VTS within the exposed reach (0.84). Also the shading upstream the exposed site is very low. The first 600 m upstream have a VSI of 0, continued by 450 m with about 0.4 and then again 0 for 1000 m.

2.2 Data collection and preparation for simulation

Using the GIS-based application TTools (BOYD and KASPER, 2003), the energy balance model Heat Source version 9 (BOYD and KASPER, 2003; GARNER, 2007) and field data, the energy fluxes along the river, hydraulics and water temperature were simulated along the Pinka.

The boundary conditions at the most upstream reach of the river consist of hourly water temperature and discharge data.

Water temperature was measured hourly with HOBO Pendant Temperature/Light Data Logger 8K – UA-002-08. Vertical and horizontal profiles were measured and no relevant temperature gradients found and the water temperature measured at the lower side of the river was found to be representative for the water temperature of the river at this point. Therefore water temperature sensors were attached with chains to the side of the river.

The sensor can measure temperatures between -20 and 70° with an accuracy from $\pm 0.53^{\circ}\text{C}$, a resolution of 0.14°C at 25°C and has a response time of 5 minutes, which is clearly smaller than the observation interval of 1 hour. Discharge data was obtained from the Hydrographischer Dienst Österreich.

Inflows are defined by hourly water temperature and discharge values. The discharge and water temperature of the main inflows could be estimated using own measurements. The water temperature data of the remaining inflows was synthetized using the daily fluctuations of the boundary station adding a fixed offset depending on the distance of the inflow to the boundary station.

Using TTools geographic coordinates and elevation were sampled from the digital elevation model every 500 m along the river center line. Topographic shade angles and gradient were also calculated.

Vegetation height, density, overhang were estimated during field surveys by the Institute of Soil Bioengi-

neering and Landscape Construction and a georeferenced vegetation data layer produced with this information (KALNY et al., 2015). This data layer was used by TTools to extract the data necessary for Heat Source. At each 500 m node along the river, seven transects extended from the river center out in star pattern in seven different directions (NE, E, SE, S, SW, W, NW). Along each transect the vegetation layer was sampled a total of nine times with each sample being 5 m apart.

Finally various morphological inputs were compiled from physical parameters sampled during field surveys including the bottom width and the inclination of the river embankment (between toe of slope and slope top). The roughness parameter Mannings n was estimated based on the type of river course (straight, bent, meandering), and the existence of longitudinal linings and horizontal obstructions (adapted according to CHOW, 1959). Hyporheic exchange was estimated with 1 % referring to PAHR (1984). All other sediment parameters were fixed using values from PELLETIER et al. (2006) (sediment thermal conductivity $2\text{ W m}^{-1}\text{ K}^{-1}$, sediment thermal diffusivity $0.0064\text{ cm}^2\text{ s}^{-1}$, sediment hyporheic thickness 0.1 m).

Porosity was estimated using the mean sediment size, which was recorded during field surveys.

Global radiation, air temperature, air humidity and wind speed was measured at a reference station located at DFS 39 km $47^{\circ} 16' 11.055''\text{ N } 16^{\circ} 13' 47.892''\text{ E}$, 300 m above sealevel. For global radiation measurement a Schenk star pyranometer was used. Air temperature and air humidity were measured with HOBO Pro v2 (U23-001). Meteorological data required for the simulations were prepared for four locations along the river, all using data from the reference station. For each 100 m of elevation difference 0.43°C was added to the air temperature to account for the adiabatic lapse rate.

In the summer of 2013 the long- and short wave radiation balance was measured using a Kipp and Zonen Net Radiometer CNR4 for validation purpose.

Two light sensors were attached to concrete plates at a horizontal and vertical fixed position. The plates were put at the middle of the river bed to record the light received in constant distance from the river bottom as a measure for water turbidity.

2.3 Calculation of energy balance and stream temperature

Using the model Heat Source version 9 the energy balance Φ_{Total} along the river is calculated:

$$\Phi_{\text{Total}} = \Phi_{\text{Evaporation}} + \Phi_{\text{Convection}} + \Phi_{\text{Longwave}} + \Phi_{\text{Solar}} + \Phi_{\text{Conduction}} \quad (2.1)$$

where Φ_{Total} is the energy balance, $\Phi_{\text{Evaporation}}$ the evaporation flux, $\Phi_{\text{Convection}}$ the convection flux, Φ_{Longwave} the long wave radiation balance all referring to the stream

surface, Φ_{Solar} is the short wave energy which is absorbed by the water column and $\Phi_{\text{Conduction}}$ the conduction flux. Positive values are directed towards the stream and add heat, negative values cool the stream.

The stream temperature increase ΔT caused by Φ_{Total} is calculated using:

$$\Delta T = \frac{\Phi_{\text{Total}} * dt}{\left(\frac{A}{W_w}\right) * c_{\text{H}_2\text{O}} * m} \quad (2.2)$$

A is the crosssectional area, W_w is the wetted width, the $c_{\text{H}_2\text{O}}$ is the specific heat capacity of water ($4182 \text{ Jkg}^{-1} * \text{C}^{-1}$), m the mass of 1 m^3 water which is 998.2 kg .

The two main components which according to literature have the strongest influence on stream temperature are short wave heat flux and evaporation, therefore these are explained in more detail.

2.3.1 Short wave radiation and its extinction

The radiation above topography is originally calculated by Heat Source using cloudiness values (BOYD and KASPER, 2003). For this study we modified the model source code to accept measured global radiation input directly (see Chapter 3.3.1). The formulas and routines used to calculate the reduction of the global radiation by the geometries of topography and vegetation are based on established formula which are adapted to the special usage within Heat Source (BOYD and KASPER, 2003).

Shading is defined by four angles, which are calculated using the height and distance of topographic obstacles to the river center: the sun elevation angle θ_s , the topographic angle θ_t , the vegetation angle θ_v , and the bank shade angle θ_b .

θ_t is calculated using the topographic angles sampled by TTools from the digital elevation model for East, South and West of the river center point. θ_v and θ_b are calculated with:

$$\theta_v = \text{atan}\left(\frac{VH + BH}{LD}\right) \quad (2.3)$$

and

$$\theta_b = \text{atan}\left(\frac{BH}{LD}\right), \quad (2.4)$$

where VH is the vegetation height and BH (bank height) is the relative elevation from the stream to the land surface and LD the distance from the river center to the landcover sampling points.

If topographic shade is occurring the direct radiation is blocked completely, the diffuse radiation above vegetation multiplied with the topographic factor TF , which is the sum of the topographic angles North, South and West of the river center divided by $3 * 90$.

If vegetation shade is occurring direct radiation is reduced, using a formulation of Beer's law, depending

on vegetation density VD of each zone depending on riparian extinction RE by the term $\Phi_{\text{SolarExtinct}}$:

$$RE = -\log\left(\frac{1 - VD}{10}\right); \quad (2.5)$$

$$\Phi_{\text{SolarExtinct}} = 1 - \exp\left(-RE * \left(\frac{LD}{\cos(\text{rad}(\theta_s))}\right)\right) \quad (2.6)$$

The diffuse radiation above vegetation is multiplied with $(1 - TF)$. The diffuse radiation below vegetation is multiplied and thereby reduced with the view to sky value VTS , which is calculated using the mean maximum θ_v of each of the seven directions multiplied with the modified vegetation density VD_{mod} :

$$VD_{\text{mod}} = (\max(\theta_v) - \max(\theta_b)) * VD_{\text{ave}} + \max(\theta_b) * \left(\frac{1}{\max(\theta_v)}\right) \quad (2.7)$$

$$VTS = 1 - \left(\frac{\max(\theta_v) * VD_{\text{mod}}}{7 * 90}\right) \quad (2.8)$$

The VTS is also used to calculate the atmospheric longwave radiation $\Phi_{\text{LongwaveAtm}}$ and longwave radiation emitted from vegetation $\Phi_{\text{LongwaveVeg}}$.

If bank shade is occurring, the direct radiation fraction is reduced by the radiation entering in the affected angles. The diffuse fraction is not concerned.

Φ_{Solar} which is finally absorbed by the water column is the amount of solar radiation entering the stream $\Phi_{\text{Solar_enter}}$ minus the amount that is absorbed in the river bed and reflected.

2.3.2 Evaporation and convection

There are two options to calculate evaporation implemented in Heat Source: Mass transfer and Penman's combination method. For Penman's combination method a set of well established empiric formula are used, which take stream temperature and air temperature, net radiation and elevation above sea level as input (DUNNE and LEOPOLD, 1978; McCUTCHEON, 1989; DINGMAN, 2002; CUENCA, 1989) and can be found in textbooks (OKE, 1987). The evaporation flux $\Phi_{\text{Evaporation}}$ is finally calculated using:

$$E = \frac{\left(\frac{\Phi_{\text{Rad}} * \Delta}{(\rho * LHV)}\right) + E_a * \gamma}{(\Delta + \gamma)} \quad (2.9)$$

and

$$\Phi_{\text{Evaporation}} = -E * LHV * \rho \quad (2.10)$$

where E is the evaporation rate [ms^{-1}] (DINGMAN, 2002), Φ_{Rad} the sum of Φ_{Longwave} and $\Phi_{\text{Solar_enter}}$, Δ the slope of the saturation vapor vs. air temperature curve, ρ is the density of water [kgm^{-3}], LHV the latent heat of vaporization [Jkg^{-1}], E_a the aerodynamic evaporation and γ is the psychrometric constant [$\text{mb}^\circ\text{C}^{-1}$].

If there is vegetation cover, the vegetation height VH is included in the calculation of the zero-plane displacement Z_d and the roughness height Z_0 (DINGMAN, 2002 p. 594), which influence the friction velocity W' , the wind function W_f and aerodynamic evaporation E_a (SHANAHAN, 1984):

$$Z_d = 0.7 * VH \quad (2.11)$$

$$Z_0 = 0.1 * VH \quad (2.12)$$

$$W' = W * 0.4 / \ln\left(\frac{(Z_m - Z_d)}{Z_0}\right) \quad (2.13)$$

$$W_f = a + b * W' \quad (2.14)$$

$$E_a = W_f * (e_s - e_a) \quad (2.15)$$

W is windspeed, Z_m is the measurement height, which is 2 m in this study. Different empirical constants have been developed for the Penman method. Here $a = 1.51E^{-09}$ and $b = 1.6E^{-09}$ are used (DUNNE and LEOPOLD 1978). e_s is the saturation vapor pressure and e_a is the vapor pressure.

Convection is calculated from evaporation via the Bowen ratio β .

$$\beta = \frac{\gamma * (T - T_{air})}{(e_s - e_a)} \quad (2.16)$$

$$\Phi_{Convection} = \Phi_{Evaporation} * \beta \quad (2.17)$$

where T is the stream temperature and T_{air} is air temperature.

2.4 Model analysis

To quantify the sensitivity of the model to different heat fluxes and meteorological input parameters, a sensitivity analysis was performed. Each factor was increased to 110 % separately to show its influence on the heat fluxes, the energy balance as such and water temperature (WT). All shown values are averaged over the study period and area. As vegetation is a known factor which influences the magnitude of the atmospheric components of the energy balance significantly no vegetation scenario V0 is used.

We also evaluated stream temperature response to different scenarios of vegetation and topographic shading.

In this paper we use a sensitivity analysis to estimate the forward propagation of reported measurement error of meteorological and shading input parameter (e.g. vegetation height and density) on simulated water temperatures.

The results will be summed up to estimate the maximum error caused by atmospheric influences (WEIHS and WEBB, 1997).

To better understand the relationship between the separate heat fluxes and their influencing parameters VTS, and stream temperature correlations are calculated for the whole river Pinka during July and August.

In addition to the sensitivity analysis we evaluate the models application for Eastern Austrian lowland rivers by comparing the model predictions for short wave radiation, long wave radiation, and stream temperature with our field measured data.

For model performance criteria we use the coefficient of determination R^2 and root mean square error, which is given by

$$R^2 = 1 - \frac{\sum_i (M_i - S_i)^2}{\sum_i (M_i - M_{mean})^2}$$

and

$$RMSE = \frac{\sum_{i=1}^N (M_i - S_i)^2}{N}$$

where N is the total number of measured values, M the measured water temperature, S the simulated water temperatures.

2.5 Scenarios

To estimate the stream temperature response from different shading elements the following scenarios are used: No topography (T0), no river bank (B0), no vegetation (V0), maximum vegetation (V100) and current condition (STQ).

STQ uses all observed and derived data for vegetation, bank shade, and topography as described above.

For T0 the topographic angles θ_i are set to 0, while river bank and vegetation are not changed.

For V0 all vegetation parameters (vegetation height, density and overhang) were set to 0 and thereby the vegetation angles θ_v reduced to 0. V100 is defined with: 30 m height, 90 % vegetation density and 8 m overhang. River bank and topography are not changed.

B0 is approximated by increasing the elevation of the stream to the elevation of the surrounding topography to reduce the bank shade angle θ_b to 0. Topography and vegetation are not changed.

3 Results

3.1 Estimation of model sensitivity to input parameter variability

3.1.1 Quantification of influences caused by mass transfer and heat fluxes

We start with a brief overview of the mass transfer and heat flux factors affecting the water temperature of the river Pinka. Mass transfer is the influence of advection, mixing and dispersion.

The mean initial water temperature at the upstream model boundary is 16.15 °C. Because the water temperature at the study site is strongly influenced by the

water temperature at the upstream model boundary, we test how the imprecisions in instrument measured flow and stream temperature at the model boundary affect the simulated water temperature. Flow volume has a data resolution $\pm 0.01 \text{ m}^3/\text{s}$ and water temperature itself a data precision of $\pm 0.53 \text{ }^\circ\text{C}$. A change in flow volume within the data resolution leads to a temperature change in $\pm 0.04 \text{ }^\circ\text{C}$. The model variation caused by the forward propagation of water temperature changes is calculated with $+0.025 \text{ }^\circ\text{C}$, the minus error with $-0.024 \text{ }^\circ\text{C}$. Laboratory measurements showed, that the precision of the water temperature sensor is much better ($< 0.1 \text{ }^\circ\text{C}$) if water temperature is below $25 \text{ }^\circ\text{C}$ and changing less than 1 K per hour, as it is the case close to the source. If the maximum possible measurement error range and no potential errors related to the model are assumed this might result in a $\pm 0.07 \text{ }^\circ\text{C}$ model variation caused by the upstream boundary water temperature input.

The influence of mixing with tributaries on the mean water temperature is shown using two simulations. First the river is simulated without tributaries. The mean water temperature at the study region is $24.6 \text{ }^\circ\text{C}$. In the second simulation tributaries are added. A mean water temperature reduction in the study region of $2.3 \text{ }^\circ\text{C}$ is produced by this change. This reduction is a measure for the temperature change that can be caused by tributaries.

Dispersion influences caused by river geometry have been calculated according to (BOYD and KASPER, 2003) and are negligible in this case ($< 0.01 \text{ }^\circ\text{C}$). Heat loss by friction is small due to the average elevation gradient of 0.005 mm^{-1} which calculated according to THEURER et al. (1984) and WEBB and ZHANG (1997) amounts to about 3.28 Wm^{-2} .

The water temperature difference between the upstream model boundary and the study area without taking account of inflows amounts to $6.18 \text{ }^\circ\text{C}$ and is caused by the net heat flux (Bal) from the upstream model boundary to the study region and is composed of the influence of short wave radiation (Sw), long wave flux (Lw), conduction (Cd), convection (Cv) and evaporation (Ev) – as described in equation (2.1).

The $6.18 \text{ }^\circ\text{C}$ gained are a result of the balance of all heat fluxes. The separate heat fluxes short wave radiation and evaporation are five times of this magnitude.

For the study period and region the sum of the mean inputs is 165 Wm^{-2} (short wave flux 114 Wm^{-2} – 69 %, convection 35 Wm^{-2} – 21 %, long wave radiation flux 9 Wm^{-2} – 6 %, conduction 7 Wm^{-2} – 4 %) is reduced by the mean outputs of 131 Wm^{-2} caused by evaporation (Table 1). The resultant mean energy balance acting on the river is 35 Wm^{-2} .

The dominating energy fluxes in this region and time period are short wave radiation flux, which is always positive and can reach a maximum of 741 Wm^{-2} at midday and evaporation flux, which is negative and can reach a minimum of -697 Wm^{-2} at midday. Conduction flux is oscillating between 58 Wm^{-2} maximum during the day and -51 Wm^{-2} minimum at night. Long

wave flux is oscillating between maximum 70 Wm^{-2} during the day and minimum -53 Wm^{-2} at night. Convection is mainly positive with maximum around midday 252 Wm^{-2} and a minimum at -155 Wm^{-2} .

For most heat fluxes these results are representative also for the whole river and July/August 2013. Only long wave radiation and convection differ clearly between upstream and downstream, because they are influenced by water temperature, which increases from the source to the mouth. Long wave radiation balance shows this clearly in its correlation with stream temperature ($R^2 = 0.94$ for July and August 2013, river Pinka). Convection shows a similar distribution along the river like long wave radiation and is also correlated to water temperature, though not so strong.

3.1.2 Sensitivity of model to atmospheric heat fluxes and meteorological input parameters

To quantify the sensitivity of the model to different heat fluxes and meteorological input parameters, a sensitivity analysis was performed, increasing each factor to 110 %.

A change in net short wave radiation and evaporation effects the energy fluxes most (Fig. 2A). This is reflected in the water temperature change (net shortwave radiation $+0.82 \text{ }^\circ\text{C}$, evaporation $-0.62 \text{ }^\circ\text{C}$) (Fig. 2B). Convection causes $+0.15 \text{ }^\circ\text{C}$, but neither 10 % increase in long wave radiation flux nor conduction affect water temperature more than $0.01 \text{ }^\circ\text{C}$ (Fig. 2B).

The model is most sensitive to a 10 % increase in the meteorological input factor air temperature, which can cause an increase in the energy balance of 23 % (Fig. 3A) or an increase in water temperature of $1.39 \text{ }^\circ\text{C}$ (Fig. 3B). The second most influential factor to a 10 % increase is long wave radiation from the atmosphere ($+0.78 \text{ }^\circ\text{C}$), followed by global radiation ($+0.69 \text{ }^\circ\text{C}$) and air humidity ($+0.29 \text{ }^\circ\text{C}$) (Fig. 3B). Wind is the least sensitive parameter and reduces the water temperature slightly ($-0.03 \text{ }^\circ\text{C}$) (Fig. 3B).

3.1.3 Riverine influences to reduce atmospheric heat fluxes

All atmospheric heat fluxes are reduced depending on the openness to the sky of the studied reach. As the view to sky increases short wave radiation and evaporation increase in magnitude (Table 2, Fig. 5). Conduction also increases. Long wave radiation on the other hand decreases. Convection increases until a VTS of 0.61 is reached and decreases again for higher values.

This is also reflected in their correlation to the VTS value (2.7) (2.8), which is strong for net short wave radiation ($R^2 = 0.89$) and evaporation ($R^2 = 0.91$) (see Fig. 4). Also long wave radiation shows a clear correlation ($R^2 = 0.8$), which is better for areas of similar water temperature ($R^2 = 0.96$ for shaded reach). Also for convection a correlation can be distinguished.

Topography and vegetation influence VTS, radiation balance and evaporation (2.3–2.15).

The influence of topography on water temperature was calculated as $0.44 \text{ }^\circ\text{C}$ for the study region, the influ-

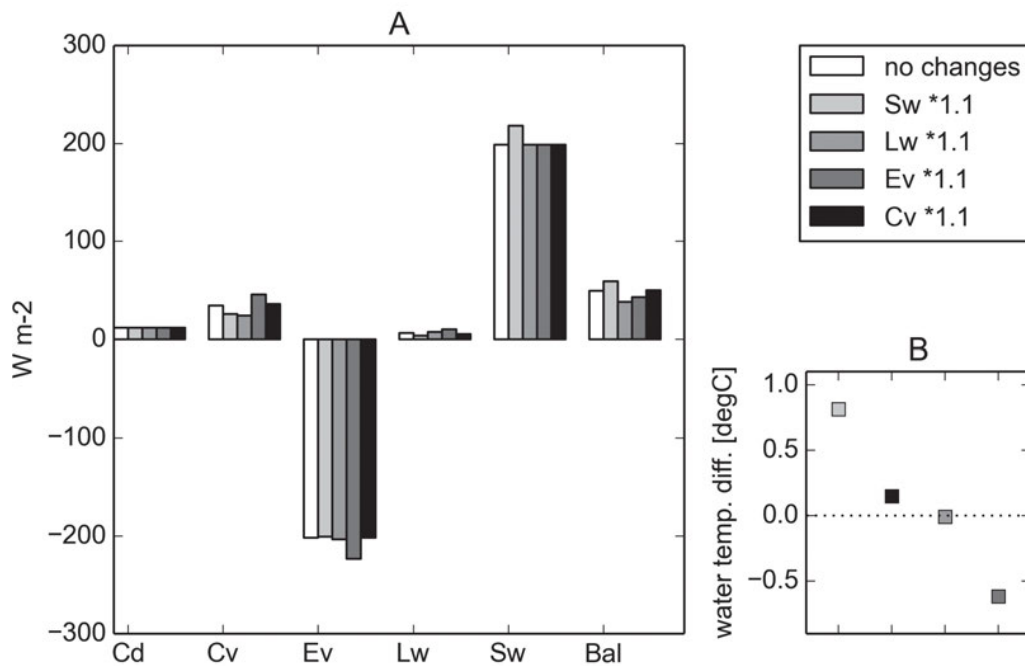


Figure 2: Influence of a 10% increased of separate heat fluxes (Cv convection, Ev evaporation, Lw long wave radiation, Sw short wave radiation) on (A) heat fluxes and (B) water temperature difference compared to “no changes” for study region and period, shading scenario: no vegetation (V0).

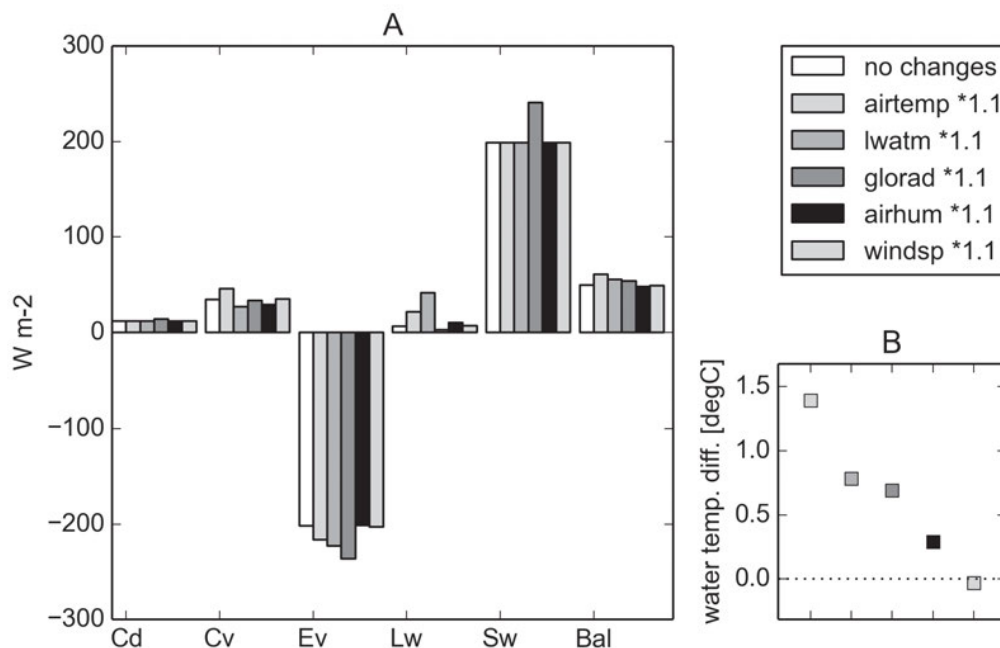


Figure 3: Influence of a 10% increase of meteorological parameters on (A) energy balance (Cd conduction, Cv convection, Ev evaporation, Lw long wave radiation, Sw short wave radiation, Bal balance) and (B) water temperature difference to “no change” for study region and period, shading scenario: no vegetation (V0).

ence of the river bank with $0.31\text{ }^{\circ}C$ (Fig. 5B). If there is vegetation the influence of topography on water temperature is less. The difference in predicted water temperature between V0 and the existing vegetation scenario (STQ) amounted to $1.68\text{ }^{\circ}C$ and to $3.81\text{ }^{\circ}C$ in the case

of scenario V100 (Fig. 5B). The heat fluxes which are affected most by vegetation changes are short wave radiation flux and evaporation (Fig. 5A).

As a more realistic example two reaches are analyzed using their actual vegetation cover.

Table 2: Influence of shading scenarios on view to sky (VTS) and heat fluxes at the river surface – convection(Cv), conduction (Cd), evaporation (Ev), long wave radiation (Lw) and short wave radiation heat flux (Sw).

	VTS	Cv	Cd	Ev	Lw	Sw
B0	1.00	30.1	14.8	-237.6	4.3	241.3
T0	0.90	32.2	13.6	-222.4	4.1	224.0
V0	0.90	37.3	12.3	-202.3	8.1	197.6
STQ	0.61	38.8	7.7	-138.5	11.3	122.8
V100	0.29	30.0	1.9	-72.9	15.7	46.5

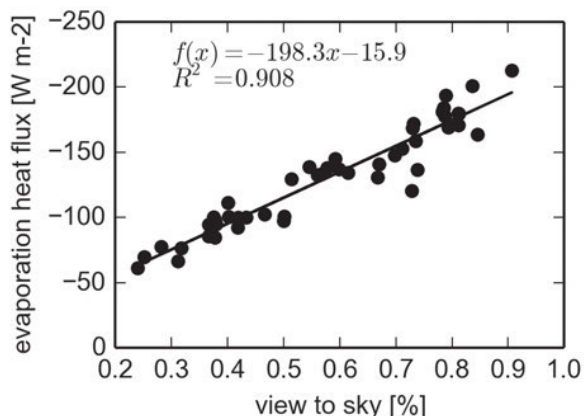


Figure 4: Correlation between evaporation flux and view to sky for study period and region.

The simulation of the heat fluxes estimates the energy balance at the shaded reach lower by 7 Wm^{-2} compared to the exposed reach on average (see Fig. 6A). At the shaded site the energy balance is negative with 1.5 Wm^{-2} , which is 58 Wm^{-2} lower than at the exposed site.

The temperature rise caused by the different heat fluxes within this reach (Fig. 6B) is calculated using formula (2.2). In both cases the short wave radiation flux is the dominating input, the dominating heat loss is evaporation leading to a water temperature change in the magnitude of about $0.8 \text{ }^\circ\text{C}$ within the reach (Fig. 6B).

Water transmissivity is another factor affecting the short wave radiation balance. The more short wave radiation is absorbed by the river, the more energy is available to heat the water. Transmissivity can be reduced after strong rainfalls, when mud is dissolved in the water. Simulations for possible turbidity scenarios were computed for the studied river during July and August and predicted a maximum possible influence of turbidity between $0.002 \text{ }^\circ\text{C}$ and $0.23 \text{ }^\circ\text{C}$. Also it became apparent that turbidity is only a relevant factor after rainfall. During low flow conditions and heat wave situations as analyzed here this it not the case, therefore it will not be included in the calculation of the total uncertainty.

3.2 Forward propagation of meteorological and shading input imprecisions

The value of short wave radiation flux measured at the river surface is influenced by global radiation sensor measurement errors and, to a greater extent, from shading by vegetation or topography. Topographic and vegetation shading elements influence all other energy fluxes as well.

Long wave radiation from the stream is mainly defined by water temperature. Atmospheric long wave radiation is a function of air temperature and cloudiness, which influences the atmospheric emissivity. In the present study cloudiness, which was only used to calculate atmospheric emissivity, was fixed at the value 1.

Evaporation is the main cooling factor. Since the Penman method includes more additional parameters than the mass transfer methods, which are of importance for energy balance we choose to use the Penman method. In our case the use of the simplified mass transfer method to calculate evaporation led to larger differences to the measurement results (see Fig. 7). The Penman method on the other hand gives more possibilities to include imprecisions via observation errors. Net radiation at the river surface, in addition to air temperature, air humidity and windspeed, is needed for the calculation. Measurement error ranges have to be considered for each parameter. Net radiation is strongly dependent on shading factors, which have been covered above.

Convection is a relevant contributor of heat input. It is directly related to evaporation (2.16), (2.17) and thus object to the same errors.

The model’s sensitivity towards meteorological and shading parameters within their maximum data imprecision was tested (Table 3). Here the existing vegetation and topography scenario (STQ) was used, to evaluate the realistic imprecision in water temperature caused by atmospheric inputs.

Air temperature changes of $\pm 0.2 \text{ }^\circ\text{C}$, relative humidity changes of $\pm 3.5 \%$ (if $< 10 \%$ or $> 90 \%$: $\pm 4.5 \%$), windspeed changes of $\pm 0.3 \text{ m/s}$ and global radiation changes of $\pm 5.25 \%$ were simulated. Variations of air temperature in this range leads to a maximum water temperature change of $\pm 0.1 \text{ }^\circ\text{C}$. Changes in air humidity, wind speed and global radiation cause changes in water temperature of $+0.233/-0.240 \text{ }^\circ\text{C}$, $+0.089/-0.117 \text{ }^\circ\text{C}$ and $\pm 0.201 \text{ }^\circ\text{C}$ respectively.

The influence of cloudiness on the calculation of atmospheric emissivity was tested by setting it to 0 and then to 1. The difference in the simulated mean water temperature between these two simulations at the study period and region is $0.078 \text{ }^\circ\text{C}$. Global radiation is effectively reduced by shading. Also shading elements reduce sky view which plays an important role in all other atmospheric heat fluxes. Therefore also the effect on predicted water temperature caused by the input parameter relevant for topographic (relative elevation $\pm 1 \text{ m}$, bottom width $\pm 1 \text{ m}$) and vege-

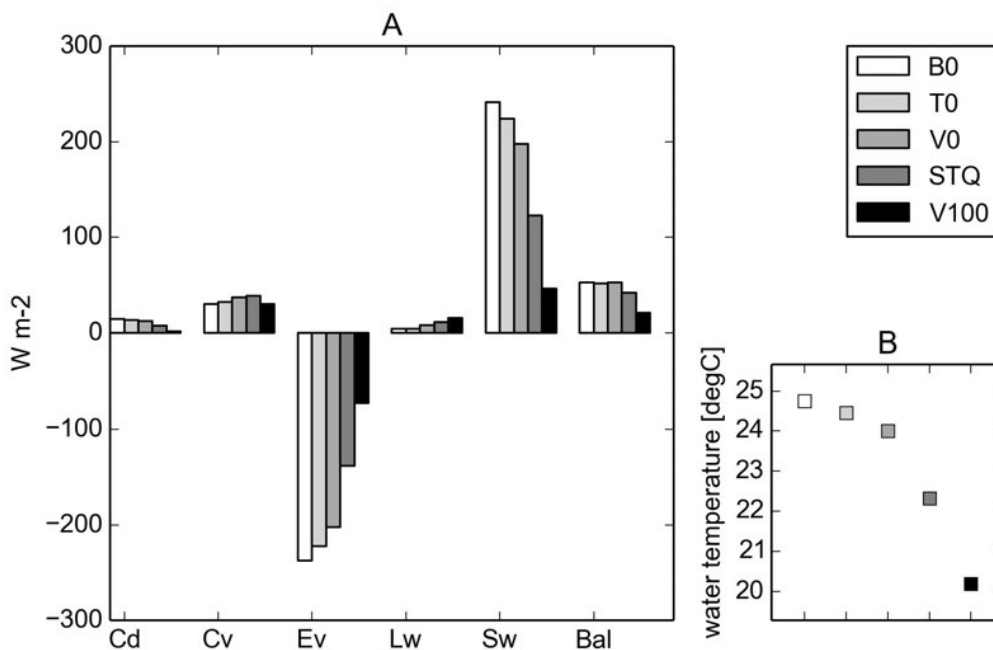


Figure 5: The influence of different shading scenarios: no topography (T0), no river bank (B0), no vegetation (V0), current conditions (STQ), full vegetation (V100) on (A) water temperature and (B) heat fluxes (Cd conduction, Cv convection, Ev evaporation, Lw long wave radiation, Sw short wave radiation, Bal balance) averaged for 2–8 August 2013, study region.

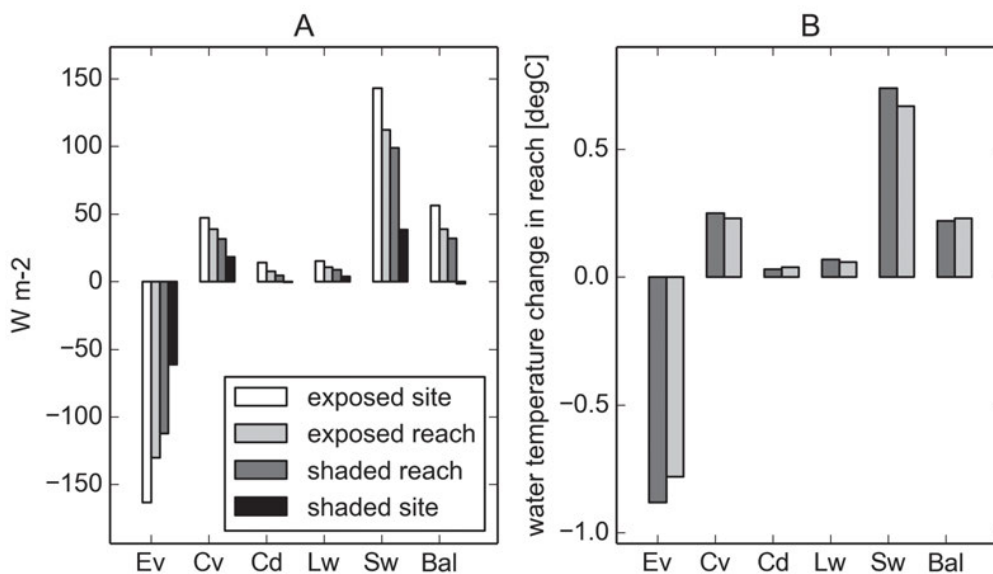


Figure 6: (A) heat fluxes (Cd conduction, Cv convection, Ev evaporation, Lw long wave radiation, Sw short wave radiation, Bal balance) and (B) water temperature change caused by heat fluxes calculated at exposed and shaded sites and reaches of 5 km, 2–8 August 2013, scenario: STQ.

tation shade (vegetation height ± 5 m, vegetation density ± 20 %, overhang ± 1 m) are tested within their data precision. A change in the relative elevation results in $+0.168/-0.211$ $^{\circ}C$. Changes in bottom width, vegetation height and overhang cause changes in water

temperature of $+0.257/-0.298$ $^{\circ}C$, $+0.367/-0.377$ $^{\circ}C$, $+0.436/-0.463$ $^{\circ}C$ and $+0.010/-0.047$ $^{\circ}C$ respectively.

A total error caused by measurement errors of the meteorological and shading input parameters is calculated with $+1.901/-2.095$ $^{\circ}C$ (Table 3).

Table 3: Estimation of error in simulated water temperature caused by measurement errors of the meteorological and shading input parameters.

	max. data imprecision	plus error [°C]	minus error [°C]
air temperature	+/-0.2 °C	0.101	-0.102
relative humidity	+/-3.5 %, > 90 %: +/-4.5 %	0.233	-0.240
wind speed	0.3 m/s	0.089	-0.117
global radiation	+/-5.25 %	0.201	-0.201
cloudiness	+/-50 %	0.039	-0.039
sum meteorological input		0.663	-0.699
relative elevation	+/-1 m	0.168	-0.211
bottom width	+/-1 m	0.257	-0.298
vegetation height	+/-5 m	0.367	-0.377
vegetation density	+/-20 %	0.436	-0.463
vegetation overhang	+/-1 m	0.010	-0.047
sum shade		1.238	-1.396
total sum		1.901	-2.095

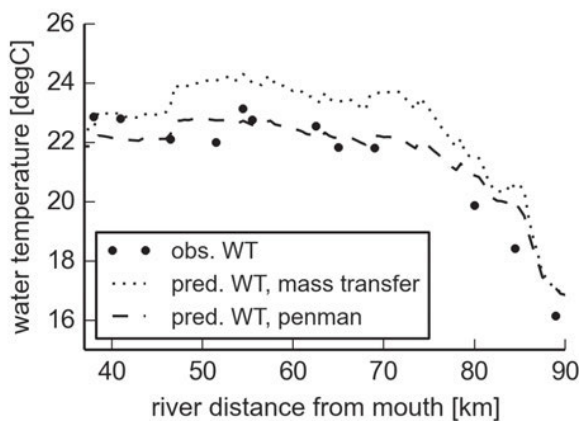


Figure 7: Comparison between mean water temperature for simulation with evaporation method Mass transfer and Penman, as a function of the river distance to the mouth 2–8 August 2013.

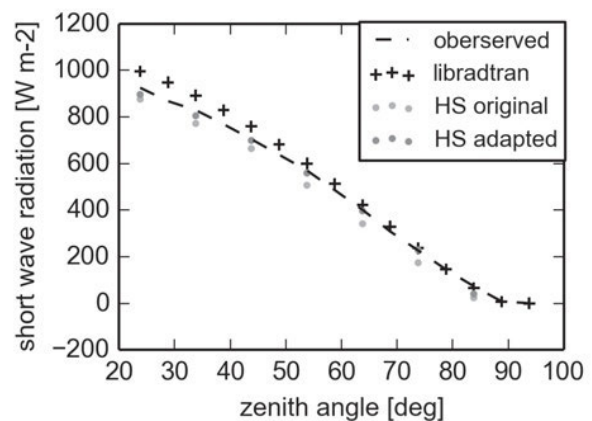


Figure 8: Comparison for clear sky maximum zenith: Measurement with Schenk starpyranometer, simulation libradtran1.4 (afglus) tau=0 (15 June 2013), the Heat Source original code and adapted code (2 July 2013).

3.3 Comparison with measurements

3.3.1 Radiation balance

Heat Source calculates global radiation above topography using astronomical data and cloudiness values. To test the precision of this approach after the first Heat Source simulation runs also simulations with the radiation model LibRadtran (MAYER et al., 2015) were performed to calculate the global as well as the direct and diffuse radiation on a reference day. Those simulations were compared to the global radiation measured at the reference station, which was not shaded by topography nor vegetation, and the Heat Source calculations of global radiation above topography. The simulations showed, that Heat Source and LibRadTran generally performed well in estimating the global radiation above topography with $R^2 > 0.999$ and a RMSE of 50.1 and 41.9 Wm^{-2} respectively.

Because we had measured global radiation data we opted to modify the Heat Source code so that the measured data could be input directly into the model calculations instead of being derived using cloudiness data. The code modification yielded an improvement to the surface short wave predictions.

While the original code resulted in a mean difference of 53.1 Wm^{-2} (5.7 %, RMSE 57.9 Wm^{-2}) and the modified code using direct global radiation input showed a mean difference of 15.0 Wm^{-2} (1.6 %, RMSE 21.2 Wm^{-2}) (Fig. 8).

The long and short wave radiation from the atmosphere and the stream was measured unobstructed next to the reference station, about 1 m above the water surface and compared to the corresponding values calculated by Heat Source (see Fig. 9). The RMSE between measured and simulated long wave radiation from the atmosphere (21.04 Wm^{-2}) and from the stream

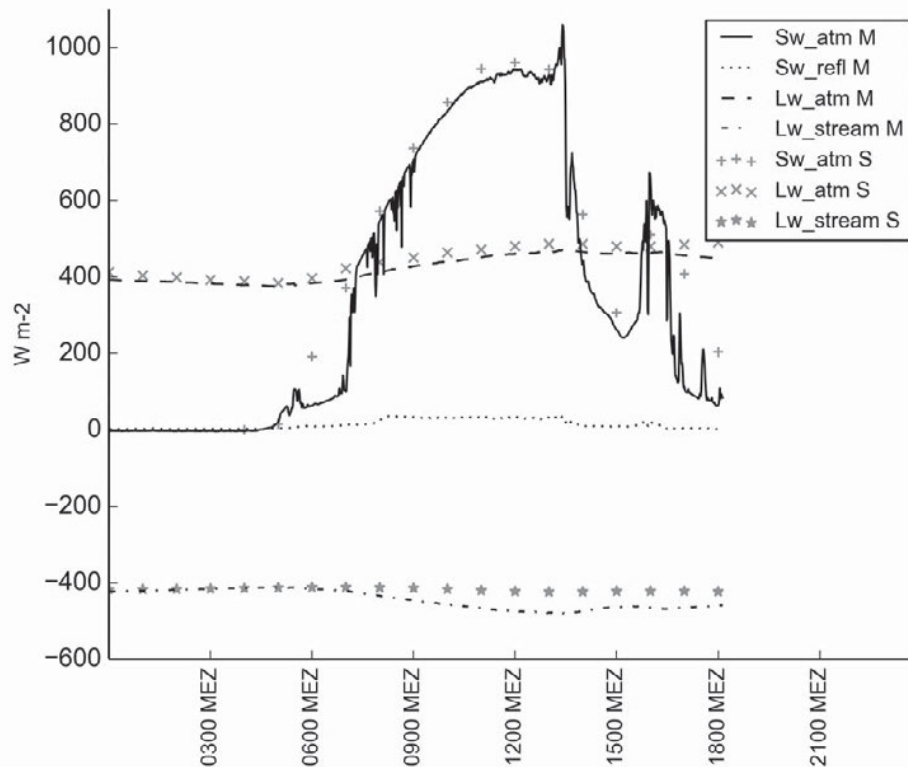


Figure 9: Long and short wave radiation balance at DFS 39 km on the 28 July 2013.

(33.10 W m^{-2}), which is about 5 % to the measured values. The reflected short wave radiation was about 3.82 % of the incoming short wave radiation.

3.3.2 Water temperature

The correlation between the simulated and measured water temperature is calculated at five different stations of different vegetation shade, which amongst others have been featured in [HOLZAPFEL and RAUCH \(2015\)](#). The adapted Heat Source version gives good correlations for situations with all vegetation intensities ([Table 4](#)).

The calculated water temperatures of the original and changed code were compared for daily values of July and August 2013 at DFS 39 km. The changed code showed slight improvement regarding their correlation to the measurements for maximal (max), minimum (min) and mean water temperatures (original code: max $R^2 = 0.91$, min: $R^2 = 0.91$, mean: $R^2 = 0.96$, incl. changes: max: $R^2 = 0.92$, min: $R^2 = 0.91$, mean: $R^2 = 0.96$). Consequently the changed code was used.

For the reference region and period we obtained a root mean square error RMSE of $0.84 \text{ }^\circ\text{C}$ (and a standard error of estimate SEE of $0.85 \text{ }^\circ\text{C}$) for the adapted code.

Also the heat wave at the beginning of August 2013 is pictured well with the model ([Fig. 10](#)). The peak air temperature of $37.508 \text{ }^\circ\text{C}$ was reached at 1400 MEZ 8 August 2013 at the reference station. The error bars indicate the total error caused by measurement errors

of the meteorological and shading input parameters ([Table 3](#)) as described in [Chapter 3.2](#). The air temperature showed an increasing trend of 0.48 during the period 2–8 August 2013. At the same time the mean measured water temperature in the study region and period has a slope of 0.28 . The simulated water temperature has only a slightly lower slope of 0.26 (see [Fig. 10](#)). In the night from 5 to 6 August the simulated values differ strongly from the measurement and don't even reach them with their error bars. This is caused by increased discharge following rainfall.

4 Discussion

4.1 Comparison with measurements

The reflected short wave radiation measured in this study was about 3.8 % of the incoming amount. This value agrees with the 3 % reported in literature ([BENYAHYA et al. 2012](#); [CAISSIE et al. 2007](#); [SINOKROT and STEFAN, 1993](#)).

In this study a difference of 5 % between measured and simulated long wave radiation is calculated. [BENYAHYA et al. \(2012\)](#) calculated long wave radiation with a precision of 3 %.

[SINOKROT and STEFAN \(1993\)](#) showed that a deterministic model is able to simulate hourly water temperatures with a precision of 0.2 to $1 \text{ }^\circ\text{C}$ standard error of estimate (SEE). For a reach comparable to Pinka and

Table 4: Correlation and RMSE between Measurements and Simulation results during July/August 2013, Vegetation Shading Index average 5000 m upstream (VSI 5000), view to sky (VTS) at the measurement station.

DFS	31 km	35 km	37 km	39 km	48 km
VSI 5000	0.49	0.64	0.50	0.35	0.65
VTS	0.38	0.42	0.60	0.79	0.37
time span	1 Jul–25 Aug	14 Jul–25 Aug	1 Jul–25 Aug	1–27 Jul	4 Jul–25 Aug
R^2 of WT max	0.92	0.92	0.86	0.90	0.87
R^2 of WT min	0.91	0.87	0.89	0.91	0.89
R^2 of WT mean	0.96	0.95	0.95	0.96	0.90
RMSE	0.8 °C	0.7 °C	0.95 °C	0.93 °C	1.24 °C
STDV of RMSE	0.36	0.28	0.59	0.63	4.97

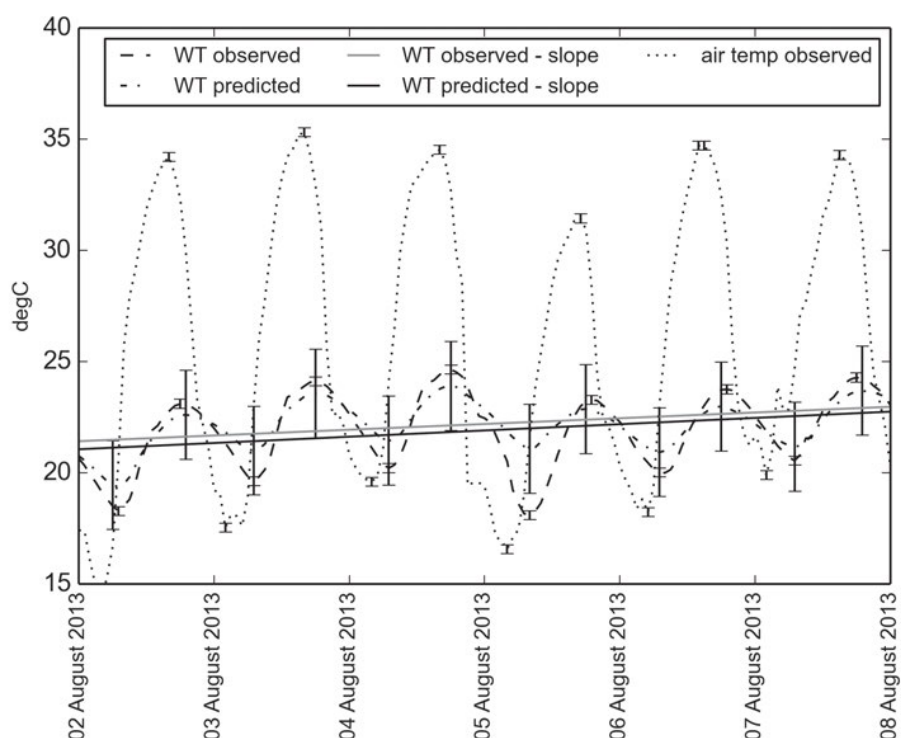


Figure 10: Measured air and stream temperature, simulated stream temperature (incl. error bars at minima and maxima) and trend lines for 2–8 August 2013, mean for the study period and region.

the timespan of this study the SEE was 0.32 °C. [MACDONALD et al. \(2003\)](#) reported the difference in observed and predicted weekly mean water temperature from forest harvesting ranged from 0.5 to 3.86 °C. [CAISSIE et al. \(2007\)](#) calculated for the years 1995–1999 a RMSE of 1.55 °C the Little Southwest Miramichi River, and 1.61 °C for the Catamaran Brook, which is more comparable to the Pinka. For summer 1999, which had air temperatures above-average and relatively low discharge, the model performed better ([CAISSIE et al., 2007](#)). [HAAG and LUCE \(2008\)](#) reported a RMSE from 0.65 °C to 1.14 °C from 1 January to 1 September 2003 for the much larger river Neckar (mean 140 m³/s) using the model LARSIM-WT. In our study for the stations within the study area in July/August R^2 ranged between 0.86

and 0.96, the RMSE between 0.7 °C and 1.24 °C, for the study period the mean RMSE is 0.84 °C. Therefore Heat Source is a valid model for simulation of summer water temperatures in Austrian lowland rivers during low flow conditions.

4.2 Model Sensitivity

The model’s sensitivity towards meteorological input parameters within their data precision was tested. All sensor error ranges are assumed at their maximum and are comparable to other studies in this field ([LEACH and MOORE, 2010](#)). Under average conditions a much better precision is expected.

In this study the stream temperature change associated with relative humidity measurement error is estimated to be ± 0.2 °C (Table 3). The model is very sensitive to changes in the atmospheric input parameter air temperature (Fig. 3B). However, air temperature sensors are very accurate resulting in simulated stream temperature changes of ± 0.1 °C (Table 3). Apart from measurement errors air temperature and humidity also local differences along the river might be not captured precise enough. Only one climate station was used to obtain air temperature and humidity data for a whole study reach. This is a common practice in comparable studies though (STORY et al., 2003; HANNAH et al., 2008). CAISSIE et al. (2007) found their model to be not so sensitive to relative humidity, so that average values of an airport station 76 km distant were used with only an RMSE increase in the simulated water temperature of less than 0.09 °C. Also BENYAHYA et al. (2012) found, that data from a remote meteorological station can be easily transferred to calculate heat fluxes of a stream.

Keeping all this in mind the heat period 2–8 August caused by increasing air temperature is pictured well.

Measurement errors in solar radiation sensor input can cause about ± 0.2 °C change in simulated water temperature (Table 3). Apart from the sensor error, solar radiation measurement data has the ability to produce a rather large error, because it is much more spatially differentiated than air temperature and air humidity, therefore attention has to be given to the correct measuring position. Imprecisions are mainly results of shading influences (BENYAHYA et al., 2012). Therefore in the current study radiation was measured at an open site, unobstructed by shade. The extinction of solar radiation is calculated using vegetation and topographic shade parameter.

The influence of the wind sensor imprecision is rather small with ± 0.1 °C change in stream temperatures (Table 3). Although the model is least sensitive to wind speed changes within sensor precision here errors of larger magnitude are possible. Windspeed can vary significantly within riparian microclimates with high vegetation cover and may not be representative to be measured at a single site according to LEACH and MOORE (2010). In the current study wind speed was measured at an open site. The wind speed reduction caused by vegetation is calculated.

The main difficulty regarding calculation of wind speed reduction is obtaining the correct roughness length Z_0 , which controls the wind function (2.14). Roughness of the surrounding area is not uniform and differs strongly from the source to the mouth. Heat Source is using vegetation height to calculate Z_0 (2.12). This is a reasonable approach, but leaves the problem how to obtain the correct vegetation height. Additionally the height and inclination of the river bank, which might have a considerable influence on Z_0 , varies and is difficult to sample. Hence also the precision of wind speed is controlled by the precision of land cover and to-

pography input. Exceptionally, in this study these values were obtained.

As in this study net short wave radiation and evaporation flux are the two most influential heat fluxes and both are influenced by the openness of the river to the sky, which is defined by vegetation cover and topography, those influences are investigated as well. The effect of the input parameter relevant for shade on water temperature are tested within their data precision. All error ranges are average values. The total water temperature sensitivity caused by vegetation and topography measurement errors is $+1.24/-1.40$ °C. The model accurately predicts measured fluxes. For the calculation of long wave radiation though, in this study a fixed cloudiness is used to calculate atmospheric emissivity. Also here the forward propagation of this error on water temperature, was calculated with ± 0.04 °C. The total water temperature sensitivity caused by the measurement errors of meteorological input is $+0.66/-0.70$ °C. The maximum error of the water temperature measurement at the reference region is ± 0.53 °C. Taking into account the observed daily water temperature amplitudes of 3.6 to 5.2 °C the errors caused by the input imprecisions are acceptable.

4.3 Magnitude of atmospheric heat fluxes during heat wave conditions

Stream temperature is dependent on many factors. If only the temperature change caused by heat fluxes and not by mass transfer is considered in literature many studies agree that the meteorological heat fluxes short wave radiation and evaporation are dominant in general (SINOKROT and STEFAN, 1993; CAISSIE et al., 2007; WEBB et al., 2008).

Also in this study, short wave radiation is found to be responsible for 69 % of the energy balance inputs during heat wave conditions for a river of diverse vegetation cover and average $0.55 \text{ m}^3 \text{ s}^{-1}$ discharge. The net short wave radiation amounts to 114.4 Wm^{-2} on average and reaches 740.8 Wm^{-2} as maximum value.

In this study an exceptional heat wave situation is presented, which is outlined by high minimum and maximum air temperatures. High minimum air temperatures limit radiative cooling at night, also higher air temperatures increase the sensible heat flux from the atmosphere towards the river. As warmer air can take up more moisture, also evaporative heat flux is affected.

Convection and long wave radiation are on average additional heat inputs (9.4 and 34.5 Wm^{-2}), but also can be heat outputs from the stream to the atmosphere. Also it is found that the main output is attributed to evaporation, which is 130.8 Wm^{-2} on average, and 697.2 Wm^{-2} maximum.

The turbulent heat fluxes evaporation and convection are dependent on the evaporation method used. The Penman combination method, which uses the net radiation at the surface of the river as input, gives more

importance to local shading. This leads to larger evaporative and convective fluxes in this study as well as to cooler water temperatures than in studies using the mass transfer method (JOHNSON, 2004; HANNAH et al., 2008; MAHEU et al., 2014).

FRITSCHEN and VAN BAVEL (1962) measured a maximum latent heat flux of approx. 500 Wm^{-2} over thin open water surfaces. OKE (1987) cites an annual average latent heat flux of 98 Wm^{-2} for all oceans.

However, turbulent heat fluxes can be limited, to an order of magnitude lower than net radiation on sunny days, due to lack of ventilation e.g. in forested environments. Under these circumstances heating effects of sensible heat and the cooling of latent heat flux tend to cancel. This can also be the case in clear-cuts or after wildfires when only defoliated trees are left in deep and narrow channels with bank sheltering (MOORE et al., 2005; LEACH and MOORE, 2010). Especially at wind and sun exposed situations high evaporation values are likely. In the current study there is enough ventilation to enable evaporation of larger magnitude.

E.g. BENYAHYA et al. (2012) found evaporation to cause 100 % of heat outputs and short wave radiation flux 71 % of inputs 7–23 June 2008 for a smaller tributary in Canada (Table 1). HANNAH et al. (2008) found evaporation to be the only non radiative energy balance output during spring and summer in a Scottish forest river.

As the evaporation calculation depends because of its complexity on empirical coefficients (DEUTSCHER VERBAND FÜR WASSERWIRTSCHAFT (DVWK), 1996), some improvement might have been achievable by fitting them to the study situation, which lies however outside the scope of this study.

Long wave radiation in some publications is also named as relevant output of the same magnitude as evaporation (MARCOTTE and DUONG, 1973; MORIN and COUILLARD, 1990). In the current study on the contrary it is part of the average heat input to the stream (6 %).

Convection on the other hand is called negligible in some studies (BROWN and BARNWELL, 1987) and here is with 21 % of the input definitely not negligible. Convection is generally only small on average. It alternates between positive and negative values, depending on the direction of the air temperature – stream temperature difference and is mainly responsible for variations in stream temperature (CAISSIE et al., 2007). The high air temperatures compared to the river temperature, as found during heat wave conditions, affect Bowen ratio and convection heat flux.

Both long wave radiation and convection are correlated to water temperature, which increases from the source to the mouth. Close to the source, where water temperature is cold compared to air temperature during summer, the water is warmed by the atmosphere and the long wave radiation balance is positive. Close to the mouth this is reversed. On average for the whole river in July and August 2013 the long wave radiation balance is negative with -2.86 Wm^{-2} . During the study period

and region otherwise it is positive with 11.24 Wm^{-2} for the same river. This can be explained with the high minimum air temperatures of 18°C on average within the study region and period. Air temperatures drop on average only 4°C below stream temperature at night while during the day they exceed stream temperature for more than 11° . Long wave emission from the atmosphere at night is still high and the long wave radiation emitted from the stream at night can not compensate the total radiation input received during day and instead adds 9.39 Wm^{-2} to the energy balance on average.

4.4 Reduction of atmospheric heat fluxes influencing stream temperature

In literature the influence of changing atmospheric heat fluxes on water temperature is pictured e.g. by the comparison between reaches who are exposed to solar radiation or reaches shaded by forests. While minimum daily temperatures show only small changes (about 1 to 2°C), summer daily temperatures ranges can increase from 1 to 3°C after logging to 7 to 8°C (MOORE et al., 2005). Maximum temperatures have the potential to show the highest increases e.g. up to 13°C (MOORE et al., 2005). COLE and NEWTON (2013) e.g. measured 1 – 3° daily maxima temperature increase before harvest and 3.8°C after harvest in 1800 – 2600 m long reaches with about $0.01 \text{ m}^3/\text{s}$ discharge.

GROOM et al. (2011) found an average stream temperature difference of 0.7°C post-harvest in private forests in Oregon. The observed range was between -0.9 and 2.5°C . If shading is underestimated compared to observed conditions the maximum stream temperatures tend to be overestimated (RUTHERFORD et al., 1997) because vegetation absorbs incoming short wave radiation and thereby reduces water temperature maxima during cloudless summer days. In a small tributary of average 1.2 m width and low flow condition (0.01 – $0.015 \text{ m}^3/\text{s}$), a daily maximum water temperature rise from 7 to 24° caused by removal of canopy was simulated within 560 m by RUTHERFORD et al. (1997) on a sunny day. JOHNSON (2004) also found a strong reduction of maximum water temperatures (-3.9°C) even on a 200 m reach caused by shading, but also mean temperatures were reduced for 0.7°C in this short distance.

In the current study the maximum influence of river bank, topography and vegetation on maximum water temperature for a 5 km reach and $0.55 \text{ m}^3/\text{s}$ discharge during heat wave conditions was simulated with 0.36 , 0.51 and 4.89°C . Mean water temperatures increased for 0.30°C , 0.41° and 3.60°C . HOLZAPFEL and RAUCH (2015) found a $+3.1^\circ\text{C}$ difference in measured daily mean maximum water temperature between beginning and end of 4 km unshaded areas (DFS 35–39) followed by a -3.2°C difference between beginning and end of 9 km more shaded areas (DFS 39–48) within the study region and period. Daily water temperature ranges were simulated with 4.29°C average for the study period

and region. [HOLZAPFEL and RAUCH \(2015\)](#) found diurnal ranges of 3.5 °C for different vegetation stands and 6.7 °C unshaded areas during summer.

5 Conclusion

In this paper we demonstrated the deterministic model Heat Source can accurately predict heat fluxes and is a valid model to use for stream temperature predictions in Eastern Austrian lowland rivers during the summer and heat wave periods.

The most influential and sensitive energy fluxes in Eastern Austrian lowland rivers during summer heat wave periods are net short wave flux and evaporation. Sensor error ranges of meteorological input global radiation and relative humidity can cause the most imprecision in simulated water temperature, therefore the inclusion of measured global radiation as a direct input, instead of being calculated within the model, can lead to an improvement in the simulated water temperature.

To model riverine temperature using a deterministic model like Heat Source high resolution input parameters are necessary. As the flow velocity and depth play an important role for stream temperature, morphologic parameters such as bottom width and the Mannings n roughness are crucial for good model results and have to be chosen with care. Also local shade parameters have to be included as precise as possible. For further research extensive use of remote sensing data, especially to obtain shading parameters, is recommended. Field completion surveys remain necessary in any case though. Meteorological input on the other hand already was available in a very rough resolution (one reference station), a fact which didn't impede valid results. This was also true for simulation tests performed using a meteorological station which was not directly positioned at the riverbank but 50 m orographically right. If no data sets as here are available linear and non-linear regression models based on air temperature, water temperature of the previous days or streamflow are helpful to predict stream temperature patterns.

All energy fluxes are influenced by reduction of sky view. Errors caused by imprecise representation of sky view exceed the error caused by meteorological input measurement errors. The most important sky obstructing elements are vegetation density and vegetation height. While the model imprecisions caused by measurement errors of meteorological input are expected much smaller under normal conditions, the imprecisions in sky view reducing parameters are realistic or even underestimated. A total model imprecision caused by the measurement errors of meteorological and shading input parameters is calculated with +1.901/−2.095 °C. The influence of existing vegetation on mean water temperature in the study region and period was simulated with 1.68 °C and 3.81 °C in the case of a maximum vegetation scenario

This demonstrates that vegetation has a significant influence on stream temperature.

6 Acknowledgement

This research was part of the project BIO_CLIC and LOWFLOW+ both funded within the Austrian Climate Reserach Programm (ACRP) by the Klima und Energiefond. Hydrological data and the digital elevation model were provided by hydrographic services and the federal state governmental geoinformation service authorities of Styria and Burgenland. Special thanks are given to the Oregon Department of Environmental Quality, who maintains the model Heat Source and opened the source code for scientific use, in particular RYAN MICHIE. Thanks to WOLFGANG LAUBE who helped in the field work, HERBERT FORMAYER, ERICH MURSCH-RADLGRUBER, DAVID LEIDINGER, STEFAN HASEL and the free and open-source software community.

7 Abbreviations

S Simulation, M Measurement

Heat fluxes: Cv convection flux, Cd conduction flux, Ev evaporation flux, Sw short wave radiation flux, Lw long wave radiation flux

Bal: energy balance

Climate input: glorad global radiation, lwatm atmospheric long wave radiation, airtemp air temperature, airhum relative air humidity, windsp wind speed

Scenarios: T0 no topography, STQ current conditions, V0 no vegetation, V100 maximum vegetation, B0 no river bank

VSI: Vegetation Shading Index

VTS: view to sky

MEZ: Middle European time zone

References

- ANDERSON, D.A., J.C. TANNEHILL, R.H. PLETCHER, 1984: Computational Fluid Mechanics and Heat Transfer. – McGraw-Hill, New York.
- ARISMENDI, I., M. SAFEEQ, J.B. DUNHAM, S.L. JOHNSON, 2014: Can air temperature be used to project influences of climate change on stream temperature? – Environ. Res. Lett. **9**, 084015.
- BENYAHYA, L., D. CAISSIE, M.G. SATISH, N. EL-JABI, 2012: Long-wave radiation and heat flux estimates within a small tributary in Catamaran Brook (New Brunswick, Canada). – Hydrol. Proc. **26**, 475–484.
- BESCHTA, R.L., J. WEATHERED, 1984: A computer model for predicting stream temperatures resulting from the management of streamside vegetation. – USDA Forest Service.
- BOYD, M., B. KASPER, 2003: Analytical methods for dynamic open channel heat and mass transfer: – Methodology for heat source model Version 7.0.
- BROWN, L., T.O.JR. BARNWELL, 1987: The Enhanced Stream Water Quality Models QUAL2E and QUAL2E-UNCAS: Documentation and USER Manual. – U.S. Environmental Protection Agency, Athens, GS.
- CAISSIE, D., 2006: The thermal regime of rivers: a review. – Freshwater Biology **51**, 1389–1406.

- CAISSIE, D., M.G. SATISH, N. EL-JABI, 2007: Predicting water temperatures using a deterministic model: Application on Miramichi River catchments (New Brunswick, Canada). – *J. Hydrol.* **336**, 303–315.
- CHOW, V., 1959: *Open-channel hydraulics*. – McGraw-Hill, New York.
- COLE, E., M. NEWTON, 2013: Influence of streamside buffers on stream temperature response following clear-cut harvesting in western Oregon. – *Canadian J. Forest Res.* **43**, 993–1005.
- CUENCA, R.H., 1989: *Irrigation System Design: An Engineering Approach*. – Englewood Cliffs, Prentice-Hall, New Jersey.
- DAVIES-COLLEY, R.J., J.M. QUINN, 1998: Stream lighting in five regions of North Island, New Zealand: Control by channel size and riparian vegetation. – *New Zealand J. Marine Freshwater Res.* **32**, 591–605.
- DEUTSCHER VERBAND FÜR WASSERWIRTSCHAFT (DVWK), 1996: Ermittlung der Verdunstung von Land- und Wasserflächen. In DVWK-Merkblätter Zur Wasserwirtschaft. – Kommissionsvertrieb, Wirtschafts- und Verlagsgesellschaft, Gas und Wasser mbH, Bonn
- DINGMAN, S.L., 2002: *Physical Hydrology*. – Prentice Hall, New Jersey.
- DUNNE, T., L.B. LEOPOLD, 1978: *Water in Environmental Planning*. – W.H. Freeman and Company, San Francisco, California.
- ERICKSON, T.R., H.G. STEFAN, 2000: Linear Air/Water Temperature Correlations For Streams During Open Water Periods. – *J. Hydrol. Engin.* **604**, Series A, 317–321.
- EVANS, E.C., G.R. MCGREGOR, G.E. PETTS, 1998: River energy budgets with special reference to river bed processes. – *Hydrological Processes* **12**, 123–133.
- FRITSCHEN, L.J., C.H.M. VAN BAVEL, 1962: Energy balance components of evaporating surfaces in arid lands. – *J. Geophys. Res.* **67**, 5179–5185.
- GARNER, C., 2007: *Modeling the Effect of Riparian Shading on Water Temperature for Portions of the Carson River*. – Thesis, University of Nevada, Reno, USA.
- GARNER, G., I.A. MALCOLM, J.P. SADLER, D.M. HANNAH, 2014: What causes cooling water temperature gradients in a forested stream reach? – *Hydrol. Earth Sys. Sci.* **18**, 5361–5376.
- GROOM, J.D., L. DENT, L.J. MADSEN, J. FLEURET, 2011: Response of western Oregon (USA) stream temperatures to contemporary forest management. – *Forest Ecol. Manag.* **262**, 1618–1629.
- HAAG, I., A. LUCE, 2008: The integrated water balance and water temperature model LARSIM-WT. – *Hydrol. Process.* **22**, 1046–1056.
- HANNAH, D.M., I.A. MALCOLM, C. SOULSBY, A.F. YOUNGSON, 2008: A comparison of forest and moorland stream microclimate, heat exchanges and thermal dynamics. – *Hydrol. Process.* **22**, 919–940.
- HOLZAPFEL, G., H.P. RAUCH, 2015: Der Einfluss der Ufervegetation auf die Wassertemperatur der Lafnitz und Pinka. – Mitteilungsblatt für die Mitglieder des Vereins für Ingenieurbioogie, Ingenieurbioogie: Neue Entwicklungen an Fließgewässern, Hängen und Böschungen, 1/2015, 4–10.
- HOLZAPFEL, G., P. WEIHS, H.P. RAUCH, 2013: Use of the Shade-a-lator 6.2 model to assess the shading potential of riparian purple willow (*Salix purpurea*) coppices on small to medium sized rivers. – *Ecol. Eng.*, <http://www.sciencedirect.com/science/article/pii/S0925857413002875>. DOI:10.1016/j.ecoleng.2013.07.036.
- HOLZAPFEL, G., H.P. RAUCH, P. WEIHS, H. TRIMMEL, 2015: The interrelationship of riparian vegetation and water temperature demonstrated with field data measurements and analysis of the rivers Pinka and Lafnitz. – EGU General Assembly 2015, Vienna, 12.–17. April 2015, *Geophys. Res. Abstracts* **17**, 11653–11653.
- INDEPENDENT MULTIDISCIPLINARY SCIENCE TEAM'S (IMST), W. ELMORE, G. STANLEY, R.M. HUGHES, W. PEARCY, C. SCHRECK, R. SHEPARD, C. YEE, 2004: *Oregon's Water Temperature Standard and its Application: Causes, Consequences, and Controversies Associated with Stream Temperature*. – Technical Report 2004-1, May 7, 2004
- JOHNSON, S.L., 2003: Stream temperature: scaling of observations and issues for modelling. – *Hydrol. Processes* **17**, 497–499.
- JOHNSON, S.L., 2004: Factors influencing stream temperatures in small streams substrate effects and a shading experiment. – *Can. J. Fish. Aquat. Sci.* **62**, 913–923.
- JOHNSON, M.F., R.L. WILBY, 2015: Seeing the landscape for the trees: Metrics for guiding riparian shade management. – *Water Resources Research* **51**, 3754–3769.
- KALNY, G., F. DOSSI, H. FORMAYER, W. GRAF, D. LEIDINGER, P. LEITNER, A. MELCHER, F. PLETTERBAUER, M. SEEBACHER, H. TRIMMEL, P. WEIHS, H.P. RAUCH, 2015: *Publizierbarer Endbericht BIO_CLIC: Das Potential der Ufervegetation zur Minderung von Effekten des Klimawandels auf biologische Lebensgemeinschaften kleiner bis mittelgroßer Fließgewässer – Klima und Energiefonds ACRP*, 42.
- KENNEDY, M.C., A. O'HAGAN, 2001: Bayesian calibration of computer models. – *J. Roy. Stat. Soc. Series B* **63**, 425–464.
- ŁASZEWSKI, M., 2013: Stream water temperature: a short review with special reference to diurnal dynamics. – *Miscellanea Geographica – Regional Studies on Development* **17**, 34–41.
- LEACH, J.A., R.D. MOORE, 2010: Above-stream microclimate and stream surface energy exchanges in a wildfire-disturbed riparian zone. – *Hydrol. Process.* **24**, 2369–2381.
- MACDONALD, J., E.A. MACISAAC, H. HERUNTER, 2003: The Effect of Variable-Retention Riparian Buffers on Water Temperatures in Small Headwater Streams in Sub-Boreal Forest Ecosystems of British Columbia. – *Canadian J. Forest Res.* **33**, 1371–1383.
- MAHEU, A., D. CAISSIE, A. ST-HILAIRE, N. EL-JABI, 2014: River evaporation and corresponding heat fluxes in forested catchments. – *Hydrol. Process.* **28**, 5725–5738.
- MARCOTTE, N., V.-L. DUONG, 1973: Le calcul de la temperature de l'eau des riviere. – *J. Hydrol.* **18**, 273–287.
- MATULLA, C., A. SCHMUTZ, A. MELCHER, T. GERERSDORFER, P. HAAS, 2007: Assessing the impact of a downscaled climate change simulation on the fish fauna in an Inner-Alpine River. – *Int. J. Biometeorol.* **52**, 127–137.
- MAYER, B., A. KYLLING, C. EMDE, R. BURAS, U. HAMANN, J. GASTEIGER, B. RICHTER, 2015: *libRadtran user's guide*. – Online available at <http://www.libradtran.org/doc/libRadtran.pdf>, last accessed: 21 December 2015
- MCCUTCHEON, S.C., 1989: *Water Quality Modeling*. – CRC Press, Boca Raton.
- MELCHER, A., F. DOSSI, W. GRAF, M. GULDENSCHUH, G. HOLZAPFEL, E. LAUTSCH, P. LEITNER, K. SCHAUFLE, M. SEEBACHER, H. TRIMMEL, 2014: Assessment of aquatic habitat availability and climate change effects in medium sized rivers. – 10th ISE Trondheim, Norway.
- MOORE, R.D., D.L. SPITTLEHOUSE, A. STORY, 2005: Riparian microclimate and stream temperature response to forest harvesting: a review. – *JAWRA* **41**, 813–834.
- MORIN, G., D. COUILLARD, 1990: Predicting river temperatures with a hydrological model. In: *Encyclopedia of Fluid Mechanics, Surface and Groundwater Flow Phenomena*. – Gulf Publishing Company, Houston, TX, 171–209.
- OKE, T.R., 1987: *Boundary Layer Climates*. – Routledge Chapman Hall, 464 pp.

- PAHR, A., 1984: Geologische Karte der Republik Österreich, Erläuterungen zu Blatt 137 Oberwart. – Geologische Bundesanstalt, Wien.
- PARKER, F.L., P.A. KRENKEL, 1969: Thermal pollution: status of the art. – Nashville, TN: Department of Environmental and Resource Engineering, Vanderbilt University.
- PELLETIER, J.D., S.B. DELONG, A.H. AL-SUWAIDI, M. CLINE, Y. LEWIS, J.L. PSILLAS, B. YANITES, 2006: Evolution of the Bonneville shoreline scarp in west-central Utah: Comparison of scarp-analysis methods and implications for the diffusion model of hillslope evolution. – *Geomorphology* **74**, 257–270.
- PEST, 2015: Model-Independent Parameter Estimation & Uncertainty Analysis. – Online available at <http://www.pesthomepage.org>, last accessed:2015-04-02.
- RUTHERFORD, J.C., S. BLACKETT, C. BLACKETT, L. SAITO, R.J. DAVIES-COLLEY, 1997: Predicting the effects of shade on water temperature in small streams. – *New Zealand J. Marine Freshwater Res.* **31**, 707–721.
- SHANAHAN, P., 1984: Water temperature modeling: a practical guide. – In: Proceedings of Stormwater and Water Quality Model Users Group Meeting, Environmental Research Laboratory, Office of Research and Development, United States Environmental Protection Agency (EPA), Athens, GA 30613, EPA-600/9-85-003, 272–295.
- SINOKROT, B.A., H.G. STEFAN, 1993: Stream temperature dynamics: Measurements and modelling. – *Water Resour. Res.* **29**, 2299–2312.
- STORY, A., R.D. MOORE, J.S. MACDONALD, 2003: Stream temperatures in two shaded reaches below cutblocks and logging roads: downstream cooling linked to subsurface hydrology. – *Canadian J. Forest Res.* **33**, 1383–1396.
- TAESLER, R., C. ANDERSON, 1984: A method for solar radiation computations using routine meteorological observations. – *Energy Buildings* **7**, 341–352.
- THEURER, F.D., K.A. VOOS, W.J. MILLER, 1984: Instream water temperature model. – US Fish Wildlife Serv. Instream Flow Information Pap. **16**.
- THEURER, F.D., I. LINES, T. NELSON, 1985: Interaction between riparian vegetation, water temperature, and salmonid habitat in the Tucannon river. – *Journal of the American Water Resources Association (JAWRA)*, **21**, Issue 1, 53–64.
- WEBB, B.W., F. NOBILIS, 1997: Long-term perspective on the nature of the air-water temperature relationship: a case study. – *Hydrol. Processes* **11**, 137–147.
- WEBB, B.W., Y. ZHANG, 1997: Spatial and seasonal variability in the components of the river heat budget. – *Hydrological Processes* **11**, 79–101.
- WEBB, B.W., Y. ZHANG, 1999: Water temperatures and heat budgets in Dorset chalk water courses. – *Hydrol. Processes* **13**, 309–321.
- WEBB, B.W., D.M. HANNAH, R.D. MOORE, L.E. BROWN, F. NOBILIS, 2008: Recent advances in stream and river temperature research. – *Hydrol. Processes* **22**, 902–918.
- WEIHS, P., A.R. WEBB, 1997: Accuracy of spectral UV model calculations 1. Consideration of uncertainties in input parameters. – *J. Geophys. Res.* **102**, 1541–1550.



Can riparian vegetation shade mitigate the expected rise in stream temperatures due to climate change during heat waves in a human-impacted pre-alpine river?

Heidelinde Trimmel¹, Philipp Weihs¹, David Leidinger¹, Herbert Formayer¹, Gerda Kalny², and Andreas Melcher³

¹Institute of Meteorology, University of Natural Resources and Life Science (BOKU), Vienna, Austria

²Institute of Soil Bioengineering and Landscape Construction (IBLB), University of Natural Resources and Life Science (BOKU), Vienna, Austria

³Institute of Hydrobiology and Aquatic Ecosystem Management (IHG), University of Natural Resources and Life Science (BOKU), Vienna, Austria

Correspondence: Heidelinde Trimmel (heidelinde.trimmel@boku.ac.at)

Received: 13 May 2016 – Discussion started: 23 May 2016

Revised: 22 November 2017 – Accepted: 26 November 2017 – Published: 18 January 2018

Abstract. Global warming has already affected European rivers and their aquatic biota, and climate models predict an increase of temperature in central Europe over all seasons. We simulated the influence of expected changes in heat wave intensity during the 21st century on water temperatures of a heavily impacted pre-alpine Austrian river and analysed future mitigating effects of riparian vegetation shade on radiant and turbulent energy fluxes using the deterministic Heat Source model. Modelled stream water temperature increased less than 1.5 °C within the first half of the century. Until 2100, a more significant increase of around 3 °C in minimum, maximum and mean stream temperatures was predicted for a 20-year return period heat event. The result showed clearly that in a highly altered river system riparian vegetation was not able to fully mitigate the predicted temperature rise caused by climate change but would be able to reduce water temperature by 1 to 2 °C. The removal of riparian vegetation amplified stream temperature increases. Maximum stream temperatures could increase by more than 4 °C even in annual heat events. Such a dramatic water temperature shift of some degrees, especially in summer, would indicate a total shift of aquatic biodiversity. The results demonstrate that effective river restoration and mitigation require re-establishing riparian vegetation and emphasize the importance of land–water interfaces and their ecological functioning in aquatic environments.

1 Introduction

Stream temperature is an important factor influencing the physical, chemical and biological properties of rivers and thus the habitat use of aquatic organisms (Davies-Colley and Quinn, 1998; Heino et al., 2009; Magnuson et al., 1979). Heino et al. (2009) suggest that freshwater biodiversity is highly vulnerable to climate change with extinction rates exceeding those of terrestrial taxa. Stream temperature is highly correlated with the assemblages of fish and benthic invertebrates along the river course (Dossi et al., 2015; Melcher et al., 2015). The duration and magnitude of the maximum summer stream temperatures in particular are limiting factors for the occurrence of many fish species. High temperatures may produce high physiological demands and stress while also reducing the oxygen saturation in the water column. The increased metabolic requirements together with the decreased oxygen availability can prove to be a limiting factor or even be lethal in combination; the average optimum temperature for cold water species is below 16 °C (Matulla et al., 2007; Pletterbauer et al., 2015).

Continuous warming of water temperatures induces changes from cold water to warm water fish species assemblages and slow altitudinal shifts of species, if the habitat is suitable and no migration barriers exist. River continuum disruption and river dimension reduce the fish zone extent significantly (Matulla et al., 2007; Bloisa et al., 2013). Extreme events where lethal thresholds of stream temperature are ex-

ceeded can cause a disruption of animal communities or even extinction of (cold water) species (Melcher et al., 2013; Pletterbauer et al., 2015). The largest uncertainties in forecasts of total suitable habitat are climate uncertainty (Wenger et al., 2013). All 230 stations of the Austrian hydrographic central office, with different elevations, distances from source and catchment areas recorded increases in stream temperature of 1.5 °C during summer (June–August) and 0.7 °C during winter (December–February) between 1980 and 2011 (0.48 °C decade⁻¹) (BMLFUW, 2011). This change is not likely to be due to natural climatic cycles but is part of a long-term trend caused by anthropogenic changes in the atmosphere (APCC, 2014).

Air temperatures have been rising and are expected to continue to rise globally within the next century (IPCC, 2013). In eastern Austria, mean air temperature has risen by 2 °C since 1880, which is more than double the 0.85 °C rise recorded globally (Auer et al., 2014). A further temperature increase within the 21st century is very likely (APCC, 2014). If emission scenario A1B is assumed, mean air temperature increases of 3.5 °C over the level of the reference period 1961–1990 by the end of the 21st century are expected in Austria (APCC, 2014; Gobiet et al., 2014).

Temperature extremes have changed markedly and extreme high temperature events, i.e. heat waves, are very likely to increase in the 21st century (APCC, 2014). Soil temperature is also expected to increase due to climate change and will influence stream temperatures via substrate heat conduction and groundwater flux (Kurylyk et al., 2015). For example, in Austria, near-surface groundwater body temperature is expected to rise by 0.5 to 1 °C on average by 2050 (BMLFUW, 2011). Austria lies between two zones of opposing precipitation trends (IPCC, 2013). Northern Europe shows an increasing trend, while the Mediterranean has a decreasing trend (Böhm, 2006). In southeastern Austria, a precipitation decrease of about 10–15 % has been recorded over the last 150 years (APCC, 2014; Böhm, 2012). Low flow discharge rates of rivers are likely to decrease by 10 to 15 % by 2021–2050 compared to 1976–2007 during all seasons (Nachtnebel et al., 2014; Mader et al., 1996; APCC, 2014).

For the study region during summer heat waves, neither changes in groundwater nor snowmelt contributions are expected (APCC, 2014). Heavy and extreme precipitation shows no clear increasing signal on average, but it is likely to increase from October to March (APCC, 2014). No clear trend of increasing wind speed (Matulla et al., 2008; Beniston, 2007) or increase in sunshine hours (Ahrens et al., 2014) has been detected but changes in the climate system may also include changes in those parameters (APCC, 2014).

Stream temperature is controlled by advection of heat, dispersion and the net energy fluxes acting on the surface and river bed. Net shortwave radiation is the dominant energy input causing diurnal and seasonal water temperature variability. Longwave radiation flux (Benyaha et al., 2012) as well as the turbulent fluxes of evaporation and convection, which are

controlled by air temperature, vapour pressure, wind speed and net radiation, play an important role (Caissie et al., 2007; Garner et al., 2014; Hannah et al., 2008; Johnson, 2004).

One of the most influential factors regulating stream temperature is riparian vegetation (Caissie, 2006; Groom et al., 2011; Johnson, 2004; Moore et al., 2005; Rutherford et al., 1997). The streamside vegetation buffer width (Clark et al., 1999), vegetation density and average tree height all have a strong influence on stream temperature (Sridhar et al., 2004). Vegetation affects the sky view of the river and thereby shortwave (Holzapfel et al., 2013) and longwave radiation flux, evaporation and convection heat flux, which are highly correlated to the openness of the sky. The reduction of shortwave radiation can contribute significantly to reducing the heating of rivers during warmer summers (Sinokrot and Stefan, 1993; Parker and Krenkel, 1969; Rutherford et al., 1997).

There are different approaches to predicting stream temperature. Water temperature can be predicted using statistical functions (stochastic models) and its correlation (regression models) to known variables (e.g. air temperature, water temperature of the previous days or streamflow). Use of air temperature as a surrogate for future water temperature can lead to errors when linear (Erickson and Stefan, 2000; Webb and Nobilis, 1997) or non-linear (Mohseni et al., 1998) regression models are applied (Arismendi et al., 2014). Stochastic models used to determine the long-term annual component of temperatures and their short-term residuals separately yield good results (Caissie et al., 2001). Including a discharge term in the regression model can improve the model's performance during heat wave and drought (low flow) conditions, when water temperatures are most sensitive to air temperature (van Vliet et al., 2011). Energy balance models resolving all energy fluxes affecting a river system are the best suited to predict stream temperature (Caissie et al., 2007) but demand the most input data. Only these models are able to simulate energy flux changes caused by increased or decreased river shade.

Though the influence of vegetation on water temperature is evident, its ability to mitigate climate change is not yet sufficiently understood. Latent and sensible heat fluxes as well as longwave radiation balance are non-linearly dependent on air temperature. It is not obvious whether the same level of shade will always lead to the same rate of heat reduction. Shading caused by tall but less dense trees may allow exchange of air, while lower riparian vegetation may cause the same level of shade but would reduce air movement. Vegetation can reduce warming but may also reduce nightly cooling by altering the energy fluxes on a local scale, which can only be modelled using deterministic methods.

The conclusion may be drawn that many studies have already addressed the influence of riparian vegetation on stream water temperature using field measurements. Other studies used different methods to make short-term forecasts of stream temperature and few tried to answer the question of how climate change might increase stream water temper-

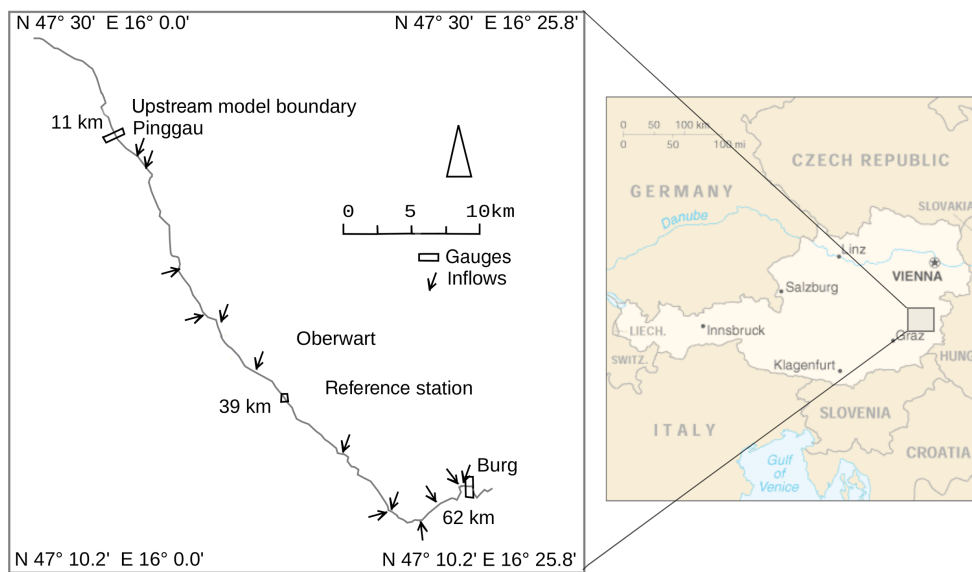


Figure 1. The study region in the Pinka showing gauges, tributaries and the reference station (kilometre markers shown as distance from source).

ature. One result or trend may however not be transferred from one river to another. Particular statements about the riparian vegetation's potential to mitigate the influence of climate change are only reliably valid for a given type of stream with its unique combination of morphologic and hydrologic parameters, local climate (Sinokrot and Stefan, 1993; Johnson, 2003; Steel and Fullerton, 2017) and regional climate change (Johnson and Wilby, 2015). Air temperature was normally used as a surrogate for stream temperature and energy flux variations in different river sections were not considered. The novel aspect of the present study is to investigate the influence of climate change and of riparian vegetation on the same river and attempt to make a realistic forecast of the riparian vegetation's potential to mitigate climate change in a specific river using a deterministic model.

The aims of the present study are therefore (1) to estimate the magnitude of stream temperature rise during extreme heat events caused by the expected rise in air temperature by the end of this century and (2) to investigate the ability of riparian vegetation to mitigate the expected water temperature rise within the habitat optimum of the site-specific aquatic fauna and (3) to analyse the possible variation of vegetation and potential interaction of vegetation and discharge with respect to climate change and their impact on water temperature.

2 Methods

Stream temperature was simulated with the 1-D energy balance and hydraulic Heat Source model (Boyd and Kasper, 2003) for 51 km along a section of river including upstream forested regions and tributaries. Temperature was simulated for each 500 m section of the river, which amounted to a total

of 103 sites. First, the longitudinal changes of energy fluxes were analysed during the maximum heat wave, which took place in eastern Austria during summer 2013. Future heat wave episodes that are likely to occur during the climate periods 2016–2045, 2036–2065 and 2071–2100 in the study region were selected. Regional climate scenarios produced by the ENSEMBLE project (Hewitt et al., 2004) were further processed and the meteorological data extracted. The future upstream model water temperature was simulated by the methodology of Caissie et al. (2001). Heat Source was used to simulate the stream temperature of the Pinka for 12 future episodes and eight vegetation scenarios.

2.1 Study region

The river Pinka originates at 1480 m above sea level (a.s.l.) in the eastern Austrian Alps and discharges about 100 km downstream at 200 m a.s.l. into the river Rába. The catchment of the Pinka is 664 km². According to Muhar et al. (2004), who categorized all Austrian rivers with catchment areas > 500 km² corresponding to their annual discharge, the Pinka falls in the smallest of the five categories with 0–5 m³ s⁻¹ mean annual discharge. The study region covers a 51 km stretch of the Pinka from the distance from source (DFS) of 11 km (559 m a.s.l.) near its most upstream gauge in Pinggau to DFS 62 km (240 m a.s.l.) close to the gauge at Burg (Fig. 1). For the first 10 km, the river has a slope of 0.017 m m⁻¹, whereas in the remaining section the slope is only 0.004 m m⁻¹. The river bankfull width varied from 4 to 10 m (Fig. 2c). The maximum depth of the different river sections varied between 0.1 and 0.5 m and was 0.17 m on average. Only 4 % of the reaches presently fall into the most nat-

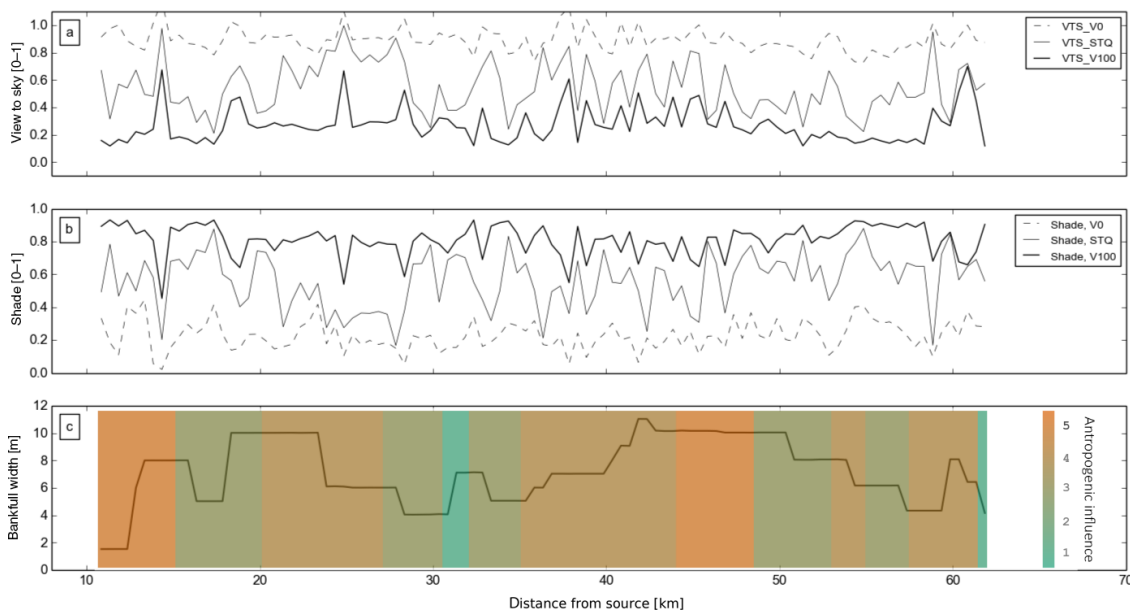


Figure 2. Characteristics of the Pinka. **(a)** The longitudinal distribution of view to sky (VTS) and **(b)** shade at the river's surface, **(c)** the bankfull width and the level of anthropogenic influence on the river. Legend on the right: entirely natural (1), slightly or not influenced (2), strongly influenced but with natural areas (3), continuously influenced with few natural areas (4) and completely regulated (5).

ural or the second category according to Ledochowski (2014) (Fig. 2c). On the other hand, 60 % of reaches are classed as continuously influenced with no or very few natural sections (Fig. 2c).

Close to the source (DFS 0–12.5 km) the vegetation consists of commercial spruce forests (*Picea abies*) which undergo management. In the middle and downstream sections of the river, the near-natural deciduous riparian vegetation includes typical floodplain species of the region such as willows (*Salix* sp.) and alders (*Alnus glutinosa* and *incana*). In the downstream 80 % of the river (from DFS 34 to 61 km), riparian vegetation is reduced to one- or two-sided sparse tree plantations lining the river course for decorative purposes. These areas are mowed on a regular basis to prevent scrub growth. Other frequent trees like ash (*Fraxinus excelsior*), hazel (*Corylus avellana*), wild cherry (*Prunus avium*) and elder (*Sambucus nigra*) can be found along the whole river course. In this region, air temperature has risen by 2 °C since 1880 (Auer et al., 2014). Precipitation has declined by 10–15 % in our study region, the largest reduction in precipitation in Austria (Auer et al., 2007; Böhm et al., 2009, 2012).

Potential changes in vegetation cover

Changes in vegetation height and density in floodplain forests in natural systems are mainly due to succession (Primack, 2000; Garssen et al., 2014; Rivaes et al., 2014). The present potential natural floodplain forest is in many areas reduced to narrow fringes accompanying the river, which are flooded at least annually. The river has been continu-

ously straightened and regulated throughout the 20th century. Flood protection measures and land use pressure have further altered the river and riparian vegetation dynamics. The vegetation behind these fringes is in the transition zone between softwood and hardwood wetland, and a further change towards upland or zonal vegetation is expected via terrestri- alization processes, well known in the Danube region (Birkel and Mayer, 1992; Egger et al., 2007). The dominant tree species present along the Pinka, *Salix alba*, *Alnus glutinosa* and *Fraxinus excelsior*, have a European-wide distribution (San-Miguel-Ayanz et al., 2016) so they are likely to defend their habitat. Some autochthonous species (*Populus alba*, *Prunus avium*, *Salix caprea*, *Fraxinus excelsior*, *Carpinus betulus*) which were present in 2013 are favoured by warmer climates (Kiermeyer, 1995; Roloff and Bärtels, 2006). Non-native species like *Robinia pseudoacacia* and *Acer negundo* are already present in the study region and might enlarge their habitat at the expense of native species (Kiermeyer, 1995; Roloff and Bärtels, 2006). Changes in tree species in favour of warmth-loving plants from downstream regions of the Rába/Danube catchment are possible (Lexer et al., 2014). Generally, changes are likely to be not only driven by climatic but also anthropogenic factors such as plantation of foreign species, which is not foreseeable.

2.2 Modelling vegetation influence on energy fluxes and stream temperature along the river

Using the deterministic model Heat Source version 9 (Boyd and Kasper, 2003; Garner, 2007) the energy fluxes, hy-

draulics and stream temperature were simulated along the Pinka. The generation of the input data sets is described in Sect. 2.3 below. Vegetation affects water temperature directly by reducing shortwave radiation input and reducing the view to sky (VTS) which affects longwave radiation balance and the turbulent heat fluxes. Longwave radiation and the turbulent heat fluxes are non-linearly dependent on air temperature. Short- and longwave energy flux, latent and sensible heat fluxes and conduction are taken into account:

$$\Phi_{\text{Total}} = \Phi_{\text{Solar}} + \Phi_{\text{Longwave}} + \Phi_{\text{Latent}} + \Phi_{\text{Sensible}} + \Phi_{\text{Conduction}}, \quad (1)$$

where Φ_{Total} is the energy balance, Φ_{Solar} is the shortwave energy which is absorbed by the water column, Φ_{Longwave} the longwave radiation balance, Φ_{Latent} the latent heat flux, Φ_{Sensible} the sensible flux and $\Phi_{\text{Conduction}}$ is the conduction flux to the stream bed flux, and all of which refer to the stream surface, so latent heat flux is mostly negative.

Shortwave radiation

The amount of radiation entering the stream ($\Phi_{\text{SolarEnter}}$) is the radiation unobstructed by shading ($\Phi_{\text{AboveTopo}}$) reduced by topographic shade ($\Phi_{\text{TopoShade}}$), bank shade ($\Phi_{\text{BankShade}}$), vegetation shade (Φ_{VegShade}) and reflected from river surface (Φ_{SolarRef}).

$$\Phi_{\text{SolarEnter}} = \Phi_{\text{AboveTopo}} - \Phi_{\text{TopoShade}} - \Phi_{\text{BankShade}} - \Phi_{\text{VegShade}} - \Phi_{\text{SolarRef}} \quad (2)$$

If topographic or bank shade is present, the direct radiation fraction is reduced by the radiation entering in the affected angles. If vegetation shade is present, the direct radiation is reduced depending on the vegetation density using a formulation of Beer's law by the term Φ_{VegShade} .

$$\text{RE} = -\log\left(\frac{1 - \text{VD}}{10}\right) \quad (3)$$

$$\Phi_{\text{VegShade}} = 1 - \exp\left(-\text{RE} \left(\frac{\text{LD}}{\cos(\text{rad}(\theta_s))}\right)\right), \quad (4)$$

where RE is the riparian extinction, VD is vegetation density, LD is the distance from the river centre and θ_s is the solar elevation angle. Φ_{Solar} , which is finally absorbed by the water column is the amount of solar radiation entering the stream ($\Phi_{\text{SolarEnter}}$) (Eq. 2) minus the amount that is absorbed in the river bed ($\Phi_{\text{SolarAbsorb}}$) and reflected ($\Phi_{\text{SolarBedRef}}$).

$$\Phi_{\text{Solar}} = \Phi_{\text{SolarEnter}} - \Phi_{\text{SolarAbsorb}} - \Phi_{\text{SolarBedRef}} \quad (5)$$

VTS and longwave radiation balance

The VTS is calculated using modified vegetation density VD_{mod} and the vegetation angle θ_v . VTS is used to calculate the diffuse radiation entering below vegetation height,

atmospheric longwave radiation $\Phi_{\text{LongwaveAtm}}$ (Eq. 7), longwave radiation emitted from vegetation $\Phi_{\text{LongwaveVeg}}$ (Eq. 6) and the reduction of wind speed at the river surface (Eq. 11).

$$\text{VTS} = 1 - \frac{\max\theta_v \cdot \text{VD}_{\text{mod}}}{7 \cdot 90} \quad (6)$$

Longwave radiation balance Φ_{Longwave} is the sum of all longwave components:

$$\Phi_{\text{LongwaveAtm}} = 0.96 \cdot \text{VTS} \cdot \varepsilon \cdot \sigma \cdot (T_{\text{airK}})^4 \quad (7)$$

$$\Phi_{\text{LongwaveVeg}} = 0.96 \cdot (1 - \text{VTS}) \cdot 0.96 \cdot \sigma \cdot (T_{\text{airK}})^4 \quad (8)$$

$$\Phi_{\text{LongwaveStream}} = -0.96 \cdot \sigma \cdot (T_{\text{prevK}})^4 \quad (9)$$

$$\Phi_{\text{Longwave}} = \Phi_{\text{LongwaveAtm}} + \Phi_{\text{LongwaveVeg}} + \Phi_{\text{LongwaveStream}}, \quad (10)$$

where ε is the emissivity of the atmosphere, σ the Stefan–Boltzmann constant, and T_{airK} the air temperature and T_{prevK} the stream temperature of the advected water in degrees Kelvin.

Latent and sensible heat fluxes

Latent heat flux (Φ_{Latent}) was calculated using the Penman method, which included the radiation balance:

$$E_a = 1.51 \cdot 10^{-9} + 1.6 \cdot 10^{-9} \cdot (w \cdot \text{VTS}) \cdot (e_s - e_a) \quad (11)$$

$$E = \frac{\Phi_{\text{Rad}} \cdot \Delta + E_a \cdot \gamma}{\Delta + \gamma} \quad (12)$$

$$\Phi_{\text{Latent}} = -E \cdot \text{LHV} \cdot \rho, \quad (13)$$

where E_a is the aerodynamic evaporation, w the wind speed (ms^{-1}), E the evaporation rate (ms^{-1}), Φ_{Rad} the sum of Φ_{Longwave} and $\Phi_{\text{SolarEnter}}$, Δ the slope of the saturation vapour vs. air temperature curve, ρ the density of water (kg m^{-3}), LHV the latent heat of vaporization (J kg^{-1}) and γ the psychrometric constant ($\text{mb } ^\circ\text{C}^{-1}$).

Sensible heat flux is calculated from evaporation via the Bowen ratio β :

$$\beta = \frac{\gamma \cdot (T_{\text{prev}} - T_{\text{air}})}{e_s - e_a} \quad (14)$$

$$\Phi_{\text{Sensible}} = \Phi_{\text{Latent}} \cdot \beta, \quad (15)$$

where T_{prev} is the stream temperature, T_{air} is air temperature, e_s is the saturated vapour pressure and e_a the air vapour pressure.

Conduction heat flux

Conduction $\Phi_{\text{Conduction}}$ is dependent on the thermal conductivity of the sediment TC_{sed} ($\text{Wm}^{-1} \text{ } ^\circ\text{C}^{-1}$), the sediment depth d_{sed} (m), sediment temperature T_{sed} and water temperature T_{prev} :

$$\Phi_{\text{Conduction}} = \frac{\text{TC}_{\text{sed}} \cdot (T_{\text{sed}} - T_{\text{prev}})}{\frac{d_{\text{sed}}}{2}}. \quad (16)$$

Water temperature

The effect of the energy balance of the water column on stream temperature was calculated taking into account flow velocity and river morphology. The stream temperature increase ΔT caused by Φ_{Total} (Eq. 1) was calculated using

$$\Delta T = \frac{\Phi_{\text{Total}} \cdot dt}{\left(\frac{A}{W_w}\right) \cdot c_{\text{H}_2\text{O}} \cdot m}, \quad (17)$$

where A is the cross-sectional area of the river, W_w is the wetted width, the $c_{\text{H}_2\text{O}}$ is the specific heat capacity of water ($4182 \text{ J kg}^{-1} \text{ }^\circ\text{C}^{-1}$) and m is the mass of 1 m^3 water which is 998.2 kg .

Conclusively, Heat Source includes all aspects of vegetation changes on stream temperature during future episodes and the main processes needed to answer the research questions can be modelled with Heat Source.

A first model set-up and validation for usage at the Pinka during heat wave conditions was done by Trimmel et al. (2016). By fine-tuning the morphological input (bottom width, roughness parameter Manning's n and sediment hyporheic thickness) and the wind parameterization, the model's validity could be considerably improved for the simulations used here. Tuning increased the coefficients of determination (R^2) for water temperature stations of different vegetation height and density at DFSs 31, 35, 37, 39 and 48 km to 0.96–0.98 (daily minimum), 0.96–0.99 (daily mean) and 0.94–0.98 (daily maximum). The measurements fit the simulation very well (hourly RMSE was $0.88 \text{ }^\circ\text{C}$ averaged for all stream measurement stations), so we concluded that all assumptions were met and the model was appropriate to be used for predictions.

2.3 Preparation of input

2.3.1 Meteorological input

During the maximum heat wave event of 2013, field measurements were collected at the study site. Global radiation, air temperature, air humidity and wind speed were measured at a reference station located at DFS 39 km $47^\circ 16' 11.055'' \text{ N}$, $16^\circ 13' 47.892'' \text{ E}$, 300 m a.s.l. To link the measured microscale meteorological data to mesoscale meteorological data, a systematic intercomparison between the local meteorological stations of the Austrian Weather Service (ZAMG) and the $1 \times 1 \text{ km}$ gridded observational data set INCA (Haiden et al., 2011) was made. Since the local permanent meteorological stations of ZAMG were used to produce the gridded INCA data set, they are highly consistent. The comparison of the INCA data with the air temperature measured at our reference station close to the river showed an RMSE of $0.67 \text{ }^\circ\text{C}$ and an R^2 of 0.99 for consecutive hourly measurements during summer half-year 2013 (1 April–30 September). So the INCA data set was used as a

Table 1. Mean 5-day air temperatures of modelled future heat wave episodes used as selection criteria, shown with equivalent values from the observed period for comparison.

	1a	5a	20a	Max
1981–2010 (OBS)	23.1	25.0	27.2	27.4
2016–2045 (2030)	23.4	26.6	27.2	29.0
2036–2065 (2050)	24.2	27.2	28.4	28.8
2071–2100 (2085)	28.1	30.6	31.0	32.0

proxy to represent the local meteorological conditions within the catchment.

To obtain future meteorological conditions at the reference station, data were extracted from the regional climate models (RCMs) ALADIN (driven by the global climate model ARPEGE; Déqué et al., 1994), REMO and RegCM3 (both ECHAM5 driven; Roeckner et al., 2003, 2004). The aim was to estimate possible maximum temperature values; therefore, data from ALADIN, the climate model with the most extreme dry and hot summers, were selected. The RCMs were bias corrected using the quantile mapping technique (Déqué, 2007) based on the E-OBS data set (Haylock et al., 2008) and scaled. In a second step, the data were spatially localized to a $1 \text{ km} \times 1 \text{ km}$ grid encompassing the area under investigation using the Austrian INCA data set (Haiden et al., 2011). In a third step, the data were temporally disaggregated from a resolution of 1 day to 1 h. Temperature was disaggregated based on the daily maximum and minimum temperatures using three piecewise continuous cosine curves (Koutsoyiannis, 2003; Goler and Formayer, 2012). The temperature data were elevation corrected with a lapse rate of $0.65 \text{ }^\circ\text{C}$ per 100 m.

Selection of extreme heat events

The period chosen as past reference period (“OBS”) was an extreme heat wave that ran from 4 to 8 August 2013, which was the most intense heat wave of 2013. The mean air temperature of this episode was comparable to a 20-year return period 5-day event (Table 1) for the period 1981–2010. Future episodes were selected by choosing future heat wave events in three periods (2016–2045: “2030”, 2036–2065: “2050”, 2071–2100: “2085”) in the summer months (June–August) that were simulated for the emission scenario A1B by the climate model ALADIN (Radu et al., 2008). The events were chosen by selecting periods when the 5-day mean air temperature exceeded different thresholds using the percentiles of the 5-day mean air temperature of the three periods, which corresponded to an event with a 1-year (1a), 5-year (5a) or 20-year (20a) return period as well as the maximum heat wave event of the period (Max). The selection criteria are shown in Table 1. The start was 14 days prior to the end of the episode to allow spin-up of the Heat Source model, so all episodes have equal length of 14 days.

2.3.2 Vegetation and morphology

The riparian vegetation cover and river morphology of this region were investigated by Ledochowski (2014). First, aerial photographs were used to define the river centre line and a 50 m buffer on both sides, because the influence of riparian vegetation on the river is negligible beyond this point. Within this zone, areas of homogeneous structure, land use and ecological function were mapped by hand. Additional information such as height, density and dominant vegetation type were recorded as attributes of mapped features. To verify and complete the attributes, field mapping was done using custom-built checklists. The checklists included two tree levels, one shrub level and one herb level. The recorded parameters for each level were height, density, overhang and dominant species. Vegetation height was estimated with a precision of ± 5 m, overhang with a precision of ± 1 m and density with a precision of ± 20 %. The inclination of the river slope as well as the roughness of the section (type of regulation, whether sinuous or straight) and type of substrate were noted. From these data sources, VTS (see Eq. 6) and percent shade were calculated (Fig. 2a, b). The river morphology parameters including river bankfull width (Fig. 2c), wetted width, average water depth and height of river to slope top were also measured.

The riparian vegetation data were obtained after the phenological phase of leaf development was finished and leaves were fully developed (Ellenberg, 2012). The river investigated here is strongly influenced anthropogenically and highly regulated. The degree of anthropogenic influence was categorized by Ledochowski (2014) according to Mühlmann (2010) into five categories: entirely natural (1), slightly or not influenced (2), strongly influenced but with natural areas (3), continuously influenced with few natural areas (4) and completely regulated (5) (see Fig. 2c). This categorization mainly describes constraints on bank and riverbed dynamics. The structure and substrate composition of stream bed and vegetation were additional parameters recorded by Ledochowski (2014). The entirely natural class is endowed with riparian vegetation of above 30 m height, vegetation densities of 76 to 100 % and a riparian zone of more than 49 m in width. The continuously influenced areas coincide with reduced riparian vegetation strips and reduced vegetation height.

Vegetation scenarios

Taking into account all likely changes in tree species, no change in maximum vegetation height or density is predictable. Potential changes can only be induced by different vegetation management strategies as intentional clearings, plantations or mowing. A total of eight vegetation management scenarios were chosen to estimate the impact of different levels of vegetation shade on future heat waves. This also makes it possible to quantify potential changes to warmth-

loving species of reduced height and density. The following scenarios have been considered.

Existing riparian vegetation (STQ) used the best available status quo input data for vegetation, bank and topographic shade as described in Ledochowski (2014). The average density including all land cover types was 66 % (standard deviation of 17 %) and the average height was 9.4 m. Only considering areas including trees larger than 15 m height, the average density rose to 76 % (standard deviation of 11 %), ranging from 2 to 90 %. At the sheltered headwaters (DFS 20 km), the vegetation density reached 0.89. For V0 within a 50 m buffer, all vegetation parameters (vegetation height, density and overhang) were set to 0 so that no vegetation shading occurred. The V0 scenario corresponded to intentional clearings and mowing. V100 was defined as 30 m height, 8 m overhang and 90 % vegetation density within a 50 m buffer which is representative of the densest riparian forests of STQ located in the Pinka catchment (Ledochowski, 2014). The V100 scenario represented the maximum possible level of vegetation shade. It is achievable by suspension of clearing and mowing activities as well as additional plantations of local tree and shrub species, which grow to different heights and form a well-structured shrub and tree layer. To maintain this scenario management, measures like replacement plantings and well-directed cuttings are necessary. An intermediate height scenario (V50) was defined as 15 m vegetation height and 90 % vegetation density. A reduced density scenario (V70) was defined as 30 m vegetation height and vegetation density of 70 %. Additionally scenarios of vegetation density of 50 % and full vegetation height (VD50, VH100), and vegetation height reduced by 50 % and vegetation density of 70 % (VD70, VH50) and vegetation density of 50 % (VD50, VH50) were considered. River bank and topography were not changed in the vegetation scenarios. No river restoration in terms of restoring natural river bank and allowing natural river dynamics was assumed.

2.3.3 Definition of sediment layer and conduction flux

Heat Source uses only one substrate temperature, which is representative of the whole sediment layer. The depth of the sediment layer is set to 1 m, which corresponds to the available geological information of the Pinka (Pahr, 1984). The substrate temperature used in the model is set equal to the stream temperature at the uppermost model point. For each consecutive model point, the substrate temperature is calculated depending on the local thermal conductivity, thermal diffusivity, layer depth, hyporheic exchange, the river morphological profile, the water temperature and the solar radiation received at the river bed. The sediment of this region is very inhomogeneous and the spatial distribution of the groundwater level is unknown (Pahr, 1984). For low flow conditions, it was assumed that there was no deep groundwater influence.

2.3.4 Definition of discharge

During the analysed period of 4–8 August 2013, low flow conditions prevailed. The river flow volume increased from $0.18 \text{ m}^3 \text{ s}^{-1}$ close to the upstream model boundary at DFS 13 km to $0.76 \text{ m}^3 \text{ s}^{-1}$ at the downstream model boundary (DFS 62 km). The mean flow velocity was 0.46 m s^{-1} and it took the river water about 30 h to traverse the studied length of the river.

The model was not sensitive to discharge rates. A decrease in discharge of the upstream boundary station of $0.01 \text{ m}^3 \text{ s}^{-1}$ (6 %) led to an increase in average stream temperature from DFS 26 to 48 km of $0.04 \text{ }^\circ\text{C}$ (0.2 %) (Trimmel et al., 2016). Because the aim was to estimate the influence of vegetation shade, clear-sky periods were chosen where no or only minor precipitation events occurred, so discharge was fixed at mean low flow (MLF) conditions. MLF was defined as the average of all daily discharges below the 5 % discharge of the climate period 1981–2010. The mean low flow conditions of the gauging station at Pinggau, DFS 13 km (MLF of $0.143 \text{ m}^3 \text{ s}^{-1}$), which is maintained by the Hydrographischer Dienst Österreich, were used in the model. At the other end of the study region, at DFS 62 km, the corresponding flow volume was $0.795 \text{ m}^3 \text{ s}^{-1}$. To take into account potential reductions of discharge, a scenario of MLF discharge – 15 % (MLF-15 of $0.122 \text{ m}^3 \text{ s}^{-1}$), which is a 5 % reduction of the mean annual discharge – was calculated.

2.3.5 Upstream boundary stream temperature

Stream temperature and discharge were used as upstream boundary conditions. For the 2013 episode, these values rely on observations of the gauging station at Pinggau which is maintained by the Hydrographischer Dienst Österreich and a stream temperature measurement station maintained by the authors. To obtain equivalent data for future conditions, the maximum water temperature was first modelled at DFS 11 km using the expected air temperature as input (Mohseni et al., 1998). The water temperature was split into two components: the long-term seasonal component (or annual component) and the short-term non-seasonal component (or residuals series) (Caissie et al., 2001). The annual component was calculated according to the method of Kothandaraman (1971) and the residuals were calculated with a stochastic second-order Markov model after Cluis (1972) and Salas et al. (1980). Observed hourly water temperatures ($N = 12,537$) over the period 7 July 2012 to 9 September 2014 were used to fit the model. The coefficient of determination R^2 between observed and predicted water temperature for this period was 0.96 and the RMSE was $0.68 \text{ }^\circ\text{C}$. For the summer half-year 2013 (April–September), the R^2 was 0.89 and the RMSE was $0.80 \text{ }^\circ\text{C}$. To take into account the climatic trend caused by the warming of the land surface (Kurylyk et al., 2015), the difference between the

moving average over a 30-year climate period and the reference period 1981–2010 was added to the annual component.

2.3.6 Input data of tributaries

The discharge levels and water temperature of the Pinka at the upstream model boundary and its five main tributaries were measured during the 2013 episode in the field by the authors and by two permanent gauging stations. The remaining unmeasured tributaries added less than 5 % discharge each. Their future water temperatures were synthesized using the daily fluctuations of the water temperature at the upstream model boundary with the adding of a fixed offset depending on the distance of the inflow to the upstream model boundary. Missing discharge information was supplemented using proportions of the discharge levels of the gauge at Burg (DFS 62 km) as measured during 2013.

3 Results

3.1 Influence of vegetation shade and energy fluxes on stream temperatures during the heat episode of 2013 along the river

In order to interpret the influence of vegetation shade on future water temperature, it is important to understand the influence of vegetation shade on the present conditions first. The mean VTS for the study region under current conditions (STQ) was 0.55. If all vegetation was to be removed (V0), there would still be some remaining shade caused by topography and the river bank, which reduces the maximum VTS value to 0.89. If maximum vegetation was assumed (V100), the value of VTS would be strongly reduced but would still amount to 0.16 on average because a 90 % vegetation density was assumed. Peaks in VTS were found at broader river sections or sections oriented east–west (Fig. 2a). The percentage shade is similar to the inverse of VTS but differs, as the south orientation is of importance (Fig. 2b).

During the STQ scenario, the most important energy inputs on the river surface during the study period were shortwave radiation flux with an average of 101.6 W m^{-2} (Fig. 3a), sensible heat flux with an average of 39.9 W m^{-2} (Fig. 3d) and longwave radiation with an average of 17.2 W m^{-2} (Fig. 3b). Conduction only amounted to 1.3 W m^{-2} on average (Fig. 3e). The relative percentage of shortwave radiation balance, longwave radiation balance and sensible heat flux was 64, 11 and 25 % of the inputs, respectively, that heated the water column. The main energy output was latent heat flux (Fig. 3c).

For the V0 and V100 scenarios, the characteristic of the longitudinal energy fluxes remained the same. During the V0 scenario, the relative percentage of shortwave radiation balance increased (73 %), while longwave radiation balance (7 %) and sensible heat flux (18 %) decreased. During the V100 scenario, the trend was opposite. Shortwave radiation

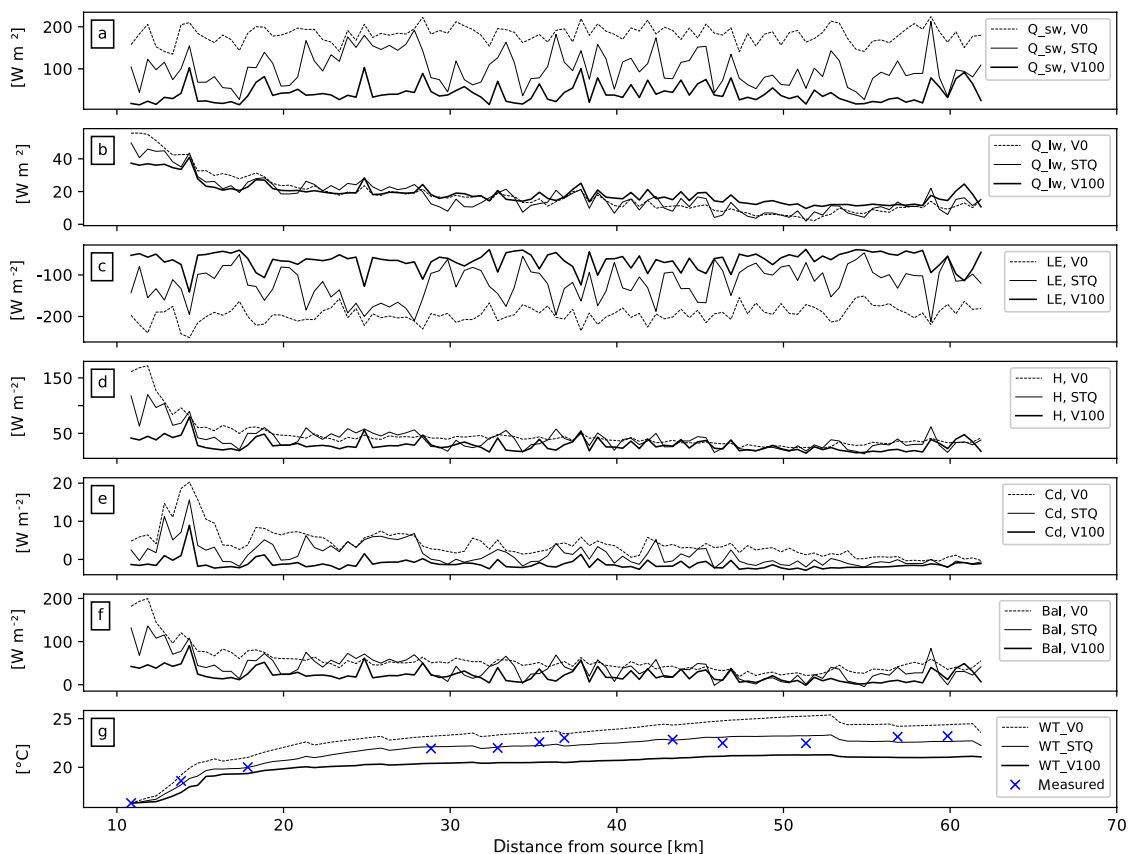


Figure 3. Comparison of (a) the calculated shortwave, (b) longwave radiation balance, (c) latent and (d) sensible heat fluxes, (e) conduction heat flux, (f) total energy balance, and (g) measured (measured) and simulated (WT) water temperature for the heat wave episode 4–8 August 2013 along the Pinka for three vegetation scenarios: no vegetation (V0), existing vegetation (STQ) and maximum vegetation (V100).

balance decreased (47 %) and longwave radiation balance (21 %) and sensible heat flux (32 %) increased (Fig. 3a–e).

Looking at the longitudinal distribution of energy fluxes along the river, it can be seen that sensible heat flux and longwave radiation flux as well as conduction showed their highest values close to the source during all vegetation scenarios. This leads to a rapid increase in the water temperature of the cool spring water, which is clearly seen in both measured and simulated data (Fig. 3g). All energy fluxes were dependent on the degree of openness to the sky and showed the same pattern along the river (Fig. 3a–f). Shortwave radiation and latent heat flux in particular were strongly influenced by the value of the VTS and showed distinct reductions of up to 70 % where shading occurred (Fig. 3a, c).

The energy balance was positive on average along the whole river (Fig. 3f). The V0 scenario showed the highest and the V100 scenario the lowest net energy with mean values of 55, 40 and 22 W m^{-2} for the V0, STQ and V100 scenarios, respectively (Fig. 3f). The greatest differences between the different vegetation scenarios were found close to the source, where, during the V0 scenario, up to 200 W m^{-2}

net energy was available to heat the water column (Fig. 3f), while during the V100 scenario the corresponding figure was only 91 W m^{-2} . The positive energy balance can explain the gradual warming of the stream temperature along the river (Garner et al., 2014) which can be seen in Fig. 3g. The continuous downstream warming is reversed at about DFSs 16, 22, 26.5, 32, 43.5 and 53.5 km by about 0.5 °C for short distances caused by the addition of cooler water from tributaries (Fig. 3g).

3.2 Future climate and advective input

The selection criteria mean air temperature of modelled scenarios increased depending on the return period of the event (Table 1). Apart from the 1a and 5a events of 2030 and the 1a event of 2050, all modelled events were warmer than the 2013 heat wave. Air humidity during the selected events decreased slightly by the end of the century (Table 2). In the 20-year return period event of 2050, wind speeds were higher (1.1 m s^{-1}) than in 2030 (0.9 m s^{-1}) and 2085 (0.8 m s^{-1}) (Table 2). The average global radiation received during

Table 2. Mean and daily maximum air temperatures, air humidity, wind speed, global radiation at the reference station and water temperature at the upstream model boundary averaged for the selected 5-day heat episodes in 2013 and the 1a, 5a, 20a and Max events of the climate periods centred on 2030, 2050 and 2085. For 2013 (OBS), measured values of the reference station 2 m above the river (M.) and interpolated measurement data from the INCA (I.) data set are shown.

	OBS		2030				2050				2085			
	M.	I.	1a	5a	20a	Max	1a	5a	20a	Max	1a	5a	20a	Max
Air temp. (mean) (°C)	26.2	27.2	23.3	26.6	27.2	29.0	24.2	27.2	28.4	28.8	28.1	30.6	31.0	32.0
Air temp (mean daily max) (°C)	34.5	35.7	30.0	33.7	34.6	37.5	29.5	33.7	35.9	36.9	34.8	38.2	39.6	39.0
Air humidity (%)	62	55	73	57	55	53	54	56	56	60	58	51	48	52
Wind speed (m s ⁻¹)	0.6	1.4	0.7	0.9	0.9	1.0	1.3	1.1	1.1	0.8	1.3	1.2	0.8	0.9
Global rad. (MJ m ⁻² d ⁻¹)	24.6	24.6	23.4	25.0	28.0	29.0	24.9	28.7	23.1	21.7	27.3	24.5	23.8	20.9
Boundary water temperature (°C)	16.3	16.3	14.1	15.9	16.0	16.8	15.6	16.2	17.0	17.5	17.5	19.4	20.4	20.3

each event per day was different for each event as well. For the 20-year return event in 2030, global radiation was 28 MJ m⁻² d⁻¹, i.e. higher than the same scenario in 2050 (23.1 MJ m⁻² d⁻¹) and 2085 (23.8 MJ m⁻² d⁻¹). During the 20-year return event of 2085, on the other hand, global radiation was higher than the Max event (20.9 MJ m⁻² d⁻¹) of this climate period (Table 2).

For the mean water temperature at the model boundary, an increase of +4.1 °C for a 20-year return event of 2085 with respect to 2013 levels was simulated (Table 2). For the Max event of 2085, which had 2.2 MJ m⁻² d⁻¹ lower global radiation input, a slightly lower temperature increase (+4.0 °C) was simulated (Table 2).

The extraction of future climate data was based on the location of the INCA grid. INCA data for the heat event in 2013 were compared with data measured directly at the river. The INCA data assume a greater distance to the river surface and show higher mean and maximum air temperatures but also lower air humidity and higher wind speed. This difference in meteorological input data resulted in 0.1 °C higher than measured mean water temperature (Table 3). Maximum water temperature was affected as well, with INCA showing a reduction of 0.3 °C below measured values. Minimum water temperature was 0.6 °C warmer when INCA data input were used. In order to directly compare the 2013 event with the future scenarios, the simulation using the INCA data of 2013 is referred to as “20a OBS” hereafter.

3.3 Future stream temperatures

3.3.1 At DFS 39 km

To analyse future changes, the initial focus was upon the reference station in the centre of the study region at DFS 39 km.

As a temporal reference, the focus was placed on the 20-year return period events of the 2071–2100 climate period as it represents the maximum expected temperature rise.

The mean water temperature of the Pinka under MLF conditions with unchanged riparian vegetation (STQ) at DFS 39 km during the 20a heat wave event for the periods 2016–2045, 2036–2065 and 2071–2100 was predicted to be 22.4, 22.6 and 25.5 °C, respectively (Fig. 4, Table 3). The corresponding predicted maximum water temperatures were 25.0, 24.8 and 27.3 °C. These predictions represent a significant increase over the mean temperatures of the 20a event of the OBS period of 22.5 °C (maximum temperature: 24.4 °C) by the end of the century.

For mean temperatures, a minor increase in water temperature was predicted for the first half of the century even for extreme heat events with a 20-year return period (Table 4). However, by the end of the century (2071–2100), a remarkable increase in minimum temperatures of +3 °C was modelled. Maximum water temperatures also showed increases. For the period 2016–2045, maximum temperatures increased more rapidly than mean temperatures with a change over baseline conditions of +0.6 °C. By 2071–2100, the increase in maximum temperatures was predicted to be 2.9 °C compared to the OBS period, which was similar to the predicted increase in mean and minimum water temperatures (Table 4).

Supposing the existing vegetation was removed (V0), the mean water temperature reached 26.7 °C during 20-year return period heat events at the end of the century, which was 4.2 °C above the level of the STQ scenario of the OBS period. Maximum temperatures reached 28.9 °C, which is 4.5 °C more than in the STQ scenario of the OBS period (Fig. 4, Tables 3, 4). Under conditions of maximum riverine vegetation (V100), the expected mean water temperature was predicted to reach only 23.9 °C, which is 1.4 °C above the level of the

Table 3. Daily minimum, mean and maximum 5-day mean water temperatures of the 5-day episodes averaged over the Pinka during the 1a, 5a, 20a and Max episodes for the climate periods centred on 2030, 2050 and 2085 and mean low flow discharge at DFS 39 km. For 2013 (OBS), the measured values of the reference station 2 m above the river (Meas.) and interpolated measurement data from the INCA data set used as input are compared.

	Max.			Mean			Min.		
	V0	STQ	V100	V0	STQ	V100	V0	STQ	V100
OBS Meas.	26.6	24.7	22.4	23.8	22.4	20.7	20.2	19.5	18.5
OBS INCA	26.1	24.4	22.1	23.7	22.5	20.8	21.0	20.1	19.2
2030_1a	24.5	23.1	20.7	21.5	20.4	18.6	16.5	16.5	16.3
2030_5a	25.9	24.3	22.1	22.5	21.3	19.7	17.8	17.2	16.5
2030_20a	27.0	25.0	22.5	22.2	22.4	20.2	19.4	18.2	17.2
2030_Max	27.2	25.7	23.5	24.8	23.4	21.6	21.9	20.8	19.5
2050_1a	24.3	22.6	20.0	21.6	20.4	18.9	19.0	18.2	17.3
2050_5a	26.5	24.8	22.2	23.7	22.3	20.5	20.4	19.5	18.4
2050_20a	26.6	24.8	23.0	23.7	22.6	21.3	20.2	19.9	18.9
2050_Max	27.5	25.9	23.7	25.1	23.9	22.2	22.5	21.5	20.4
2085_1a	28.6	24.9	23.1	26.2	22.5	21.7	22.3	18.8	18.8
2085_5a	29.0	27.3	25.0	26.5	25.3	23.7	24.1	23.0	21.7
2085_20a	28.9	27.3	25.5	26.7	25.5	23.9	23.6	22.9	21.7
2085_Max	29.3	27.8	25.7	27.1	26.0	24.6	25.0	24.1	23.0

Table 4. Differences between the 20a event of the OBS period (2013) (with mean low flow discharge) of predicted maximum, mean and minimum water temperatures for the 1a, 5a, 20a and Max events at DFS 39 km for the climate periods centred on 2030, 2050 and 2085 for vegetation scenario V0 (no vegetation), STQ (vegetation unchanged) and V100 (maximum vegetation).

	Max.			Mean			Min.		
	V0	STQ	V100	V0	STQ	V100	V0	STQ	V100
OBS INCA	1.7	0	-2.3	1.2	0	-1.7	0.9	0	0.9
2030_1a	0.1	-1.3	-3.7	-1	-2.1	-3.9	-3.6	-3.6	-3.8
2030_5a	1.5	-0.1	-2.3	0	-1.2	-2.8	-2.3	-2.9	-3.6
2030_20a	2.6	0.6	-1.9	0.3	-0.1	-2.3	-0.7	-1.9	-2.9
2030_Max	2.8	1.3	-0.9	2.3	0.9	-0.9	1.8	0.7	-0.6
2050_1a	-0.1	-1.8	-4.4	-0.9	-2.1	-3.6	-1.1	-1.9	-2.8
2050_5a	2.1	0.4	-2.2	1.2	-0.2	-2	0.3	-0.6	-1.7
2050_20a	2.2	0.4	-1.4	1.2	0.1	-1.2	0.1	-0.2	-1.2
2050_Max	3.1	1.5	-0.7	2.6	1.4	-0.3	2.4	1.4	0.3
2085_1a	4.2	0.5	-1.3	3.7	0	-0.8	2.2	-1.3	-1.3
2085_5a	4.6	2.9	0.6	4	2.8	1.2	4	2.9	1.6
2085_20a	4.5	2.9	1.1	4.2	3	1.4	3.5	2.7	1.6
2085_Max	4.9	3.4	1.3	4.7	3.5	2.1	4.9	4	2.9

STQ scenario during 2013 (Fig. 4, Tables 3, 4). The maximum temperature reached in this scenario is 25.5 °C which is only 1.1 °C above the maximum event of the OBS period (Fig. 4, Tables 3, 4).

Vegetation was not able to compensate fully for the temperature increase expected by the end of the century. For the climate period 2036–2065 though, riverine vegetation had the potential to more than compensate for climate change during extreme events and could even cause a cooling of -1.2 on average and -1.4 °C with respect to maximum temperatures (Table 4).

3.3.2 Longitudinal distribution

During the 2013 heat wave event for the STQ scenario, the stream temperatures increased between the upstream model boundary at DFS 11 km and DFS 62 km by about 7 °C (Fig. 3). Looking at the longitudinal distribution of water temperature along the river, it can be seen that increases in mean stream temperature caused by increases of future air temperature affected all parts of the river (Fig. 5a–c).

The maximum values showed a similar pattern to the mean values on a higher level. The average difference between mean and maximum values of the STQ scenario was 3.92,

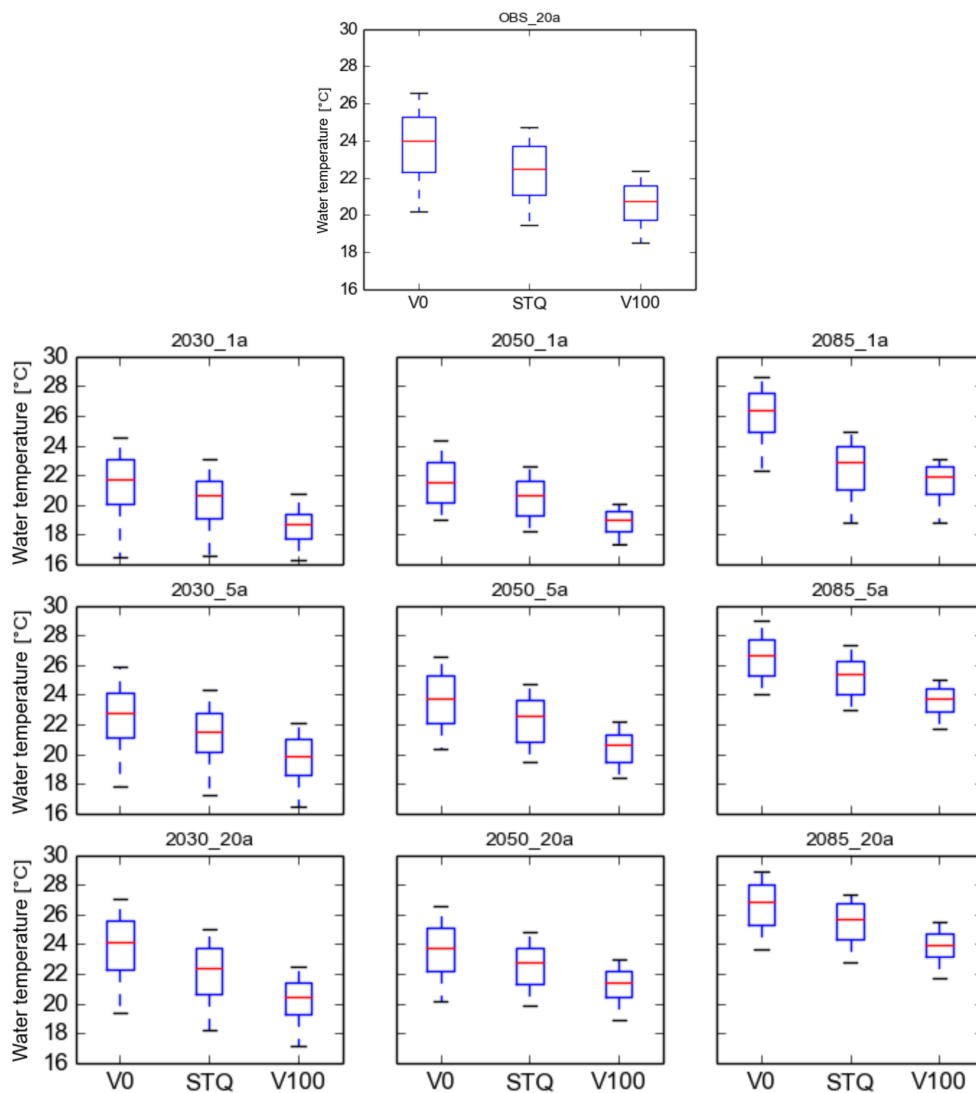


Figure 4. Box-and-whisker plots showing the 5-day mean water temperature distributions during the 1a, 5a and 20a episodes for the climate periods centred on 2030, 2050, 2085 with mean low flow discharge at DFS 39 km. The hourly values of V0 (no vegetation) and V100 (full vegetation) are significantly different from STQ in all episodes ($p < 0.0001$).

3.35 and 3.91 °C, the maximum difference was 5.51, 4.89 and 5.51 °C and the standard deviation of this difference was 0.71, 0.66 and 0.71 for 2030, 2050 and 2085, respectively (Fig. 5a–c).

V0 scenarios were always warmer than STQ scenarios and V100 scenarios were always cooler than the STQ scenarios. The mean differences along the river between V0 and STQ were 1.25, 1.26 and 1.13 °C, the maximum difference was 1.81, 1.85 and 1.66 °C, the standard deviation was 0.35, 0.36 and 0.32 for 2030, 2050 and 2085, respectively. The mean difference between STQ and V100 was 1.42, 1.52 and 1.26 °C, the maximum difference was 1.92, 2.05 and 1.72 °C, the standard deviation of this difference was 0.46, 0.49 and 0.41 for 2030, 2050 and 2085, respectively (Fig. 5c).

Water temperature was especially sensitive to the removal of vegetation within the first 10 km (DFS 11–21 km) where there were dense forests which prevented the cool headwaters from warming (Fig. 5d). In this region, temperatures increased by 1.4 °C under the no-vegetation scenario (V0–STQ). Additional tree cover (V100) caused a temperature reduction of 0.9 °C compared to the STQ scenario (Fig. 5d). This can be explained by the slower flow velocities in the lower reaches (last 30 km – DFS 32–62 km: 0.003 m m^{-1} , 0.4 m s^{-1}) in comparison to the steeper upstream sections (first 10 km – DFS 11–21 km: 0.017 m m^{-1} , 0.6 m s^{-1}), which gives shortwave radiation in unshaded sections more time to heat the water column. For the Pinka, the benefit of additional tree cover maximizing riparian shade became more distinct in the downstream sections (DFS 25–

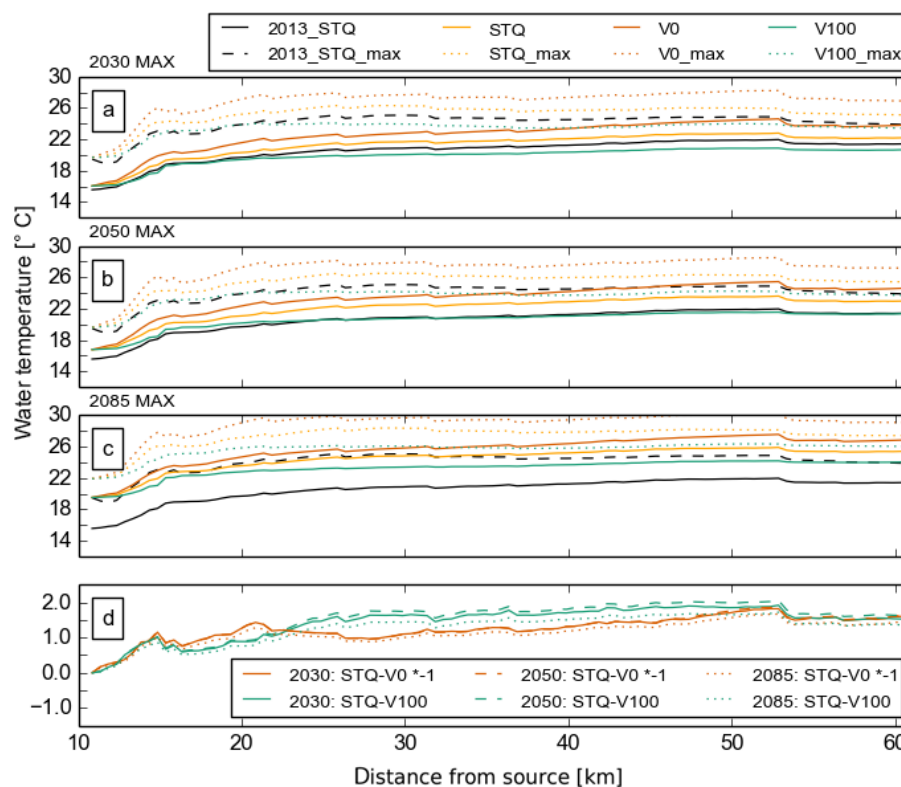


Figure 5. Mean and maximum water temperatures averaged during the maximum events predicted for the climate periods centred on (a) 2030, (b) 2050 and (c) 2085 along the Pinka using vegetation scenarios V0 (no vegetation), STQ and V100 (full vegetation) in comparison to the maximum event recorded in 2013. (d) The difference between STQ and V100 (green) and STQ and V0 ($* - 1$) (red).

55 km) where the additional tree cover caused a change of -1.75°C , while removal only caused a change of around $+1.25^{\circ}\text{C}$ (Fig. 5).

3.3.3 Diurnal ranges

For aquatic species, the mean stream temperature is not the only relevant temperature parameter. The daily temperature range, the absolute minima and maxima as well as the timing when extremes take place are of importance as well. These vary along the river and change depending on the different vegetation shade intensities and discharge volumes (Fig. 6). In the contour plot shown in Fig. 6, the warming along the longitudinal gradient is clearly visible, but it is also obvious that the stream is warming to a higher peak each day until the end of the heat episode. In the lower panel of Fig. 6, the daily water temperature amplitude is plotted, along with the energy balance components acting on the river surface for the two locations marked by the black bars in the contour plots. Here, the absolute values, amplitude and timing of extremes can be seen. While the energy balance shows the energy input taking place directly at the location, the water temperature includes the energy input of the whole water volume upstream. An upstream site (DFS 20 km) is compared to a downstream site (DSF 61 km). They are both open (VTS of V0 = 0.9, 1) but

differ in average water depth (0.09, 0.31 m) and discharge levels ($0.34\text{ m}^3\text{ s}^{-1}$, $0.8\text{ m}^3\text{ s}^{-1}$).

The daily amplitude of the water temperature is strongly damped by the larger flow volume which can be seen in the comparison of the upstream and downstream sites (Fig. 6). A decrease in discharge of -15% can also be seen to affect the daily minima and maxima of stream temperature in open sections (V0). During the V100 scenario, the 15% discharge reduction has no visible effect ($\ll 0.1^{\circ}\text{C}$).

The daily amplitude of the energy fluxes is not affected by flow volume but is reduced by vegetation shade. The hourly values of all energy fluxes are reduced synchronously. Decreased solar input and wind access close to the river surface caused by an increase in vegetation density lowers the energy fluxes. From V0 to V100, the maxima can increase more than 2°C (Figs. 6 and 7). However, changes in vegetation density of as little as 20% can cause an increase of maximum water temperature of more than 0.5°C (Fig. 7). A change from, e.g. 100 to 70% raises the heat input by shortwave radiation ($+17\text{ Wm}^{-2}$), convection ($+5.6\text{ Wm}^{-2}$) and longwave radiation ($+3.7\text{ Wm}^{-2}$) but only increases heat loss by evaporation from the river surface (-21 Wm^{-2}) (Fig. 7). The shading affects the maximum as well as the minimum water temperatures and leads to a reduction of the daily amplitude (Figs. 6

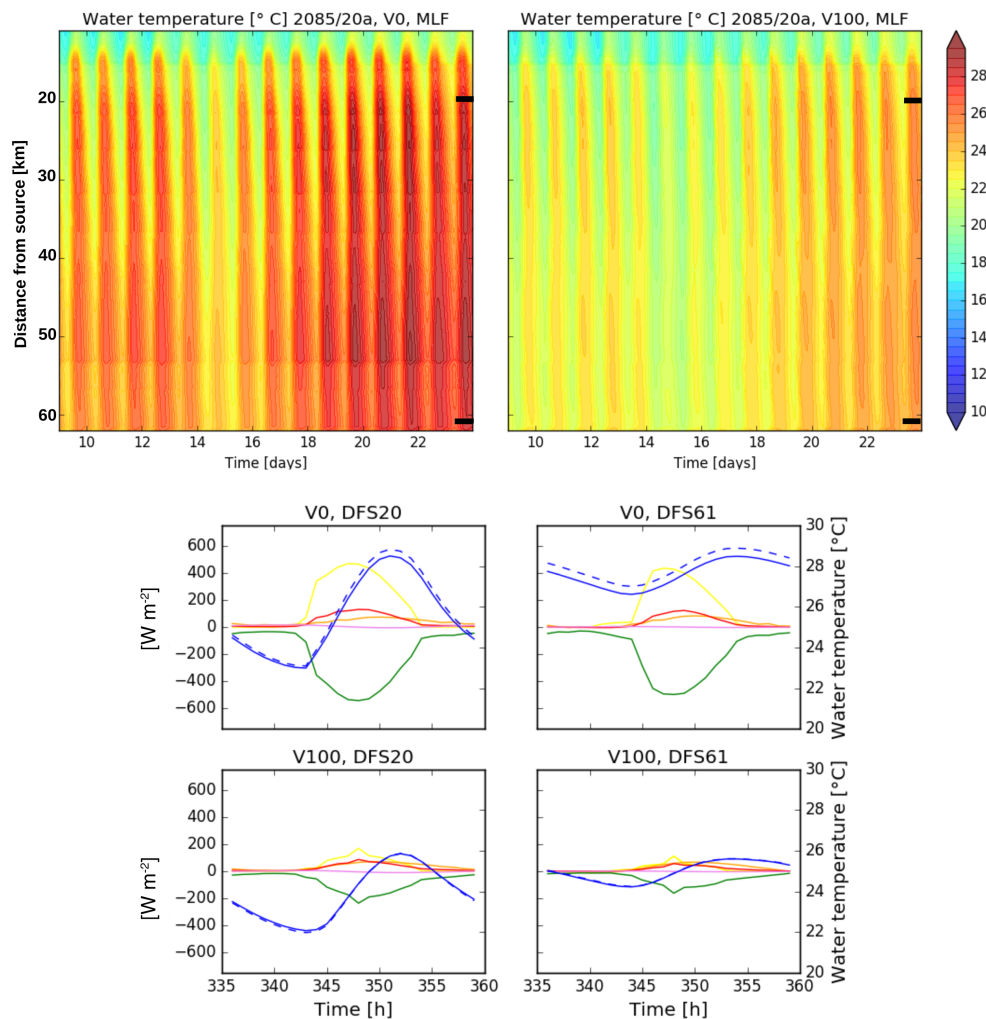


Figure 6. Upper panel: water temperature along the Pinka and the whole 20-year return period event centred on 2085 for no vegetation (V0) and full vegetation (V100). The black lines mark the location of the data shown below. Lower panel: the effect of a 15 % discharge reduction (MLF of 15 %) of the mean low flow conditions (blue, dashed) on stream temperature compared to MLF (blue, solid) and the diurnal amplitude of all energy fluxes (shortwave radiation balance is yellow, latent heat flux is green, longwave radiation balance is red, sensible heat flux is orange and conduction heat flux is violet) for an upstream (DFS 20 km) location and a downstream (DFS 61 km) location for the 20-year return period event centred on 2085 for no vegetation (V0) and maximum vegetation (V100).

and 7). An interesting aspect is that the peak of stream temperature occurs about 1 h later when vegetation is included. With a vegetation density reduction of 50 % (VD50), the diurnal range and especially the maximum temperatures are further increased (Fig. 7). It is interesting to note that halving vegetation height has a similar or less significant effect as reducing vegetation density by 20 % (Fig. 7).

3.3.4 Trends

The trend lines were calculated by minimizing the square error. An ANCOVA (analysis of covariance) showed significant interactions between vegetation and air temperature ($p < 0.001$). The equal slope assumption failed; the equal variance test was passed. Mean, maximum and minimum

stream temperatures increase as air temperature increases (Fig. 8). Under the assumption of full vegetation, the intercept of the regression line is lowest for the mean and maxima, while under the assumption of no vegetation it is lowest for the minima. The difference between the vegetation scenarios is greatest for the maxima and smallest for the minima. The slope, on the other hand, is smallest for the maxima and greatest for the minima. All scenarios and values show a squared Spearman's rank correlation coefficient between 0.78 and 0.93. For mean and maximum temperatures, the trend line of V0 is steeper than that of V100 (17 %), which means that, supposing no vegetation, the maximum temperatures will increase at a higher rate. For the daily minima, the difference in slope is even greater (30 %). The regres-

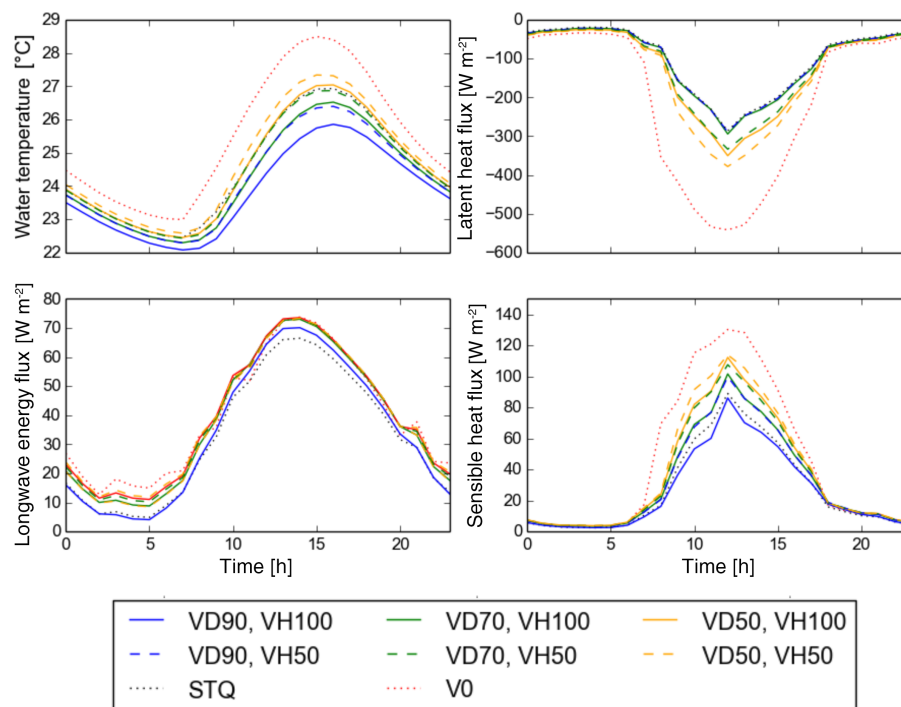


Figure 7. The effect of the vegetation scenarios of maximum vegetation height (VH100) and 50 % vegetation height (VH50), natural dense vegetation (VD90), natural light vegetation (VD70), sparse vegetation (VD50), V0 (no vegetation) and STQ (actual vegetation) on the diurnal amplitude of water temperature and the air-temperature-dependent energy fluxes longwave radiation, sensible and latent heat fluxes for the 20-year return period events of the final day of the climate periods centred on 2085 for mean low flow conditions (MLF) for an upstream location (DFS 20 km).

sion lines of the halved vegetation height scenario (V50) and the reduced vegetation density scenario (V70) cross for minima, mean and maxima values. The change in slope though is small (3.6, 1.4 and 5.8 % for the mean, minima and maxima, respectively) and statistically not significant.

4 Discussion

4.1 Energy fluxes during heat waves

In the present article, evaporative heat flux was responsible for 100 % of heat loss from river water on average. Short-wave radiation balance, longwave radiation balance and sensible heat flux were 64, 11 and 25 % of the total energy input, respectively.

During summer periods of high air temperature, the difference between air and water temperature increases, which can trigger intensified evaporative flux that cools the river but can also cause sensible heat flux to heat the water column (Benyahya et al., 2012). Benyahya et al. (2012) found that evaporative heat flux accounted for 100 % of energy outputs during 7–23 June 2008 while shortwave radiation balance, longwave radiation balance and sensible heat flux were 72.53, 24.05 and 2.03 % of the energy input, respectively.

4.2 Magnitude of stream temperature rise

The modelled 20-year return period heat wave (20a) in the climate period 2071–2100 showed a +3.8 °C increase in air temperature with respect to the observed period. Increases in maximum, mean and minimum stream temperatures of close to +3 °C with respect to the observed period were simulated for this episode. During the Max event, the modelled increases of maximum, mean and minimum temperatures were 3.4 °C, 3.5 and 4 °C, respectively. When looking at the whole river, mean changes of 3.3 °C for the maximum and 3.9 °C mean temperatures were calculated. Melcher et al. (2014) also found that average and maximum temperatures show similar warming trends. An increase of 3.9 °C from the OBS period to 2085 corresponds to an increase of 0.43 °C decade⁻¹. An increase of 3 °C equates to an increase of 0.33 °C decade⁻¹.

The relatively low values of water temperature predicted for the 20a 2050 heat wave might be explained by higher wind speeds and lower air humidity causing higher evaporation rates and lower solar radiation energy input compared to 2013. The relatively low modelled temperatures were most evident in maximum water temperatures. For the V0 scenario, relatively low water temperatures were also predicted, which was caused by increased evaporation. The maximum

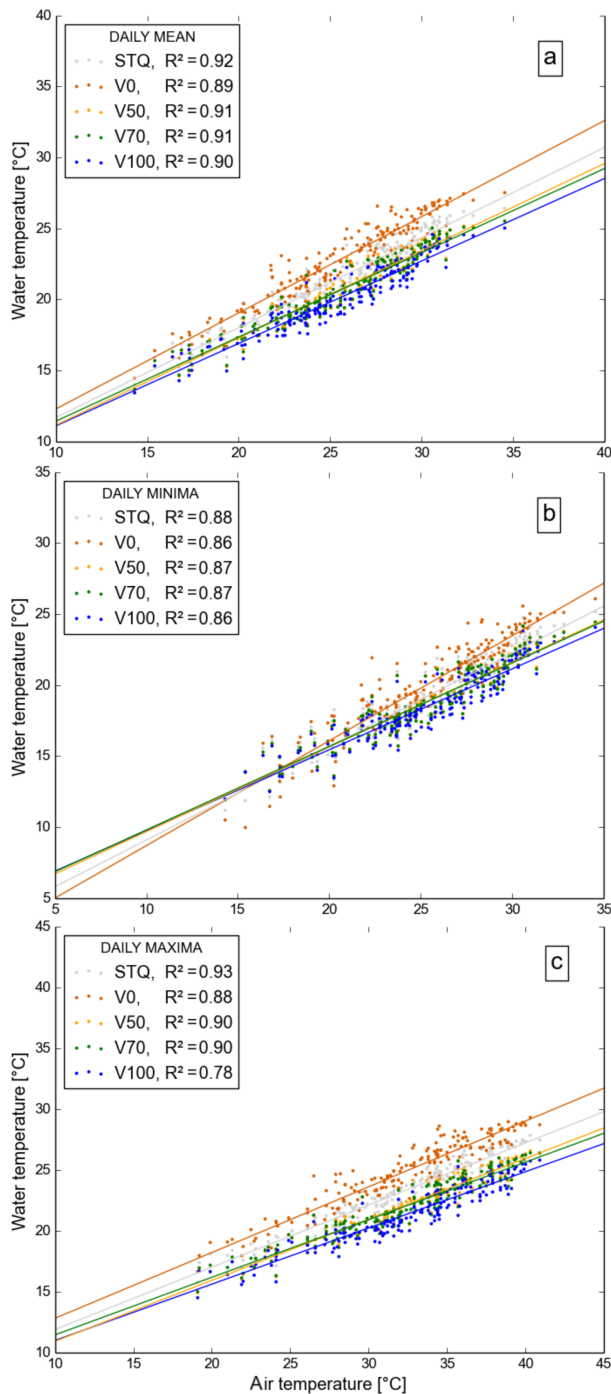


Figure 8. Correlations between water temperature and the daily (a) mean, (b) minima and (c) maxima air temperatures for the 1a, 5a, 20a and Max episodes of the climate periods centred at 2030, 2050 and 2085 for existing vegetation (STQ), no vegetation (V0), vegetation height of 50 % (V50), vegetation of 70 % density (V70) and full vegetation (V100) reported with the squared Spearman rank correlation coefficient. ANCOVA showed significant interactions between vegetation and air temperature ($p < 0.001$).

vegetation scenario (V100) shows similar stream temperatures to 2013.

Temperature increase in Austrian stream waters is well documented and ubiquitous. All 230 stations of the Austrian hydrographic central office, with different elevations, distances from source and catchment areas recorded increases of stream temperature of an average of 1.5°C ($0.48^{\circ}\text{C decade}^{-1}$) from 1980 to 2011 (BMLFUW, 2011). The data were elevation corrected using external drift top kriging (Skøien et al., 2006) and a mean trend was calculated using the Mann–Kendall test (Burn and Hag Elnur, 2002). Melcher et al. (2013) analysed 60 stations and found a similar trend of 1°C within the last 35 years for mean August temperatures, which was independent of the river type ($0.29^{\circ}\text{C decade}^{-1}$). The annual mean temperature of the Danube has been rising (Webb and Nobilis, 1995) and is likely to continue to rise to reach a value between 11.1 and 12.2°C by 2050 compared to around 9°C at the beginning of the 20th century at the border with Slovakia (Nachnebel et al., 2014). Dokulil (2013) extrapolated the quadratic regression of the period 1900–2006 of the Danube near Vienna and predicted an increase of up to 3.2°C by 2050 with respect to 1900 ($0.21^{\circ}\text{C decade}^{-1}$). Using linear regression, the increase was only 2.3°C ($0.15^{\circ}\text{C decade}^{-1}$), but using the linear trend beginning from 1970, the increase was 3.4°C ($0.23^{\circ}\text{C decade}^{-1}$). Due to the size of the Danube, daily amplitudes and extremes are not comparable to the Pinka, but trends in mean water temperature values are comparable though. The temperature values predicted by this study were clearly greater than the model uncertainty and lie in the upper region of the values published by other studies (BMLFUW, 2001; Dokulil, 2013; Melcher et al., 2013, 2014).

Considering a likely discharge decrease (Nachnebel et al., 2014), a slightly higher temperature rise might be expected. Van Vliet et al. (2011) analysed 157 river temperature stations globally for the 1980–1999 period and predicted increases of annual mean river temperature of 1.3 , 2.6 and 3.8°C under air temperature increases of 2 , 4 and 5°C , respectively. Discharge decreases of 20 and 40% increased the modelled water temperature rises by 0.3 and 0.8°C on average (Van Vliet et al., 2011).

4.3 Ability of riparian vegetation to mitigate the expected stream temperature rise

How will riparian vegetation systems behave in the future? What are the feedback mechanisms of increased shading under a warmer heat wave scenario? Decrease in discharge caused by increased evaporation from the river surfaces caused by missing riparian vegetation (V0 compared to V100) was calculated to be $-0.001\text{ m}^3\text{ s}^{-1}$ at the lower boundary of the river (DFS 61 km). Also, during an MLF reduced by 15% , the loss of water to evaporation was only $-0.001\text{ m}^3\text{ s}^{-1}$. Therefore, mass loss was not found to be a significant driver of temperature rise in a river of this size.

Further, there might be a potential decrease of discharge caused by increased withdrawal of river water by the riparian vegetation under warmer climates. As species of the floodplain forest are “spender”-type plants that do not economize their water use, this needs to be considered. In this study, a simulation is included with a discharge decrease of 15 %, a level that is presently expected from past observations. This estimation includes precipitation losses as well as increased evapotranspiration by the soil–vegetation system of the catchment area and increased evapotranspiration by the riparian vegetation via rises in air temperature. Different discharge scenarios were not simulated for all episodes, because whether a low flow situation was considered or not was more dominant than the reduction expected by climate change.

The increased air humidity and reduced air temperature caused by transpiration of riparian vegetation close to the river reduce air humidity and air temperature gradients. The effect on water temperature was calculated to be a maximum of around 0.2 °C. More directly, vegetation affects water temperature by reducing shortwave radiation input, but also it reduces the view to sky which affects longwave radiation balance and the turbulent heat fluxes. Community changes which might affect vegetation height and density are possible within the next century, though changes in vegetation height and density in floodplain forests in natural systems are mainly due to succession. Primack (2000), Garssen et al. (2014) and Rivaes et al. (2014) studied the effect of climate change on natural riparian vegetation cover via changes in the hydrological regime including inundation periods and intensity, days since rain and the decline of water table. As the Pinka is anthropogenically influenced and will be regulated for the foreseeable future, no dynamical changes and no natural succession dynamics are expected which could cause an extreme change in vegetation cover.

Different vegetation scenarios were simulated in this study to quantify the potential effects of shading and wind reduction caused by vegetation. Compared to the status quo (STQ) scenario, additional riparian vegetation (V100) could reduce maximum stream temperatures during extreme heat waves by 2.2 °C, mean temperatures by 1.6 °C and minimum temperatures by 0.9 °C (Table 4). Removal of existing vegetation (V0) amplified stream temperature increases and could cause an average increase of maximum, mean and minimum stream temperatures of 1.8, 1.3 and 1.0 °C, respectively, in comparison with the STQ vegetation scenario (Table 4).

Removal of vegetation (V0) magnified stream temperatures during 20-year return period events by the end of the century by up to 4.2 (mean) and 4.5 °C (daily maximum). Additional riparian vegetation (V100), on the other hand, mitigated part of the rise in maximum temperatures, so there was only a 1.1 °C increase. Although the increase of mean temperatures was reduced to about 1.4 °C, riparian vegetation management alone was not enough to compensate for the predicted warming caused by climate change. The water temperature reduction rates predicted in the present article

lie within the range of observed changes of pre- and post-harvest situations found in the literature (Cole and Newton, 2013; Moore et al., 2005).

The maximum water temperatures during heat waves in particular could be reduced significantly by vegetation shade. Daily mean and daily maximum temperatures tend to increase more strongly for higher air temperatures if less vegetation is present. Daily minimum temperatures increase at an even higher rate. These trends are in agreement with findings about experimental data analysed by Kalny et al. (2017).

Vegetation height and density can alter the slope of the temperature trend line. For example, with dense low vegetation, water temperature starts lower and ends higher for the same air temperature compared to the high vegetation and less dense scenario, which indicates that there is some impeding of cooling during the night by lower vegetation compared to higher vegetation. Water temperatures rise more rapidly for dense low vegetation than high vegetation of reduced density. High vegetation of lower density cannot compete with dense high vegetation in terms of reduction of stream water temperature though.

During heat wave situations, the reduction in air exchange causes an important lag in temperature rise, so the time of maximum solar exposure does not coincide with the maximum heat stress caused by water temperature. This lag is known in the literature (Brown and Krygier, 1970). Apart from its influence on stream temperature, vegetation can cast spatially differentiated shade, which results in areas of different Sun exposure and energy balance. This heterogeneity can provide ecological niches which are important for different development stages of river fauna (Clark et al., 1999).

4.4 Limitations

Vegetation mainly causes lower maximum stream temperatures by reducing the solar radiation input at the river surface by shading. This effect is strong during times of clear skies and high solar irradiation. Under cloudy conditions, this effect is less pronounced, and during nighttime it is absent, but outgoing longwave radiation is still impeded. This in turn could lead to higher mean and minimum temperatures, which can be also seen in the simulated low global radiation scenarios.

Although vegetation can have important effects on stream temperature, there will be river sections which will not be affected by the addition (or removal) of vegetation due to upstream or lateral, surface or subsurface advection of heat or topographic shade (Johnson and Wilby, 2015). Groundwater influence was not measured and no groundwater influence was assumed in the model. Although the model performed well (RMSE of 0.88 °C) there might be some groundwater influence between DFS 45 and 55 km where the measurements lie below the simulation results. Other possible future alterations to the river via development or climate change were not considered here. These include potential anthro-

pogenic heat sources or sinks like discharges of tempered waste water, possible changes in stream velocity and shading, sediment changes caused by impoundments, regulation and canalization, or discharge changes such as withdrawal of water for irrigation. The climate input used only one possible emission scenario simulated by one regional climate model. The percentage contributions of surface, subsurface, groundwater and/or snowmelt still have to be analysed in more detail (Johnson and Wilby, 2015). Apart from rising air temperatures and discharge changes, anthropogenic influences like discharges from waste water treatment plants and cooling water can influence stream temperatures in a negative way and are therefore presently illegal in Austria (WRG, 1959). Other possible consequences of climate change are changes in sediment loads in river systems due to changes in mobilization, transport and deposition of sediment, which is expected to be very likely (APCC, 2014). Sediment changes might alter the bed conduction flow as well as flow velocity, which can influence the magnitude and variability of stream temperature. Artificial changes which deteriorate the situation are presently illegal in Austria as well (WRG, 1959).

5 Conclusions

In this study, the influence of expected changes in heat wave intensity during the 21st century on stream temperature in the rithron to upper potamal section of the human-impacted eastern Austrian Pinka was simulated and the mitigating effect of riparian vegetation shade on the radiant and turbulent energy fluxes was analysed. By the end of the century (2071–2100), in the study region, an air temperature increase of 3.8 to 5.6 °C was predicted during annual or less frequent extreme heat waves in comparison to the observed period of 1981–2010. Stream water temperature increases of less than 1.5 °C were modelled for the first half of the century. For the period 2071–2100, a more significant increase of 3 °C in maximum, mean and minimum stream temperatures was predicted for a 20-year return period heat event.

Discharge changes, caused by increased evaporation due reduced shade, were not found to be significant. Discharge changes caused by precipitation and increased evapotranspiration in the catchment area as expected from past observations was found to be insignificant compared to the changes caused by vegetation shade.

Vegetation could reduce stream temperature during heat waves when conditions of high solar radiation predominate. Even when maximum vegetation extent with maximum height and density including plantations and replacement plantings was assumed, the additional riparian vegetation was not able to fully mitigate the expected temperature rise caused by climate change. However, during extreme heat waves, maximum stream temperatures could be reduced by 2.2 °C and mean temperatures by 1.6 °C. Removal of existing vegetation amplified stream temperature increases and could

cause an increase of maximum and mean stream temperatures by 1.8 and 1.3 °C, respectively, in comparison with the status quo vegetation scenario. With complete vegetation removal, maximum stream temperatures in annual heat events at the end of the century could increase by more than 4 °C compared to the present time.

Daily amplitudes were reduced by riparian vegetation and the timing of the peak temperature was delayed by about 1 h. A reduction of vegetation density by 20 % had shown a similar effect as a 50 % reduction of vegetation height. Vegetation can reduce maximum temperatures more effectively on an absolute scale but also reduced the trends significantly compared to the no-vegetation scenario. Minimum temperatures increased most.

This study shows that it is very likely that during extreme events a temperature increase of 2 °C will be exceeded during this century. This is the magnitude of the temperature differentiation of fish zones and in particular for the occurrence of native cold-water-preferring and warm-water-preferring fish species (Logez et al., 2013; Melcher et al., 2013; Pletterbauer et al., 2015). At a stream temperature of 20 °C, cold-water-adapted species begin to experience temperature-induced mortality (Melcher et al., 2014; Schaufler 2015). During a simulated annual heat wave event in the period 2016–2035, this threshold was never exceeded in the most upstream region (DFS 13 km), which is presently populated by the cold-adapted species brown trout (Guldenschuh 2015). At the end of the century, during a heat wave event of a 20-year return period, the threshold was likely to be exceeded for 72 of 120 h. At the lower boundary of the trout zone (DFS 20 km), the 20 °C mark was exceeded for 70 of the 120 h during heat waves at the beginning of the century, but riparian vegetation shade could reduce this period to 9 h in total. The mitigation possibilities of vegetation were limited though and could not fully compensate for the whole predicted temperature raise. At the end of the century, in heat waves of a 5-year or shorter return period, even if maximum vegetation was assumed, 20 °C was exceeded during the whole heat wave event.

Global warming has multiple impacts on changes in aquatic ecosystems, whereas in combination with loss of habitat and other human pressures, this is leading to a deadly anthropogenic-induced cocktail (Schinegger et al., 2011). The study affirmed the importance of shading and riparian vegetation along river banks for aquatic biodiversity and indicates the added value of riparian vegetation to mitigate climate change effects on water temperature. During this study, no economic evaluation of the vegetation scenarios could be done. While maximum vegetation height and densities of 50 % can easily be reached without external efforts, this process can certainly be accelerated as well as high densities assured by planting additional trees. This comes at a certain cost, but it might be worth it to invest. The used method provides a model for weighting of interactions of environmental parameters especially during heat wave events. The find-

ings and recommendations gained with this methodology can help key decision makers in choosing the right restoration measures. The study in general emphasizes the importance of land–water interfaces and their ecological functioning in aquatic environments.

Appendix A

Abbreviations

DFS	distance from source
INCA	integrated nowcasting through comprehensive analysis
VTS	view to sky

Climate episodes

1a, 5a, 20a	episodes of 1-, 5-, 20-year return periods within a 30-year climate period
Max	maximum event of a 30-year climate period
OBS	observed period (1981–2010)
2030, 2050, 2085	30-year climate period centred on 2030 (2016–2045), 2050 (2036–2065), 2085 (2071–2100)

Discharge scenarios

MLF	mean low flow of the gauging station at DFS 13 km: $0.143 \text{ m}^3 \text{ s}^{-1}$, DFS 62 km: $0.795 \text{ m}^3 \text{ s}^{-1}$
MLF-15	MLF minus 15 % discharge

Vegetation scenarios

STQ	“status quo”, existing/actual vegetation
V100	“maximum vegetation” – vegetation height 30 m, vegetation density 90 % (VD90, VH100)
V70	“reduced density” – vegetation height 30 m, vegetation density 70 % (VD70, VH100)
V50	“intermediate vegetation height” – vegetation height 15 m, vegetation density 90 % (VD90, VH50)
V0	“no vegetation”
VD50, VH100	vegetation density 50 %, vegetation height 100 % (30 m)
VD70, VH50	vegetation density 70 %, vegetation height 50 % (15 m)
VD50, VH50	vegetation density 50 %, vegetation height 50 % (15 m)

Code availability. The last official version of Heat Source software used is available online at <http://www.oregon.gov/deq/wq/tmdls/Pages/TMDLs-Tools.aspx>. The changes included in Heat Source within this study will be implemented in the next version, which will be available at the same location.

Data availability. The simulation input and result data sets for the present and future heat wave episodes used in this article are published on the freshwater biodiversity data portal (<https://doi.org/10.13148/BFFWM8>). As they are part of the research project BIO_CLIC, the metadata are published together with the other vegetation, morphological and biological data sets produced in the project in the Freshwater Metadata Journal (<https://doi.org/10.15504/fmj.2017.22>).

Author contributions. AM was in charge of the hydrobiological aspects. PW helped to better understand the energy fluxes of the riverine system. HF selected the climate episodes and helped to interpret the significance of the results. LD produced the climate episode data and the upstream boundary water temperature. GK organized the field campaigns and helped Valeria Ledochowski to build the basic vegetation and morphology data set. HT organized and executed the water temperature measurements further processed the all input data for the use of Heat Source, adapted and validated the model. She ran the Heat Source simulations for all selected episodes and prepared the manuscript.

Competing interests. The authors declare that they have no conflict of interest.

Acknowledgements. This research was part of the project BIO_CLIC and LOWFLOW+ both funded within the Austrian Climate Research Programme (ACRP) by the Klima und Energiefond. The regional climate model data sets used to produce the climate episodes were developed in the ENSEMBLES project supported by the European Commission's Sixth Framework Programme through contract GOCE-CT-2003-505539. The INCA data set was created by the Zentralanstalt für Meteorologie und Geodynamik (ZAMG). Hydrological data and the digital elevation model were provided by hydrographic services, which are part of the Federal Ministry of Agriculture, Forestry, Environment and Water management and the federal state governmental geoinformation service authorities of Styria and Burgenland. Bernhard Spangl from the Institute of Applied Statistics and Computing (IASCBOKU) gave advice regarding statistics. Special thanks are given to the Oregon Department of Environmental Quality, who maintain the Heat Source model and opened the source code for scientific use.

Edited by: Anas Ghadouani

Reviewed by: four anonymous referees

References

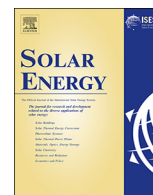
- Ahrens, B., Formayer, H., Gobiet, A., Heinrich, M., Hofstätter, M., Matulla, C., Prein, A. F., and Truhetz, H.: Zukünftige Klimaentwicklung/Future Climate Developments, in: Österreichischer Sachstandsbericht Klimawandel 2014 (AAR14), Austrian Panel on Climate Change (APCC), Verlag der Österreichischen Akademie der Wissenschaften, Wien, Österreich, 301–346, 2014.
- APCC: Österreichischer Sachstandsbericht Klimawandel 2014 (AAR14), Herausgeber: Kromp-Kolb, H., Nakicenovic, N., Steininger, K., Gobiet, A., Formayer, H., Köppl, A., Prettenhaler, F., Stötter, J., and Schneider, J., Verlag der Österreichischen Akademie der Wissenschaften, Wien, Österreich, 1096 pp., 2014.
- Arismendi, I., Safaeq, M., Dunham, J. B., and Johnson, S. L.: Can air temperature be used to project influences of climate change on stream temperature?, *Environ. Res. Lett.*, 9, 084015, <https://doi.org/10.1088/1748-9326/9/8/084015>, 2014.
- Auer, I., Böhm, R., Jurkovic, A., Lipa, W., Orlik, A., Potzmann, R., Schöner, W., Ungersböck, M., Matulla, C., Briffa, K., Jones, P., Efthymiadis, D., Brunetti, M., Nanni, T., Maugeri, M., Mercalli, L., Mestre, O., Moisselin, J.-M., Begert, M., Müller-Westermeier, G., Kveton, V., Bochnicek, O., Stastny, P., Lapin, M., Szalai, S., Szentimrey, T., Cegnar, T., Dolinar, M., Gajic-Capka, M., Zaninovic, K., Majstorovic, Z., and Nieplova, E.: HISTALP – historical instrumental climatological surface time series of the Greater Alpine Region, *Int. J. Climatol.*, 27, 17–46, <https://doi.org/10.1002/joc.1377>, 2007.
- Auer, I., Foelsche, U., Böhm, R., Chimani, B., Haimberger, L., Kerschner, H., Koinig, K. A., Nicolussi, K., and Spötl, C.: Vergangene Klimaänderung in Österreich, in: Österreichischer Sachstandsbericht Klimawandel 2014 (AAR14), Austrian Panel on Climate Change (APCC), Verlag der Österreichischen Akademie der Wissenschaften, Wien, Österreich, 227–300, 2014.
- Beniston, M., Stephenson, D. B., Christensen, O. B., Ferro, C. A. T., Frei, C., Goyette, S., Halsnaes, K., Holt, T., Jylhä, K., Koffi, B., Palutikof, J., Schöll, R., Semmler, T., and Woth, K.: Future extreme events in European climate: an exploration of regional climate model projections, *Climatic Change*, 81, 71–95, <https://doi.org/10.1007/s10584-006-9226-z>, 2007.
- Benyahya, L., Caissie, D., Satish, M. G., and El-Jabi, N.: Long-wave radiation and heat flux estimates within a small tributary in Catamaran Brook (New Brunswick, Canada), *Hydrol. Process.*, 26, 475–484, 2012.
- Birkel, I. and Mayer, A.: Ökologische Zusammenfassung der Flussauen an Iller, Lech, Isar, Salzach und Donau und ihre Unterschützstellung, Bayerisches Landesamt für Umweltschutz, München, 1992.
- Bloisa, J. L., Williams, J. W., Fitzpatrick M. C., Jackson, S. T., and Ferrier, S.: Space can substitute for time in predicting climate-change effects on biodiversity, *P. Natl. Acad. Sci. USA*, 110, 9374–9379, 2013.
- BMLFUW: Bundesministerium für Land- und Forstwirtschaft, Umwelt und Wasserwirtschaft, Herausgeber: Schöner, W., Böhm, R., Haslinger, K., Blöschl, G., Kroiß, H., Merz, R., Blaschke, A. P., Viglione, A., Parajka, J., Salinas, J. L., Drabek, U., Laaha, G., and Kreuzinger, N.: Anpassungsstrategien an den Klimawandel für Österreichs Wasserwirtschaft, Studie der Zen-

- tralanstalt für Meteorologie und Geodynamik und der Technischen Universität Wien, Wien, 486 pp., 2011.
- BMLFUW: Abteilung I/4 – Wasserhaushalt, Hydrographisches Jahrbuch von Österreich 2013, Wien, 2015.
- Böhm, R.: ALP-IMP (EVK-CT-2002-00148) Multi-centennial climate variability in the Alps based on Instrumental data, Model simulations and Proxy data, final report for RTD-project, ZAMG, Central Institute for Meteorology and Geodynamics, Vienna, Austria, 2006.
- Böhm, R.: Changes of regional climate variability in central Europe during the past 250 years, *Eur. Phys. J. Plus*, 127, 13 pp., <https://doi.org/10.1140/epjp/i2012-12054-6>, 2012.
- Böhm, R., Auer, I., Schöner, W., Ganekind, M., Gruber, C., Jurkovic, A., Orlik, A., and Ungersböck, M.: Eine neue Webseite mit instrumentellen Qualitäts-Klimadaten für den Grossraum Alpen zurück bis 1760, *Wiener Mitteilungen Band 216: Hochwässer: Bemessung, Risikoanalyse und Vorhersage*, 2009.
- Boyd, M. and Kasper, B.: Analytical methods for dynamic open channel heat and mass transfer: Methodology for heat source model Version 7.0, available at: <http://www.deq.state.or.us/wg/TMDLs/tools.htm> (last access: 11 January 2018), 2003.
- Brown, G. W. and Krygier, J. T.: Effects of Clear-Cutting on Stream Temperature, *Water Resour. Res.*, 6, 1133–1139, 1970.
- Burn, D. H. and Hag Elnur, M. A.: Detection of hydrologic trends and variability, *J. Hydrol.*, 255, 107–122, 2002.
- Caissie, D.: The thermal regime of rivers: a review, *Freshw. Biol.*, 51, 1389–1406, <https://doi.org/10.1111/j.1365-2427.2006.01597.x>, 2006.
- Caissie, D., Nassir, E.-J., and Mysore, G. S.: Modelling of maximum daily water temperatures in a small stream using air temperatures, *J. Hydrol.*, 251, 14–28, 2001.
- Caissie, D., Satish, M. G., and El-Jabi, N.: Predicting water temperatures using a deterministic model: Application on Miramichi River catchments (New Brunswick, Canada), *J. Hydrol.*, 336, 303–315, 2007.
- Capon, S. J., Chambers, L. E., Mac Nally, R., Naiman, R. J., Davies, P., Marshall, N., Pittock, J., Reid, M., Capon, T., Douglas, M., Catford, J., Baldwin, D. S., Stewardson, M., Roberts, J., Parsons, M., and Williams, S. E.: Riparian Ecosystems in the 21st Century: Hotspots for Climate Change Adaptation?, *Ecosystems*, 16, 359–381, <https://doi.org/10.1007/s10021-013-9656-1>, 2013.
- Chen, J., Franklin, J. F., and Spies, T. A.: Contrasting microclimates among clearcut, edge, and interior of old-growth Douglas-fir forest, *Agr. Forest Meteorol.*, 63, 219–237, 1993.
- Clark, E., Webb, B. W., and Ladle, M.: Microthermal gradients and ecological implications in Dorset rivers, *Hydrol. Process.*, 13, 423–438, 1999.
- Cluis, D.: Relationship between stream water temperature and ambient air temperature – A simple autoregressive model for mean daily stream water temperature fluctuations, *Nord. Hydrol.*, 3, 65–71, 1972.
- Cole, E. and Newton, M.: Influence of streamside buffers on stream temperature response following clear-cut harvesting in western Oregon, *Can. J. Forest Res.*, 43, 993–1005, 2013.
- Davies-Colley, R. J. and Quinn, J. M.: Stream lighting in five regions of North Island, New Zealand: Control by channel size and riparian vegetation, *New Zeal. J. Mar. Freshw.*, 32, 591–605, <https://doi.org/10.1080/00288330.1998.9516847>, 1998.
- Déqué, M.: Frequency of precipitation and temperature extremes over France in an anthropogenic scenario: model results and statistical correction according to observed values, *Glob. Planet. Change*, 57, 16–26, 2007.
- Déqué, M., Drevet, C., Braun, A., and Carilolle, D.: The ARPEGE/IFS atmosphere model: a contribution to the French community climate modelling, *Clim. Dynam.*, 10, 249–266, <https://doi.org/10.1007/BF00208992>, 1994.
- Dokulil, M. T.: Impact of climate warming on European inland waters, *Inland Waters*, 4, 27–40, <https://doi.org/10.5268/IW-4.1.705>, 2013.
- Dossi, F., Leitner, P., Steindl, E., and Graf, W.: Der Einfluss der Wassertemperatur auf die benthische Evertebratenzönose in mittelgrossen Fließgewässern am Beispiel der Flüsse Lafnitz und Pinka (Burgendland, Steiermark) in Österreich, *Mitteilungsblatt für die Mitglieder des Vereins für Ingenieurbioökologie, Ingenieurbioökologie: Neue Entwicklungen an Fließgewässern, Hängen und Böschungen*, 1, 22–28, 2015.
- Egger, G., Drescher, A., Hohensinner, S., and Jungwirth, M.: Riparian vegetation model of Danube River (Machland, Austria): changes of processes and vegetation patterns, Conference Paper at the 6th International Symposium on Ecohydraulics, New Zealand, 18–23 February 2007.
- Ellenberg, H. and Leuschner, H.: *Vegetation Mitteleuropas mit den Alpen*, 6. Auflage, Verlag Eugen Ulmer, Stuttgart, XXIV + 1134 pp., 2012.
- Erickson, T. R. and Stefan, H. G.: Linear Air/Water Temperature Correlations For Streams During Open Water Periods, *Journal of Hydrologic Engineering*, July 2000, St. Anthony Falls Laboratory Technical Paper No. 604, Series A, 317–321, 2000.
- Garner, C.: Modeling the Effect of Riparian Shading on Water Temperature for Portions of the Carson River, Thesis, University of Nevada, Reno, USA, 2007.
- Garner, G., Malcolm, I. A., Sadler, J. P., and Hannah, D. M.: What causes cooling water temperature gradients in a forested stream reach?, *Hydrol. Earth Syst. Sci.*, 18, 5361–5376, <https://doi.org/10.5194/hess-18-5361-2014>, 2014.
- Garssen, A. G., Verhoeven, J. T. A., and Soons, M. B.: Effects of climate-induced increases in summer drought on riparian plant species: a meta-analysis, *Freshwater Biol.*, 59, 1052–1063, 2014.
- Gobiet, A., Kotlarski, S., Beniston, M., Heinrich, G., Rajczak, J., and Stoffel, M.: 21st century climate change in the European Alps – A review, *Sci. Total Environ.*, 493, 1138–1151, <https://doi.org/10.1016/j.scitotenv.2013.07.050>, 2014.
- Goler, R. A. and Formayer, H.: Temporal disaggregation of daily meteorological data to 15-minute intervals for use in hydrological models, in: EMS Annual Meeting Abstracts, Vol. 9, EMS2012-174-1, available at: <http://meetingorganizer.copernicus.org/EMS2012/EMS2012-174-1.pdf> (last access: 11 January 2018), 2012.
- Groom, J. D., Dent, L., Madsen, L. J., and Fleuret, J.: Response of western Oregon (USA) stream temperatures to contemporary forest management, *Forest Ecol. Manag.*, 262, 1618–1629, <https://doi.org/10.1016/j.foreco.2011.07.012>, 2011.
- Guldenschuh, M.: Longitudinal zonation of habitat parameters and fish species assemblages in the Austrian lowland rivers Lafnitz and Pinka, M.S. thesis, University of Natural Resources and Life Sciences, Vienna, 2015.

- Haiden, T., Kann, A., Wittmann, C., Pistotnik, G., Bica, B., and Gruber, C.: The Integrated Nowcasting through Comprehensive Analysis (INCA) System and Its Validation over the Eastern Alpine Region, *Weather Forecast.*, 26, 166–183, <https://doi.org/10.1175/2010WAF2222451.1>, 2011.
- Hannah, D. M., Malcolm, I. A., Soulsby, C., and Youngson, A. F.: A comparison of forest and moorland stream microclimate, heat exchanges and thermal dynamics, *Hydrol. Process.*, 22, 919–940, 2008.
- Haylock, M. R., Hofstra, N., Klein Tank, A. M. G., Klok, E. J., Jones, P. D., and New, M.: A European daily high-resolution gridded data set of surface temperature and precipitation for 1950–2006, *J. Geophys. Res.*, 113, D20119, <https://doi.org/10.1029/2008JD010201>, 2008.
- Heino, J., Virkkala, R., and Toivonen, H.: Climate change and freshwater biodiversity: detected patterns, future trends and adaptations in northern regions, *Biol. Rev.*, 84, 39–54, <https://doi.org/10.1111/j.1469-185X.2008.00060.x>, 2009.
- Holzappel, G., Weihs, P., and Rauch, H. P.: Use of the Shade-a-lator 6.2 model to assess the shading potential of riparian purple willow (*Salix purpurea*) coppices on small to medium sized rivers, *Ecol. Eng.*, 61P, 697–705, <https://doi.org/10.1016/j.ecoleng.2013.07.036>, 2013.
- IPCC: The Physical Science Basis, Contribution of Working Group I to the Fifth Assessment Report of the Intergovernmental Panel on Climate Change, in: *Climate Change 2013*, edited by: Stocker, T. F., Qin, D., Plattner, G.-K., Tignor, M. M. B., Allen, S. K., Boschung, J., Nauels, A., Xia, Y., Bex, V., and Midgley, P. M., Cambridge University Press, Cambridge, United Kingdom and New York, NY, USA, 1535 pp., 2013.
- Johnson, S.: Stream temperature: scaling of observation and issues for modelling, *Hydrol. Process.*, 17, 497–499, 2003.
- Johnson, S. L.: Factors influencing stream temperatures in small streams substrate effects and a shading experiment, *Can. J. Fish. Aquat. Sci.*, 62, 913–923, 2004.
- Johnson, M. F. and Wilby, R. L.: Seeing the landscape for the trees: metrics to guide riparian shade management in river catchments, *Water Resour. Res.*, 51, 3754–3769, <https://doi.org/10.1002/2014WR016802>, 2015.
- Citation of dataset: Kalny, G., Dossi, F., Formayer, H., Graf, W., Rauch, H.P., Trimmel, H., Weihs, P., Melcher, A.: Abiotic and biotic data of the rivers Pinka and Lafnitz 2012–2014, <https://doi.org/10.13148/BFFWM8>, 2016.
- Kalny, G., Laaha, G., Melcher, A., Trimmel, H., Weihs, P., and Rauch, H. P.: The influence of riparian vegetation shading on water temperature during low flow conditions in a medium sized river, *Knowl. Manag. Aquat. Ecosyst.*, 418, 14 pp., <https://doi.org/10.1051/kmae/2016037>, 2017.
- Kiermeyer, P.: *Die Lebensbereiche der Gehölze*, Verlagsges, Grün ist Leben, 108 pp., 1995.
- Kothandaraman, V.: Analysis of Water Temperature Variations in Large Rivers, *ASCE Journal of Sanitary Engineering Division*, 97, 19–31, 1971.
- Koutsoyiannis, D.: Rainfall disaggregation methods: Theory and applications, in: *Proceedings of the Workshop on Statistical and Mathematical Methods for Hydrological Analysis*, Università degli Studi di Roma La Sapienza, Rome, 1–23, 2003.
- Kurylyk, B. L., MacQuarrie, K. T. B., Caissie, D., and McKenzie, J. M.: Shallow groundwater thermal sensitivity to climate change and land cover disturbances: derivation of analytical expressions and implications for stream temperature modeling, *Hydrol. Earth Syst. Sci.*, 19, 2469–2489, <https://doi.org/10.5194/hess-19-2469-2015>, 2015.
- Kysel, J., Kalvová, J., and Květoň, V.: Heat waves in the south Moravian region during the period 1961–1995, *Stud. Geophys. Geod.*, 44, 57–72, 2000.
- Leach, J. A. and Moore, R. D.: Above-stream microclimate and stream surface energy exchanges in a wildfire-disturbed riparian zone, *Hydrol. Process.*, 24, 2369–2381, <https://doi.org/10.1002/hyp.7639>, 2010.
- Ledochowski, V.: Changes of riparian vegetation and river morphology, as well as its influence on the water temperature at the river Pinka, Master thesis at the University of Natural Resources and Life Sciences, Vienna, 2014.
- Lexer, M. J., Rabitsch, W., Grabherr, Dokulil, M., Dullinger, S., Eitzinger, J., Englisch, M., Essl, F., Gollmann, G., Gottfried, M., Graf, W., Hoch, G., Jandl, R., Kahrer, A., Kainz, M., Kirisits, T., Netherer, S., Pauli, H., Rott, E., Schleper, C., Schmidt-Kloiber, A., Schmutz, S., Schopf, A., Seidl, R., Vogl, W., Winkler, H., and Zechmeister, H.: Der Einfluss des Klimawandels auf die Biosphäre und Ökosystemleistungen/Climate Change Impact on the Biosphere and Ecosystem Services, in: *Österreichischer Sachstandsbericht Klimawandel/Austrian Assessment Report 2014 (AAR14)*, Austrian Panel on Climate Change (APCC), Verlag der Österreichischen Akademie der Wissenschaften, Wien, Österreich, 468–556, 2014.
- Li, G., Jackson, C. R., and Kraseski, K. A.: Modeled riparian stream shading: Agreement with field measurements and sensitivity to riparian conditions, *J. Hydrol.*, 428/429, 142–151, <https://doi.org/10.1016/j.jhydrol.2012.01.032>, 2012.
- Logez, M., Bady, P., Melcher, A., and Pont, D. A.: continental-scale analysis of fish assemblage functional structure in European rivers, *Ecography*, 36, 80–91, 2013.
- Mader, H., Steidl, T., and Wimmer, R.: *Ablussregime österreichischer Fließgewässer*, Umweltbundesamt/Federal Environment Agency – Austria, Wien, 1996.
- Magnuson, J. J., Crowder, L. B., and Medvick, P. A.: Temperature as an Ecological Resource, *Am. Zool.*, 19, 331–343, 1979.
- Maheu, A., Caissie, D., St-Hilaire, A., and El-Jabi, N.: River evaporation and corresponding heat fluxes in forested catchments, *Hydrol. Process.*, 28, 5725–5738, <https://doi.org/10.1002/hyp.10071>, 2014.
- Matulla, C., Schmutz, A., Melcher, A., Gerersdorfer, T., and Haas, P.: Assessing the impact of a downscaled climate change simulation on the fish fauna in an Inner-Alpine River, *Int. J. Biometeorol.*, 52, 127–137, 2007.
- Matulla, C., Schöner, W., Alexandersson, H., Storch, H., and Wang, X. L.: European storminess: late nineteenth century to present, *Clim. Dynam.*, 31, 125–130, <https://doi.org/10.1007/s00382-007-033-y>, 2008.
- Melcher, A., Pletterbauer, F., Kremser, H., and Schmutz, S.: Temperaturansprüche und Auswirkungen des Klimawandels auf die Fischfauna in Flüssen und unterhalb von Seen, *Österreichische Wasser- und Abfallwirtschaft*, 65, 408–417, <https://doi.org/10.1007/s00506-013-0118-y>, 2013.
- Melcher, A., Dossi, F., Wolfram Graf, Guldenschuh, M., Holzappel, G., Lautsch, E., Leitner, P., Schaufler, K., Seebacher, M., Trimmel, H., Weihs, P., and Rauch, H. P.: Assessment of aquatic habi-

- availability and climate change effects in medium sized rivers, 10th ISE Trondheim, Norway, 2014.
- Melcher, A., Pletterbauer, F., Guldenschuh, M., Rauch, P., Schaufler K., Seebacher, M., and Schmutz S.: Einfluss der Wassertemperatur auf die Habitatpräferenz von Fischen in mittelgroßen Flüssen, *Mitteilungsblatt für die Mitglieder des Vereins für Ingenieurbioogie, Ingenieurbioogie: Neue Entwicklungen an Fließgewässern, Hängen und Böschungen*, 1, 15–21, 2015.
- Melcher, A., Kalny, G., Dossi, F., Formayer, H., Graf, W., Pletterbauer, F., Schaufler, K., Trimmel, H., Weihs, P., and Rauch, H. P.: Der Einfluss der Ufervegetation auf die Wassertemperatur unter gewässertypspezifischer Berücksichtigung von Fischen und benthischen Evertebraten am Beispiel von Lafnitz und Pinka, *Österreichische Wasser- und Abfallwirtschaft*, <https://doi.org/10.1007/s00506-016-0321-8>, 2016.
- Mohseni, O., Stefan, H. G., and Erickson, T. R.: A nonlinear regression model for weekly stream temperatures, *Water Resour. Res.*, 34, 2685–2692, 1998.
- Moore, R. D., Spittlehouse D. L., and Story, A.: Riparian microclimate and stream temperature response to forest harvesting: a review, *J. Am. Water Res. Assoc.*, 41, 813–834, 2005.
- Muhar, S., Poppe, M., Egger, G., Schmutz, S., and Melcher, A.: Flusslandschaften Österreichs: Ausweisung von Flusslandschaftstypen anhand des Naturraums, der Fischfauna und der Auenvegetation. Bundesministerium für Bildung, Wissenschaft und Kultur, Wien, 2004.
- Mühlmann, H.: Leitfaden zur hydromorphologischen Zustandserhebung von Fließgewässern, Bundesministerium für Land- und Forstwirtschaft, Umwelt und Wasserwirtschaft, Wien, 2010.
- Nachtnebel, H. P., Dokulil, M., Kuhn, M., Loiskandl, W., Sailer, R., and Schöner, W.: Der Einfluss des Klimawandels auf die Hydrosphäre/Climate Change Impact on the Hydrosphere, in: *Österreichischer Sachstandsbericht Klimawandel/Austrian Assessment Report 2014 (AAR14)*, Austrian Panel on Climate Change (APCC), Verlag der Österreichischen Akademie der Wissenschaften, Wien, Österreich, 411–466, 2014.
- Pahr, A.: Geologische Karte der Republik Österreich, Blatt 137 Oberwart, Geologische Bundesanstalt, Wien, 1984.
- Parker, F. L. and Krenkel, P. A.: Thermal pollution: status of the art, Department of Environmental and Resource Engineering, Vanderbilt University, Nashville, TN, 1969.
- Pletterbauer, F., Melcher, A. H., Ferreira, T., and Schmutz, S.: Impact of climate change on the structure of fish assemblages in European rivers, *Hydrobiologia*, 744, 235–254, <https://doi.org/10.1007/s10750-014-2079-y>, 2015.
- Primack, A. G. B.: Simulation of climate-change effects on riparian vegetation in the Pere Marquette River, Michigan, *Wetlands*, 20, 538–547, 2000.
- Radu, R., Déqué, M., and Somot, S.: Spectral nudging in a spectral regional climate model, *Tellus*, 60, 898–910, 2008.
- Rivaes, R. P., Rodríguez-González P. M., Terreira, M.T. Pinheiro, A. N., Politti, E., Egger, G., García-Arias, A., and Francés, F.: Modeling the Evolution of Riparian Woodlands Facing Climate Change in Three European Rivers with Contrasting Flow Regimes, *PLOS ONE*, 9, e110200, <https://doi.org/10.1371/journal.pone.0110200>, 2014.
- Roeckner, E., Bäuml, G., Bonaventura, L., Brokopf, R., Esch, M., Giorgetta, M., Hagemann, S., Kirchner, I., Kornblueh, L., Manzini, E., Rhodin, A., Schlese, U., Schulzweida, U., and Tompkins, A.: The atmospheric general circulation model ECHAM 5, PART I: Model description, Max Planck Institute for Meteorology, Report No. 349, 141 pp., 2003.
- Roeckner, E., Brokopf, R., Esch, M., Giorgetta, M., Hagemann, S., Kornblueh, L., Manzini, E., Schlese, U., and Schulzweida, U.: The atmospheric general circulation model ECHAM5 – Part II: Sensitivity of simulated climate to horizontal and vertical resolution, Max Planck Institute for Meteorology, Report No. 354, 65 pp., 2004.
- Roloff, A. and Bärtels, A.: *Flora der Gehölze – Bestimmung, Eigenschaften, Verwendung*, Ulmer, Stuttgart, 847 pp., 2006.
- Rutherford, J. C., Blackett, S., Blackett, C., Saito, L., and Davies-Colley, R. J.: Predicting the effects of shade on water temperature in small streams, *New Zeal. J. Mar. Freshw.*, 31, 707–721, 1997.
- Salas, J. D., Delleur, J. W., Yevjevich, V., and Lane, E. L.: *Applied Modelling of Hydrological Time Series*, Water Resources Publications, Colorado, p. 484, 1980.
- San-Miguel-Ayanz, J., de Rigo, D., Caudullo, G., Houston Durrant, T., and Mauri, A. (Eds.): *European Atlas of Forest Tree Species*, Publication Office of European Union, Luxembourg, available at: <http://forest.jrc.ec.europa.eu/european-atlas-of-forest-tree-species/> (last access: 11 January 2018), 2016.
- Schaufler, K.: Water temperature effects on fish in pre-alpine, medium-sized rivers, M.S. thesis, University of Natural Resources and Life Sciences, Vienna, 2015.
- Schinegger, R., Trautwein, C., Melcher, A., and Schmutz, S.: Multiple human pressures and their spatial patterns in European running waters, *Water Environ. J.*, 26, 261–273, <https://doi.org/10.1111/j.1747-6593.2011.00285.x>, 2012.
- Settele, J., Scholes, R., Betts, R., Bunn, S. E., Leadley, P., Nepstad, D., Overpeck, J. T., and Taboada, M. A.: Global and Sectoral Aspects. Contribution of Working Group II to the Fifth Assessment Report of the Intergovernmental Panel of Climate Change, in: *Terrestrial and inland water systems. Climate Change 2014: Impacts, Adaptation, and Vulnerability*, edited by: Field, C. B., Barros, V. R., Dokken, D. J., Mach, K. J., Mastrandrea, M. D., Bilir, T. E., Chatterjee, M., Ebi, Estrada Y. O., Genova, R. C., Girma, B., Kissel, E. S., Levy, A. N., K. L., MacCracken, S., Mastrandrea, P. R., and White, L. L., Cambridge University Press, Cambridge, United Kingdom and New York, NY, USA, 271–359, 2014.
- Sinokrot, B. A. and Stefan, H. G.: Stream Temperature Dynamics: Measurements and Modeling, *Water Resour. Res.*, 29, 2299–2312, 1993.
- Skøien, J. O., Merz, R., and Blöschl, G.: Top-kriging – geostatistics on stream networks, *Hydrol. Earth Syst. Sci.*, 10, 277–287, <https://doi.org/10.5194/hess-10-277-2006>, 2006.
- Sridhar, V., Sansone, A. L., LaMarche, J., Dubin, T., and Lettenmaier, D. P.: Prediction of stream temperatures in forested watersheds, *J. Am. Water Res. Assoc.*, 40, 197–213, 2004.
- Steel, E. A. and Fullerton, A.: *Thermal Networks – Do You Really Mean It?*, StreamNotes – The Technical Newsletter of the National Stream and Aquatic Ecology Center, United States Department of Agriculture, Fort Collins, Colorado, November, 2017.
- Trimmel, H., Gagneux, C., Kalny, G., and Weihs, P.: Application of the model “Heat Source” to assess the influence of meteorological components on stream temperature and simulation ac-

- curacy under heat wave conditions, *Meteorol. Z.*, 25, 389–406, <https://doi.org/10.1127/metz/2016/0695>, 2016.
- Trimmel H., Kalny G., Dossi F., Formayer H., Graf W., Leitner P., Leidinger D., Nadeem I., Rauch H. P., Weihs P., and Melcher A.: Abiotic and biotic data of the rivers Pinka and Lafnitz 2012–2014, *Freshwater Metadata Journal*, 22, 1–12, <https://doi.org/10.15504/fmj.2017.22>, 2017.
- van Vliet, M. T. H., Ludwig, F., Zwolsman, J. J. G., Weedon, G. P., and Kaba, P.: Global river temperatures and sensitivity to atmospheric warming and changes in river flow, *Water Resour. Res.*, 47, W02544, <https://doi.org/10.1029/2010WR009198>, 2011.
- van Vliet, M. T. H., Wiberg, D., Leduc, S., and Riahi, K.: Power-generation system vulnerability and adaptation to changes in climate and water resources, *Nature Climate Change*, 6, 375–380, <https://doi.org/10.1038/nclimate2903>, 2016.
- Webb, B. W. and Nobilis, F.: Long term water temperature trends in Austrian rivers, *Hydrol. Sci. J.*, 40, 83–96, <https://doi.org/10.1080/02626669509491392>, 1995.
- Webb, B. W. and Nobilis, F.: Long-term perspective on the nature of the air-water temperature relationship: a case study, *Hydrol. Process.*, 11, 137–147, 1997.
- Webb, B. W., Hannah, D. M., Moore, D. R., Brown, L. E., and Nobilis, F.: *Advances in Stream and River Temperature Research*, *Hydrol. Process.*, 22, 902–918, 2008
- Wenger, S. J., Som, N. A., Dauwalter, D. C., Isaak D. J., Neville, H. M., Luce, C. H., Dunham, J. B., Young M. K., Fausch, K. D., and Rieman, B. E.: Probabilistic accounting of uncertainty in forecasts of species distributions under climate change, *Glob. Change Biol.*, 19, 3343–3354, <https://doi.org/10.1111/gcb.12294>, 2013.
- WRG: Wasserrechtsgesetz (water right law), BGBl. Nr. 215/1959, <https://www.ris.bka.gv.at/GeltendeFassung.wxe?Abfrage=Bundesnormen&Gesetzesnummer=10010290> (last access: 11 January 2018), 1959.



Potential increase of solar irradiation and its influence on PV facades inside an urban canyon by increasing the ground-albedo



Michael Revesz^{a,b,*}, Sandro Michael Oswald^b, Heidelinde Trimmel^b, Philipp Weihs^b, Shokufeh Zamini^a

^a AIT Austrian Institute of Technology GmbH, Center for Energy, Photovoltaic Systems, Giefinggasse 2, 1210 Vienna, Austria

^b University of Natural Resources and Life Sciences, Department of Water-Atmosphere-Environment, Institute of Meteorology, Gregor-Mendel-Straße 33, 1180 Vienna, Austria

ARTICLE INFO

Keywords:

Photovoltaics
Facade-integrated photovoltaics
Ground-reflected irradiance
Urban canyon

ABSTRACT

Due to the large demand for electricity in cities, photovoltaic (PV) installations inside the urban environment will increase in the near future. It is known that the yield of PV systems on facades can be increased by increasing the ground-albedo. White surfaces are also proposed for urban heat island mitigation. Thus, increasing the ground-albedo inside the urban environment has multiple advantages. However, solar potential simulation tools are not yet designed for simulating in an urban canyon. The ground-reflected irradiance is either neglected or the known approximation is applied. The potential contribution of ground-reflected irradiance to the electricity production of PV facades in an urban canyon is not yet investigated. Therefore, measurements were made in a street canyon to show the potential effect of an increased ground-albedo on the power output of south-facing, vertically mounted PV modules and the total in-plane irradiance. Further, the potential increase of PV yield on a reference point was estimated, when asphalt on an approximately 15 m wide street canyon was replaced with a highly reflective concrete and an albedo of 0.5. For the latter case, at a wall point 12 m above ground and with a ground view factor of 0.16, it was found that during an eleven days reference period in August 2016, in Vienna, the PV yield increases by 7.3%.

1. Introduction

Today, many governments strive to increase the use of renewable energies, particularly photovoltaics (PV). Given that most electricity is consumed in cities, it is proposed that PV systems will play a more important role in urban environments in the future. Decentralised systems can then provide electricity close to where it is consumed (Fechner et al., 2016; IEA, 2014; Krawietz et al., 2016). In Vienna, for example, the city council already addressed those topics and developed strategies to increase the amount of PV installations in the city (Dvorak, 2016).

In the past, several institutions have created tools to estimate the solar potential of residential areas (Freitas et al., 2015). In early and simple solar potential estimations only roofs were considered (Freitas et al., 2015). The urban solar potential algorithm SOL was one of the first algorithms to address the solar potential on walls in addition to roofs. However, ground reflections are neglected in SOL (Redweik et al., 2013). Only more recently have tools been developed that include the ground-reflected irradiance on facades, e.g. SEBE (Solar Energy on

Building Envelope) (Lindberg et al., 2015).

Usually, the ground-reflected irradiance is estimated by the term $1/2 \rho G (1 - \cos \beta)$, where ρ is the albedo, β is the tilt of the receiving plane and G is the global horizontal irradiance. This approach assumes an isotropic reflecting and infinitely large ground surface and is argued to be sufficiently accurate (Ineichen et al., 1990). Nevertheless, the authors of this paper argue that this approach overestimates the contribution of ground-reflected irradiance to the total irradiance on facades inside an urban canyon. The obvious reason is that the ground view factor is significantly limited inside an urban canyon, which is inconsistent with the assumption of an infinitely large ground area.

Previous studies regarding the effect of ground-albedo on the performance of PV modules focus on either the spectral effects of albedo or the effect of snow (Andrews and Pearce, 2013, 2012; Brennan et al., 2014). Additional potential PV yield due to increasing ground-albedo has not yet been addressed.

In the meantime, urban climatologists have been researching methods to mitigate urban heat island effects. Adding white surfaces to cities is one of many suggested methods to reduce the heat island effect

* Corresponding author at: AIT Austrian Institute of Technology GmbH, Center for Energy, Photovoltaic Systems, Giefinggasse 2, 1210 Vienna, Austria.
E-mail address: revesz.michael@gmail.com (M. Revesz).

in urban environments (Mohajerani et al., 2017; Santamouris, 2014; Taha, 1997). Technological developments on reflective pavements and their effects are discussed in Qin (2015a), Santamouris (2013). Positive and negative effects of reflective pavements inside urban canyons are discussed as well. Examples include their effect on cooling and heating loads in buildings (Yaghoobian and Kleissl, 2012) and their effect on the thermal and visual comfort of pedestrians (Rosso et al., 2016). Preliminary results of a recent case study within the PVOPTI-Ray project also show that increasing the ground-albedo up to 0.56 does not significantly effect human thermal comfort (Revesz et al., 2017).

Considering the reported benefits of an increased albedo of the ground surface to the urban climate, the shortcoming in irradiance estimation for predicting the PV power output in an urban environment, as described before, leads to two important questions: How much irradiance is realistically reflected from the ground onto a wall inside an urban canyon? And how much does increasing the ground-albedo increase the solar irradiation and thus increase the yield of PV facades inside an urban canyon? This work attempts to address these questions.

For this purpose, gains were measured at the University of Natural Resources and Life Sciences (BOKU) in Vienna during August 2016. In addition, the potential effect of replacing asphalt with highly reflecting concrete on the total irradiance inside an urban canyon was estimated.

2. Methods

Measurements were made to investigate the potential increase of electricity production of vertically mounted PV modules due to an increase in ground reflectance. Those measurements validate a simple method to estimate the ground-reflected irradiance on a wall point. In addition, simulations were performed assuming a more reflective ground surface material. Whenever irradiance was estimated the diffuse sky irradiance and the irradiance reflected from the ground or the building facade (except for the glass facade) were assumed to be isotropic.

2.1. Measurements inside an urban canyon

The area between two buildings of the University of Natural Resources and Life Sciences (BOKU) in Vienna, Austria, was used for

measurements. Fig. 1 shows the surrounding of the measurement site. The location “C” marks the position of measurement equipment inside the street canyon. Facing south, three vertical multicrystalline silicon PV modules and one vertical irradiance (G_v) sensor were mounted. Further, the horizontal irradiance (G_h), ambient air temperature (T_a), and module temperature (T_m) on each of the PV modules’ backside were measured. Fig. 2 shows the installed equipment, which was mounted about 3.5 m above ground. BP solar SX 10 M modules were used and their short circuit current (I_{sc}) was measured. The vertical and horizontal irradiance sensors were EMS 11 which are silicon diode irradiance sensors with a calibration error of max. 7% (EMS Brno, 2016) and are expected to have a similar spectral response as the PV modules. The data-logger for those two irradiance sensors had a resolution corresponding to about 1.4 W m^{-2} and 1.8 W m^{-2} respectively. Within this work the position of the vertical irradiance sensor is referred to as “wall point”.

On the roof of Schwackhöfer-Haus the global horizontal irradiance (G) and the direct normal irradiance (DNI) were measured, using a EKO MS-802 pyranometer and Kipp & Zonen CHP-1 pyrheliometer, respectively. Their position is marked in Fig. 1 with “R”. The measurements of both devices were compared to measurements within the ARAD network (Olefs et al., 2016). The diffuse horizontal irradiance (DHI) component was estimated from G and DNI . All values were measured at 5 s intervals and aggregated by the data-loggers to record a 1-minute mean value. For the evaluation of the gain the data was further aggregated to 5-minute mean values.

The ground-albedo was measured 80 cm above the ground using two silicon diode irradiance sensors of type EMS 11 (by EMS Brno), one oriented upwards and one downwards (see Fig. 2(a)). In this configuration the influence of the equipment itself on the reflected radiation is negligible, while providing a good estimate of ground-albedo of a brighter surface with limited surface area. Further, Apogee SN-500 were used to determine the albedo of the non-glass facade and for occasional measurement of incoming irradiance onto the centre point of the plastered facade, opposite of the PV modules.

Measurements were performed for a period of one month in August 2016. During the measurements, the “low ground-albedo” condition was for asphalt in between the two buildings with $\rho = 0.13$. Several times, “high ground-albedo” measurements were made by placing

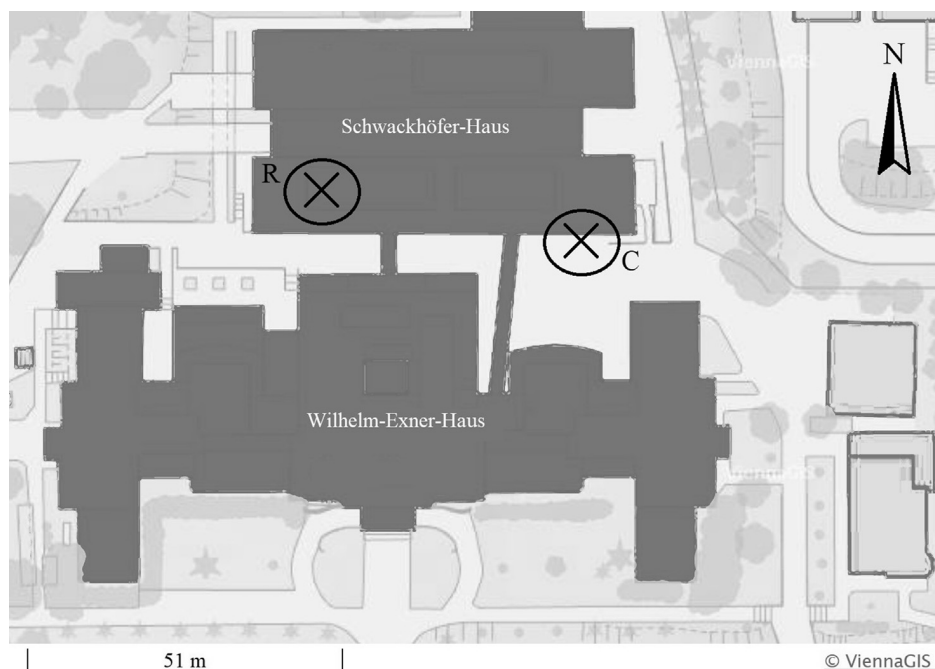


Fig. 1. Measurement site at University of Natural Resources and Life Sciences (BOKU) in Vienna between Schwackhöfer-Haus and Wilhelm-Exner-Haus (lat. 48.237 N, lon. 16.332 E). The location of the PV modules and the vertical irradiance sensor in the canyon is labelled with “C” and the location for the irradiance measurement on the roof is labelled with “R”. Source of base-map: www.wien.gv.at/viennagis/

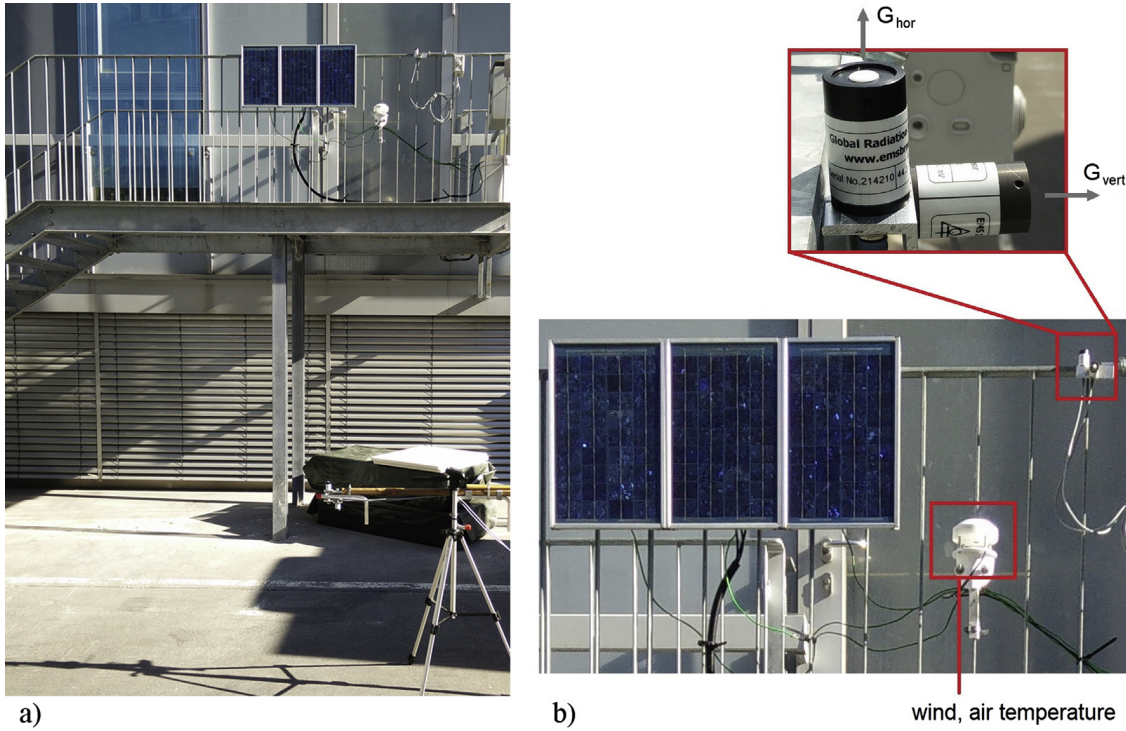


Fig. 2. Measurement equipment: (a) mounting in the canyon in front of Schwackhöfer-Haus; (b) enlarged view on the measurement equipment (PV modules, irradiance sensors, wind speed, wind direction and air temperature).



Fig. 3. View of south-facing PV modules taken with a camera with a fish-eye lens. The placement of the white Styrofoam panels in front of the PV modules is shown.

30 m² of white painted Styrofoam panels with $\rho = 0.77$ on the asphalt in front of the PV modules (see Fig. 3).

2.2. Evaluation of the irradiance gain

In this study the ground-albedo was temporary altered at the same location. Due to temporal variations of the humidity, aerosol content, dust and clouds the irradiance levels varied with time (Ineichen and Perez, 2002; Remund et al., 2003). Therefore, it was required to use a

reference irradiance for comparison with the measured vertical irradiance during different days and to evaluate the gain due to different ground-albedos.

For this purpose, the vertical irradiance in the canyon (at the position of the vertical irradiance sensor) was estimated from the irradiance components that were measured on the roof. As suggested by e.g. Qin (2015b) the contribution from multiple reflections was considered, herein up to the second degree. Thus, the total vertical irradiance was calculated, using:

$$G_v = G_{sky} + \sum_i G_{gnd,i} \cdot f_{gnd,i} \cdot \rho_{gnd,i} + G_{b1} \cdot f_{b1} \cdot \rho_{b1} \quad (1)$$

where the first term G_{sky} refers to the direct and diffuse irradiance from the sun incident onto the wall point, the second term refers to the radiation reflected from the ground and the third term refers to the radiation reflected from the building on the opposite side of the canyon. In the second term a summation over sub-surfaces of the ground with different ground-albedos is used, if applicable, and it consists of the irradiance G_{gnd} received by the ground, the view factor $f_{gnd,i}$ of the ground's sub-area i that is visible to the wall point and the albedo $\rho_{gnd,i}$ of the i -th ground's surface. The variables in the third term with subscript $b1$ refer to the respective variables for the building opposing the PV modules. Here f_{b1} is the view factor of building $b1$ as seen by the wall point and ρ_{b1} is the albedo of the facade on building $b1$.

The irradiance received by the wall point from the sky is simply

$$G_{sky} = DNI \cdot \cos\theta + DHI \cdot f_{sky} \quad (2)$$

where θ is the solar angle of incidence on the tilted (in this case vertical) plane and f_{sky} is the sky view factor of the receiving wall point.

The irradiance received by the building $b1$ consists of contributions from the sky, the reflections from the ground (summation over different ground surfaces with different albedo, if applicable) and from the building with the receiving wall point (subscript $b2$) and is written as:

$$G_{b1} = G_{b1,sky} + \sum_i G_{gnd,sky} \cdot f_{b1,gnd,i} \cdot \rho_{gnd,i} + (G_{b2,sky} \cdot \rho_{b2}) \cdot f_{b1,b2} \quad (3)$$

where $G_{b1,sky}$ is the irradiance received by building b1 from the sky, $G_{gnd,sky}$ is the irradiance received by the ground surface from the sky, $f_{b1,gnd,i}$ is the view factor of the ground area i that is visible to the building b1, $\rho_{gnd,i}$ is the albedo of the ground area i , $G_{b2,sky}$ is the irradiance received by the building b2 from the sky, ρ_{b2} is a specular reflectance of the glass facade and $f_{b1,b2}$ is the view factor of the building b2 that is visible to the building b1. The following equations show the calculation of the irradiance onto the three relevant surfaces used in Eq. (3):

$$G_{b1,sky} = DHI \cdot f_{b1,sky}, \quad (3a)$$

$$G_{gnd,sky} = DNI \cdot \cos\theta_{gnd} \cdot sh + DHI \cdot f_{gnd,sky}, \quad (3b)$$

$$(G_{b2,sky} \cdot \rho_{b2}) = DNI \cdot \cos\theta_{b2} \cdot \rho_{b2,dif} + DHI \cdot f_{b2,sky} \cdot \rho_{b2,dif}, \quad (3c)$$

where $f_{b1,sky}$ is the sky view factor of b1, θ_{gnd} is the solar angle of incidence onto the ground, sh is a factor accounting for the fraction of shadow on the ground surface, $f_{gnd,sky}$ is the sky view factor of the ground, θ_{b2} is the solar angle of incidence onto the facade of b2, $f_{b2,sky}$ is the sky view factor of b2 and $\rho_{b2,dif}$ and $\rho_{b2,dif}$ are parameters referring to the specular reflectance for diffuse and direct irradiance from b2.

At last, the irradiance onto the ground's surfaces is calculated similarly to Eq. (3) as:

$$G_{gnd} = G_{gnd,sky} + G_{b1} \cdot f_{gnd,b1} \cdot \rho_{b1} + (G_{b2,sky} \cdot \rho_{b2}) \cdot f_{gnd,b2}, \quad (4)$$

where $G_{gnd,sky}$, G_{b1} and the term $(G_{b2,sky} \cdot \rho_{b2})$ are as calculated according to the Eqs. (3a), (3b) and (3c), respectively and $f_{gnd,b1}$ and $f_{gnd,b2}$ are the view factor of the buildings b1 and b2, respectively, that are visible to the ground.

All values of surface albedo were determined from measurements, except for the specular reflectance of the glass facade. The specular reflectance $\rho_{b2,dif}$ and $\rho_{b2,dif}$ were determined by linear regression to measured data and are the only parameters that had to be determined by other means than measurement. The view factors were determined from fish-eye images in a central point of the respective surface relative to the canyon or the position of the reference wall point. Further, it was assumed that the view factors are representative for the whole surface, although it is known that the view factors depend on the exact location on a surface. The shadow factor sh for the ground is set to 1 when the wall point is known to be in shadow. Otherwise, it is estimated to be around 0.5 for most of the time. For simplicity the shadow factor is assumed to be constant.

To calculate the gain of the irradiance at the wall point, the irradiance at the wall point was estimated for each of the two ground-surface conditions as described in Section 2.1 and using Eq. (1). The respective values for the ground's albedo were used in the estimations. The gain of the irradiance at the wall point (g_G) is then calculated as:

$$g_G = \frac{G_{v,sim}(\rho_{high})}{G_{v,sim}(\rho_{low})}, \quad (5)$$

where $G_{v,sim}(\rho_{high})$ is the vertical irradiance simulated at the wall point for the condition with the higher ground-albedo and $G_{v,sim}(\rho_{low})$ is the vertical irradiance simulated at the wall point for the condition with the lower ground-albedo. In addition, the gain is presented as the quotient of the respective irradiation over a given time.

2.3. Evaluation of the PV power gain

The gain in PV power output for a vertical, south-facing PV panel was evaluated by calculating the PV power at the PV module's maximum power point. As reference and for the assessment of the estimations' quality the PV power was calculated using the measured short circuit current. First, the effective irradiance was calculated according to King et al. (2004) as:

$$G_e = \frac{I_{sc}}{I_{sc,0} \cdot [1 + \alpha_{Isc} \cdot (T_m - T_0)]}, \quad (6)$$

where G_e is the effective irradiance, I_{sc} is the measured short circuit current, $I_{sc,0}$ is the short circuit current at reference condition of 1000 W/m^2 and $25 \text{ }^\circ\text{C}$, α_{Isc} is the temperature coefficient of the short circuit current, T_m is the module temperature (measured at the back of the PV module), and T_0 is the reference temperature of $25 \text{ }^\circ\text{C}$. Results referring to this method are called "measured".

Afterwards, the PV power was calculated according to the following formulas by King et al. (2004):

$$I_{mp} = I_{mp,0} \cdot [C_0 \cdot G_e + C_1 \cdot G_e^2] \cdot [1 + \alpha_{Imp} \cdot (T_m - T_0)], \quad (7)$$

$$V_{mp} = V_{mp,0} + C_2 \cdot N_s \cdot \delta(T_m) \cdot \ln(G_e) + C_3 \cdot N_s \cdot [\delta(T_m) \cdot \ln(G_e)]^2 + \beta_{Vmp} \cdot (T_m - T_0), \quad (8)$$

$$P_{mp} = I_{mp} \cdot V_{mp}, \quad (9)$$

where I_{mp} and V_{mp} are the current and the voltage of the PV module at its maximum power point, $I_{mp,0}$ and $V_{mp,0}$ are the current and the voltage at the modules maximum power point under a reference condition of 1000 W/m^2 and $25 \text{ }^\circ\text{C}$, α_{Imp} and β_{Vmp} are the temperature coefficients for the current and the voltage at the maximum power point, C_0 , C_1 , C_2 and C_3 are empirical coefficients determined for the PV module, $\delta(T_m)$ is the thermal voltage at T_m , N_s is the number of cells connected in series in a PV module, and P_{mp} is the electric power of the PV module at its maximum power point. All relevant PV module related coefficients are taken from a database available on <https://sam.nrel.gov/libraries> (Gilman, n.d.), except of $I_{sc,0}$, $I_{mp,0}$ and $V_{mp,0}$, which were determined in a laboratory for the PV modules in use.

Eqs. (7) and (8) were simplified by neglecting the influence of air-mass on the spectrum and the losses with increased angle of incidence. Further, the module backside temperature was used as the cell temperature. These effects will cancel as the ratio of two PV powers will be calculated for evaluating the gain.

For the evaluation of the gain in PV power, however, the effective irradiance in Eq. (6) was calculated from estimated irradiance at the wall point according to $G_e = G_v / (1000 \text{ W/m}^2)$. The irradiance used in this case was estimated using the irradiance components measured on the roof and as described in Section 2.2. Those values of PV power are referred to as being "simulated".

Finally, the PV power gain due to different ground-albedos was calculated as:

$$g_{PV} = \frac{P_{mp}(\rho_{high})}{P_{mp}(\rho_{low})}, \quad (10)$$

where $P_{mp}(\rho_{high})$ is the PV power resulting from the high albedo compared to $P_{mp}(\rho_{low})$, which is resulting from the lower albedo.

In addition, the gain is expressed as the quotient of the respective PV yields over a specified period. The yield is the energy produced (in units of Wh) divided by the nominal peak power (in units Wp) of the PV module under reference condition. Providing PV yields makes the results comparable for arbitrary PV installations. When PV power is stated in the results-section, the average value of the three PV modules was calculated and multiplied with the average peak power of the three PV modules under reference condition (9.2 W).

2.4. Evaluating the effect of highly reflective concrete

The measurements described previously show the impact of ground-reflected irradiance inside an urban canyon. However, they represent unrealistic conditions as the highly reflective surface had limited ground coverage. Therefore, the impact of highly reflective concrete which covers the entire ground surface of the urban canyon was estimated.

The new scenario was the same canyon as for the measurements

described above. The albedo for the asphalt was 0.13 and the albedo of the highly reflective concrete was assumed to be 0.50 (Krispel et al., 2017). The irradiation and the PV yield on a south-facing wall were estimated as described in Section 2.2 for a wall point 3.5 m above ground, corresponding to the position of the vertical irradiance sensor in the canyon, and for a wall point about 12 m above ground. The latter point was chosen because this is the point at the centre of the facade, for which fish-eye images were taken. Further, the installation of PV modules at that height and above is reasonable.

The irradiance data used was from the measurements described above. The irradiation and PV yield were estimated for the period 17. to 28. August 2016. In this period the sky conditions were clear sky, scattered clouds, as well as two days of overcast sky.

3. Results

3.1. Accuracy of the model

In the following the accuracy of the overall model and the two models for the irradiance onto the ground surface and onto a central point on the facade of the building b1, opposite of the wall point, are presented. In addition to the standard deviation and the mean bias error of the modelled data and the available measured data, also the deviation between the total irradiation over the period of available data is stated.

The estimated irradiance onto the building b1, calculated using Eq. (3), has a standard deviation of $\sigma = 8.0 \text{ W m}^{-2}$ and a mean bias error of -2.4 W m^{-2} . The difference to the total measured irradiation is -4.1% . For the estimated irradiance onto the ground-surface the modelled (see Eq. (4)) compared to the measured data has a standard deviation of $\sigma = 38 \text{ W m}^{-2}$ and a mean bias error of 3.3 W m^{-2} . In this case, the difference to the total measured irradiation is 2.0% .

The final model for the irradiance onto the wall point of interest (see Eq. (1)) exhibits a standard deviation of $\sigma = 20 \text{ W m}^{-2}$ and a mean bias error of -5.0 W m^{-2} . Over the period from 13. until 28. August 2016 the total estimated irradiation is 4.9% lower than the measured irradiation. The comparison of the estimated data with the measured data is shown in Fig. 4, where the points with residuals larger than the residuals' standard deviation are marked as dark-orange triangles. The points with extreme deviation (see the area at the bottom of the figure) relate to points during the transition when the wall point becomes shaded or the shading ends.

For comparison, the irradiance onto the wall point was estimated ignoring second degree reflections. In that case, the standard deviation was $\sigma = 21 \text{ W m}^{-2}$ and the mean bias error -8.5 W m^{-2} . More significant was the difference for the total estimated irradiation, which is 6.9% lower than the measured irradiation.

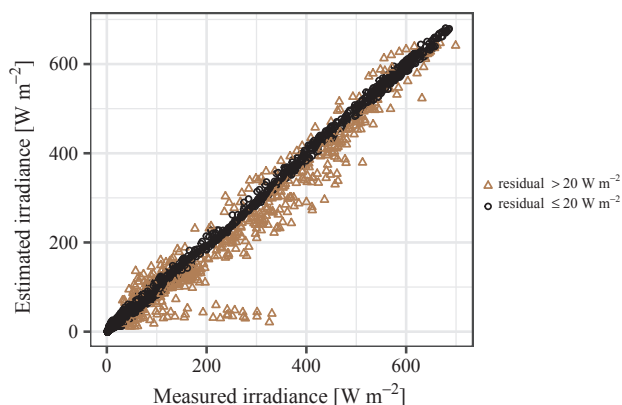


Fig. 4. Estimated irradiance versus the measured irradiance. Dark-orange triangles depict data points those absolute residual is larger than the residual standard deviation of the model.

3.2. Measurements

The results for the evaluation of the measurements are presented here. Useable data is available from 13. to 28. August 2016. For this period the irradiance was estimated once for a ground with bare asphalt and with an albedo of 0.13. In addition, the irradiance was estimated for the same period with Styrofoam panels with an albedo of 0.77 being placed on the ground, as described in Section 2.1. Within this period the total irradiation onto the south-facing wall point increased from 36.6 kWh m^{-2} to 41.7 kWh m^{-2} due to the described change of the ground's albedo. This corresponds to an increase by 13.8% . Looking only at a four-days period of clear sky, from 25. to 28. August 2016, by increasing the ground's albedo the irradiation in that period increased by 12.0% from 12.0 kWh m^{-2} to 13.4 kWh m^{-2} .

For the PV modules the estimated gain in energy yield due to increasing the ground's albedo is 3.15 Wh/Wp for the period 13. to 28. August 2016. This corresponds to a gain by 12.8% . For the four-days period of clear sky the energy yield is estimated to increase by 1.19 Wh/Wp , which is a gain by 11.3% . The relative gain in PV yield is slightly lower than the gain in irradiation. This is because of the PV module's temperature coefficient. Increased irradiation causes a higher temperature inside the PV module and thus, reduces the PV module's power.

Fig. 5 shows the measured irradiance on the wall point for 25. to 28. August 2016 in comparison with the estimated irradiance for the cases of low ground-albedo (asphalt) and the increased ground-albedo. During the first two days in this figure, the ground surface is only asphalt. Thus, the estimated irradiance for the same ground condition corresponds well to the measurement. Similarly, for the other two days the measured irradiance is well represented by the estimated irradiance for the respective ground-surface condition, where white Styrofoam was placed on the ground. Though, one can also see that during morning and afternoon the deviation between measurement and estimation is larger than around noon. Fig. 6 shows the gain in irradiance for those four days of clear sky; Fig. 6(a) the absolute gain and (b) the relative gain. As expected, the relative difference is smaller the higher the portion of direct irradiance.

In Fig. 7 the increase of PV power due to the two different conditions of ground-albedo is shown. The corresponding curves of the simulated PV power for each of those two conditions are shown in Fig. 7(a). In addition, the "measured" PV power, which was calculated based on the measured I_{sc} , is shown in Fig. 7(a). The gain g_{PV} , which was calculated from the simulated PV power for the condition with lower albedo and the condition with larger albedo, is shown in Fig. 7(b).

3.3. Effect of highly reflective concrete

In the following, the potential effect of highly reflective concrete compared to asphalt is presented. The two scenarios that were simulated are described in Section 2.4. Based on irradiance measurements between 17. and 28. August 2016 the following results were found when increasing the ground's albedo: The total irradiation on a south-facing wall point 12 m above ground was estimated to increase by 7.4% compared to a total of 37.5 kWh m^{-2} for asphalt. The PV yield was estimated to increase for the same case by 7.3% compared to the case of asphalt with a total yield of 32.8 Wh/Wp .

For the wall point in only 3.5 m above ground the gain is significantly larger, as expected. It is around 20% compared to asphalt as a ground-surface, for which the total irradiation is 28.1 kWh m^{-2} and the PV yield is 24.2 Wh/Wp . Nevertheless, at a wall point in 12 m above ground and even with asphalt, the PV yield would still be larger than at the lower wall point with increased ground-albedo.

Figs. 8 and 9 show the results for each day in this period. In Fig. 8(a) one can see the PV yield for each of the assumed ground-albedos, on the left in 12 m above ground and on the right in 3.5 m above ground.

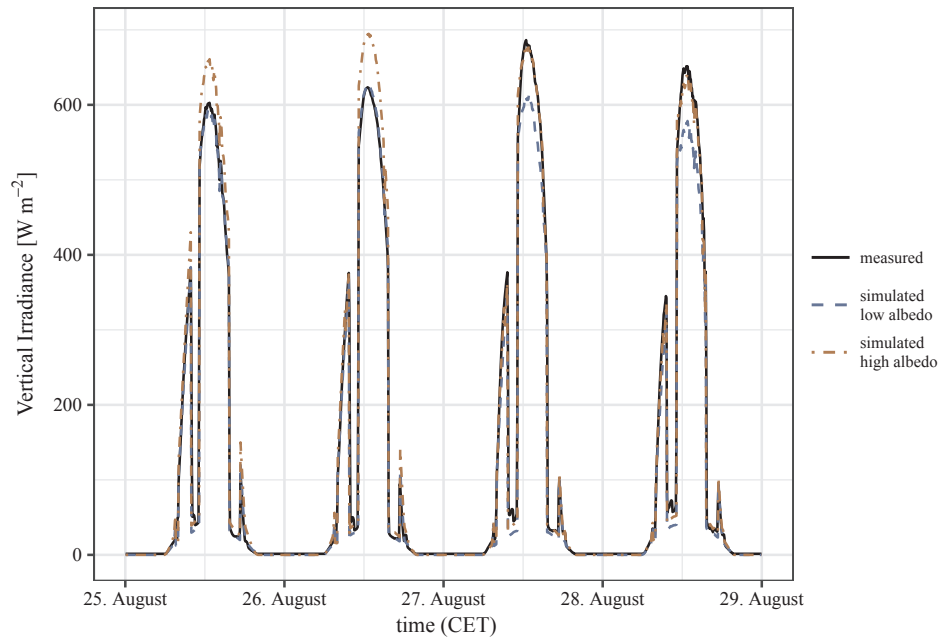


Fig. 5. Comparison of measured vertical irradiance with estimated irradiance for different conditions of the ground’s albedo. The low albedo is 0.13 for asphalt during 25. – 26. August 2016 and the high albedo is asphalt with partial Styrofoam cover with an albedo of 0.77 during 27. – 28. August 2016 in Vienna.

Fig. 8(b) shows the resulting absolute gain in PV yield due to increasing the ground-albedo from 0.13 to 0.50. A comparison of days with overcast sky and clear sky shows that the benefit of the higher albedo for overcast sky is around half in 12 m above ground, despite the yield being only a quarter to a third. In Fig. 9 the absolute gain in irradiation is shown for those two wall points and shows similar results as the PV yield. This result clearly shows that the potential gain in PV yield inside an urban canyon is significant if bright concrete is chosen for the ground surface in cities.

4. Discussion

The chosen method for evaluation of the gain of vertical irradiance and PV power due to an increased ground-albedo seems reasonable under the present conditions. An advantage was the use of fish-eye images, taken from various surfaces inside the urban canyon and the availability of measurement data for irradiance onto ground of building surfaces. This allowed estimations with only a limited amount of model-calibration being required.

The rather large standard deviation of the residuals with 20 W m^{-2} for the wall point of interest can clearly be attributed to the transition

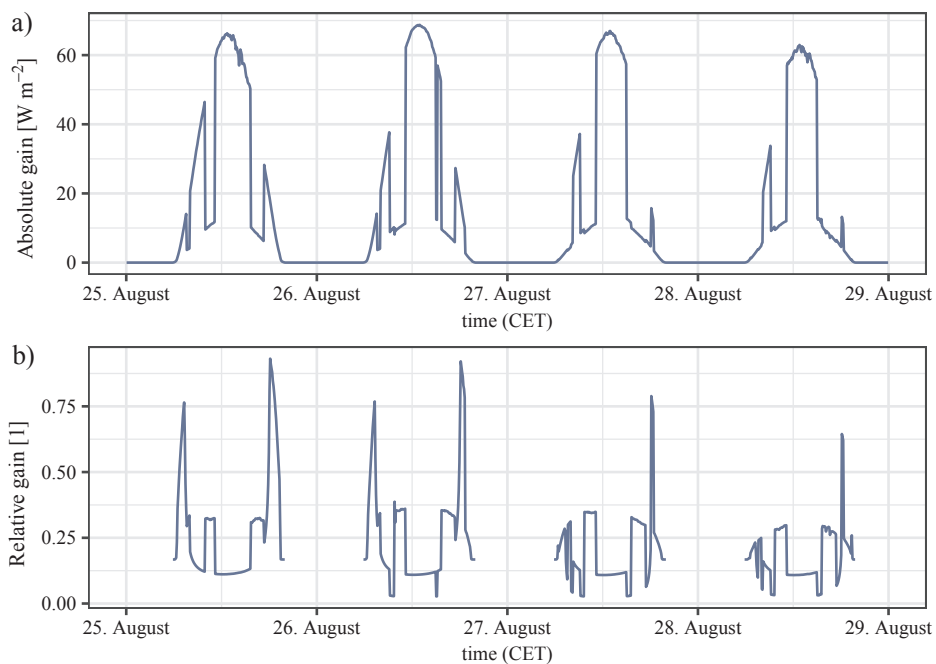


Fig. 6. Increase of irradiance on a south-facing wall point due to an increase of the ground’s albedo. Based on estimated irradiance values in Vienna. 25. – 26. August 2016: asphalt with an albedo of 0.13; 27. – 28. August 2016: Styrofoam with an albedo of 0.77 on asphalt. a) Absolute difference; b) relative difference (gain).

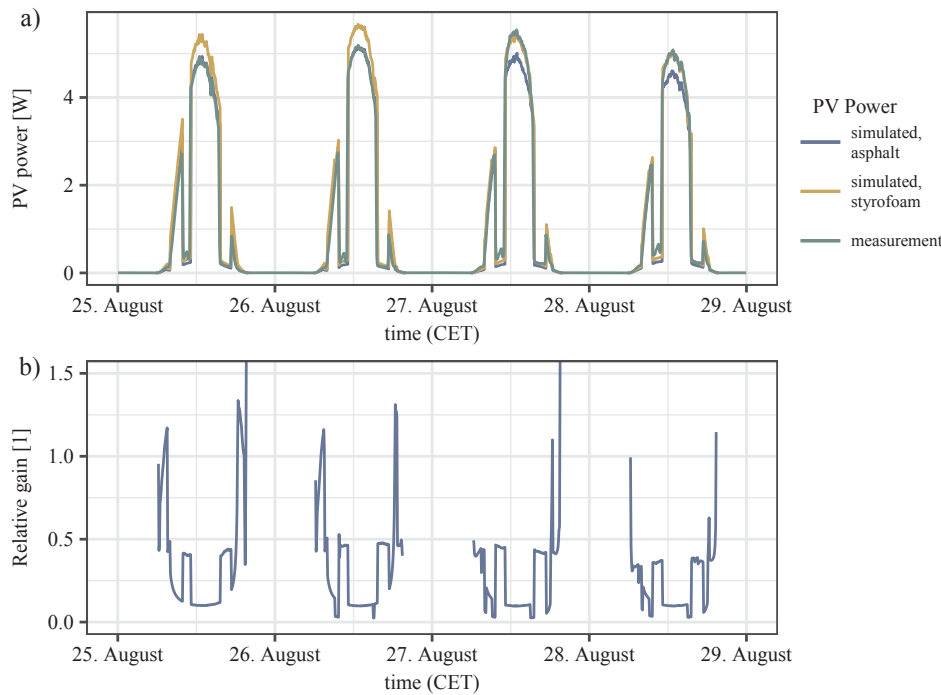


Fig. 7. Comparison of the power of a vertical, south-facing PV module (nominal power of 9.2 W) for different conditions of ground-albedo. The low albedo is 0.13 for asphalt (measured 25. – 26. August 2016 in Vienna) and the higher albedo is asphalt with partial Styrofoam cover with an albedo of 0.77 (measured 27. – 28. August 2016). (a) Power output calculated from estimated vertical irradiance (blue and orange) and from measured I_{sc} (green); (b) relative gain.

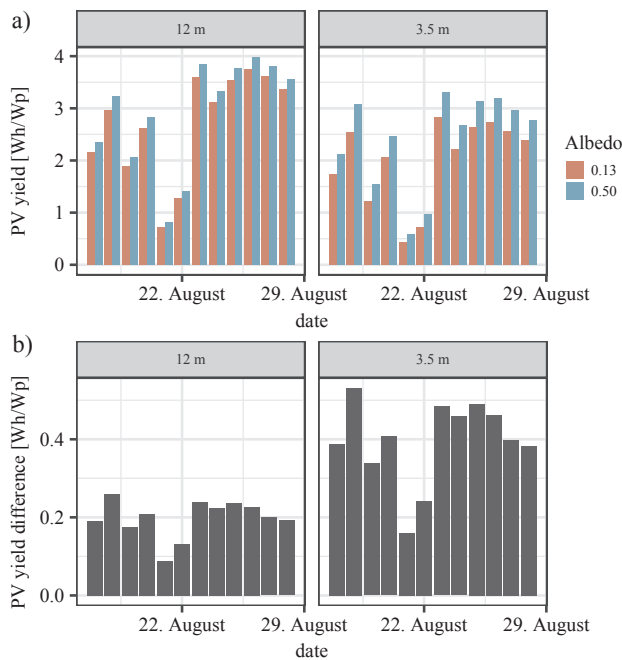


Fig. 8. Estimated PV yield on a south-facing wall point for a ground-albedo of 0.13 and 0.50 and the resulting gain. Based on irradiance measurements in Vienna, between 17. and 28. August 2016. Left: at wall point in 3.5 m above ground; right: in 12 m above ground. (a) Absolute PV yield; (b) resulting gain.

between sunlit and shaded. For the estimations it was not possible to clearly define this transition phases. Though, the definition of shading was required as the pyranometer and pyrhelimeter on the roof, which were used for estimating the irradiance in the canyon, were not shaded in contrast to the irradiance sensor and PV modules in the canyon.

In Section 3.2 it was noted that in the morning and the afternoon the deviation between measurement and estimation is relatively larger than around mid-day. It is believed this is due to the difficulty of accurately estimating the portion of ground that is shaded by the building in the

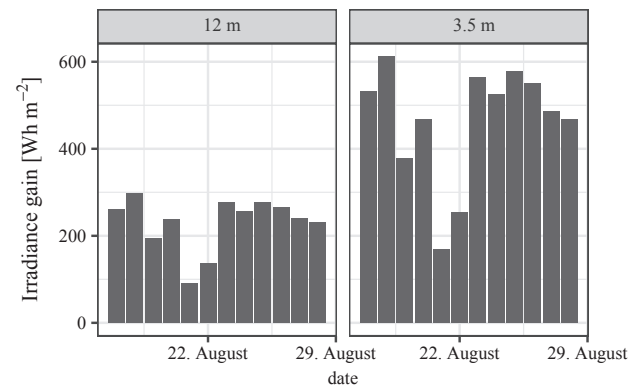


Fig. 9. Increase of irradiation on a south-facing wall point in 3.5 m above ground (as for the measurements) and in 12 m above ground, due to an increase of the ground-albedo from 0.13 to 0.50. Estimated results for an urban canyon in Vienna, based on irradiance measurement between 17. and 28. August 2016.

south of the canyon. It is not clear how much this is contributing to the error. However, any bias from the estimated portion of shadow on the ground, plus the neglected contribution from multiple reflections of higher order than two, can only be in the magnitude of the stated 5% bias of the total irradiation between 13. and 28. August 2016. Overall, this method provides reasonable results and deems suitable for the evaluation of the measurement and further estimations.

For future studies, it is recommended to analyse different scenarios, especially regarding different urban geometries. Those include different ratios of building height to street width, for which the portion of shadow on the ground is the main influence, and different canyon orientations. Notably PV systems that are oriented easterly or westerly are expected to benefit from an increase of the ground-albedo, compared to south oriented PV modules in an east-west oriented canyon. That is because when the sun azimuth corresponds to the canyon direction and the angle of incidence on the PV modules becomes small, most of the electricity will be generated from the diffuse sky irradiance and the radiation reflected from the ground. At that time, the ground will have the lowest amount of shadow and the global horizontal irradiance will

be rather large. Increasing the ground-albedo will then significantly increase the contribution of ground reflected irradiation to the PV yield. Altering the building height to street width ratio changes the fraction of shadow on the ground, too, and thus, has an impact on the total radiation reflected from the ground.

5. Conclusion

Measurements inside an urban canyon at the site of the University of Natural Resources and Life Sciences (BOKU) in Vienna, Austria, were used to show the increase of PV yield by increasing the ground's albedo. During several days in August 2016, 30 m² of white painted Styrofoam panels with an albedo of approximately 0.77 were placed on the ground in front of a vertical irradiance sensor and PV-modules, about 3.5 m above ground.

The total PV yield during a period of 16 days was shown to increase by almost 13% under the stated increase of the ground's albedo. During a four-days period of clear sky the energy yield was estimated to increase by 11.3%, or 1.19 Wh/Wp.

Under the assumption of replacing the asphalt on the ground by highly reflective concrete with an albedo of 0.5, it was estimated that the PV yield would increase by 20% on a wall point 3.5 m above ground. At a point 12 m above ground, which is a usual position for PV installations inside such a canyon, the PV yield was estimated to still increase by 7.3% compared to asphalt. The total yield produced for a selected period and with asphalt on the ground was 32.8 Wh/Wp. For the same time the incident irradiation was estimated to increase from a total of 37.5 kWh m⁻² by 7.4%.

This study clearly shows that the amount of radiation reflected from the ground cannot be neglected for PV yield estimations of facade

installations inside an urban canyon. Further, increasing the ground's albedo can have a significant impact on the yield of PV facades in an urban environment. However, for the assessment of economic aspects of PV installations inside an urban environment and PV potential analysis better simulation tools are required. Those are required to calculate the ground-reflected irradiance on facades inside an urban canyon more accurately. Besides accuracy, algorithms should require only short computational time such that larger urban areas can be simulated within a reasonable amount of time.

For an extensive study of the potential PV yield inside an urban canyon it will be required to assess various scenarios. Those scenarios should account for different urban geometries (e.g. canyon orientation and building height to street width ratio) and different ground-surface materials. The PV yield should also be calculated over the period of a full year to account for the varying sun altitude with its implications. In conjunction with studies of on cool pavements, the assessment of synergy effects between PV yield and compensation of energy consumption in buildings is a relevant topic.

6. Declaration of interest

None.

Acknowledgement

The research leading to these results has received funding from the Austrian Research Programme (Stadt der Zukunft, 3. Ausschreibung 2015) under grant agreement number 854691. The authors thank Eamon McDermott and Sean Philipp for their input during revision.

Appendix

List of symbols

α_{imp}	temperature coefficient of PV current
α_{isc}	temperature coefficient of the short circuit current
β	tilt of the receiving plane
β_{vmp}	temperature coefficient of PV voltage
$\delta(T_m)$	thermal voltage at temperature T_m
θ	solar angle of incidence on the wall point
θ_{b2}	solar angle of incidence onto facade of building b2 (facade at wall point)
θ_{gnd}	solar angle of incidence onto the ground
ρ	ground albedo
ρ_{b1}	albedo of the facade on building b1 (opposing the wall point)
ρ_{b2}	specular reflectance of building b2 (glass, facade at wall point)
$\rho_{b2,dif}$	specular reflectance for diffuse irradiance of building b2
$\rho_{b2,dir}$	specular reflectance for direct irradiance of building b2
$\rho_{gnd,i}$	albedo of the i th subpart of the ground surface
ρ_{high}	albedo for condition with the higher ground-albedo
ρ_{low}	albedo for condition with the lower ground-albedo
C_0, C_1	empirical coefficients for PV module
C_2, C_3	empirical coefficients for PV module
DHI	diffuse horizontal irradiance
DNI	direct normal irradiance
f_{b1}	view factor from the wall point to the building b1 (opposing the wall point)
$f_{b1,b2}$	view factor from building b1 to building b2 (facade at wall point)
$f_{b1,gnd,i}$	view factor from building b1 to the i th subpart of the ground surface
$f_{b1,sky}$	sky view factor for facade of building b1 (opposing the wall point)
$f_{b2,sky}$	sky view factor for facade of building b2 (facade at wall point)
$f_{gnd,b1}$	view factor from the ground to building b1
$f_{gnd,b2}$	view factor from the ground to building b2
$f_{gnd,i}$	view factor from the wall point to the i th subpart of the ground surface
$f_{gnd,sky}$	sky view factor for the ground
f_{sky}	sky view factor for the wall point
G	global horizontal irradiation

G_{b1}	total irradiance onto the facade of building b1 (opposing the wall point)
$G_{b1,sky}$	total irradiance from the sky onto building b1 (opposing the wall point)
$G_{b2,sky}$	total irradiance from the sky onto building b2 (facade at wall point)
G_e	effective irradiance
g_G	gain of the irradiance at the wall point
G_{gnd}	total irradiance onto the ground surface
$G_{gnd,sky}$	total irradiance from the sky onto the ground surface
G_h	irradiance at a wall point in horizontal plane
g_{PV}	gain of PV power at the wall point
G_{sky}	total irradiance from the sky onto a wall point
G_v	irradiance at a wall point in vertical plane (herein facing south)
$G_{v,sim}$	simulated vertical irradiance onto the wall point
I_{mp}	current at maximum power point
$I_{mp,0}$	current at maximum power point at standard condition
I_{sc}	short circuit current of PV module
$I_{sc,0}$	short circuit current at reference condition of 1000 W/m ² and 25 °C
N_s	number of PV cell connected in series
P_{mp}	PV power at maximum power point
sh	fraction of shadow on the ground surface
T_0	reference temperature of 25 °C
T_a	ambient air temperature
T_m	PV module backside temperature
V_{mp}	voltage at maximum power point
$V_{mp,0}$	voltage at maximum power point at standard condition

References

- Andrews, R.W., Pearce, J.M., 2013. The effect of spectral albedo on amorphous silicon and crystalline silicon photovoltaic device performance. *Sol. Energy* 91, 233–241. <https://doi.org/10.1016/j.solener.2013.01.030>.
- Andrews, R.W., Pearce, J.M., 2012. Prediction of energy effects on photovoltaic systems due to snowfall events. In: 2012 38th IEEE Photovoltaic Specialists Conference (PVSC). Presented at the 2012 38th IEEE Photovoltaic Specialists Conference (PVSC), pp. 003386–003391. <https://doi.org/10.1109/PVSC.2012.6318297>.
- Brennan, M.P., Abramase, A.L., Andrews, R.W., Pearce, J.M., 2014. Effects of spectral albedo on solar photovoltaic devices. *Sol. Energy Mater. Sol. Cells* 124, 111–116. <https://doi.org/10.1016/j.solmat.2014.01.046>.
- Dvorak, E., 2016. PV im dicht verbauten Gebiet - Treiber und Hemmnisse aus Sicht der Stadt Wien.
- EMS Brno, 2016. Global radiation sensor EMS 11 [WWW Document]. URL http://emsbrno.cz/r.axd/pdf_v.EMS11_u.pdf.jpg?ver= (Accessed 8.16.16).
- Fechner, H., Mayr, C., Schneider, A., Rennhofer, M., Peharz, G., 2016. Technologie-Roadmap für Photovoltaik in Österreich (Report for energy and environmental research No. 15/2016). *Berichte aus Energie- und Umweltforschung*. Bundesministerium für Verkehr, Innovation und Technologie, Austria, Vienna, Austria.
- Freitas, S., Catita, C., Redweik, P., Brito, M.C., 2015. Modelling solar potential in the urban environment: State-of-the-art review. *Renew. Sustain. Energy Rev.* 41, 915–931. <https://doi.org/10.1016/j.rser.2014.08.060>.
- Gilman, P., n.d. Sandia National Laboratories Modules Database [WWW Document]. Syst. Advis. Model SAM - Libr. Databases. URL <https://sam.nrel.gov/sites/default/files/sam-library-sandia-modules-2015-6-30.csv> (Accessed 2.4.16).
- IEA, 2014. *Technology Roadmap: Solar Photovoltaic Energy, 2014 edition*. OECD/IEA, Paris.
- Ineichen, P., Guisan, O., Perez, R., 1990. Ground-reflected radiation and albedo. *Sol. Energy* 44, 207–214. [https://doi.org/10.1016/0038-092X\(90\)90149-7](https://doi.org/10.1016/0038-092X(90)90149-7).
- Ineichen, P., Perez, R., 2002. A new airmass independent formulation for the Linke turbidity coefficient. *Sol. Energy* 73, 151–157. [https://doi.org/10.1016/S0038-092X\(02\)00045-2](https://doi.org/10.1016/S0038-092X(02)00045-2).
- King, D.L., Boyson, W.E., Kratochvil, J.A., 2004. Photovoltaic Array Performance Model (No. SAND2004-3535). Sandia National Laboratories.
- Krawietz, S., Poortmans, J., Masson, G., Pause, F., Palm, J., Schlatmann, R., 2016. BIPV Position Paper - Building Integrated Photovoltaics (BIPV) as a core Element for Smart Cities.
- Krispel, S., Peyerl, M., Maier, G., Weihs, P., 2017. Urban Heat Islands – Reduktion von innerstädtischen Wärmeinseln durch Whitetopping. *Bauphysik* 39, 33–40. <https://doi.org/10.1002/bapi.201710002>.
- Lindberg, F., Jonsson, P., Honjo, T., Wästberg, D., 2015. Solar energy on building envelopes – 3D modelling in a 2D environment. *Sol. Energy* 115, 369–378. <https://doi.org/10.1016/j.solener.2015.03.001>.
- Mohajerani, A., Bakaric, J., Jeffrey-Bailey, T., 2017. The urban heat island effect, its causes, and mitigation, with reference to the thermal properties of asphalt concrete. *J. Environ. Manage.* 197, 522–538. <https://doi.org/10.1016/j.jenvman.2017.03.095>.
- Olefs, M., Baumgartner, D.J., Obleitner, F., Bichler, C., Foelsche, U., Pietsch, H., Rieder, H.E., Weihs, P., Geyer, F., Haiden, T., Sch, W., ner, 2016. The Austrian radiation monitoring network ARAD – best practice and added value. *Atmos Meas Tech* 9, 1513–1531. <https://doi.org/10.5194/amt-9-1513-2016>.
- Qin, Y., 2015a. A review on the development of cool pavements to mitigate urban heat island effect. *Renew. Sustain. Energy Rev.* 52, 445–459. <https://doi.org/10.1016/j.rser.2015.07.177>.
- Qin, Y., 2015b. Urban canyon albedo and its implication on the use of reflective cool pavements. *Energy Build.* 96, 86–94. <https://doi.org/10.1016/j.enbuild.2015.03.005>.
- Redweik, P., Catita, C., Brito, M., 2013. Solar energy potential on roofs and facades in an urban landscape. *Sol. Energy* 97, 332–341. <https://doi.org/10.1016/j.solener.2013.08.036>.
- Remund, J., Wald, L., Lefèvre, M., Ranchin, T., Page, J.H., 2003. Worldwide Linke turbidity information. In: *ISES Solar World Congress 2003*. International Solar Energy Society (ISES), Göteborg, Sweden, pp. 13.
- Revesz, M., Oswald, S., Trimmel, H., Schneider, A., Weihs, P., Zamini, S., Peyerl, M., Krispel, S., 2017. PVOPTI-Ray: Optimisation of reflecting materials and photovoltaic yield in an urban context. In: *Proceedings of 33rd European Photovoltaic Solar Energy Conference and Exhibition*. Presented at the 33rd European Photovoltaic Solar Energy Conference and Exhibition, Amsterdam, pp. 2130–2134. <https://doi.org/10.4229/EUPVSEC20172017-6DO.11.4>.
- Rosso, F., Pisello, A.L., Cotana, F., Ferrero, M., 2016. On the thermal and visual pedestrians' perception about cool natural stones for urban paving: A field survey in summer conditions. *Build. Environ.* 107, 198–214. <https://doi.org/10.1016/j.buildenv.2016.07.028>.
- Santamouris, M., 2014. Cooling the cities – A review of reflective and green roof mitigation technologies to fight heat island and improve comfort in urban environments. *Sol. Energy* 103, 682–703. <https://doi.org/10.1016/j.solener.2012.07.003>.
- Santamouris, M., 2013. Using cool pavements as a mitigation strategy to fight urban heat island—A review of the actual developments. *Renew. Sustain. Energy Rev.* 26, 224–240. <https://doi.org/10.1016/j.rser.2013.05.047>.
- Taha, H., 1997. Urban climates and heat islands: albedo, evapotranspiration, and anthropogenic heat. *Energy Build.* 25, 99–103. [https://doi.org/10.1016/S0378-7788\(96\)00999-1](https://doi.org/10.1016/S0378-7788(96)00999-1).
- Yaghoobian, N., Kleissl, J., 2012. Effect of reflective pavements on building energy use. *Urban Clim.* 2, 25–42. <https://doi.org/10.1016/j.uclim.2012.09.002>.



Coupling of urban energy balance model with 3-D radiation model to derive human thermal (dis)comfort

Sandro M. Oswald¹ · Michael Revesz² · Heidelinde Trimmel¹ · Philipp Weihs¹ · Shokufeh Zamini² · Astrid Schneider² · Martin Peyrer³ · Stefan Krispel³ · Harald E. Rieder⁴ · Erich Mursch-Radlgruber¹ · Fredrik Lindberg⁵

Received: 11 May 2018 / Revised: 24 September 2018 / Accepted: 28 October 2018
© The Author(s) 2018

Abstract

While capabilities in urban climate modeling have substantially increased in recent decades, the interdependency of changes in environmental surface properties and human (dis)comfort have only recently received attention. The open-source solar long-wave environmental irradiance geometry (SOLWEIG) model is one of the state-of-the-art models frequently used for urban (micro-)climatic studies. Here, we present updated calculation schemes for SOLWEIG allowing the improved prediction of surface temperatures (wall and ground). We illustrate that parameterizations based on measurements of global radiation on a south-facing vertical plane obtain better results compared to those based on solar elevation. Due to the limited number of ground surface temperature parameterizations in SOLWEIG, we implement the two-layer force-restore method for calculating ground temperature for various soil conditions. To characterize changes in urban canyon air temperature (T_{can}), we couple the calculation method as used in the Town Energy Balance (TEB) model. Comparison of model results and observations (obtained during field campaigns) indicates a good agreement between modeled and measured T_{can} , with an explained variance of $R^2 = 0.99$. Finally, we implement an energy balance model for vertically mounted PV modules to contrast different urban surface properties. Specifically, we consider (i) an environment comprising dark asphalt and a glass facade and (ii) an environment comprising bright concrete and a PV facade. The model results show a substantially decreased T_{can} (by up to -1.65 °C) for the latter case, indicating the potential of partially reducing/mitigating urban heat island effects.

Keywords SOLWEIG · PV energy balance · Surface temperature parameterization · UTCI

Electronic supplementary material The online version of this article (<https://doi.org/10.1007/s00484-018-1642-z>) contains supplementary material, which is available to authorized users.

✉ Sandro M. Oswald
sandro.oswald@boku.ac.at

- ¹ Institute of Meteorology, University of Natural Resources and Life Sciences (BOKU), Vienna, Austria
- ² AIT Austrian Institute of Technology GmbH, Vienna, Austria
- ³ Smart Minerals GmbH, Vienna, Austria
- ⁴ Wegener Center for Climate and Global Change and IGAM/Institute of Physics, University of Graz, Graz, Austria
- ⁵ Department of Earth Sciences, University of Gothenburg, Gothenburg, Sweden

Introduction

Today about half of the world's population resides in urban areas. Future projections show pronounced urbanization rates and it is expected that by 2050, about two thirds of the world's population will be urban (UN 2014). Several studies report on increased thermal heat stress in urban microclimates, e.g., Grimmond et al. (2010). In order to adapt to climate change, some countries aim to reduce solar absorption in urban environments by maximizing the area of highly reflective surfaces through installation of the so-called white roofs. Also, at a time where sustainable energy production becomes more and more important, "solar cities" aim on maximizing "solar harvest", i.e., the solar yield from photovoltaic (PV) modules, by directing their roofs and

facades towards the sun to avoiding shadowing. Reflections from the ground and surrounding buildings cause an increase of the solar radiation directed to the PV module, thus increased PV yield (Kotak et al. 2015; Lindberg et al. 2015). The role of PV modules in a city or as a facade in an urban canyon was discussed in the work of Brito et al. (2017). This study has shown that for specific study areas, the non-baseload electricity demand can be satisfied by cost-effective PV investments on roofs and facades at today's market conditions for up to 10 months of the year. Further, winter mid-day electricity demand can only be achieved if the solar yield of PV facades is taken into account.

In terms of human thermal stress, this increase in reflection can cause more discomfort. Human (dis)comfort is commonly described by various bioclimatic indices. The Universal Thermal Climate Index (UTCI) (Fiala et al. 2001; Bröde et al. 2011; Blazejczyk et al. 2011) aggregates many of these in one standardized metric. The UTCI is based on complex multi-node thermophysiological models and allows to predict whole body thermal effects (e.g., hypothermia and hyperthermia; heat and cold discomfort) as well as localized effects (e.g., frostbite). Thereby, UTCI allows addressing all kinds of thermal stress and discomfort (e.g., extreme cold or warm) as well as conditions in which the human heat balance and the perceived outdoor temperature are affected by solar radiation. The accuracy of UTCI depends on a suite of input parameters; among these, especially a precise calculation of the mean radiant temperature T_{mrt} is of uttermost importance (Weihs et al. 2011).

To provide T_{mrt} with highest accuracy, we employ here an updated version (see below) of the open-source solar long-wave environmental irradiance geometry (SOLWEIG) model which is a part of the urban multi-scale environmental predictor (UMEP) (Lindberg et al. 2018). SOLWEIG is a state-of-the-art model which combines building and vegetation surface models and spatial variations of 3-D radiative fluxes in complex urban settings. SOLWEIG has been extensively evaluated in urban environments over the last decade (Lindberg et al. 2008; Lindberg and Grimmond 2011; Lindberg et al. 2016).

In its present configuration (Lindberg and Grimmond 2016), SOLWEIG uses only observed ambient air temperature, independent of its measurement height, to estimate the temperatures of surrounding surfaces (i.e., wall and ground temperature) via a simple parameterization scheme. Moreover, according to the authors' knowledge, to date, no evaluation and simulation tools are available for urban areas, which can estimate the effects of a broad rollout of photovoltaic facade and different ground surfaces in urban districts necessary to characterize the change of ambient air temperature and in general microclimate in urban street canyons.

This study aims on closing this gap by coupling SOLWEIG with parts of the Town Energy Balance (TEB) model (Masson 2000). Below, we detail the model setup as well as results from a recent field campaign for model evaluation. During this field campaign, measurements of short-wave radiation, wind speed, air, and surface temperatures were performed. The campaign took place between August 2016 and September 2017 on the campus of the University of Natural Resources and Life Sciences (BOKU) in Vienna.

The study focuses on (i) the simulation of canyon air temperature based on measured input parameters and its comparison to observed canyon air temperature in the study domain (see dashed yellow box in Figure S1 in the supplemental material); and (ii) evaluating the impact of potential changes in the surface structure parameters of wall and ground (i.e., albedo and energy balance of the PV module) on the canyon air temperature and human comfort.

Methods

Based on the standard meteorological input file of SOLWEIG, we developed a model structure which uses only the required and available variables (ambient air temperature T_a , wind speed U , relative humidity RH , barometric pressure p_a , and incoming short-wave global radiation G_h on a horizontal plane).

Instrumentations

For model development and evaluation, measurements which are routinely performed at the meteorological monitoring platform located at the rooftop of the Schwackhöfer-Haus (at approximately 26-m height above ground) have been used. Additional measurements have been performed within a street canyon nearby (southward-orientated at 3 m above ground). Figure 1a and b shows both platforms and the related measurements; Figure S1 in the supplemental material shows the measurement sites from the top (dark green ellipse = rooftop, green point = canyon). During the campaign, radiation measurements were performed with two types of pyranometer: on the rooftop with a MS-802 global radiation pyranometer (EKO Instruments) with a wavelength range of 285–3000 nm; in the urban canyon with a vertically mounted EMS 11 silicone diode sensor (EMS Brno) covering a wavelength range of 400–1100 nm. The ambient air temperature and relative humidity at the rooftop have been measured with a thermocouple type K combined with a humidity sensor (inside a radiation shield) in direct vicinity to the wind sensor (for speed and direction) on the rooftop (see Fig. 1a). Air temperature and wind speed measurements in the canyon were performed with a

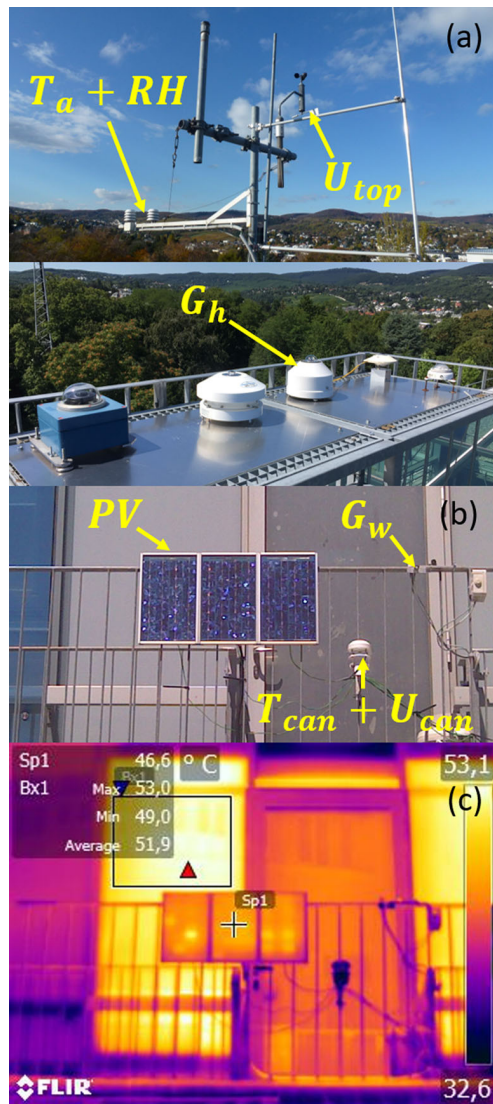


Fig. 1 Measurement setup used in this study. **a** The observational platform of the University of Natural Resources and Life Sciences (BOKU), located at the rooftop of the Schwachhöfer-Haus. **b** Additional instrumentation in the studied urban canyon. **c** Infrared picture of the setup shown in **b** taken on 19 June 2017 at 11:12 UTC. The acronyms in **a** and **b** indicate individual meteorological variables obtained; arrows point towards the corresponding instrument/sensor. These are ambient air temperature T_a and relative humidity RH ; both measured with a thermocouple located 26 m above ground; wind speed U_{top} at the rooftop, measured with a Kroneis anemometer 27 m above ground; horizontal global radiation G_h , obtained with a MS-802 pyranometer (EKO Instruments); global radiation on a south-oriented vertical plane G_w in the urban canyon, obtained with an EMS 11 global radiation silicone diode sensor (EMS Brno); canyon air temperature T_{can} and canyon wind speed U_{can} , both obtained with a DS-2 sonic anemometer (METER Group, Inc). The three photovoltaic modules PV are of type SX10M (SOLAREX). In the upper left of panel **c**, surface temperatures of the PV modules (Sp1) and the building facade of the Schwachhöfer-Haus (Bx1) are given

DS-2 sonic anemometer (METER Group, Inc.) with a speed range of $0\text{--}30\text{ m s}^{-1}$ and an accuracy of 0.3 m s^{-1} (see

Fig. 1b). The measurement outputs of the individual sensors in the urban canyon have been aggregated to 10-min averages to match the temporal resolution of the routine rooftop measurements.

The surface temperatures were additionally measured with an infrared camera of type FLIR E60bx (FLIR Systems), which has an accuracy of $\pm 2\%$ between 0 and $650\text{ }^\circ\text{C}$ (see Fig. 1c).

The potential electricity production inside the urban canyon was determined with three PV modules of type SX10m (SOLAREX). The surface temperature was measured with three thermocouples on the back side of the PV modules.

Parameterization of wall surface temperature

Bogren et al. (2000) proposes to estimate the surface temperatures T_s (horizontal or vertical) via a linear relationship between maximum solar elevation and the maximum difference between measured T_a and T_s under clear-sky conditions (Lindberg et al. 2008). Here, we propose a different approach, using global radiation measured on a south-oriented vertical plane G_w instead of solar elevation. G_w is calculated as

$$G_w = G_h \frac{\sin(\alpha + \beta)}{\sin(\alpha)} \tag{1}$$

where β is the tilt angle of the vertical plane measured from the horizontal and α is a function of the geographical latitude ϕ and the declination angle δ given by

$$\begin{aligned} \delta = & (180/\pi) \cdot (0.006918 - 0.399912 \cdot \cos(B) \\ & + 0.070257 \cdot \sin(B) - 0.006758 \cdot \cos(2B) \\ & + 0.000907 \cdot \sin(2B) - 0.002697 \cdot \cos(3B) \\ & + 0.00148 \cdot \sin(3B)), \end{aligned} \tag{2}$$

$$\alpha = 90 - \phi - \delta \tag{3}$$

where $B = (n - 1) \frac{360}{365}$ with the n th day of the year (Spencer 1971; PVEducation 2017).

To obtain the wall surface temperature T_w , we apply the amplitude from the before mentioned linear relationship to a sinusoidal wave function with maximum temperature difference at 15:00 (local time) (Lindberg et al. 2016).

Parameterization of ground surface temperature

To calculate the ground temperature T_g , we apply the force-restore method following Blackadar (1976) with a two-layer approximation, i.e., with a parameterization of the sensible heat flux H_s (2nd term in Eq. 4) and the ground heat flux

H_g (3rd term in Eq. 4). The change in T_g per time step is given as:

$$\frac{\partial T_g}{\partial t} = \frac{F}{S z_g} - a_{FR} (T_g - T_{as}) - \Omega (T_g - T_m) \quad (4)$$

Here, F represents the net radiation balance at the ground surface (which can be directly calculated with SOLWEIG), S is the soil heat capacity given as a product of a materials density ρ and its specific heat capacity c , Ω is the angle velocity of the Earth, and a_{FR} which is a time-of-day dependent factor ($3 \times 10^{-4} \text{ s}^{-1}$ for daytime, $1 \times 10^{-4} \text{ s}^{-1}$ for nighttime). T_m is the approximately constant temperature of the bottom slab. The depth of the thermal active layer z_g is calculated using time period τ and thermal conductivity λ (Stull 1988):

$$z_g = \sqrt{\frac{\tau \lambda}{4 \pi S}} \quad (5)$$

It follows that the near-surface air temperature T_{as} has to be simulated based on measurements of T_a on the rooftop. To model such continuous time series of T_g at time step $(t + 1)$, we apply the Euler method with a given T_g at time step (t) and the rate of change from Eq. 4 times a value i for the size of every step:

$$T_g(t + 1) = T_g(t) + \frac{\partial T_g}{\partial t} \cdot i \quad (6)$$

Parameterization of urban canyon air temperature

As detailed above, we are interested in the air temperature near the ground surface T_{as} . For simplification, we set T_{as} as \widehat{T}_{can} which is calculated in analogy to the TEB model.

$$\widehat{T}_{can} = \frac{\frac{T_g}{RES_g} + \frac{2h}{w} \frac{T_w}{RES_w} + \frac{T_a}{RES_{top}}}{\frac{1}{RES_g} + \frac{2h}{w} \frac{1}{RES_w} + \frac{1}{RES_{top}}} \quad (7)$$

Note we did not parameterize the anthropogenic sensible heat flux and snow cover terms given the general lack of traffic at the case study site and summer time conditions. Further required terms for estimating \widehat{T}_{can} are $\frac{h}{w}$, the canyon aspect ratio (building height h to street width w) and RES , the aerodynamic resistance for the ground (RES_g), wall (RES_w), and rooftop (RES_{top}), respectively, given as:

$$RES_g = RES_w = \frac{c_p \rho a}{(11.8 + 4.2 \sqrt{U_{can}^2 + (u_* + w_*)^2})} \quad (8)$$

$$RES_{top} = (U_{top} C_d)^{-1} \quad (9)$$

whereby U_{can} (parameterized as in the TEB model) and U_{top} (measured) are the wind speeds for canyon and rooftop, respectively. The characteristic scale of turbulent wind $u_* + w_*$ is calculated using T_a , U_{top} , and the drag coefficient C_d (computed with the roughness length $z_{0,down} = \frac{h}{10}$ and \widehat{T}_{can} of the previous time step) (Moigne

2012). For estimating the surface heat flux, we consider the rate of warming $\left(\frac{\partial T_a}{\partial t}\right)_r$ at the rooftop as representative for the whole convective boundary layer:

$$u_* + w_* = \sqrt{C_d} U_{top} + \left[\frac{g h^2}{T_a} \left(\frac{\partial T_a}{\partial t}\right)_r\right]^{1/3} \quad (10)$$

where g is the gravitational constant (Arya 2001).

Energy balance model for PV modules

Following the concept of the heat dynamics model for building-integrated photovoltaic (BIPV) systems of Lodi et al. (2012), we introduce a modified energy balance model for PV module(s) mounted in urban canyons. As model input, we use besides global radiation information (see above) the measured surface temperature on the back side of the PV module T_{bPV} , and information from a 2-D sonic anemometer. At our study site, the thermal radiative heat transfer between the back side of the PV module and the gray glass facade of the Schwachhöfer-Haus (see Fig. 1b) behind can be calculated following:

$$Ql_b = \frac{A_{PV} \sigma}{\frac{1}{\varepsilon_{bPV}} + \frac{1}{\varepsilon_w} - 1} (T_{bPV}^4 - T_w^4) \quad (11)$$

where A_{PV} represents the area of the photovoltaic module with a value of 0.11 m^2 . ε_{bPV} and ε_w are the emissivity for the back side of PV modules and the facade of the Schwachhöfer-Haus, respectively. T_{PV} , the front temperature of the PV module (which might be higher than T_{bPV}), can be calculated following:

$$T_{PV} = T_{bPV} + \frac{G_w}{1000 \text{ W m}^{-2}} \Delta T \quad (12)$$

where ΔT is the temperature difference between the front and back sides of the PV module. ΔT is set to 1.9° C at an irradiance level of 1000 W m^{-2} (King et al. 2004).

Now, the long-wave radiation exchange Ql_f between the sky, ground, the opposite building (Exner-Haus, see Figure S1 in the supplemental material), and the front side of the PV module is given as:

$$Ql_f = A_{PV} \sigma \left(\Psi_{sky} \varepsilon_c T_{sky}^4 + \Psi_g \varepsilon_c T_g^4 + \Psi_b \varepsilon_c T_b^4 - \varepsilon_{gl} T_{PV}^4 \right) \quad (13)$$

The parameter Ψ is the view factor for surrounding surfaces. Figure S2 in the supplemental material shows a fisheye lens picture of the PV module perspective combined with three digitalized images for the sky, for the ground, and for buildings. The respective area percentage calculation yields a sky view factor of $\Psi_{sky} = 0.23$, ground view factor $\Psi_g = 0.43$, and a building's view factor of $\Psi_b = 0.35$. For the emissivity ε_c , we assume a combined value of 0.95. Due to the available information of dew point temperature T_{dew} on

the rooftop, the sky temperature T_{sky} can be calculated using the method of Duffie and Beckman (2013). The temperature of the Exner-Haus T_b , which is shaded throughout the day, is set to T_a (Lindberg and Grimmond 2011).

To determine the convective heat transfer Q_C between the front (Eq. 14) and back sides (Eq. 15) of the PV module and the surrounding air, we apply Newton’s law of cooling following Palyvos (2008) and Sharples (1984):

$$Q_{c_f} = A_{PV} (7.35 + 3.75 \cdot U_{can}) (T_{can} - T_{PV}), \quad (14)$$

$$Q_{c_b} = A_{PV} (1.8 + 1.93 \cdot U_{can}) (T_{can} - T_{b_{PV}}) \quad (15)$$

The absorbed solar radiation is estimated through the transmittance-absorptance product $(\tau\alpha)_{PV} \cong 1.01 \tau_{gl} \alpha_{PV}$ (Duffie and Beckman 2013) and the incidence angle modifier $IAM(\theta_{aoi})$ (Barker and Norton 2003):

$$Q_s = A_{PV} 1.01 \tau_{gl} \alpha_{PV} G_w IAM(\theta_{aoi}) \quad (16)$$

The remaining term of the heat transfer process is transformed solar energy (i.e., electricity production of the PV module), which is given as a function of T_{PV} :

$$Q_e = A_{PV} G_w IAM(\theta_{aoi}) \eta_{ref} [1 - \beta_0 (T_{PV} - T_{PV,ref})] \quad (17)$$

where η_{ref} is the reference PV module efficiency (determined by laboratory measurements), β_0 is a temperature coefficient (see Table 1), and $T_{PV,ref} = 25 \text{ }^\circ\text{C}$ is the reference temperature at 1000 W m^{-2} (manufacturer provided).

Continuous Time Stochastic Modeling for unknown parameters

Continuous Time Stochastic Modeling (CTSM) is widely used to estimate unknown parameters of non-linear systems (Jazwinski 1970; Nielsen et al. 2000). Following the scheme of a gray box model, which combines prior physical knowledge and information from measurements, one can use a set of stochastic differential equations (SDEs) of form

$$dX_t = f(X_t, U_t, t, \Theta) dt + W(X_t, U_t, \Theta) d\omega_t \quad (18)$$

and a set of discrete time observation equations of form

$$y_k = M(X_k, U_k, t_k, \Theta) + e_k \quad (19)$$

where t is the time, X_t is a vector of state variables, U_t is a vector of input variables, Θ is a vector of unknown parameters, and y_k is a vector of output variables. $f(\cdot)$, $W(\cdot)$, and $H(\cdot)$ are non-linear functions, ω_t is a Wiener process, and e_k is the Gaussian white noise with the covariance \sum_t . The CTSM package in R (Juhl 2016) applies

a maximum likelihood estimation of a time series with joint probability density function

$$L(\Theta) = \left(\prod_{k=1}^N p(y_k | \Upsilon_{k-1}, \Theta) \right) p(y_0 | \Theta) \quad (20)$$

with $\Upsilon_N = [y_0, y_1, \dots, y_k, \dots, y_N]$ as a time series of N observations. CTSM-R computes the likelihood function and uses an optimization method to locate the most probable set of parameters (Juhl et al. 2016).

Given the relatively small area of the PV module used in this study (compared to, e.g., modules used in Jones and Underwood (2001) and Lodi et al. (2012)), we considered a single-state model to predict the average cell temperature. In our case, the unknown parameters are the absorptivity of the cells inside PV modules α_{PV} and the heat capacity C_{PV} . The non-linear system for the photovoltaic energy balance model to estimate these parameters is given as:

$$\begin{aligned} dT_{PV} &= C_{PV}^{-1} (Q_{c_f} + Q_{c_b} + Q_{l_f} \\ &\quad + Q_{l_b} + Q_s - Q_e) dt + W d\omega_t, \\ T_{PV,m} &= T_{PV} + e_k \end{aligned} \quad (21)$$

Once the unknown parameters are determined, the Euler method from Eq. 6 can be used to calculate the estimated PV module temperature $\hat{T}_{PV}(i)$ based on knowledge of global radiation (on a vertical plane), wind speed, and ambient air temperature at the rooftop, the angle of incidence of the current step (i), and the back-side PV module temperature with the canyon air temperature from the previous time step ($i - 1$).

Results

Model evaluation for wall, ground, and air temperature

As shown in Lindberg et al. (2016), the surface temperature parameterization in SOLWEIG affects the mean radiant temperature. Thus, precise measurements of the temperature of surrounding surfaces are needed to accurately simulate the canyon air temperature.

To this aim, infrared measurements (with a FLIR E60bx) were taken of the facade behind the PV modules around the time of maximum solar elevation. Due to the possible settings in FLIR Tools (FLIR Systems 2016), the position where pictures were taken was 5 m in front looking normal to the wall of the Schwackhöfer-Haus and the emissivity was set to $\epsilon_w = 0.95$.

Following Lindberg et al. (2016), we show in Fig. 2a the difference in wall surface temperature T_w and air (in our case canyon) temperature T_{can} , as a function of the maximum solar elevation. The regression coefficients found

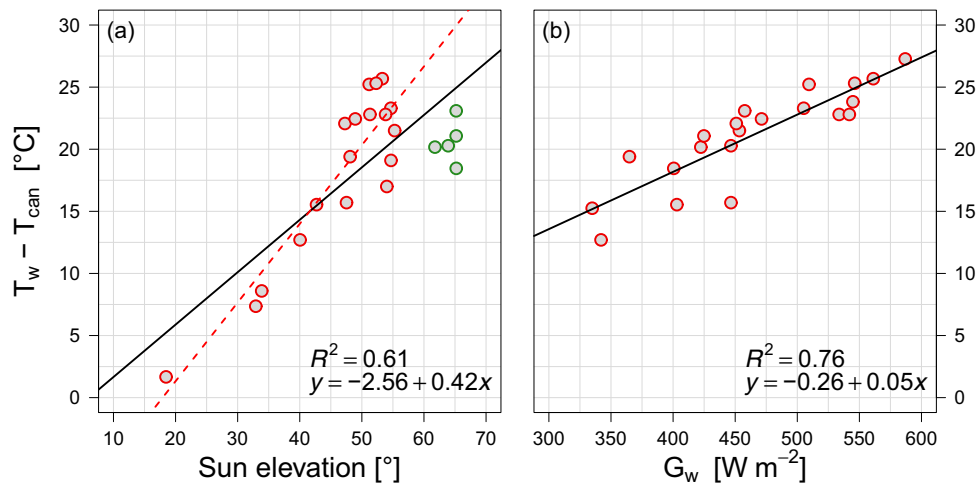


Fig. 2 Scatter plots of the difference in temperature between the wall surface temperature (T_w) and canyon air temperature (T_{can}) as a function of **a** the solar elevation and **b** global radiation on a south-facing vertical wall (G_w). The green points in panel **a** mark the outliers from the theoretical curve (dashed red line) describing higher surface

temperature at higher solar elevation. The squared Pearson correlation coefficient (R^2) and the regression analysis with the coefficients are provided in each panel. Note the number of measurements in **a** and **b** are not the same as global radiation measurements have not been available on 2 days

in the present analysis are in close agreement with those originally described by Lindberg et al. (2016). Despite a general agreement, a few individual measurements (marked in green) deviate from the theoretical curve (dashed red line) describing higher surface temperature at higher solar elevation. However, the study of Lindberg et al. (2016) considered only temperatures at solar elevation below 56° due to the higher geographic latitude in Sweden compared to Vienna. Figure 2b shows a new method regarding the difference of T_w and T_{can} as a function of the observed values G_w . The explained variance of the temperature difference is strongly improved using G_w as predictor (compare $R^2 = 0.61$ in panel (a) with $R^2 = 0.76$ in panel (b)).

Calculating the ground temperature with the force-restore method, we apply the following quantities: the heat capacity of asphalt given as $S_{asphalt} = 920 \text{ J kg}^{-1} \text{ K}^{-1} \cdot 2120 \text{ kg m}^{-3} = 1.95 \times 10^6 \text{ J m}^{-3} \text{ K}^{-1}$ and the thermal conductivity $\lambda_{asphalt} = 0.7 \text{ W m}^{-1} \text{ K}^{-1}$ (Lumitos 2017). T_m was set as an average of the daily mean of T_a and the annual average temperature in 2 m depth of 12°C to account for seasonal ground temperature variations (possible maximum temperature was measured in 2-m depth of 18.6°C) (ZAMG 2018). To obtain F in Eq. 4 with highest accuracy in SOLWEIG, measurements of the albedo of the Schwackhöfer-Haus (gray panels faced with glass in the upper part of Figure S3 in the supplemental material) yielded a value of 0.27.

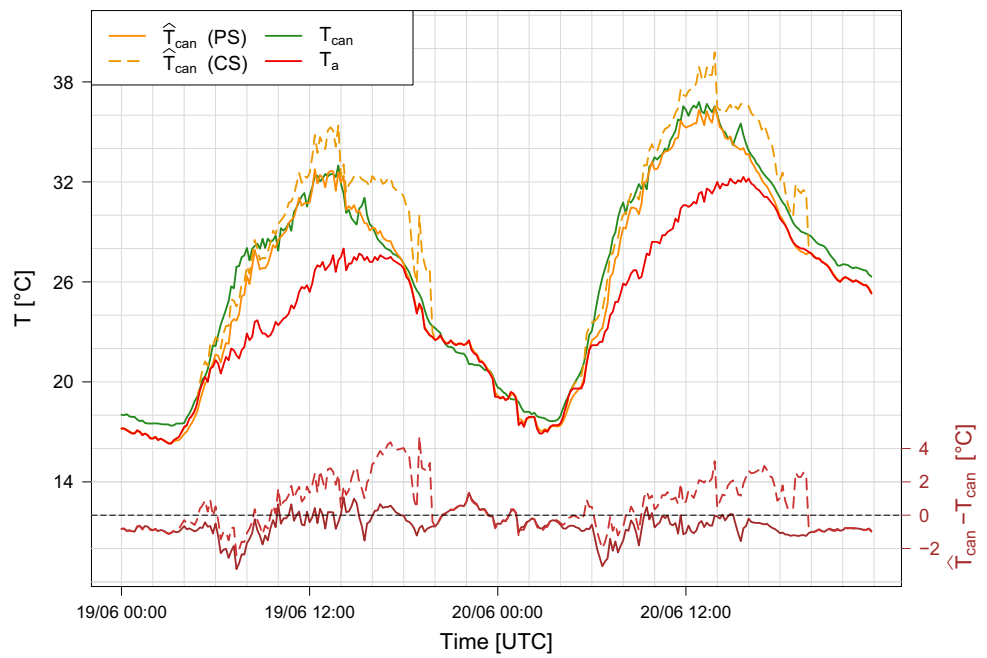
The canyon aspect ratio was calculated taking the average height of both buildings and a street width of 17 m which yields a value of $\frac{\bar{h}}{w} = \frac{20.2 \text{ m}}{17 \text{ m}} \approx 1.19$. As now all required

parameters for the calculation of the canyon air temperature \hat{T}_{can} are available, we derive it following Eq. 7.

Figure 3 provides a time series of the measured and simulated air temperature inside and above the urban canyon. We show the estimates for \hat{T}_{can} for both the currently implemented SOLWEIG scheme (CS) and the here proposed calculation scheme (PS). While both, CS and PS agree quite well with the measurements of T_{can} , a closer comparison reveals structural differences among the two approaches. Estimates from CS agree closer with observations during morning hours (before 10:00 UTC), while estimates from PS are closer to the measured canyon air temperature around noon and during the afternoon/early evening (until about 19:00 UTC). A disadvantage of CS compared to PS is the circumstance that the ground temperature decreases immediately to T_a due to the shadow matrix. This is clearly visible in Figure S4 (supplemental material) where at around 14:00 UTC, $T_{asphalt}$ (CS) rapidly decreases due to shading of the canyon (by the bridge marked with yellow lines in Figure S1). The two outliers in CS between 18:00 and 20:00 UTC stem from the fractional cloud cover function as described in Lindberg et al. (2008). Due to application of the parameterization throughout the night, the simulated air temperatures are too low, especially at the end of the time series after a pronounced heat wave.

The statistical analysis of the modeled versus observed canyon air temperature for CS and PS is shown in Fig. 4a and b, respectively. While both parameterization schemes work generally well, PS shows an improved explained variance (squared Spearman's rank correlation coefficient) compared to CS. More importantly though, the root mean

Fig. 3 Time series of the air temperature (T) measured at the rooftop (T_a , red) and inside the urban canyon (T_{can} , green), and simulated canyon air temperature with the currently implemented SOLWEIG scheme (CS) (\hat{T}_{can} , orange, dashed line) and the proposed calculation scheme (PS) (\hat{T}_{can} , orange, solid line). Time series of the difference between T_{can} and \hat{T}_{can} , respectively, is shown in the lower part (brown dashed (CS) and solid (PS) lines)



square error (RMSE) for PS is reduced compared to CS. In summary, the here-presented calculation scheme (PS) performs better than the standard scheme (CS). Nevertheless, also PS shows slight underestimations in the heating phase of the urban canyon.

Parameter estimation and simulation for PV modules

As manufacturers commonly do not provide optical or thermal specifications of a PV module, this information was compiled through literature review (see Table 1). The initial value of C_{PV} for the CTSM system was estimated using

a value given in Jones and Underwood (2001) with a total heat capacity of 2918 J K^{-1} and a total area of 0.51 m^2 . Assuming the mounted PV modules are very similar to the ones in Jones and Underwood (2001), the heat capacity of each module is $2918 \text{ J K}^{-1} \cdot \frac{0.11 \text{ m}^2}{0.51 \text{ m}^2} \approx 650 \text{ J K}^{-1}$ (scaled by total area). The final value of C_{PV} is given in Table 1. α_{PV} was also estimated by CTSM using an initial value of Moralejo-Vázquez et al. (2015).

Lodi et al. (2012) suggests parameter estimation based on data from partly cloudy days, given that the modeled heat transfer processes are less correlated under cloudy than under clear-sky conditions. For the present study, parameter estimation is based on data taken on 18 June 2017 between

Fig. 4 Scatter plots of measured (T_{can}) and simulated (\hat{T}_{can}) canyon air temperature for **a** the proposed calculation scheme and **b** the currently implemented SOLWEIG scheme. Each panel provides the squared Spearman’s rank correlation coefficient (R^2) and the root mean square error (RMSE)

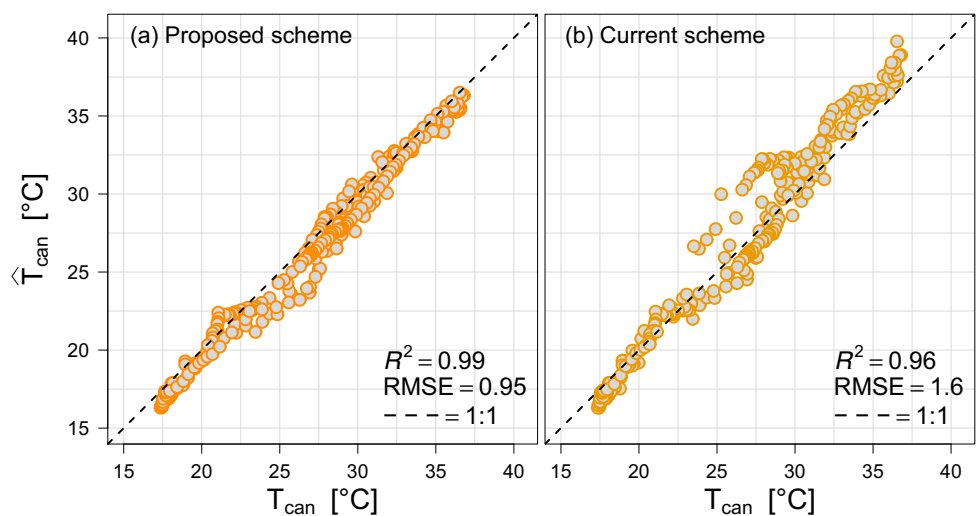
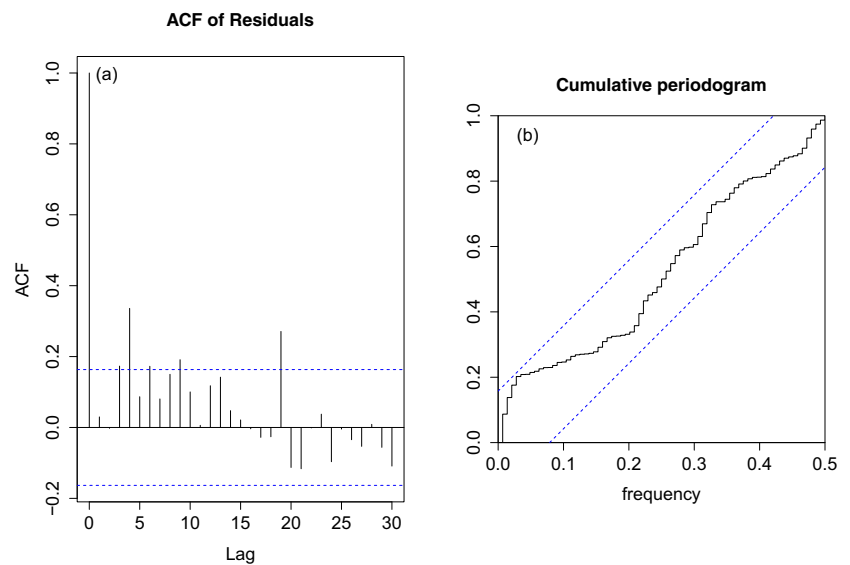


Fig. 5 **a** The auto-correlation function (ACF) and **b** the cumulated periodogram of the residuals for the continuous time stochastic model used for the mounted photovoltaic module. The blue dashed lines mark the 95% confidence limits for random noise



00:00 and 23:50 UTC with 10-min temporal resolution. Measurements include several input values for the CTSM system including G_w , U_{can} , T_a , T_{can} , T_{dew} , and $T_{b_{PV}}$. Ground temperature T_g in front of the PV module and wall temperature T_w behind the PV module have been simulated with the PS scheme in SOLWEIG. T_g was averaged over an area of $7 \cdot 7 \text{ m}^2$ (see Figure S1 in the supplemental material, red square), seen as the distance from the PV module to parked cars. In Fig. 5, we show the white noise verification of the model considering the auto-correlation function (ACF, panel (a)) and the cumulative periodogram (panel (b)). Here, the blue dashed lines mark the confidence level of 95% under the hypothesis that the model residuals are white noise. The PS describes heat transfer in and around the PV module enough sufficiently. We note in passing that for characterizing a larger PV unit, the model would need to be expanded to a two-state model as used for example by Lodi et al. (2012).

Applying the estimated parameters (Table 1) in Eq. 21 combined with the Euler method, the PV module temperature is predicted. The output of the simulated $\hat{T}_{b_{PV}}$ is compared with the measured $T_{b_{PV}}$ for 18 to 20 June 2017 in Fig. 6a. In panel (b), we show the difference between model prediction and observations. The model shows most satisfactory results on June 18, a day with partial cloud cover. In contrast, larger differences are found for 19 and 20 June 2017, which have been characterized by prevailing clear-sky conditions. Clear-sky days are more difficult to model due to overall higher temperatures and reflections of obstacles in the environment (see second sun in Figure S3 in the supplemental material). However, the statistical analysis of the CTSM-based system (provided in Fig. 7) shows good agreement throughout the time series, with an explained variance of $R^2 = 0.99$ and a RMSE = $1.2 \text{ }^\circ\text{C}$ ($N = 432$).

Simulations for various surface conditions

Urban planning strives to reduce the urban canyon air temperature and generally undesirable effects of the urban heat island. Therefore, the UTCI can describe human thermal comfort inside different surface structures and is thus an important planning quantity.

This study seeks to model the urban thermal environment at a study site in Vienna, Austria. We compare the influence of the current urban structure at the study site (dark asphalt on the ground combined with a glass facade) with those of a ground of bright concrete combined with a

Table 1 Technical specifications of the three PV modules used in this study

Type of solar cell		Poly-crystalline ¹
Total aperture area	0.11	m^2
Voltage at MPP ²	16.80	V
Current at MPP ²	0.59	A
Nominal power	10.00	W
PV module efficiency ³ η_{ref}	8.07	%
Temperature coefficient β_0	0.50	% K^{-1}
Absorptivity of cell α_{PV}	0.84	
Emissivity of glass ⁴ ε_{gl}	0.91	
Transmittance of glass ⁵ τ_{gl}	0.90	
Emissivity of back side ⁴ $\varepsilon_{b_{PV}}$	0.85	
Heat capacity C_{PV}	754.95	J K^{-1}

¹p-Si

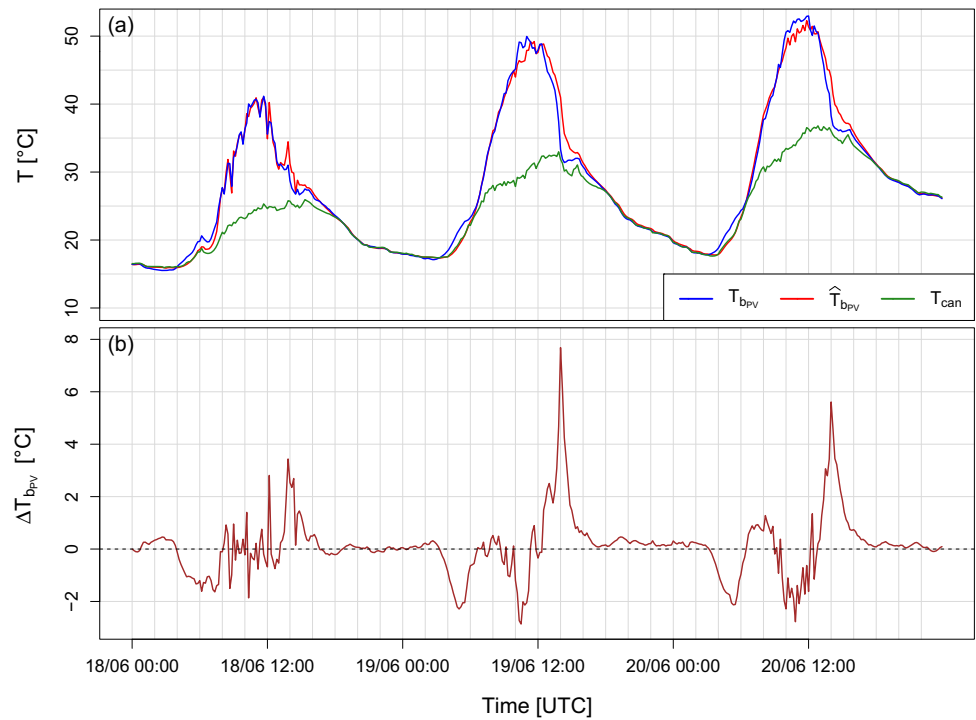
²Maximum Power Point

³Average of all three PV modules

⁴(Armstrong and Hurley 2010)

⁵(Herrando et al. 2014)

Fig. 6 Time series of **a** the temperature (T) measured inside the urban canyon (T_{can} , green) and at the back side of the PV module ($T_{b_{pv}}$, blue) and simulated at the back side of the PV module ($\hat{T}_{b_{pv}}$, red) and **b** the difference ($\Delta T_{b_{pv}}$) between the measured and simulated back-side photovoltaic module temperature



photovoltaic facade. To this aim, we assume conditions where PV modules cover the whole southern wall of the building in the study domain, as the distance between the PV modules and the back-side wall is large enough to assume that the convective heat transfer is the same as used in the CTSM system. The largest uncertainty of this

assumption is that we do not have knowledge about the surface temperature of the back-side wall which is an input variable for thermal radiative heat transfer. Therefore, we need to make assumptions for T_w . Here, we assume that it can be calculated with the same regression coefficients as given in Fig. 2b but considering addition of an average value of \hat{T}_{can} , T_a , and daily average of T_a (considering that the daily average will not change its value, only the amplitude varies). Further, we make the assumption that the calculated U_{can} as in the TEB model can be taken as wind speed for calculating the UTCI.

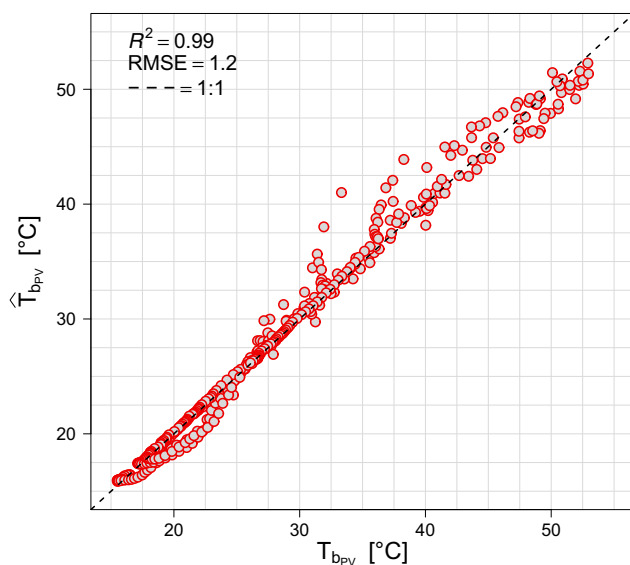


Fig. 7 Scatter plot of the measured temperature ($T_{b_{pv}}$) and simulated temperature ($\hat{T}_{b_{pv}}$) of the PV module. The upper-left corner provides the squared Spearman's rank correlation coefficient (R^2) and the root mean square error (RMSE)

After defining the new modeling systems, a comparison of the canyon air temperature between different surface conditions can be done. For such calculations, the albedo κ of each surface has to be defined. The albedo value for asphalt $\kappa_g = 0.18$ was chosen based on Lindberg et al. (2016). The value for concrete $\kappa_g = 0.56$ was measured in the work of Krispel et al. (2017) and the value for the PV modules $\kappa_{PV} = 0.10$ was taken from Moralejo-Vázquez et al. (2015).

Figure 8a, b, and c shows time series of \hat{T}_{can} and the UTCI for these different surface conditions including an additional simulation for UTCI with T_a . The related differences, $\Delta\hat{T}_{can}$ and ΔUTCI , are shown in Fig. 8d, e, and f, respectively. Our results show that a bright ground surface and a slightly decreased wall temperature (see Figures S4 and S5 in the supplemental material) can substantially reduce air temperature (by up to -1.30 °C) and the UTCI (by up to -1.10 °C) in the sun between 7:00 and 14:00

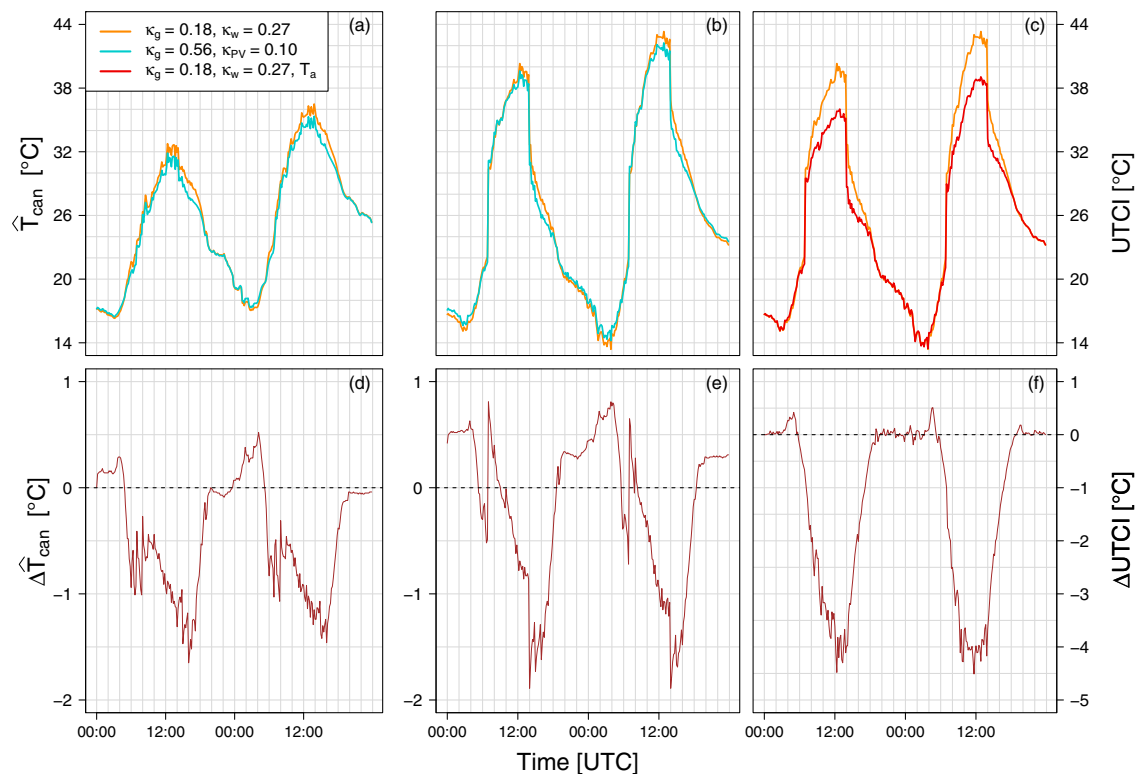


Fig. 8 Time series of **a** the modeled urban canyon air temperature (\hat{T}_{can}), **(b, c)** the modeled Universal Thermal Climate Index (UTCI) with \hat{T}_{can} (orange and cyan), and the air temperature measured at the rooftop T_a (red) between 19 and 20 June 2017. The legend in panel **a** shows the reflectance (κ) for different surfaces ($\kappa_g = 0.18$ for

asphalt, $\kappa_w = 0.27$ for glass facade, $\kappa_g = 0.56$ for concrete, and $\kappa_{PV} = 0.10$ for photovoltaic facade). Panels **d, e,** and **f** provide the difference between each surface condition regarding \hat{T}_{can} and UTCI, respectively

UTC. Even larger reductions are found in the shade between 14:00 and 16:00 UTC for both canyon air temperature (by up to -1.65 °C) and UTCI (by up to -1.85 °C). Further, Fig. 8f shows that an air temperature measured at a site which is not related to the actual surrounding surfaces results in a highly erroneous estimate of thermal (dis)comfort. In our case, Δ UTCI simulated with T_a shows a difference up to -4.50 °C and misses the very strong occurring heat stress (defined as UTCI between 38 and 46 °C) on the first day of the simulation period (see Fig. 8c).

These results indicate that even small, local changes to the surface and thus albedo can have a measurable effect on air temperature and UTCI in an urban canyon. While this decrease between -1 and -2 °C seems to be noticeable but yet small, it shall not be underestimated in its effect on human comfort in a warmer future climate.

Discussion and conclusions

This study seeks to improve the simulation of air temperature in urban canyons. To this aim, field measurements have been performed in 2016 and 2017, to evaluate/update

the wall and ground temperature parameterization and an energy balance model for photovoltaic (PV) modules within the solar and long-wave environmental irradiance geometry (SOLWEIG) model and couple it with parts of the Town Energy Balance (TEB) model.

For the parameterization of the wall surface temperature, we take infrared pictures of the Schwackhöfer-Haus at the University of Natural Resources and Life Sciences (BOKU), Vienna, with a FLIR E60bx to evaluate the accuracy of the current calculation scheme in SOLWEIG. Results show a clear overestimation of the surface temperature at solar elevation angles over 56° ($R^2 = 0.61$). We use global radiation measurements on a vertical plane instead to generate new regression coefficients ($R^2 = 0.76$).

We implement an updated calculation scheme for simulating ground temperature, which allows considering surface with user-specified albedo value and thermal conductivity properties. To develop this scheme, we used the force-restore method combining the radiation, sensible, and ground heat flux with the Euler method to estimate a time series of the ground temperature.

At the BOKU site, the ambient air temperature has been measured routine at the rooftop (26-m height above ground)

but outputs show a difference up to 6 °C to the measured canyon air temperature (3 m height above ground). This huge difference is compensated with parts of the TEB model calculating the canyon air temperature.

We compare the performance of the currently implemented SOLWEIG scheme (CS) and the here-proposed calculation scheme (PS). The results of the canyon air temperature show a better performance of PS, particularly a substantial reduction in RMSE. While the PS shows generally satisfactory skill in predicting temperatures inside the studied urban canyon, we note that further updates are needed for the representation of open areas, street crossings, and different canyon orientations. Further, an implementation of the glazing ratio for buildings would also increase the overall quality of SOLWEIG.

Considering the importance of sustainable energy production and climate warming, we perform scenario calculations to investigate effects of potential changes to the wall surface inside an urban canyon. We do so by evaluating a heat transfer single-state model for a vertically mounted photovoltaic (PV) module.

A comparison between model results for current surface conditions (dark asphalt on the ground combined with a glass facade) and possible modification conditions (ground covered with bright concrete and a PV facade) was performed. The results indicate a robust decrease in canyon air temperature by up to -1.65 °C for the modified canyon environment. To estimate human thermal comfort, we focus to calculate the Universal Thermal Climate index (UTCI). UTCI decreases by approx. -1.00 °C in the sun and -1.85 °C in the shade considering a change from present to modified conditions. We note in passing that future work should focus on effects of brighter surfaces for potentially increased human thermal stress.

We note in closing that additional field experiments for PV facades or building-integrated PV systems on large scales (e.g., a size of $60 \cdot 20$ m² like the south-facing wall of the Schwachhöfer-Haus) would strongly increase the quality of energy balance models, as the one presented here, and the possibility to mitigate, at least partially, urban heat island effects.

Acknowledgements The authors thank Meteo France and Valéry Masson for providing the Town Energy Balance model. The authors are grateful to Christian Gützer (University of Natural Resources and Life Sciences (BOKU), Vienna) for the technical support. This work received financial support from the University of Natural Resources and Life Sciences (BOKU) in Vienna.

Funding information This work was supported by the project “Optimizing reflecting materials and photovoltaics in urban areas regarding the radiation balance and bioclimatic” funded by the Austrian Research Promotion Agency (FFG) and the project “Influence of urban expansions on the urban heat island in Vienna” funded by the Klima- und Energiefonds.

Abbreviations *a*, time-of-day dependent factor (force-restore method) (1/s); *A*, area (m²); *B*, day of the year dependent factor (declination angle) (–); *c*, specific heat capacity (J); *C*, heat capacity (J/K); *C_d*, drag coefficient (–); CS, currently implemented SOLWEIG scheme; CTSM, continuous time stochastic model; *e*, Gaussian white noise (–); *f*, non-linear function; *F*, net radiation balance (W/m²); *g*, gravitational constant (m/s²); *G*, global radiation (W/m²); *h*, building height (m); \bar{h} , average building height (m); *H*, heat flux (W/m²); *i*, value for the size of every step (Euler method) (–); IAM, incidence angle modifier (–); *M*, non-linear function; *n*, day of the year (–); *N*, number of observations (–); *p*, pressure (hPa); PS, proposed calculation scheme; *Q*, heat transfer (W/m²); *Q_c*, convective heat transfer (W/m²); *Q_l*, long-wave heat transfer (W/m²); *RES*, aerodynamic resistance (s/m); *RH*, relative humidity (%); *S*, soil heat capacity (J/m³ K); *t*, time (s); *T*, measured temperature (°C); \hat{T} , modeled temperature (°C); $u_* + w_*$, turbulent wind (m/s); *U*, wind speed (m/s); *w*, street width (m); *W*, non-linear function; *y*, discrete time observation; *z*, depth of thermal layer (m); *z₀*, roughness length (m).

Greek symbols α , absorptivity (–); β , tilt angle of a vertical plane from the horizontal (°); β_0 , temperature coefficient of photovoltaic module (%/K); δ , declination angle (°); ΔT , temperature difference (K); ε , emissivity (–); η , photovoltaic module efficiency (%); θ_{aai} , angle of incidence (°); Θ , vector of unknown parameters; κ , reflectance (–); λ , thermal conductivity (W/(m K)); ρ , material density (kg/m³); σ , Stefan-Boltzmann constant (W/(m² K⁴)); Σ , covariance; Υ , time series of *N* observations; ϕ , geographical latitude (°); Ψ , view factor (–); ω , Wiener process; Ω , Earth’s angle velocity (1/s).

Subscripts *a*, air; *as*, near-surface air; *asphalt*, index for asphalt properties; *b*, back side; *b_{PV}*, back side of photovoltaic module; *c*, combined value; *can*, urban canyon; *dew*, dew point; *e*, electricity; *f*, front side; *g*, ground; *gl*, glass; *h*, horizontal plane; *m*, approximately constant value; *p*, constant pressure; *PV*, photovoltaic module; *r*, rate; *ref*, reference; *s*, solar; *sky*, sky; *top*, rooftop; *w*, wall.

Open Access This article is distributed under the terms of the Creative Commons Attribution 4.0 International License (<http://creativecommons.org/licenses/by/4.0/>), which permits unrestricted use, distribution, and reproduction in any medium, provided you give appropriate credit to the original author(s) and the source, provide a link to the Creative Commons license, and indicate if changes were made.

References

- Armstrong S, Hurley WG (2010) A thermal model for photovoltaic panels under varying atmospheric conditions. *Appl Therm Eng* 30(11-12):1488–1495
- Arya P (ed.) (2001) Introduction to micrometeorology, Academic Press
- Barker G, Norton P (2003) Building america system performance test practices: part 1 – photovoltaic systems, technical report, Office of Scientific and Technical Information (OSTI)
- Blackadar AmKa (1976) Modeling the nocturnal boundary layer, Reprints third symp. Atmospheric turbulence, diffusion and air quality, Raleigh, Am Meteorol Soc, pp 46–49
- Blazejczyk K, Epstein Y, Jendritzky G, Staiger H, Tinz B (2011) Comparison of UTCI to selected thermal indices. *Int J Biometeorol* 56(3):515–535
- Bogren J, Gustavsson T, Karlsson M, Postgard U (2000) The impact of screening on road surface temperature. *Meteorological Applications* 7(2):97–104

- Brito MC, Freitas S, Guimarães S, Catita C, Redweik P (2017) The importance of facades for the solar PV potential of a mediterranean city using LiDAR data. *Renew Energy* 111:85–94
- Bröde P, Fiala D, Błażejczyk K, Holmér I, Jendritzky G, Kampmann B, Tinz B, Havenith G (2011) Deriving the operational procedure for the universal thermal climate index (utci). *Int J Biometeorol* 56(3):481–494
- Duffie JA, Beckman WA (2013) *Solar engineering of thermal processes*. Wiley, New York
- Fiala D, Lomas KJ, Stohrer M (2001) Computer prediction of human thermoregulatory and temperature responses to a wide range of environmental conditions. *Int J Biometeorol* 45(3):143–159
- FLIR Systems Inc. (2016) <http://www.flir.com>
- Grimmond CSB, Blackett M, Best MJ, Barlow J, Baik J-J, Belcher SE, Bohnenstengel SI, Calmet I, Chen F, Dandou A et al (2010) And The international urban energy balance models comparison project: first results from phase 1. *J Appl Meteorol Climatol* 49(6):1268–1292
- Herrando M, Markides CN, Hellgardt K (2014) A UK-based assessment of hybrid PV and solar-thermal systems for domestic heating and power: system performance. *Appl Energy* 122:288–309
- Jazwinski AH (1970) *Stochastic processes and filtering theory*, Elsevier, pp vii–viii
- Jones AD, Underwood CP (2001) A thermal model for photovoltaic systems. *Sol Energy* 70(4):349–359
- Juhl R (2016) Ctsmr: Ctsm for r. R package version 0.6.10
- Juhl R, Moller J, Madsen H (2016) ctsmr - continuous time stochastic modeling in r, *The R Journal*
- King DL, Boyson WE, Kratochvil JA (2004) Photovoltaic array performance model, <http://energy.sandia.gov/download/21046/>
- Kotak Y, Gul MS, Muneer T, Ivanova SM (2015) Investigating the impact of ground albedo on the performance of pv systems
- Krispel S, Peyerl M, Maier G, Weihs P (2017) Urban heat islands - reduktion von innerstädtischen wärmeinseln durch whitetopping. *Bauphysik* 39(1):33–40
- Lindberg F, Grimmond CSB, Gabey A, Huang B, Kent CW, Sun T, Theeuwes NE, Järvi L, Ward HC, Capel-Timms I (2018) Urban multi-scale environmental predictor (umep): an integrated tool for city-based climate services. *Environ Model Softw* 99:70–87
- Lindberg F, Grimmond CSB (2011) The influence of vegetation and building morphology on shadow patterns and mean radiant temperatures in urban areas: model development and evaluation. *Theor Appl Climatol* 105(3-4):311–323
- Lindberg F, Grimmond CSB (2016) Solweig, <http://urban-climate.net/umep/SOLWEIG>
- Lindberg F, Holmer B, Thorsson S (2008) SOLWEIG 1.0 – modelling spatial variations of 3d radiant fluxes and mean radiant temperature in complex urban settings. *Int J Biometeorol* 52(7):697–713
- Lindberg F, Jonsson P, Honjo T, Wästberg D (2015) Solar energy on building envelopes - 3d modelling in a 2d environment. *Sol Energy* 115:369–378
- Lindberg F, Onomura S, Grimmond CSB (2016) Influence of ground surface characteristics on the mean radiant temperature in urban areas. *Int J Biometeorol* 60(9):1439–1452
- Lodi C, Bacher P, Cipriano J, Madsen H (2012) Modelling the heat dynamics of a monitored test reference environment for building integrated photovoltaic systems using stochastic differential equations. *Energy and Buildings* 50:273–281
- Lumitos GmbH (2017) <http://www.chemie.de/>
- Masson V (2000) A Physically-based scheme for the urban energy budget in atmospheric models. *Bound-Layer Meteorol* 94(3):357–397
- Moigne PL (2012) *Surfex scientific documentation*
- Moralejo-Vázquez FJ, Martín-chivelet N, Olivieri L, Caamaño-martín E (2015) Luminous and solar characterization of PV modules for building integration. *Energy and Buildings* 103:326–337
- Nielsen JN, Madsen H, Young PC (2000) Parameter estimation in stochastic differential equations: an overview. *Annu Rev Control* 24:83–94
- Palyvos JA (2008) A survey of wind convection coefficient correlations for building envelope energy systems' modeling. *Appl Therm Eng* 28(8-9):801–808
- PVEducation (2017) <http://pvcfrom.pveducation.org/SUNLIGHT/MODTILT.HTM>
- Sharples S (1984) Full-scale measurements of convective energy losses from exterior building surfaces. *Build Environ* 19(1):31–39
- Spencer JW (1971) <http://www.mail-archive.com/sundial@uni-koeln.de/msg01050.html>
- Stull RB (ed.) (1988) *An introduction to boundary layer meteorology*, Springer Netherlands
- UN (2014) *World urbanization prospects*, United Nations. visited on <https://esa.un.org/unpd/wup/Publications/Files/WUP2014-Highlights.pdf>
- Weihs P, Staiger H, Tinz B, Batchvarova E, Rieder H, Vuilleumier L, Maturilli M, Jendritzky G (2011) The uncertainty of UTCI due to uncertainties in the determination of radiation fluxes derived from measured and observed meteorological data. *Int J Biometeorol* 56(3):537–555
- ZAMG HoheWarte (2018) *Meteorological measurements, data set from 1981 to 2017*, Central Institution for Meteorology and Geodynamics



Thermal conditions during heat waves of a mid-European metropolis under consideration of climate change, urban development scenarios and resilience measures for the mid-21st century

HEIDELINDE TRIMMEL^{1,6*}, PHILIPP WEIHS¹, STÉPHANIE FAROUX², HERBERT FORMAYER¹, PAUL HAMER⁶, KRISTOFER HASEL^{1,4}, JOHANNES LAIMIGHOFER⁵, DAVID LEIDINGER¹, VALÉRY MASSON², IMRAN NADEEM¹, SANDRO M. OSWALD^{1,3}, MICHAEL REVESZ¹ and ROBERT SCHOETTER²

¹Institute of Meteorology and Climatology, University of Natural Resources and Life Sciences (BOKU), Vienna, Austria

²CNRM, Université de Toulouse, Météo-France, Toulouse, France

³Zentralanstalt für Meteorologie und Geodynamik (ZAMG), Vienna, Austria

⁴Department of Meteorology and Geophysics, University of Vienna, Vienna, Austria

⁵Institute of Statistics, University of Natural Resources and Life Sciences (BOKU), Vienna, Austria

⁶Norsk institutt for luftforskning (NILU), Kjeller, Norway

(Manuscript received June 9, 2019; in revised form October 25, 2019; accepted October 28, 2019)

Abstract

In this study we produce two urban development scenarios estimating potential urban sprawl and optimized development concerning building construction, and we simulate their influence on air temperature, surface temperatures and human thermal comfort. We select two heat waves representative for present and future conditions of the mid 21st century and simulations are run with the Town Energy Balance Model (TEB) coupled online and offline to the Weather Research and Forecasting Model (WRF). Global and regional climate change under the RCP8.5 scenario causes an increase of daily maximum air temperature in Vienna by 7 K. The daily minimum air temperature will increase by 2–4 K. Changes caused by urban growth or densification mainly affect air temperature and human thermal comfort locally where new urbanisation takes place and does not occur significantly in the central districts. A combination of near zero-energy standards and increasing albedo of building materials on the city scale accomplishes a maximum reduction of urban canyon temperature achieved by changes in urban parameters of 0.9 K for the minima and 0.2 K for the maxima. Local scale changes of different adaptation measures show that insulation of buildings alone increases the maximum wall surface temperatures by more than 10 K or the maximum mean radiant temperature (MRT) in the canyon by 5 K. Therefore, measures to reduce MRT within the urban canyons like tree shade are needed to complement the proposed measures. This study concludes that the rising air temperatures expected by climate change puts an unprecedented heat burden on Viennese inhabitants, which cannot easily be reduced by measures concerning buildings within the city itself. Additionally, measures such as planting trees to provide shade, regional water sensitive planning and global reduction of greenhouse gas emissions in order to reduce temperature extremes are required.

Keywords: urban sprawl, climate change, heat waves, urban scenarios, resilience, TEB, WRF, UTCI

1 Introduction

The urban environment influences the atmospheric conditions at the surface in various ways. Air temperature is higher mainly at night in comparison to rural areas, which is well known as the urban heat island effect, (UHI, LANDSBERG, 1981; OKE, 1982; GRIMMOND et al., 2010). In addition, vapour pressure or specific humid-

ity can be lower due to reduced water availability, and the radiation and wind fields are strongly altered by the three-dimensional building structures (GRIMMOND et al., 2010).

These effects might further increase due to strong urbanization trends, which includes densification and growth of existing urban agglomerations. For instance, until 2030, the population within the metropolitan area of Vienna is expected to increase by 10% (ÖROK, 2017). This will cause an increase in the demand for gross floor area resulting in urban densification and/or urban expansion. However, even under current conditions, the population in Vienna is suffering from heat

*Corresponding author: Heidelinde Trimmel, Institute of Meteorology and Climatology, University of Natural Resources and Life Sciences (BOKU), Gregor Mendelstrasse 33, 1180 Vienna, Austria, e-mail: heidelinde.trimmel@boku.ac.at

stress during the summer months (MATZARAKIS et al., 2011; MUTHERS et al., 2010; MA 22, 2018). In the present article, we research the impact of the projected urban development in Vienna on human thermal comfort.

Rises in air temperature that can be expected due to climate change (APCC, 2014) present an additional threat to human thermal comfort in the urban realm. Air temperature has been rising and is expected to continue to rise globally within the next century (IPCC, 2013). In eastern Austria, mean air temperature has risen by 2 K since 1880, which is more than double the 0.85 K rise recorded globally (AUER et al., 2014). Emission scenario A1B projects that by the end of the 21st century mean air temperature increases of 3.5 K above the level of the reference period 1961–1990 are expected in Austria (APCC, 2014; GOBIET et al., 2014). Cities themselves contribute to climate change by the emissions caused by e.g., ground and air traffic, industrial processes, heating, electricity generation, waste and production of building material (DE PEE et al., 2018; BARDOW and GREEN, 2018; KENNEDY et al., 2009).

Heat waves have been recognized as a lethal threat to humans around the world within the last decades (McMICHAEL et al., 2003; VALLERON and BOUMENDIL, 2004; KIM and KYSELÝ, 2009; GRIMMOND et al., 2010; GABRIEL and ENDLICHER, 2011) and also Vienna (HUTTER et al., 2007). Additionally, the combination of the elevated air temperature during heat waves and high irradiation (OTANI et al., 2017; SCHREIER et al., 2013), humidity (STEADMAN, 1979a, b) or air pollution (KALISA et al., 2018; SCHNELL and PRATHER, 2017; ZHANG et al., 2017) poses a threat to human health.

It has been found that the heat wave length and intensity will increase in the future, e.g., for Paris (LEMONSU et al., 2013) and also for Vienna (FORMAYER et al., 2007). Kyselý days are defined as days of a heat-wave period, which is characterised by at least three subsequent days with daily maximum air temperature larger than 30 °C and continues until the daily maximum air temperature drops below 25 °C or until the mean daily maximum air temperature of the period drops below 30 °C (KYSSELÝ et al., 2000). An increase of the number of Kyselý days by up to a factor of 10 from 1961–1990 to the end of the 21st century is expected by FORMAYER et al. (2007) for Vienna (Scenario A2, Model: HadRM3H; JONES et al., 2001). This alarming fact has caused various heat warning systems to be developed (MICHELOZZI et al., 2004; TAN et al., 2007).

To be able to project the thermal strain caused by future heat waves and urban growth it is necessary to have the appropriate tools that can take into account as many of the involved physical processes as possible (especially in the context of a changing climate). This includes microscale processes such as reflections within the urban canyon, wind reduction, energy uptake and storage in roads and buildings resolved, e.g., by the town and energy balance scheme TEB (MASSON, 2000; MASSON et al., 2002; BUENO et al., 2012; PIGEON

et al., 2014). Furthermore, representations of evapotranspiration by urban vegetation, which have been implemented in TEB (LEMONSU et al., 2012; DEMUNCK et al., 2013), city scale effects caused by spatial inhomogeneity (e.g., potential thermal breezes), and topography (e.g., topographically-generated or modified winds) are of key importance. Finally, the interaction between the surface layer and the atmosphere and its effects on the evolution of the urban boundary layer are crucial (OKE, 1987; STULL, 1988, BORNSTEIN and LIN, 2000; GRIMMOND et al., 2010) as it is done in atmospheric models, e.g., the weather research and forecasting model WRF (SKAMAROCK et al., 2008).

In this study we will work with resilience measures, because we want to point out that the aim of urban development should be to make the city more resilient – or to better cope and maintain function during climatic extremes (ZOMMERS and ALVERSON, 2018). Resilience covers the more holistic approach of urban planning (SHARIFI and YAMAGATA, 2018; ÜRGE-VORSATZ et al., 2018). Here, we will apply some basic changes in material properties as a first and important step to help to reduce thermal strain in urban agglomerations and thus increase resilience.

To measure the subjective perception of temperature there are many indices describing human thermal comfort (PMV (FANGER, 1970), PET (MAYER and HÖPPE, 1987), UTCI (FIALA et al., 2001; BRÖDE et al., 2012; JENDRITZKY et al., 2012)), heat stress or apparent temperature (humidex, wind chill, wet-bulb globe temperature). Generally important factors for the human organism are the radiation received by humans, the ambient air temperature, humidity and wind speed (MAYER and HÖPPE, 1987). There is a positive relationship between human thermal stress and increasing MRT for the warm part of the thermal comfort spectrum. In this thermal comfort range the relation to air temperature and water vapour pressure even increases with higher air temperatures (DOU, 2014). In this study the Universal Thermal Climate Index (UTCI) is used.

The aim of this article is, to present:

1. The setup of a mesoscale meteorological model coupled to an urban energy balance model (Section 2.1)
2. Future urban scenarios for Vienna (Section 2.3 and 2.4)
3. The change of the 2 m air temperature for a selected present and a future heat wave on city level (Section 3.1):
 - Daily maximum temperature, as a factor for human thermal strain
 - Daily minimum temperature, to quantify the nocturnal canopy urban heat island (CUHI) magnitude
 - The influence of urban sprawl and densification

4. Analysis of the effects of different resilience measures on a local level (Section 3.2):
 - Energy flux differences, which are transferred from the urban surface to the atmospheric model
 - The surface temperatures of roof, wall and road, to understand the air temperature changes
5. Analysis of canyon parameters to estimate thermal strain in the idealized canyon (Section 3.3)

We do not address the detail planning within the street canyons, but urban development regarding urban material choice, distribution and density of built land on a scale > 100 m.

2 Materials and methods

2.1 Modelling Framework

In this study, the open-source mesoscale atmospheric model WRFv3.9.1 (SKAMAROCK et al., 2008) is used in combination with an urban canopy model called the Town Energy Balance (TEB; MASSON, 2000; MASSON et al., 2002) model. Both models are coupled and run online. Additionally, offline simulation runs were done by forcing TEB as it is integrated in SURFEXv8 (BOONE et al., 2017) with the output of WRF-TEB.

WRF is used to downscale the ECMWF Analysis Data Set for present-day conditions (temporal resolution of 6 hours, horizontal resolution of 9 km (<https://www.ecmwf.int/en/forecasts/datasets/set-i>) via two intermediate nests (3 km and 1 km resolution) using one-way grid nesting to a 333 m resolution domain covering the city of Vienna (Figure A-1). There are 40 vertical levels in the WRF simulations, thereof 7 below 1000 m. For the topographical elevation, the SRTM1Arc:30 m data set is used. The Yonsei University Scheme is used for the Planetary Boundary Layer scheme together with the NOAA Land Surface Model to model the land-atmosphere interaction. For the land cover information, the Corine data (EEA, 2012) was reclassified to USGS classes (30 non-urban, 3 urban) (Table B-1) in order to be consistent with WRF (SCHICKER et al., 2016).

For the future heat wave conditions, we use selected events from regional climate model simulations forced by different representative concentration pathways (RCPs) to force our WRF-TEB simulations. The details of the regional climate model simulations, the heat wave selection process, and the coupling with WRF are described in Section 2.5.

Our different future urban development scenarios representing urban densification and sprawl are created by modifying the Corine land surface dataset using specific information regarding expected urban growth. The details of these urban development scenarios, and how they are created and applied is described in Section 2.4.

TEB version 1.1550 is implemented in the Weather Research and Forecasting (WRF) model. The Town

Energy Balance (TEB) model developed by MASSON (2000) is a physically based single-layer urban canopy scheme that is designed for urban surface parameterization of atmospheric models. The building energy model (BEM) that has been integrated in the TEB scheme (BUENO et al., 2012) is also deployed in the coupling. BEM-TEB makes it possible to represent the energy effects of buildings and building systems on the local urban climate and to provide estimations of the building energy consumption at the city scale with a resolution of down to 100 m.

The TEB scheme takes meteorological parameters at the lowest level of WRF as input. These parameters are air temperature and specific humidity, wind speed and direction, air pressure, direct and diffuse downwelling solar radiation, downwelling longwave radiation and precipitation. In return, TEB provides roof, road and wall temperature, emissivity, latent, sensible heat and momentum fluxes to the WRF model as output. In addition, 2-m temperature, 2-m humidity, and 10-m wind are obtained from the diagnosed TEB canyon temperature, humidity, and wind, respectively.

The URBPARAM.TBL and registry files in WRF have also been modified to accommodate urban parameters required by TEB-BEM and to write out urban parameters in the model output. All necessary conversions (e.g., specific humidity to mixing ratio) are done. We use the canyon temperature calculated by TEB for the calculation of the 2 m air temperature of WRF-TEB within urban areas. The coupled model WRF-TEB uses the same spatial resolution as the original WRF.

Offline simulations using SURFEXv8 were done due to different reasons. First, the simulation time was much faster and so more resilience measures could be simulated, as would have been possible with the online version, second some resilience measures (green roofs and photovoltaic on roofs) have not been implemented in WRF-TEB, but in SURFEXv8 and third SURFEXv8 offers the calculation of the thermal index UTCI. We analysed various results from the offline simulations: the energy fluxes, surface temperature, canyon air temperature, mean radiant temperature and UTCI. Here, mainly shaded UTCI is used, which is the UTCI calculated only from influences by diffuse radiation, without the direct component. Therefore, it can also be calculated when no buildings are present. The direct component is so pronounced, that in this study we found that there is no way to improve the UTCI in the sun during summer heat waves, only conditions can be made more bearable in the shadow.

2.2 Validation and uncertainties

The energy fluxes and surface temperatures of roof, wall and road temperatures calculated by TEB have been validated by MASSON et al. (2002) for Vancouver and Mexico City. For Mexico City the road and roof temperatures showed a bias of 4 and 1.9 K, and a RMSE of 4.2 and 4.5 K. The radiation, turbulent (sensible+latent) and

storage fluxes showed a bias of 10, -3 and 13 W m^{-1} , respectively, and a RMSE of 32, 25 and 38 W m^{-1} . For Vancouver the wall and roof temperatures showed a bias of 2.3 and 2.5 K and a RMSE of 3 and 7.3 K. Further TEB was validated for Marseille (LEMONSU et al., 2004), Ouagadougou (OFFERLE et al., 2005) and cold climates, which is not relevant here. The BEM was validated by PIGEON et al. (2014) for Paris. In addition, we validated the 2 m air temperature in different Viennese urban canyons and found a mean absolute error for WRF-TEB between 0.99 and 1.51 K, and the RMSE was between 1.3 and 1.89 (Table A-1).

The water vapour pressure calculated from WRF-TEB is compared to measurements at Wien Hohe Warte (Figure A-7) and Wien Innere Stadt (Figure A-8). An RMSE of 2.68 and 2.03, a bias of 1.55 and 0.28, respectively, were found. Under the circumstances described above, the imprecisions lead to an uncertainty of 0.2–0.3 K in the UTCI.

If we use the meteorological conditions of the future heat wave to estimate the forward propagation of a potential error of air temperature in the range of the calculated RMSE of 1.9 K, then we find that the UTCI increases directly with the air temperature, so this error would result in an increase of 1.9 K in UTCI as well.

The MRT and UTCI calculated by TEB was compared with the results of the higher spatially resolved model SOLWEIG. The validation is described in more detail in Annex A.

2.3 Definition of urban parameters of Vienna

In order to run the simulations, the urban parameters were derived for Vienna. First, they were obtained for the finest available scale, then aggregated on block scale of the Viennese municipal land use map (Realnutzungskartierung – <https://www.wien.gv.at/stadtentwicklung/grundlagen/stadtforschung/siedlungsentwicklung/realnutzungskartierung/pdf/rnk-2012.pdf>). This method was oriented on the study by CORDEAU (2016) and a graphical overview can also be found in the Annex (Figure B-1). The surface ratios of built, sealed and unsealed surface were derived from the highly detailed vector land cover data set (Flächenmehrzweckkarte – Viennese building height model (Baukörpermodell – <https://www.wien.gv.at/stadtentwicklung/stadtvermessung/geodaten/bkm>).

Building roughness height was estimated as $1/10^{\text{th}}$ of building height. The vertical to horizontal wall ratio was calculated using the above-mentioned vector data sets. The physical building parameters were derived by linking a dataset of building age and typology with typical building parameters obtained from different studies (BERGER et al., 2012; AMTMANN and ALTMANN-MAVADDAT, 2014) and the OIB (Austrian Institute of Construction Engineering). More information about the mapping of physical building parameters can be found in Annex B. Because the selected outer model domain covers $417 \text{ km} \times 297 \text{ km}$ (Figure A-1)

and thus is much larger than the area for which the LCZ map could be produced and WRF is not able to include all LCZ classes, so the Corine 2012 data set was used in this study. Unlike the LCZs and the UrbanAtlas, Corine 2012 is available for all WRF domains, and there is existing methodology for how to use Corine in WRF (PINEDA et al., 2004; SCHICKER et al., 2016). Corine is updated every 6 years. After this there might be even update cycles of 5 years, which makes it a very useful dataset.

While the standard version of WRF reclassifies Corine to USGS classes and thereby regroups all urban classes of Corine (1–11) to one urban class (PINEDA et al., 2004), WRF-TEB is enhanced to support the use of 3 urban classes. In order to take into account non-built and vegetated urban areas, some urban classes of Corine are reclassified to USGS Nature classes (Table B-1). The parameters are thus extracted for these classes. The final model setup is listed in Table B-2.

2.4 Urban Scenarios

In this study next to the actual Corine land use data set two adapted “future” Corine data sets were created which show differing urban distributions (see Annex C). A further additional five scenarios, where only urban parameters were changed are prepared (2.4.2). An overview of the parameters used is given in Table 1. The “reference scenario” (REF) is the base scenario and shows the distribution of urban area according to the Corine 2012 data set, generalized to USGS Classes (Fig. 1a). The two urban development scenarios “urban sprawl” (SPR) and “optimized city” (OPT) both assume the same increase of population and estimated gross floor area demand (see Annex C, Table C-1), but under different spatial distribution (see Annex C, Table C-2). SPR assumes the same material property as REF. OPT uses modified urban parameters as described in Section 2.4.1.

2.4.1 Change in material properties

Apart from the spatial changes, the OPT scenario differs in two aspects, which are intended to represent selected effective resilience measures which can potentially be implemented in Vienna to counteract climate change and to reduce the urban heat island within the possibility of the modelling framework (Table 1). This reduction is aimed to be achieved mainly by reduction of heat uptake by increasing reflection and by preventing heat transfer into the building and not by increasing the latent heat flux to avoid sultriness, which can play an important role at high air temperatures (STEADMAN, 1979a, b). Tree shade, which is a very important measure to improve human thermal comfort at street level could not be included in the study due to model constraints. It is assumed that the same resilience measures are applied to all three urban categories to obtain maximum effects.

Table 1: Overview of all presented scenarios: reference scenario (REF), the urban development scenarios: urban sprawl (SPR), optimized city (OPT), the resilience measure scenarios: increased albedo (ALB), decreased thermal conductivity of urban materials (INS), increased urban density (DEN), implementation of green roofs (GRR), installation of photovoltaic panels on roofs (PVR).

Name of urban scenario:	REF	SPR	OPT	ALB	INS	DEN	GRR	PVR
Total built urban area [km ²]	929	1115	939	929	929	929	929	929
relative to “REF” [%]	100 %	120 %	101 %	100 %	100 %	100 %	100 %	100 %
built area in urban category:								
<i>low density residential</i> [%]	22	22	24.2	22	22	24.2	22	22
<i>high density residential</i> [%]	46	46	46.2	46	46	46	46	46
<i>commercial</i> [%]	16	16	24.2	16	16	24.2	16	16
Thermal conductivity, roof [W/mK]	1.7	1.7	0.1	1.7	0.1	1.7	1.7	1.7
Thermal conductivity, wall [W/mK]	1.4	1.4	0.1	1.4	0.1	1.4	1.4	1.4
Thermal conductivity, ground [W/mK]	0.9	0.9	0.4	0.9	0.4	0.9	0.9	0.9
Albedo, roof [-]	0.15	0.15	0.68	0.68	0.15	0.15	0.154	0.1
Albedo, wall [-]	0.2	0.2	0.3	0.3	0.2	0.2	0.2	0.2
Albedo, ground [-]	0.138	0.138	0.3	0.3	0.138	0.138	0.138	0.138
Green roof fraction [-]	0	0	0	0	0	0	1	0
Photovoltaic fraction on roofs [-]	0	0	0	0	0	0	0	1
WRF-TEB online forcing for SURFEX offline simulations	REF	SPR	OPT	REF	REF	REF	REF	REF

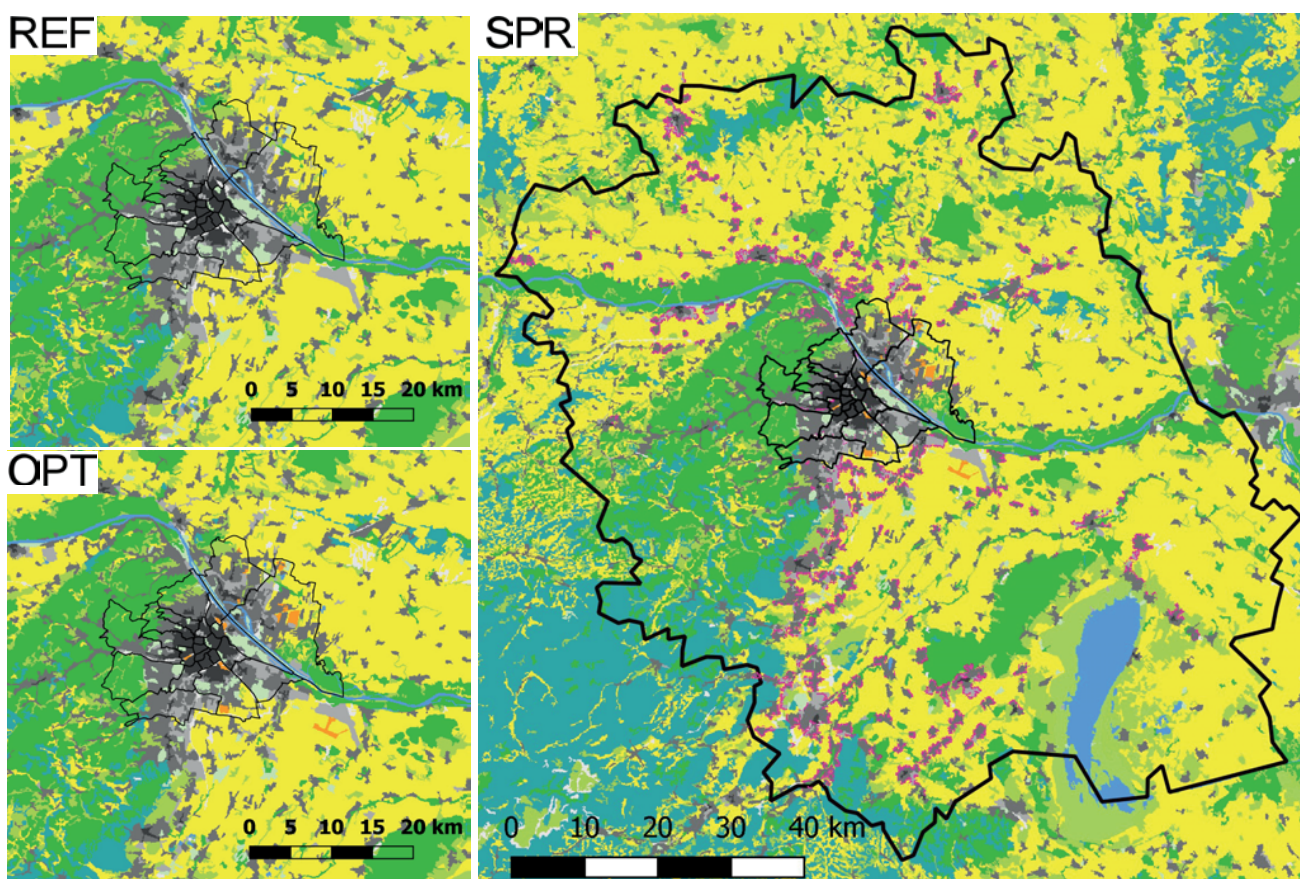


Figure 1: Spatial location of urban area in the three urban development scenarios: a) REF (up left), b) SPR (right) and c) OPT (down left). Actual urban areas are dark, middle and bright grey (high density residential, low density residential and commercial). Additional urban sprawl areas are purple. Known development areas are orange. Vegetation areas: yellow: dryland cropland and pasture (USGS class 2), bright green: mixed dryland/irrigated cropland and pasture (USGS class 4), brown-green: crops, shrubs, woodland mosaic (USGS classes 6+9), dark-green: deciduous forest (USGS class 11), blue-green: mixed forest (USGS class 15). The green areas surrounding the lake Neusiedel (south east of the region) is herbaceous wetland. The district borders of Vienna are thin black lines. The thick black line shows the border of stadregion+ (PGO 2011).

The pre-1919 structure of Vienna is rather uniform, consisting of mainly brick, partly lime stone walls of about 50 cm thickness. They are not insulated, have double glazing windows and a steep roof constructions covered with clay bricks. The more recent buildings are more diverse regarding morphology as well as physical parameters related to building construction practices (e.g., the main wall material and insulation material).

The first measure consists of enhancing the building insulation. The thermal conductivity of the roof and walls is decreased to 0.1 W/mK, which is the nearly zero-energy standard and required for all new buildings after 2020 according to the Energy Performance of Buildings Directive EPBD (<http://data.europa.eu/eli/dir/2018/844/oj>; AMTMANN and ALTMANN-MAVADDAT, 2014). The thermal conductivity of windows is decreased to 0.9 W/mK, which is a typical value used in refurbishment of multi-storied buildings (AMTMANN and ALTMANN-MAVADDAT, 2014). The thermal conductivity of roads is decreased to 0.4 W/mK, which is the lower boundary for medium concrete (https://www.engineeringtoolbox.com/thermal-conductivity-d_429.html). This change in material properties leads to a strong reduction of heat uptake by urban materials during the day, which is expected to cool the city during the evening, thus it might be an important factor for more effective cooling of rooms that have heated up. During the day, the well insulated urban structure is expected to take up less energy, which could lead to higher air temperatures during the day.

The second measure is intended to counteract the higher air temperature during the day due to the enhanced building insulation. The albedo of the walls and roads is only slightly increased from 0.2 and 0.13, respectively, to 0.3, which increases reflection of solar radiation, but also can help to reduce air temperatures (KRISPEL et al., 2017; WEIHS et al., 2018). The albedo of the roof is increased to 0.68, which is technically possible and more effective in order to reduce sensible heat flux, as has been investigated in various studies (TAHA et al., 1997; MORINI et al., 2016; ŽUVELA-ALOISE et al., 2018). FALLMANN et al. (2016) showed further that such measures are not likely to have known negative effects on the boundary layer height and pollutant concentrations. The albedo increase mainly counteracts the increase in air temperature during sunlit hours. Therefore, all negative effects of decreased thermal conductivity should be mitigated. RAMAMURTHY et al. (2015) analyzed the effectiveness insulation and high reflective roofs with an urban canopy model and suggests a combination. We note that the increase in albedo values does not depend on water availability and space demands, but it does compete with available surface areas for photovoltaic and green roof surfaces.

2.4.2 Resilience measures

The different resilience measures used in the OPT scenario are simulated separately in order to allow for a

precise attribution of their effect. In the following, the reduction of thermal conductivity is referred hereinafter as INS, the increase of albedo as ALB, and the densification caused by changes of built area from 0.22 (low residential areas) and 0.16 (commercial areas) to 0.242 as DEN. In addition, further potential mitigation and adaptation measures are investigated. These are a green roof (referred hereinafter as GRR) and a photovoltaic roof (referred hereinafter as PVR) scenario. For the GRR, the green roof module is used (DE MUNCK et al., 2013). An extensive roof coverage using sedum is assumed. For PVR, the photovoltaic roof module is used (MASON et al., 2014) assuming an efficiency of 20 % and an albedo of 10 % for the solar panels. An overview of all employed scenarios is given in Table 1. All these measures are applied on 100 % of the roof surface, which is a first and rather extreme approximation to estimate the potential maximum effects of such resilience measures. Apart from being adaptation measures, which mitigate the urban heat island by reducing air temperatures by conversion of sunlight to either electric current or photosynthesis and evapotranspiration at roof level, PVR is an effective mitigative measure, which helps to avoid greenhouse gas emissions. Green roofs, as active soil and vegetation layer could help to mitigate high greenhouse gas concentrations in the atmosphere as a carbon sink (LI and BABCOCK, 2014).

2.5 Present and future heat wave

An analysis of 15-yearly events is done in order to select suitable heat waves from external data that can be used to force the WRF simulations. The selected heat waves are 15 year return period events taken from the historical climate period (1988–2017, centred at 2002, “hw15yACT”) and also a future climate period (2036–2065, centred at 2050, “hw15ySCE”). The selection is based on the average daily maximum 2 m air temperature of heat waves (5 days). The historical heat wave is selected using observational data at the station Wien Hohe Warte supplied by the Austrian weather service ZAMG. The 5 day average daily maximum air temperature is calculated for the last 30 years (1988 to 2017) and the return period of these 5 day events is estimated using the Generalized Extreme Value Distribution (GEV; FISHER and TIPPETT, 1928). Due to the strong positive trend of more than 2 K within the last three decades for daily maximum air temperature, the data are detrended before applying the GEV.

As a reference heat wave for present-day modelling we choose the most intense 5 day heat wave of 1988–2017, which occurred in summer of 2015 with a 5 day temperature maximum mean of 36.3 °C (Table 2). According to the GEV distribution this event represents a heat wave with a return period of 15 years.

The regional climate change scenarios are based on the ensemble ÖKS 15 (LEUPRECHT et al., 2017; BMNT, 2016), a selection of 26 regional climate model scenarios from EURO-CORDEX (JACOB et al., 2014), derived

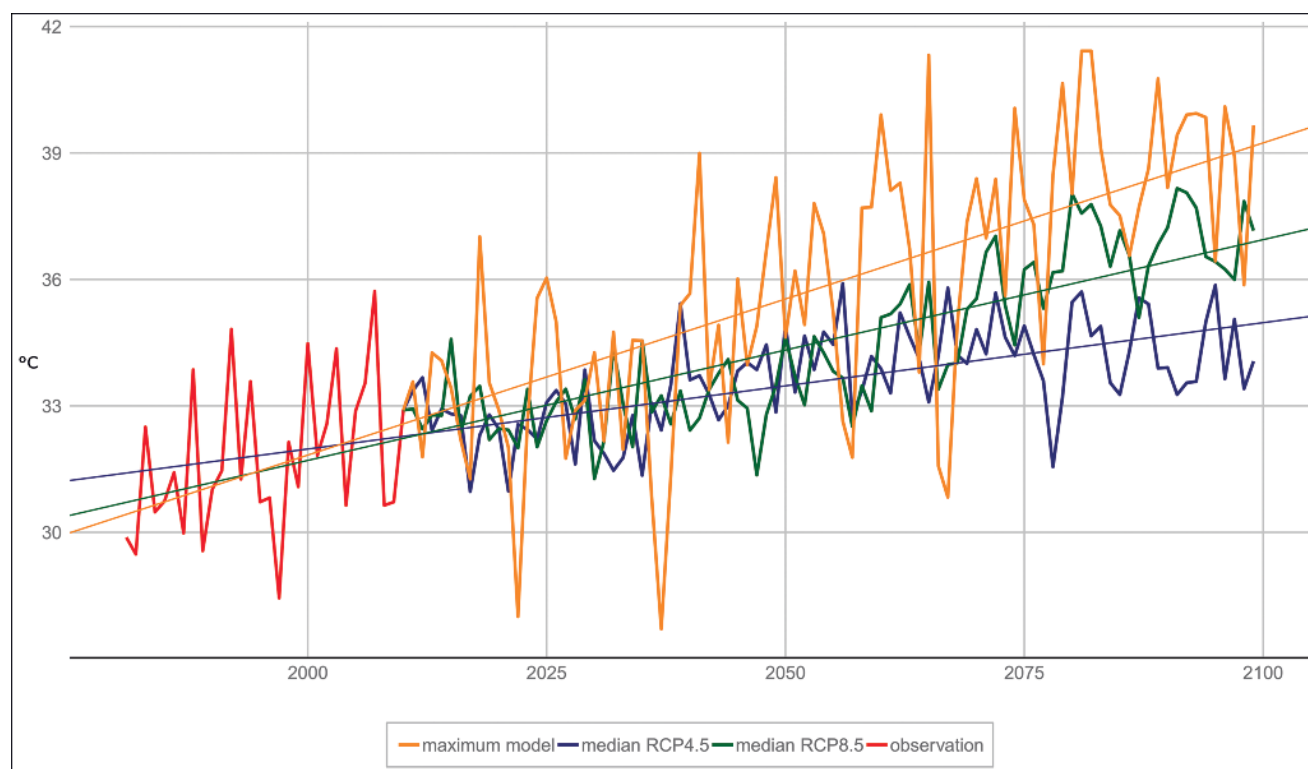


Figure 2: Maximum 5 day heat wave temperature (average of the daily temperature maximum of five consecutive days) per year at Vienna Hohe Warte observed (red), median of all scenarios forced with RCP4.5 (blue), median of all scenarios forced with RCP8.5 (green), scenario with the strongest trend of the whole ensemble (orange) and linear trend lines.

Table 2: Average daily maximum 2 m air temperature of heat waves (5 days) with 1, 2 and 15 year return periods derived from the station observations of Vienna Hohe Warte for the period 1988–2017 (first row) and climate change signals (2036–2065 versus 1988–2017) for this indicator based on the ÖKS 15 scenarios (LEUPRECHT et al., 2017) at a 1 km² grid cell at the same location.

Emission scenario/Return period	1 year	2 year	15 year
Observation (1988–2017) [°C]	28.7	31.6	36.3
RCP 4.5 ensemble median [K]	1.5	2.2	2.5
RCP 8.5 ensemble median [K]	1.8	2.7	2.2
Ensemble maximum [K]	5.9	3.7	4.8

from different global (TAYLOR et al., 2012) and regional climate models and forced with the emission scenarios RCP4.5 and RCP8.5. The ÖKS15 ensemble provides bias-corrected and localized (1 km) scenarios for daily minimum and maximum temperature, daily precipitation and daily radiation. Bias correction was done using a quantile mapping as described in SWITANEK et al. (2017). As only the daily maximum temperature is used for the quantification of the meteorological trend of the maximum temperature during 5 day heat waves, the spatial resolution of 1 km is sufficient.

For every ensemble member of ÖKS 15, we calculate the annual maximum 5-day mean of the daily maximum air temperature for the grid cell representing Hohe Warte in Vienna. Using the same GEV method we calculate

the heat wave air temperature for return periods of 1, 2 and 15 year events for the historical period 1988–2017 and the future period of 2036–2065. In Fig. 2, the development of the maximum 5-day heat wave air temperature per year is shown for observations (red), the ensemble median of all scenarios forced with RCP4.5 (blue), RCP8.5 (green) and the scenario with the strongest trend in heat wave air temperature of the whole ensemble (orange).

The observed heat wave air temperature at Wien Hohe Warte for 1, 2 and 15 year events of the period 1988–2017 and the climate change signal until the middle of the 21st century is given in Table 2. There are no large differences for the ensemble means between the two emission scenarios until the middle of the century. For the 15 year event, the RCP4.5 ensemble shows even a 0.3 K stronger warming than RCP8.5. However, there is a more pronounced warming seen when the more extreme heat waves occur. The 1 year events show a warming between 1.5 and 1.8 K and the 2 and 15 year events have a warming between 2.2 and 2.7 K. For the ensemble maximum scenario this relation is not seen and the strongest warming is for the 1 year event.

For the selection of the future scenario we chose the historical 15 year event heat wave air temperature (36.3 °C) and added the climate change signal of the 15 year event from the most extreme scenario (4.8 K). This choice can be interpreted as a plausible worst case scenario until the middle of the 21st century. This ex-

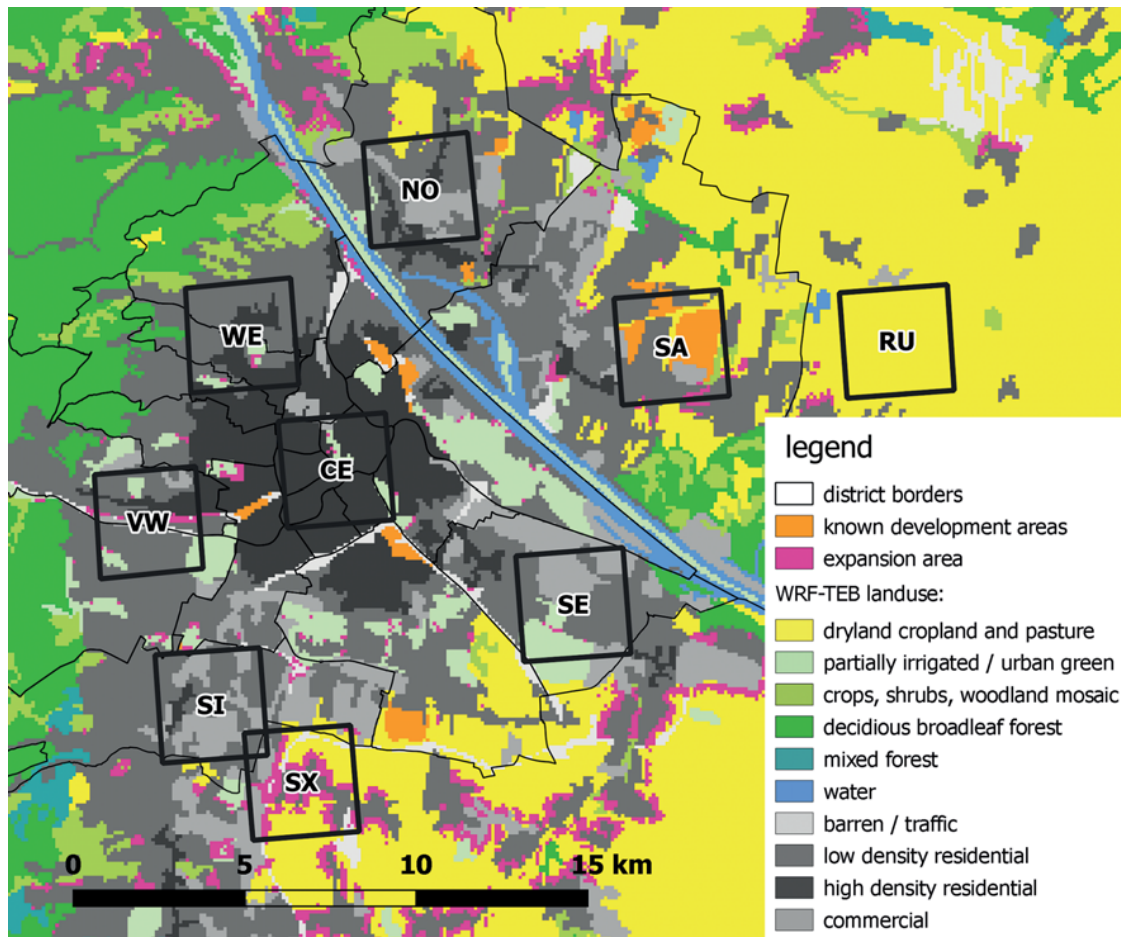


Figure 3: Subregions chosen for further analysis (clockwise): Central Districts (CE), North-Rim (NO), New development areas: Seestadt Aspern (SA), South-eastern rim (SE), South-industrial (SI), South expansion (SX), Valley of Wien (VW), West – elevated low density residential (WE), Rural area (RU).

Table 3: Mean values for Town Fraction (FRAC_TOWN) as they were calculated within this study, Built fraction [-] (D_BLD), Unsealed fraction [-] (D_GARDEN), Building height [m] (D_BLD_HEIG) and Vertical to horizontal wall factor [-] (D_WALL_O_H) for the Subregions of Fig. 3.

	CE	NO	RU	SA	SE	SI	SX	VW	WE
FRAC_TOWN	0.95	0.9	0.05	0.46	0.89	0.95	0.47	0.84	0.88
D_BLD	0.43	0.23	0.16	0.21	0.19	0.21	0.19	0.25	0.25
D_GARDEN	0.19	0.5	0.54	0.53	0.53	0.52	0.53	0.47	0.47
D_BLD_HEIG	18.75	11.44	11.2	10.68	10.9	11.13	10.85	12.11	11.85
D_WALL_O_H	1.75	1.11	0.5	1.08	0.83	1	0.89	1.2	1.27

tre climate scenario should also maximise the impact of the change of the urban structure (temperature increase) and should help to identify possible interactions between climate and land-use changes.

The lateral boundary conditions for a heat wave that fulfils the air temperature criteria (41.3 °C average 5 day daily maximum air temperature) are taken from a high-resolution regional climate scenario simulation. This simulation is based on the global model GFDL-CM3 (DONNER et al., 2011) forced with the RCP8.5 emission scenario and downscaled with the WRF model (MICHALAKES et al., 2001) with an optimized set up for

the Alpine region (ARNOLD et al., 2011). The regional model has a 10 km² spatial resolution and was run for the Alpine region and the whole 21st century. In addition to the 5-day period, a spin-up period of two–three days is used.

2.6 Study regions

For the presentation of the results, 9 areas of 9 × 9 model grid cells each (total of each area: 81 cells, 9 km²) are chosen to represent the variety within Vienna (Fig. 3, Table 3). The main subregion covers the central districts.

The magnitude of the urban heat island is quantified by calculating the spatial mean difference in the daily minimum values in 2 m air temperature between the grid cells of the central districts subregion (CE) and the rural (RU) subregion. The new development areas around Seestadt Aspern (SA) are chosen to quantify the change caused by the erection of this new built urban area. North-Rim (NO), South-industrial (SI), South-eastern rim (SE), are chosen as areas with high industrial coverage, which is likely to be densified, but are in suburban areas in different cardinal directions and thus exposed to different wind regimes. South expansion (SE) is chosen as another suburban area where urban densification is unlikely but urban sprawl is likely. Furthermore, a subregion in the west-elevated low density residential (WE) was chosen as representative for the climatological situation in the areas influenced by the far reaching forested and hilly areas west of Vienna and without change in the land use. Finally, an area in the Valley of Wien (VW) shall give information about changes in this area, which is climatologically distinct due to a valley breeze.

3 Results

Two reference heat waves were run for present (hw15yACT) and future (hw15ySCE) conditions. They were selected by their air temperature value. They both have very low wind speeds during the night (1 m/s) – so there is hardly any air advected (Figure D-1). During the day the wind ranges between 3 and 4 m/s. For hw15yACT it is from East to Southeast, for hw15ySCE it is from East to Northeast (Figure D-1). There were some disturbances in the downward shortwave flux at the ground surfaces (Figure D-2). So, these days were excluded together with the spin up time. Consequently, for hw15yACT 9, 10, 12 and 13 August 2015 (day 4, 5, 7 and 8) is used. For hw15ySCE 7 and 8 July 2069 (day 7 and 8) is used. The minima and maximum values for 2 m air temperature, MRT, canyon air temperature and UTCI shade are calculated using all daily extremes of each of the 81 grid cells of the cloud free days of the selected period. For the present heat wave these are 324 values (4 days), for the future heat wave there are 162 values (2 days).

The air advected from either of these directions stems mainly from agricultural plains. The 2 m air temperature in these agricultural regions are rather uniform with spatial differences smaller than 1 K for hw15yACT and 2 K for hw15ySCE (Figure D-3). Also, the simulated humidity field is uniform with spatial deviations from less than 2 g kg^{-1} (Figure D-4). The future heat wave shows temperatures above 40°C with a mixing ratio of 10 g kg^{-1} (mean water vapour pressure of 13.5 hPa). Both simulations have a surface pressure below 1000 hPa. For the present heat wave the dew point temperature did not surpass critical levels to cause sultriness. Also, for the future heat wave non-sultry conditions are expected. Soil moisture is declining near the surface during the heat wave (Figure D-5).

3.1 Viennese future heat load (T_{\max}) and UHI (T_{\min})

3.1.1 Reference scenario

The average daily maximum air temperature simulated by WRF-TEB (T_{\max}) increases by about 7 K between the historical and future heat wave (Fig. 5). Simulated average daily minimum air temperature (T_{\min}) increases between 2 and 4 K (Fig. 5). In the central districts the mean increases are 6.7 K and 3.2 K, respectively. The median values are slightly higher (6.8 K and 3.4 K). The variation of T_{\min} between the different areas is higher than that of T_{\max} . The urban-rural difference of the T_{\min} between Vienna city centre (CE) and the eastern agricultural areas (RU) for the present heat wave is 3.0 K. For the future heat wave, the urban-rural difference is greatly increased to 4.6 K (Fig. 4, 5, 6).

3.1.2 Future urban scenarios

The urban scenarios show a larger effect on minimum than on maximum air temperature (Fig. 5, 6). The influence on air temperature is generally less than 1 K, which is low compared to the air temperature increase due to climate change projected by the climate models (Fig. 5, 6). While SPR increases T_{\min} , OPT decreases T_{\min} for hw15yACT (Fig. 4 upper middle and right) and for hw15ySCE (Fig. 6). For SPR, the T_{\max} changes less than 0.1 K (Fig. 5). For OPT, the T_{\max} decreases in the range of 0.5 K for the subregions CE, SI, SX, VW and WE (Fig. 5).

3.2 Effects of resilience measures

The components of the OPT scenario (ALB, INS, DEN) as well as GRR and PVR are further analyzed.

First, the general influence on the town heat fluxes is shown for CE (3.2.1). Then the surface temperature of roof, ground and wall show more information (3.2.2).

3.2.1 Town energy fluxes in the central districts

At daytime for the ALB scenario, a reduction of up to 180 W/m^2 in net radiation and of about 100 W/m^2 in sensible heat flux is simulated. The effects are relatively constant throughout the heat wave (Fig. 7a). The INS scenario shows during the day on the one hand a decrease of the ground heat flux up to 150 W/m^2 , but an increase of the same magnitude of the sensible heat flux. During nighttime, the sensible heat flux is decreased up to 100 W/m^2 (Fig. 7b) and thus also air temperature is lower at night. The change in energy balance is mainly negative, with a declining trend. Also, the difference of sensible heat flux during the day shows a declining trend towards the end of the heat wave. For the DEN scenario, the ground heat flux increases by 100 W/m^2 during the day and decreases by 30 W/m^2 during the night (Fig. 7c). The implementation of green roofs (GRR) increases net radiation by up to 80 W/m^2 during the day – an effect

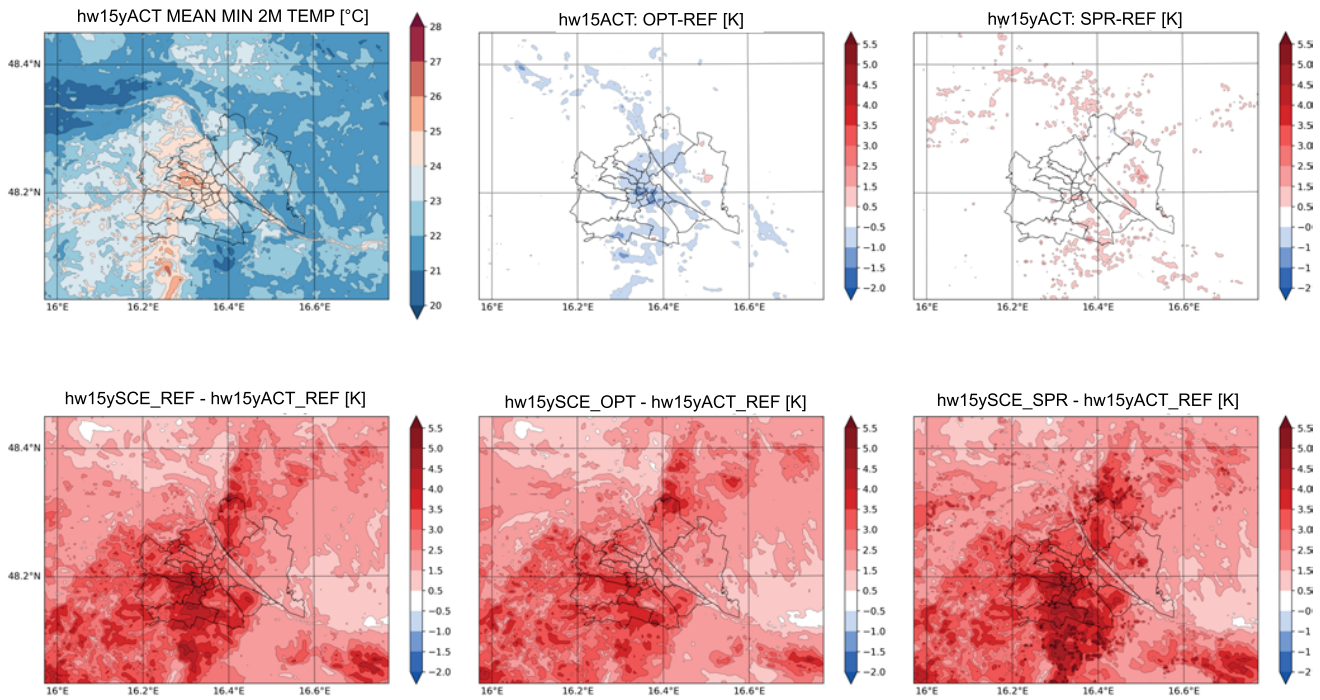


Figure 4: Mean minimum of the selected cloud free days for each grid cell for the daily 2 m minimum air temperature for the present heat wave hw15yACT (upper left). Differences between reference scenario hw15yACT and urban development scenarios OPT (middle) and SPR (right) (upper panels). Differences between reference scenario for present (hw15yACT) and future (hw15yrSCE) for the REF (left), OPT (middle) and SPR (right) urban development scenario (lower panels).

that diminishes to the end of the heat wave (Fig. 7d). The latent heat flux increases by up to 230 W/m^2 , the sensible heat flux decreases by up to 100 W/m^2 . The implementation of solar panels (PVR) decreases both the sensible heat flux and the net radiation by about 100 W/m^2 (Fig. 7e).

3.2.2 Surface temperatures of roof, wall and road in the central districts

On the roof five resilience measures show different properties. This causes a different increase in roof surface temperature during the day (Fig. 8a). The strongest diurnal amplitude is seen in INS. GRR and ALB both have cooler roof surfaces than REF. PVR stays coolest under the assumptions of this study.

The surfaces within the canyon are only altered in ALB and INS, therefore only these resilience measures are shown for wall and road. On the unsealed fraction there are no changes done. The wall surfaces show that INS strongly alters the wall surface temperature compared to REF. During daytime, there is an increase by more than 10 K and during night a decrease of up to 5 K (Fig. 8b).

The road surface temperatures show the least changes, but also here it can be seen that INS increases the maximum surface temperature whereas ALB decreases it (Fig. 8c).

3.3 Canyon parameters and human thermal stress

Finally, the parameters relevant to quantify human thermal stress or comfort are analyzed within the street canyon. For the canyon wind speed no changes greater than 0.5 m/s have been found. Also, the canyon humidity changes are $\ll 0.01 \text{ kg/kg}$. For the MRT and canyon air temperature there do exist notable changes. During heat waves after MRT, the air temperature has a great impact on determining whether the UTCI reaches thermal stress levels or stays in the human thermal comfort region. Therefore, the effect of the separate measures on the mean radiant temperature and canyon air temperature was analyzed. In Fig. 9 timeseries of MRT and canyon air temperature during the whole heat wave hw15ySCE are shown for the central districts (CE). Table 4, 5 and 5 give additional information about the minima and maxima in the subregions.

3.3.1 MRT

The MRT maxima for the reference scenario increase by 6.6 K in the shade and 7.6 K in the sun between the present and future scenario for the central districts (Table 4a). For GRR, DEN and PVR the difference in MRT maxima to the reference scenario was less than 0.2 K (Table 4b, 4c) for all subregions. For ALB the mean increase of maximum MRT is 2.3 (Table 4c, Fig. 9a) for CE. For INS the MRT increased during day up to 8 K

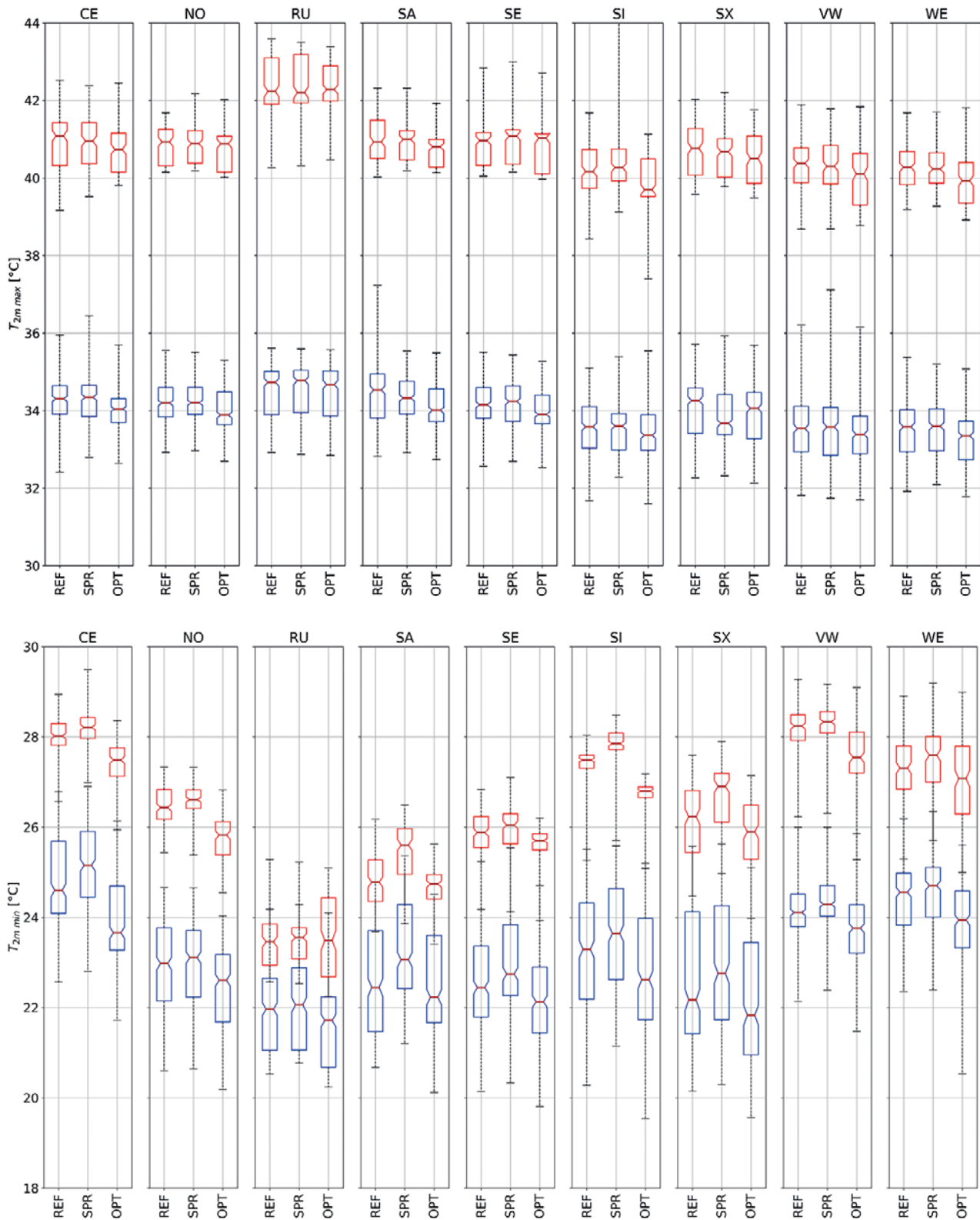


Figure 5 and 6: 2 m air temperature for the selected cloud free days of the chosen climate episode for present (hw15yACT, blue) and future (hw15ySCE, red) and the 3 different urban development scenarios (sh. Table 1) for daily maximum temperature (above) and daily minimum temperature (below) in the 9 different subregions (Fig. 3): Central Districts (CE), North-Rim (NO), New development areas: Seestadt Aspern (SA), South-eastern rim (SE), South-industrial (SI), South expansion (SX), Valley of Wien (VW), West – elevated low density residential (WE), Rural area (RU).

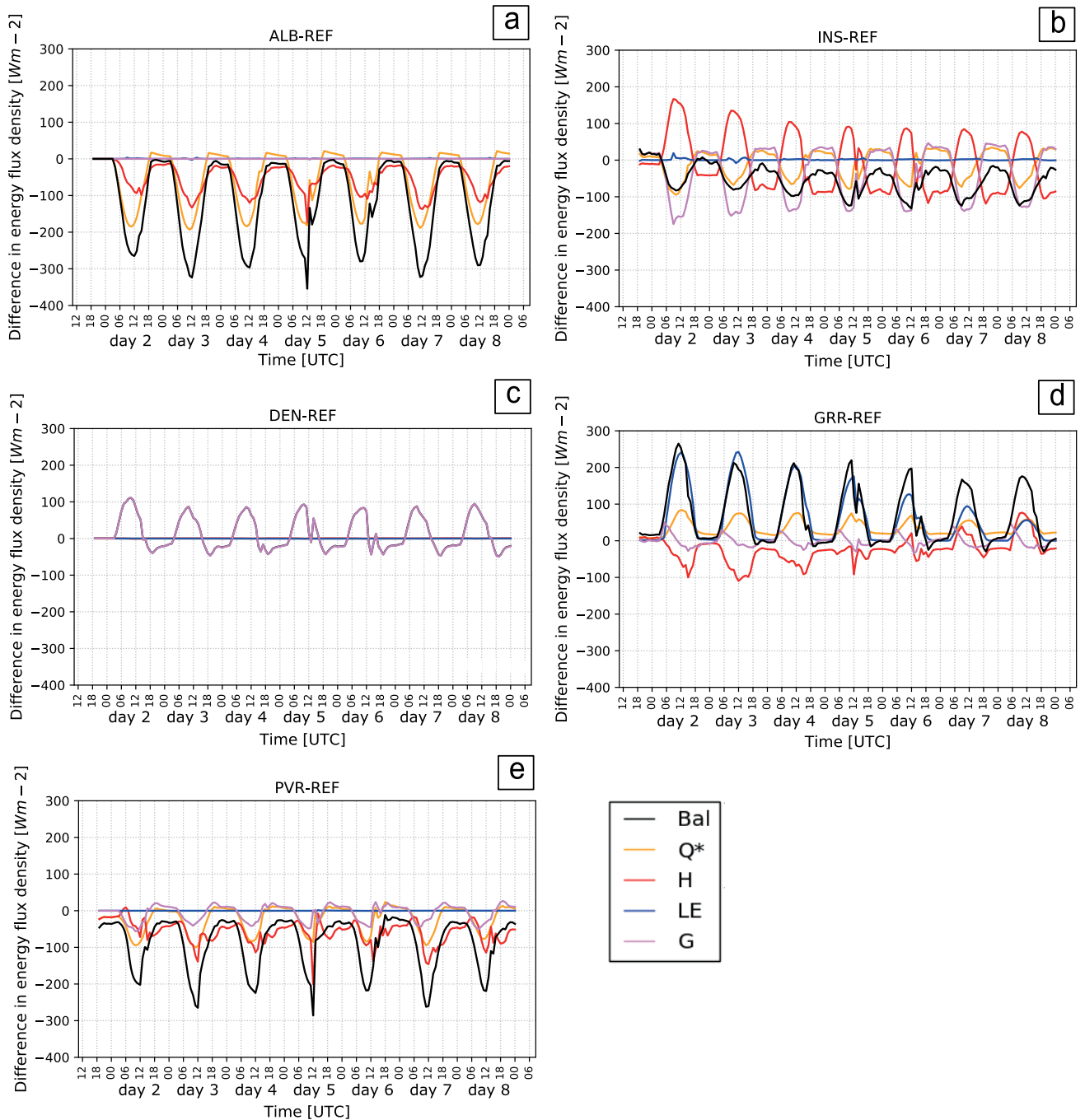


Figure 7: Timeseries differences compared to reference (REF) of radiation balance (Q^*), sensible (H), latent (LE) (positive downwards), ground (G) heat flux and energy balance (Bal) during the hw15ySCE in the Central Districts (CE) for different measures: ALB (increased albedo), INS (insulation), DEN (density), GRR (green roof) and PVR (photovoltaic roof)

and decreased at night up to 3 K (Fig. 9b) for CE. On average this is an increase of 5 K (Table 4c) for CE. Both the daily maxima and minima of both variables show a declining trend for CE (Fig. 9b).

3.3.2 Canyon air temperature

For SPR the maximum canyon air temperature increases by 0.2 K (Table 5b) in the central districts (CE). For OPT, both the minimum and maximum canyon temperature decrease by 0.2 and 0.9 K in CE (Table 5b, 5c)

respectively. In the new urbanized areas (SA) itself the maximum and minimum canyon temperature increase by 0.7 and 1.0 K for SPR. In the OPT scenario, the mean increase is only 0.5 K and 0.3 K in SA (Table 5b, 5c) while for the median of the 2 m air temperature calculated by WRF-TEB there is even a decrease (Fig. 5 and 6).

For ALB the canyon air temperature maxima and minima decrease by not more than 0.2 K and 0.1 K, respectively in all subregions (Table 5b, 5c). For INS

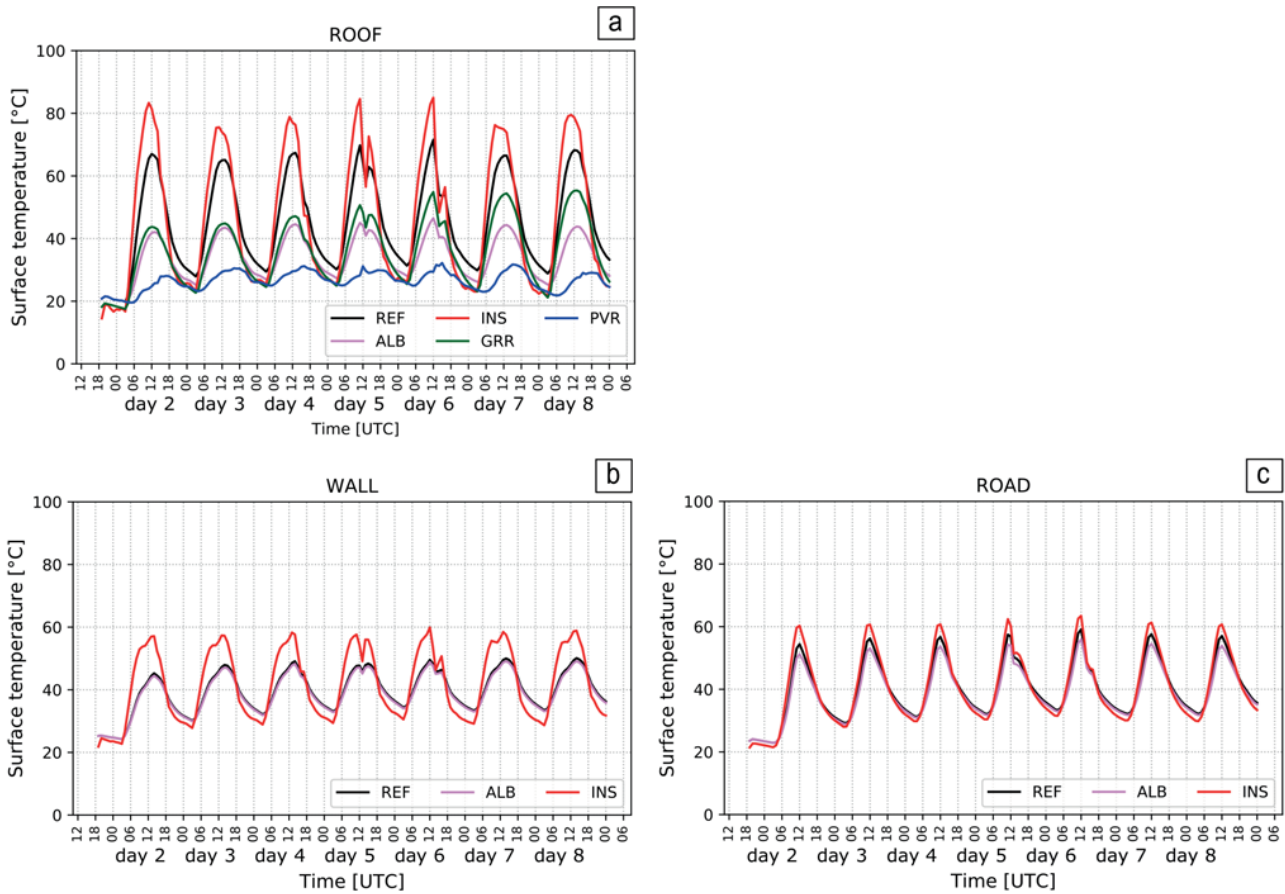


Figure 8: Time series of the surface temperature of roof (a), wall (b) and road (c) of the resilience measures where changes have been applied to these surfaces – during the future episode (hw15ySCE) for the Central Districts (CE).

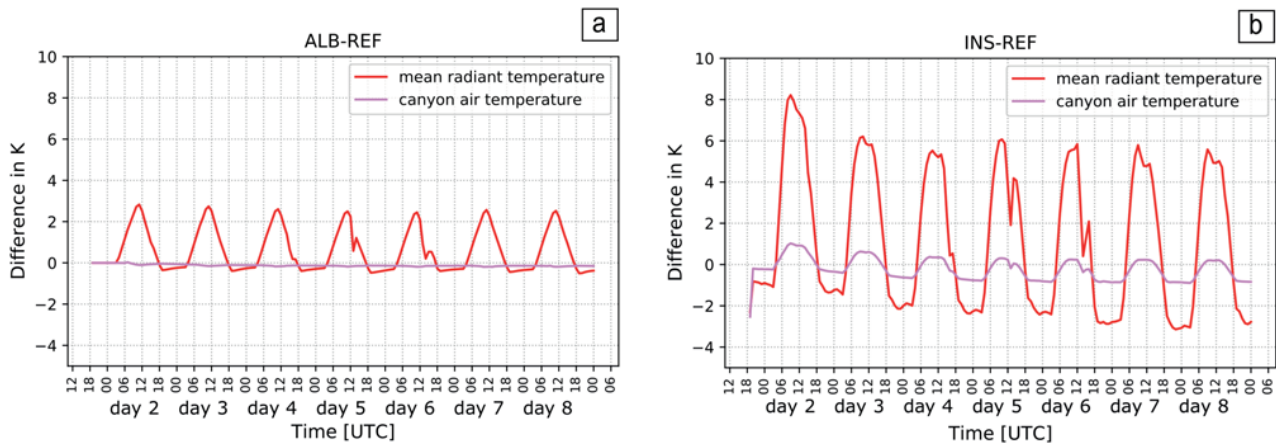


Figure 9: Difference of time series of two elements of UTCI, changed by the resilience measures: Mean radiant temperature in the shade and canyon air temperature during the future episode (hw15ySCE) for the Central Districts (CE).

the maximum canyon temperature does not increase by more than 0.1 K while the minimum canyon temperature decreases up to 0.8 K, where 0.8 K are only reached in the central districts (Table 5b, 5c). For DEN the changes for maximum and minimum canyon air temperature are below 0.1 K in all subregions (Table 5b, 5c). For GRR

both maximum and minimum canyon air temperature decrease by 0.1 K and 0.2 K, respectively, in CE and are lower in all other subregions (Table 5b, 5c). For PVR both maximum and minimum canyon air temperature decrease by 0.2 K and 0.2 K in CE and are lower in all other subregions (Table 5b, 5c), respectively.

Table 4: a) absolute maximum and minimum radiant temperature (MRT) values [°C] of the actual (hw15yACT – “ACT”) and future heat wave (hw15ySCE – “SCE”) of the reference run and differences [K] of b) maximum MRT in the sun c) maximum MRT in the shade and d) minimum MRT (shade = sun) to the reference run hw15ySCE for the cloud free days of the selected episode, for all urban scenarios and resilience measures spatial mean in the 9 different subregions (Fig. 3): Central Districts (CE), North-Rim (NO), New development areas: Seestadt Aspern (SA), South-eastern rim (SE), South-industrial (SI), South expansion (SX), Valley of Wien (VW), West – elevated low density residential (WE), Rural area (RU) – which is *only based on 4 values. Differences over +/-1 are marked red/blue.

a) MRT		CE	NO	RU*	SA	SE	SX	SI	VW	WE
REF ACT	Shade, max	47.8	50.8	50.4	51.9	50.9	51.3	51.0	50.5	50.7
REF ACT	Shade, min	27.5	23.6	20.2	23.2	22.3	22.6	23.2	24.1	24.7
REF ACT	Sun, max	73.2	75.9	75.2	76.5	75.8	76.2	76.1	75.6	24.8
REF SCE	Shade, max	54.4	56.6	54.2	57.07	56.0	55.1	55.4	55.8	56.1
REF SCE	Shade, min	30.9	25.9	21.1	25.16	24.2	24.6	25.8	27.3	27.4
REF SCE	Sun, max	80.8	82.4	80.6	82.73	81.9	81.4	81.7	81.9	82.1
b) maximum MRT in the sun, differences to REF (both: hw15ySCE)										
SPR		-0.1	-0.1	0.3	-0.9	0.1	0.3	0.2	0.0	0.0
OPT		0.6	0.2	0.5	-0.5	0.4	0.5	0.5	0.4	0.6
ALB		1.9	1.5	1.6	1.4	1.5	1.6	1.6	1.6	1.6
INS		4.0	2.3	1.3	2.2	1.9	1.6	1.8	2.2	2.4
DEN		0.0	0.1	0.1	0.0	0.1	0.1	0.1	0.1	0.1
GRR		-0.1	-0.0	-0.0	-0.0	-0.0	-0.0	-0.0	-0.1	-0.1
PVR		-0.1	-0.1	-0.0	-0.1	-0.1	-0.1	-0.1	-0.1	-0.1
c) maximum MRT in the shade, differences to REF (both: hw15ySCE)										
SPR		-0.1	-0.1	0.6	-1.3	0.1	0.5	0.3	0.1	0.1
OPT		0.3	-0.1	0.6	-1.1	0.2	0.4	0.6	0.3	0.50
ALB		2.3	1.8	2.0	1.8	1.8	1.9	1.9	2.0	1.9
INS		5.0	3.0	1.7	2.8	2.6	2.0	2.3	2.8	3.0
DEN		0.0	0.1	0.1	0.0	0.1	0.1	0.1	0.1	0.1
GRR		-0.1	-0.1	-0.0	-0.1	-0.0	-0.0	-0.1	-0.1	-0.1
PVR		-0.2	-0.1	-0.0	-0.1	-0.1	-0.1	-0.1	-0.1	-0.1
d) minimum MRT, differences to REF (both: hw15ySCE)										
SPR		0.0	0.2	0.1	2.2	0.1	0.8	0.1	0.1	0
OPT		-0.4	0.2	0.2	2.3	0.3	0.2	0.1	0.2	0.3
ALB		-0.3	-0.3	-0.2	-0.2	-0.3	-0.3	-0.3	-0.3	-0.3
INS		-3.1	-2.6	-1.9	-2.6	-2.5	-2.5	-2.6	-2.6	-2.8
DEN		0.0	0.5	0.4	0.6	0.5	0.5	0.5	0.5	0.5
GRR		-0.2	-0.1	-0.1	-0.1	-0.1	-0.1	-0.1	-0.1	-0.1
PVR		-0.2	-0.1	-0.1	-0.1	-0.1	-0.1	-0.1	-0.1	-0.1

3.3.3 Universal Thermal Comfort Index (UTCI)

Both MRT and canyon air temperature influence the magnitude of UTCI. Here, mainly UTCI shade is used. The maximum future UTCI in the sun for hw15ySCE is included as reference in Table 6e. Values of 51.0 °C in the central districts (CE) and 49.6 °C in the rural region (RU) are extremely heat stressed (BRÖDE et al., 2012), so that we did not think it feasible to reduce it to a comfortable range by applying resilience measures. Between the present (hw15yACT) and future (hw15ySCE) heat wave there is already an increase of 5.3–6.3 K for the absolute maximum UTCI shade averaged over the different subregions (Table 6a). The absolute minimum UTCI changes least in the rural areas, but within the urban areas can increase up to 3 K (Table 6c).

Compared to the reference scenario (REF), in the urban sprawl scenario (SPR), the UTCI increases excluding SA (maximum UTCI by less than 0.1, minimum

UTCI by up to 0.4), whereas in the optimized urban development scenario (OPT), the UTCI is reduced (maximum by up to 0.2 K, and the minimum by up to 0.7 K) in most areas. The largest differences are simulated in the new development areas (SA) where new urban districts are constructed on formerly unbuilt land (Table 6b, 6d). Here also in the OPT scenario there are increases of maximum and minimum UTCI by 0.9 K and 0.4 K, respectively. In the SPR scenario in the new development areas (SA) the UTCI maximum increases by 0.6 K and the minimum by 1.3 K. Also, in other areas of potential spread of settlement area, especially the minimum UTCI is increased, e.g., in South expansion areas (SX) by 0.4 K (Table 6d).

For ALB the average daily maximum UTCI increases by 0.2 K, while the average daily minimum decreases by 0.1 K in CE (Table 6b, 6d). For INS the daily maximum UTCI increases by 1.2 K, while the daily minimum decreases by 1.2 K in CE (Table 6b, 6d).

Table 5: a) absolute maximum and minimum canyon air temperature values [°C] of the future heat wave (hw15ySCE) for the reference run. b) differences [K] for the maximum canyon air temperature and c) differences [K] for the minimum canyon air temperature to the reference run hw15ySCE. average values for the cloud free days of the selected episode for all urban scenarios and *resilience measures* spatial mean in the 9 different subregions (Fig. 3): Central Districts (CE), North-Rim (NO), New development areas: Seestadt Aspern (SA), South-eastern rim (SE), South-industrial (SI), South expansion (SX), Valley of Wien (VW), West – elevated low density residential (WE), Rural area (RU) – which is *only based on 4 values. Differences over ± 0.25 are marked red/blue.

a) canyon air temperature	CE	NO	RU*	SA	SE	SX	SI	VW	WE
REF max	43.8	42.6	42.2	42.3	42.3	42.2	42.1	42.3	42.1
REF min	29.9	27.4	24.2	25.9	26.5	27.5	28.3	29.3	28.2
b) maximum canyon air temperature, differences to REF (both: hw15ySCE)									
SPR max	-0.0	-0.0	-0.0	0.7	0.1	0.1	-0.0	0	0.0
OPT max	-0.2	-0.1	-0.3	0.5	0.1	-0.2	-0.1	-0.2	-0.1
ALB max	-0.2	-0.1	-0.1	-0.1	-0.1	-0.1	-0.2	-0.1	-0.1
ISO max	0.1	0.1	0.0	0.1	0.1	0.1	0.0	0.1	0.1
DEN max	0	0.0	-0.0	0.0	0.0	0.0	0.1	0.0	0.1
GRR max	-0.1	-0.0	-0.0	-0.0	-0.0	-0.0	-0.0	-0.0	-0.1
PVR max	-0.2	-0.1	-0.0	-0.0	-0.1	-0.1	-0.0	-0.1	-0.1
c) minimum canyon air temperature, differences to REF (both: hw15ySCE)									
SPR min	0.2	0.3	0.2	1.0	0.0	0.3	0.3	0.1	0.2
OPT min	-0.9	-0.8	-0.1	0.3	-0.1	-0.3	-0.7	-0.8	-0.5
ALB min	-0.1	-0.1	-0.1	-0.1	-0.1	-0.1	-0.1	-0.1	-0.1
ISO min	-0.8	-0.3	-0.0	-0.3	-0.3	-0.3	-0.3	-0.3	-0.3
DEN min	0.0	0.1	0.1	0.1	0.1	0.1	0.1	0.1	0.0
GRR min	-0.2	-0.1	-0.1	-0.1	-0.1	-0.0	-0.1	-0.1	-0.1
PVR min	-0.2	-0.1	-0.1	-0.1	-0.1	-0.1	-0.1	-0.1	-0.1

For DEN the changes of UTCI of both maxima and minima are below 0.1 K on average in the central districts, where no densification takes place. In the densified districts with widespread commercial/industrial areas (SE, SI and NO), canyon air temperature is increasing, but changes are still below 0.1 K. The daily maximum UTCI increases only below 0.1 K whereas the daily minimum UTCI increases by 0.2 K (Table 6b, 6d). For GRR the daily maximum UTCI decreases by 0.1 K whereas the daily minimum UTCI decreases by 0.2 K (Table 6b, 6d) in CE. For PVR the daily maximum UTCI decreases by 0.2 K and the daily minimum UTCI by 0.2 K (Table 6b, 6d) in CE.

Most scenarios show a significant difference to the reference in their extreme values with $p \ll 0.05$ using the T-Test for related samples in the central districts. Only SPR does not show a significant difference in minima and maxima UTCI when the central districts are compared.

4 Discussion

4.1 Global climate change and influence on the Vienna region

4.1.1 Air temperature (T_{\max} and T_{\min}):

The lateral boundary conditions of the future heat wave are taken from regional climate scenarios, which are based on the global model GFDL-CM3 (DONNER et al.,

2011) forced with the RCP8.5 emission. The air temperature calculated for the selected 9 km² subregions of Vienna using 3 nests in this study increases by up to 7 K for the T_{\max} and 2 to 4 K for the T_{\min} values from the heat waves hw15y2015ACT to hw15ySCE. This means that both heat waves have Kysely days (KYSELY et al., 2000) and tropical nights ($T_{\min} > 20^\circ\text{C}$). This shows a strong increase in T_{\max} for extreme heat waves compared to the mean annual air temperature increase of 3.5 K published by APCC (2014) and GOBIET et al. (2014), which also refers to AIB instead of the more extreme RCP8.5. For France increases of 6–13 K for different regions by 2100 have been projected by BADOR et al. (2017). SENEVIRATNE et al. (2018) found positive air temperature anomalies of 8 K for Central Europe for the 21st century. Soil moisture – temperature feedbacks after early and intensified depletion of root-zone soil moisture contribute significantly to the Central European strong increases in extreme temperature (VIDALE et al., 2007; VOGEL, 2018).

It is interesting to note that the projected increase in T_{\max} (Fig. 5) is more than twice as strong as the increase projected for the mean annual temperature in Austria (3.5 K), while the T_{\min} (Fig. 5) are projected to increase about the amount of the mean annual temperature. As a result, the daily temperature range is projected to increase. Such an increase in daily temperature range was also found by CATTIAUX et al. (2015) and be could also be partly attributed to the decreasing surface evaporation due to soil moisture depletion in future European summers (JASPER et al., 2006). This also affects the ru-

Table 6: a) absolute maximum UTCI shade values [°C] of present (hw15yACT – cloud free days: 4, 5, 7, 8) and future (hw15ySCE – cloud free days: 7, 8) of the reference run followed by the difference [K] between the two heat waves and b) differences [K] to the reference run hw15ySCE average values for the cloud free days of the selected episode for all urban scenarios and *resilience measures* spatial mean in the 9 different subregions (Fig. 3): Central Districts (CE), North-Rim (NO), New development areas: Seestadt Aspern (SA), South-eastern rim (SE), South-industrial (SI), South expansion (SX), Valley of Wien (VW), West – elevated low density residential (WE), Rural area (RU). Differences over ± 0.5 are marked red/blue. c) and d) show the same for minimum UTCI shade, e) shows absolute maximum UTCI sun values for the hw15ySCE.

a) max UTCI shade	CE	NO	RU	SA	SE	SX	SI	VW	WE
hw15yACT	38.9	38.8	38.1	38.2	38.2	38.3	38.7	38.6	38.3
hw15ySCE	45.2	44.4	43.9	44.2	44.2	43.7	44.0	44.1	44.0
hw15ySCE-hw15yACT	6.3	5.6	5.8	5.6	6.0	5.4	5.3	5.5	5.7
b) max UTCI shade, differences to REF (both: hw15ySCE)									
SPR max	0.0	0.0	0.1	0.6	-0.1	0.1	-0.2	0.1	-0.0
OPT max	-0.1	-0.1	-0.0	0.4	-0.1	-0.0	-0.2	-0.1	0.2
ALB max	0.2	0.3	0.2	0.3	0.3	0.3	0.3	0.3	0.3
INS max	1.2	0.8	0.3	0.6	0.6	0.5	0.5	0.7	0.7
DEN max	0.0	0.0	0.0	0.1	0.0	0.0	0.1	0.1	0.1
GRR max	-0.1	-0.0	0.5	0.1	-0.0	-0.0	-0.1	-0.0	-0.0
PVR max	-0.2	-0.1	0.5	0.0	-0.1	-0.0	-0.1	-0.1	-0.1
c) min UTCI shade	CE	NO	RU	SA	SE	SX	SI	VW	WE
hw15yACT	26.6	23.5	21.7	23.3	22.0	23.1	23.9	24.4	25.3
hw15ySCE	28.8	25.8	22.1	24.5	24.9	25.4	26.4	27.4	26.9
hw15ySCE-hw15yACT	2.2	2.3	0.4	1.2	2.9	2.3	2.5	3.0	1.6
d) minimum UTCI shade, differences to REF (both: hw15ySCE)									
SPR min	0.2	0.3	0.3	1.3	0.0	0.4	0.2	0.1	-0.1
OPT min	-0.7	-0.5	0.1	0.9	0	-0.3	-0.6	-0.6	-0.4
ALB min	-0.1	-0.1	-0.0	-0.0	-0.0	-0.1	-0.1	-0.1	-0.1
INS min	-1.2	-0.9	-0.8	-1.0	-0.7	-0.9	-0.8	-1.0	-0.8
DEN min	0.0	0.2	0.2	0.2	0.2	0.2	0.2	0.2	0.2
GRR min	-0.2	-0.1	-0.1	-0.1	-0.1	-0.1	-0.1	-0.1	-0.1
PVR min	-0.2	-0.1	-0.1	-0.1	-0.1	-0.1	-0.1	-0.1	-0.1
e) maximum UTCI sun, absolute values									
hw15ySCE	51.0	50.3	49.5	50.0	50.0	49.4	49.7	49.8	49.8

ral surroundings, which are even more affected by reduced soil moisture than urban areas with high sealing fractions. Drier soils have a lower heat capacity and can cool more strongly than wetter soils. Also, in this study a decrease of soil moisture was simulated (Figure D-5). This can explain the high values of T_{\max} in the rural subregion during day but also the low values of T_{\min} during night, thus this could be the reason of the increase of the future nocturnal urban-rural difference.

The nocturnal canopy UHI is expected to increase from 3 to 4.6 K which is caused rather by the lower increase of minimum temperatures in the rural areas than within the city.

The actual and future UHI is strongly dominated by the mesoscale thermal regime and especially the future UHI is affected by high temperature reinforced by dry fields in the surroundings, which is a known process during heat waves (FISCHER and SENEVIRATNE, 2007; HARTMANN, 1994). FISCHER and SENEVIRATNE (2007) analyzed the interactions between soil moisture and atmosphere for the 2003 summer heat wave in Europe and found that precipitation deficits, early vegetation growth and positive radiation anomalies preceded

ing the heat wave contributed to rapid loss of soil moisture. ZAMPIERI et al. (2009) showed that drought in the Mediterranean region can favour heat waves conditions in Europe at a continental scale by change in atmospheric circulation and hot air mass advection. This would suggest, that soil moisture deficits ought to be reduced by suitable methods on a continent-scale rather than only regional scale. DUCHEZ et al. (2016) and KORNHUBER et al. (2017) name a stationary jet stream position, caused by global scale circulation patterns, that coincides with observed European temperature extremes, including the 2015 event.

4.1.2 Thermal comfort index UTCI

The Universal Thermal Climate Index (UTCI) is used by meteorological services to quantify outdoor human thermal comfort and has been included in TEB to provide standardized information about human thermal comfort for grid resolutions > 100 m and with highly parameterized building morphology. It takes into account whole body thermal effects thanks to a multi-node thermophysiological model. It is derived by the air temperature, water vapour pressure and MRT, which is a quantity that

describes the shortwave and longwave radiation balance of the human body at 2 m and wind speed at 10 m height (JENDRITZKY et al., 2012; WEIHS et al., 2012). In this study first WRF-TEB uses the different urban roughness of the three used building morphologies to calculate a 10 m wind, which is 10 m above the mean building height – so around 30 m agl in the city centre. Within the UTCI calculation a 6th order polynomial is used that assumes a uniform roughness length of 0.01 and a logarithmic profile, which reduces the 10 m wind to 70 % at 1.3 m. Although the roughness length is low this attenuation is very similar to the attenuation between above roof and within canyon wind speeds presented in ERELL et al. (2011), which is based on PEARLMUTTER et al. (2005). They found an attenuation of around 60 % and 70 % caused by street canyons of a height/width ratio 0.66 and 1.0, as they are common in the Viennese city structure, which varies $\pm 10\%$ dependent on the wind direction or ‘angle of attack’. The influence of the low roughness was further calculated by first applying the Hellman’s exponential law (URBAN and KYSELY, 2014; KETTERER et al., 2017) with the maximum roughness assumed for Vienna ($z_0=2$) to calculate a more realistic reduction of wind speed from the 10 m level to 1.3 agl. Using this second approach the average wind speeds occurring in heat waves analysed in this study of 2.2 m/s were reduced to 0.3 m/s. Then the 10 m wind was recalculated with the agreed UTCI logarithmic profile and a z_0 of 0.01. For the future heat wave situation of an air temperature of 40 °C, an MRT shade of 50 °C, an average water vapour pressure of 13.5 hPa, this change in wind speed results in a UTCI change of 0.3 K during the period of maximum MRT. For water vapour pressure of 20 hPa the change is only 0.1 K UTCI.

A recent comparison has been done by ZARE et al., 2018, which shows that UTCI and PET are highly correlated. URBAN and KYSELY (2014) found for two regions in Bohemia that the simplification and underestimation of urban roughness only affects the prediction during cold spells, while PET and UTCI are both suitable to predict thermal discomfort during heat waves.

The maximum UTCI changes during extreme heat waves projected for the climate period 2050 from strong (32–38 °C UTCI) to very strong (38–46 °C UTCI) heat stress. This goes with other studies regarding future human thermal comfort. For example, MUTHERS et al. (2010) projected that even heat-related mortality could increase up to 129 % in Vienna until the end of the century, if no adaptation takes place. MATZARAKIS and ENDLER (2010) showed for Freiburg an increase of days with heat stress (PET>35 °C) in the order of 5 % (from 9.2 % for 1961–1990) per year.

4.2 City scale urban scenarios

4.2.1 Urban sprawl scenario

Urban sprawl of the Viennese agglomeration affects urban energy fluxes and temperature mainly in areas

where new urban fabric is constructed on formerly vegetated areas. The sensible heat flux increases by up to +400 W/m² (not shown in the Figures), T_{\min} by 1 K and the daily minimum UTCI by 1.3 K. No significant differences are simulated in the central districts, and no significant influence on the nocturnal UHI was found.

KOHLER et al. (2017) presented a similar study for the Strasbourg–Kehl urban region (France–Germany). They conclude that under realistic assumptions urban sprawl until the year 2030 will not affect the UHI intensity significantly. Significant warming was only observed at atmospheric grid cells for which the urban fraction was increased more than 20 % compared to the initial case.

4.2.2 Optimized urban scenario

The optimized urban development scenario (OPT), which includes densification, slightly reduces air temperatures during the day, but clearly reduces them at night by 0.9 K. This leads to a slight reduction of nocturnal UHI by about 0.5 K. Also, the daily minimum UTCI is reduced by up to 0.7 K. The changed material properties can therefore counteract the negative effects of densification, which shows that the existing densification strategy of the city of Vienna (MA 18 (2014a+b)) is promising. SALAMANCA et al. (2012) simulated a reduction of 1–2 K in UHI by assuming high albedo roofs and increased insulation for Madrid using WRF. Also, in their study the reduction of the heat ejected by air conditioning systems is mentioned as an important factor.

4.3 Local resilience measures

No coupled WRF-TEB simulations have been made for the quantification of the effect of single resilience measures. For this reason, the meteorological parameters above the urban canopy layer from the REF simulation has been used as forcing for offline simulations with SURFEX. With this modelling approach, the potential modification of the meteorological parameters above the urban canopy layer is not considered, and only the local effects can be seen, as if the rest of the city would still be built as REF. This part of the analysis shows what effects are to be expected locally if certain measures are not realized on a city scale but only on a local scale.

4.3.1 Albedo increase (ALB)

Increase of albedo is widely discussed as a cheap and effective measure to mitigate urban heat during summer heat episodes. e.g., RAFAEL et al. (2016) simulated using the WRF-SUEWS modelling system and roofs with an albedo of 80 % for Porto (Portugal) a maximum reduction in sensible heat flux of 62.8 W/m². RAMAMURTHY et al. (2015) showed that the wintertime penalty of white roofs, also for cool climates with 5 times more heating degree days than cooling degree days is insignificant compared to the summertime benefits. ŽUVELA-ALOISE et al. (2018) simulated using MUKLIMO for Vienna a reduction of up to 6 summer

days when assuming a roof albedo of 70 %. In many cities this measure is widely discussed, e.g., Los Angeles (<https://albedomap.lbl.gov/>) or even has already been implemented (<https://www.coolrooftoolkit.org/knowledgebase/white-roofs-in-brooklyn-new-york/>).

In Vienna itself there are no real life examples so far and potential legal difficulties and hindrances to implement bright roofs are yet unknown.

For street canyons, WEIHS et al. (2018) found that wall albedo increases from 0.1 to 0.2 during periods of high solar irradiation in a canyon of height/width ratio 1 can reduce air temperature in the canyon by about 1 K, dependent on the canyon geometry and reduce UTCI by about the same value. SCHRIJVERS et al. (2016) found a reduction in canyon air temperatures as well, and an increase of UTCI for high albedo values. For a height/width ratio of 0.5 SCHRIJVERS et al. (2016) recommend a uniform albedo of 0.2, while for height/width ratio 1 they recommend a gradient from high albedo close to the roof to low albedo on the ground. LEE and MAYER (2018) found that during heat wave conditions also starting for low albedo values there is a positive linear relationship between albedo increases (0.2–0.8) within the canyon and the human thermal comfort index PET. Also, in this study the ALB scenario shows an increase in the UTCI human thermal comfort index. Therefore, only increases in roof albedo, not within the canyon are recommended.

4.3.2 Decreased thermal conductivity of urban materials (INS)

Increasing the albedo of a very low insulation roof from 0.05 to 0.75 is roughly equivalent to adding 14 cm of insulation thickness (RAMAMURTHY et al., 2015). While it is a challenge to maintain the reflective properties of a white roof, insulations have longer lasting effects (RAMAMURTHY et al., 2015). ROMAN et al. (2016) found that increasing insulation results in an increase in sensible heat flux and surface temperatures during the day and a reduction at night. Here the same patterns are found. Increases of daily maximum as well as decreases of minimum air temperature and UTCI of about 1 °C/1 K caused by insulation was found by WEIHS et al. (2018) for historical climate. In this study, the daily maximum UTCI increases by more than 1.2 °C for a future heat wave with a 15 year return period. This is a clear negative effect of such a measure during daytime. However, the analysis of the energy fluxes during the heat wave shows that the longer the heat wave persists, the more the positive effects of building insulation prevail. Decreased thermal conductivity due to better building insulation is currently being adopted in widespread fashion in Vienna mainly to reduce the need for heating and reduce green house gas emissions during winter.

4.3.3 Increased building density (DEN)

Increase in building density within feasible ranges in Vienna has only limited effect on the sensible heat flux

(an increase of 10 W/m² is simulated) and leads to a slight increase of the daily minimum UTCI (0.2 K) and maximum UTCI (up to 0.1 K). In the present study increasing height of buildings is not considered, as those are still restricted and there is still enough attic space to be developed and changes in building height are still low. Beyond 2050 it is possible that the building height will further increase and lead to a densification and could cause a damping of the diurnal air temperature and increased nocturnal temperatures (COUTTS et al., 2007) caused by the reduced sky view. Without improving insulation this is likely to lead to an increase in mean air temperature and intensified UHI (RAD et al., 2017).

4.3.4 Evaporation of vegetation surfaces (GRR)

DE MUNCK et al. (2018) found that green roofs have nearly no influence on street level air temperature, but are a good strategy to reduce energy consumption all year round. The evaporative cooling is strongly dependent on available soil moisture. Also, in this study the changes caused in the air canyon are marginal. The roof temperatures on the other hand are reduced by over 10 K. Also, here it could be seen, that the cooling potential of green roofs decline towards the end of the heat wave as latent heat flux goes down (Fig. 7d).

The maximum cooling generated during heat wave conditions caused by evapotranspiration of vegetation (not shading) within the city modelled by DE MUNCK et al. (2018) varied between 0.5 and 2 K. The influence in terms of additional humidity caused by urban vegetation appears tolerable in comparison to the benefits. Additional water vapour pressure caused by forest vegetation compared to an open site in Oxford (UK) was quantified by MORECROFT et al. (1998) to be below 2 hPa. As an extreme scenario MAHMOOD et al. (2008) could show that the influence of irrigation of agricultural fields during a long term measurement series increases the average near ground dew point temperature during growing season by 1.56 K in the North American Great Plains. Apart from this, the water vapour pressure of cities can also exceed the rural values due to different reasons (KUTTLER et al., 2007). Maximum differences of 5 hPa between urban and rural (agricultural) areas were found by FORTUNIAK et al. (2006) for Łódź (Poland).

4.3.5 Photovoltaic panels on roofs (PVR)

The use of photovoltaic panels on roofs shows a slight reduction of temperature and thermal stress, which is in correspondence with findings from MASSON et al. (2014), who found that solar panels can reduce the UHI by 0.2 K during day and 0.3 K at night. WEIHS et al. (2018) found that photovoltaic used on roofs could lead to a temperature reduction of 1.5 K and a reduction of UTCI of 1.5 K. Therefore, this article encourages the use of photovoltaic on roofs within the city.

4.3.6 Shade and urban trees

(Tree) shade is a fundamental method to reduce mean radiant temperature (MRT) and thus improve human thermal comfort during clear sky conditions. Although we do not take into account the influence of tree shade on wall, road and canyon temperatures, we demonstrate the main influence of tree shade, which is the reduced direct radiation, by presenting the MRT in the sun and shade. So, the shade caused by buildings in this study can serve as a proxy for the influence of tree shade. By now tree shade has been implemented in one fork of TEB by REDON *et al.* (2017), but the code is not implemented in the main code tree yet. WANG *et al.* (2018) simulated the effect of radiative cooling (not evapotranspiration) of trees in the built environment of contiguous United States and found an average decrease in near surface air temperatures of 3.06 K. They show that not only do trees reduce incoming solar radiation during daytime they also increase radiative cooling at night. The ground heat flux is reduced in intensity in the shaded areas. Although the sensible heat flux is increased at night, it is strongly reduced during daytime. MATZARAKIS and ENDLER (2010) could show that by reducing global radiation by assuming tree shade in urban areas the number of days with heat stress could be reduced by more than 10 % in Freiburg. KETTERER and MATZARAKIS (2015) increased the number of trees in an area in Stuttgart and found a decrease in PET by 0.5 K at 22:00 CET but by maximum 27 K at 14:00 CET. Also, in this study we found a decrease of 26 K between the maximum MRT in the sun and in the shade.

The vitality of urban trees declined drastically over the last 3–4 decades (BRADSHAW *et al.*, 1995) and trees in Viennese parks (DRLIK, 2010) and some species used in Viennese streets (SCHIMANN, 2015; NEUWIRTH, 2015) and cities close to Vienna (ZEILER, 2015) are documented to be under stress due to multiple stressors including summer heat waves and there is likely to be a low shade transition phase between our historical tree stock dying and new more tolerant trees being planted and growing to a state where they can provide perceptible shade.

Generally urban green infrastructure improves air quality (ABHIJITH *et al.*, 2017). Only in urban canyons air pollution can deteriorate (ABHIJITH *et al.*, 2017), which can be avoided by reducing emissions.

5 Conclusions and Outlook

- We coupled WRF and TEB to simulate two urban development scenarios of Vienna, which are presented here, for two heat waves representative for present and future climatic conditions of the mid-21st century. Further extreme changes in building material parameters have been done to estimate the potential to reduce air temperatures and maintain human thermal comfort by altering buildings themselves.

- Global and regional climate change subject to the RCP8.5 scenario causes an increase in the mean daily maximum air temperature in Vienna by 7 K. The mean daily minimum air temperature will increase by 2–4 K. This increase is stronger than the global average. One important factor may be low soil water content in the agricultural region Northeast to Southeast of Vienna. This increase needs to be mitigated on a global level by reducing the emission of greenhouse gases, but also land use on the regional level is of importance.
- City scale changes caused by urban growth or densification, which will mainly affect air temperature and human thermal comfort locally at the place where new urbanisation takes place and not to a significant degree in the central districts. Using a combination of adoption of nearly zero-energy building standard, as demanded by the European Union under the Energy Performance of Buildings Directive and increasing albedo of building materials on city scale, a maximum reduction of urban canyon temperature achieved by changes in urban parameters of 0.9 K for the minima and 0.2 K for the maxima is accomplished. The effects on human thermal comfort are even smaller with 0.7 K UTCI and 0.1 K UTCI respectively.
- Local scale changes of different adaptation measures show, that insulation of buildings used alone increases the maximum wall surface temperatures by more than 10 K or the maximum MRT in the canyon by 5 K.
- Therefore, measures to reduce MRT within the urban canyon preferably by tree shade, which was not possible to include in this study, are expected to complement the proposed measures and are urgently recommended.

This study concludes that the rising air temperatures expected by climate change puts an unprecedented heat burden on the Viennese inhabitants, which cannot easily be reduced by measures concerning buildings within the city itself. Therefore, in addition to those measures, small scale measures such as planting trees to provide shade, water sensitive planning in the agricultural plains surrounding Vienna and global measures such as the reduction of greenhouse gas emissions in order to reduce temperature extremes are required.

Acknowledgements

This research was mainly done within the project URBANIA (ACRP 8th call: KR14AC7K11944) funded by the Klima und Energiefond (KliEN). The finalization of the manuscript was done during a stay at NILU, Norway funded by the MARIETTA BLAU scholarship of OeAD. We would like to thank JÜRGEN PREISS, the MA 18 and BEATRIX GASIENICA-WAWRYTKO for their feedback and comments. Finally, we want to thank the two reviewers who helped to improve the manuscript.

References

- ABHIJITH, K.V., P. KUMAR, J. GALLAGHER, A. McNABOLA, R. BALDAUF, F. PILLA, B. BRODERICK, S. DI SABATINO, B. PULVIRENTI, 2017: Air Pollution Abatement Performances of Green Infrastructure in Open Road and Built-up Street Canyon Environments – A Review. – *Atmos. Env.* **162**, 71–86 DOI:10.1016/j.atmosenv.2017.05.014.
- AMTMANN, M., N. ALTMANN-MAVADDAT, 2014: Eine Typologie österreichischer Wohngebäude. (in German) – Österreichische Energieagentur. – Austrian Energy Agency, TABULA/EPISCOPE, http://episcope.eu/fileadmin/tabula/public/docs/brochure/AT_TABULA_TypologyBrochure_AEA.pdf (last access: 05.08.2019).
- APCC, 2014: Österreichischer Sachstandsbericht Klimawandel 2014 (AAR14). – KROMP-KOLB, H., N. NAKICENOVIC, K. STEININGER, A. GOBIET, H. FORMAYER, A. KÖPPL, F. PRETENTHALER, J. STÖTTER, J. SCHNEIDER, Verlag der Österreichischen Akademie der Wissenschaften, Wien, Österreich, 1096 pp.
- ARNOLD, D., I. SCHICKER, P. SEIBERT, 2011: Towards high-resolution environmental modelling in the Alpine region. – In: *Air Pollution Modeling and its Application XXI*. 269–273, Springer.
- AUER, I., U. FOELSCH, R. BÖHM, B. CHIMANI, L. HAIMBERGER, H. KERSCHNER, K.A. KOINIG, K. NICOLUSSI, C. SPÖTL, 2014: Vergangene Klimaänderung in Österreich, In: Österreichischer Sachstandsbericht Klimawandel 2014 (AAR14). – Austrian Panel on Climate Change (APCC), Verlag der Österreichischen Akademie der Wissenschaften, Wien, Österreich, 227–300.
- BADOR, M., L. TERRAY, J. BOÉ, S. SOMOT, A. ALIAS, A.L. GIBELIN, B. DUBUISSON, 2017: Future Summer Mega-Heatwave and Record-Breaking Temperatures in a Warmer France Climate. – *Env. Res. Lett.* **12**, 074025, 12, DOI:10.1088/1748-9326/aa751c.
- BARDOW, A., D. GREEN, 2018: Low-Carbon Process Industries Through Energy Efficiency and Carbon Dioxide Utilisation, European Commission – Directorate-General for Research and Innovation, <https://publications.europa.eu/en/publication-detail/-/publication/df9afa95-025d-11e8-b8f5-01aa75ed71a1/language-en> (last access: 05.06.2019).
- BERGER, T., H. FORMAYER, R. SMUTNY, C. NEURURER, R. PASSAWA, 2012: Auswirkungen des Klimawandels auf den thermischen Komfort in Bürogebäuden (in German). – *Berichte aus Energie- und Umweltforschung* 7/2012, Bundesministerium für Verkehr, Innovation und Technologie, https://www.nachhaltigwirtschaften.at/resources/hdz_pdf/enderbericht_1207_thermischer_komfort.pdf (last access 05.09.2012).
- BOONE, A., P. SAMUELSSON, S. GOLLVIK, A. NAPOLY L. JARLAN, E. BRUN, B. DECHARME, 2017: The interactions between atmosphere land surface model with a multi-energy balance (ISBA-MEB) option in SURFEXv8 Part 1: Model description. – *Geosci. Model Develop.* **10**, 843–872 DOI:10.5194/gmd-10-843-2017.
- BORNSTEIN, R., Q. LIN, 2000: Urban heat islands and summertime convective thunderstorms in Atlanta: Three case studies. – *Atmos. Env.* **34**, 507–516.
- BRADSHAW, A., B. HUNT, T. WALMSLEY, 1995: *Trees in the Urban Landscape: Principles and Practice*. – NY:E&FNSpon, London, New York,.
- BRÖDE, P., D. FIALA, K. BLAZEJCZYK, I. HOLMÉR, G. JENDRITZKY, B. KAMPMANN, B. TINZ, G. HAVENITH, 2012: Deriving the operational procedure for the universal thermal climate index (utci). – *Int. J. Biometeorol.* **56**, 481–494.
- BUENO, B., G. PIGEON, L.K. NORFORD, K. ZIBOUCHE, C. MARACHADIER, 2012: Development and evaluation of a building energy model integrated in the TEB scheme. – *Geosci. Model Develop.* **5**, 433–448 DOI:10.5194/gmd-5-433-2012.
- BUNDESMINISTERIUM FÜR NACHHALTIGKEIT UND TOURISMUS (BMNT), 2016: Endbericht ÖKS15 – Klimaszenarien für Österreich, Daten – Methoden – Klimaanalyse. – Zentralanstalt für Meteorologie und Geodynamik (ZAMG), Wegener Center für Klima und globalen Wandel (WEGC) und dem Interfakultären Fachbereich Geoinformatik der Universität Salzburg (Z_GIS), https://www.bmnt.gv.at/umwelt/klimaschutz/klimapolitik_national/anpassungsstrategie/klimaszenarien.html (last access: 20.05.2019).
- CATTIAUX, J., H. DOUVILLE, R. SCHOETTER, S. PAREY, P. YIOU, 2015: Projected increase in diurnal and interdiurnal variations of European summer temperatures. – *Geophys. Res. Lett.* **42**, 899–907 DOI:10.1002/2014GL062531.
- CORDEAU, E., 2016: Les îlots morphologiques urbains (IMU) (in French). – IAU îdF, https://www.iau-idf.fr/fileadmin/NewEtudes/Etude_1270/Les_îlots_morphologiques_urbains.pdf (last access: 05.08.2019).
- COUTTS, A.M., J. BERINGER, N.J. TAPPER, 2007: Impact of Increasing Urban Density on Local Climate: Spatial and Temporal Variations in the Surface Energy Balance in Melbourne, Australia. – *J. Appl. Meteor. Climatol.* **46**, 477–493 DOI:10.1175/JAM2462.1.
- DE MUNCK, C.S., A. LEMONSU, R. BOUZOUIDJA, V. MASSON, R. CLAVERIE, 2013: The GREENROOF module (v7.3) for modelling green roof hydrological and energetic performances within TEB. – *Geosci. Model Develop.* **6**, 1941–1960. DOI:10.5194/gmd-6-1941-2013.
- DE MUNCK, C.S., A. LEMONSU, V. MASSON, J. LE BRAS, M. BONHOMME, 2018: Evaluating the impacts of greening scenarios on thermal comfort and energy and water consumptions for adapting Paris city to climate change. – *Urban Climate* **23**, 260–286. DOI:10.1016/j.uclim.2017.01.003.
- DE PEE, A., D. PINNER, O. ROELOFSEN, K. SOMERS, E. SPEELMAN, M. WITTEVEEN, 2018: Decarbonization of industrial sectors: the next frontier. – McKinsey & Company, <https://www.mckinsey.com/business-functions/sustainability/our-insights/how-industry-can-move-toward-a-low-carbon-future> (last access: 05.06.2019).
- DONNER, L.J., B.L. WYMAN, R.S. HEMLER, L.W. HOROWITZ, Y. MING, M. ZHAO, J.-C. GOLAZ, P. GINOUX, S.J. LIN, M.D. SCHWARZKOPF, J. AUSTIN, G. ALAKA, W.F. COOKE, T.L. DELWORTH, S.M. FREIDENREICH, C.T. GORDON, S.M. GRIFFIES, I.M. HELD, W.J. HURLIN, S.A. KLEIN, T.R. KNUTSON, A.R. LANGENHORST, H.-C. LEE, Y. LIN, B.I. MAGI, S.L. MALYSHEV, P.C.D. MILLY, V. NAIK, M.J. NATH, R. PINCUS, J.J. PLOSHAY, V. RAMASWAMY, C.J. SEMAN, E. SHEVLIKOVA, J.J. SIRUTIS, W.F. STERN, R.J. STOUFFER, R.J. WILSON, M. WINTON, A.T. WITTENBERG, F. ZENG, 2011: The Dynamical Core, Physical Parameterizations, and Basic Simulation Characteristics of the Atmospheric Component AM3 of the GFDL Global Coupled Model CM3. – *Journal of Climate* **24**, 13, 3484–3519.
- DOU, Y., 2014: The influence of urban planning on urban thermal comfort. – Master Thesis, Wageningen University, the Netherlands, https://www.wur.nl/upload_mm/8/f/f/a3db8019-a442-4270-9a43-d7e06e834169_Dou_Yuehan_THE_LUP80436_201407.pdf (last access: 2019.08.29).
- DUCHEZ, A., E. FRAJKA-WILLIAMS, S.A. JOSEY, D.G. EVANS, J.P. GRIST, R. MARSH, G.D. MCCARTHY, B. SINHA, D.I. BERRY, J.J.M. HIRSCHL, 2016: Drivers of Exceptionally Cold North Atlantic Ocean Temperatures and Their Link to the

- 2015 European Heat Wave. – Environmental Research Letters, **11**, 7, 074004.
- DRLIK, S., 2010: Klimawandelanpassung der Pflege und Erhaltung öffentlicher Grünanlagen in Grossstädten unter Berücksichtigung des Konzepts der Nachhaltigen Entwicklung, untersucht am Fallbeispiel Wien. (in German) – Dissertation, https://zidapps.boku.ac.at/abstracts/download.php?dataset_id=7703&property_id=107 (last access: 11.10.2019).
- EEA (European Environment Agency), 2012: Corine land cover data set 2012, <https://www.eea.europa.eu/data-and-maps/data/clc-2012-raster> (last access: 23.05.2018).
- ERELL, E., D. PEARLMUTTER, T. WILLIAMSON, 2011: Urban Microclimate – Designing the Spaces Between Buildings. – Earthscan, Washington, USA, 266 pp.
- FALLMANN, J., R. FORKEL, S. EMEIS, 2016: Secondary effects of urban heat island mitigation measures on air quality. – Atmos. Env. **125**, 199–211, DOI:10.1016/j.atmosenv.2015.10.094.
- FANGER, P.O., 1970: Thermal Comfort, Analysis and Applications in Environmental Engineering. – McGraw-Hill Company, US, 244 pp.
- FIALA, D., K.J. LOMA, M. STOHRER, 2001: Computer prediction of human thermoregulatory and temperature responses to a wide range of environmental conditions. – Int. J. Biometeorol. **45**, 143–159.
- FISCHER, E.M., S.I. SENEVIRATNE, 2007: Soil Moisture – Atmosphere Interactions during the 2003 European Summer Heat Wave. – J. Clim., **20**, 5081–5099, DOI:10.1175/JCLI4288.1.
- FISHER, R., L. TIPPETT, 1928: Limiting forms of the frequency distributions of the largest or smallest member of a sample. – Proc Camb Philos Soc. **24**, 180–190.
- FORMAYER, H., P. HAAS., M. HOFSTÄTTER., S. RADANOVICS, H. KROMP-KOLB, 2007: Räumlich und zeitlich hochaufgelöste Temperaturszenarien für Wien und ausgewählte Analysen bezüglich Adaptionstrategien. – Bericht im Auftrag der Wiener Umweltschutzabteilung – MA 22 der Stadt Wien gemeinsam mit der MA 27 – EU-Strategie und Wirtschaftsentwicklung, <https://www.wien.gv.at/wirtschaft/standort/pdf/temperaturszenarien.pdf> (last access: 05.08.2019).
- FORTUNIAK, K., K. KLYSIK, J. WIBIG, 2006: Urban–Rural Contrasts of Meteorological Parameters in Łódź. – Theor. Appl. Climatol. **84**, 91–101, DOI:10.1007/s00704-005-0147-y.
- GABRIEL, K.M.A., W.R. ENDLICHER, 2011: Urban and rural mortality rates during heat waves in Berlin and Brandenburg, Germany. – Env. Poll. **159**, 2044–2050.
- Gobiet, A., S. Kotlarski, M. Beniston, G. Heinrich, J. Rajczak, M. Stoffel, 2014: 21st century climate change in the European Alps – A review. – Sci. Total Env. **493**, 1138–1151 DOI:10.1016/j.scitotenv.2013.07.050.
- GRIMMOND, C.S. B., M. ROTH, T.R. OKE, Y.C. AU, M. BEST, R. BETTS, G. CARMICHAEL, H. CLEUGH, W. DABBERDT, R. EMMANUEL, E. FREITAS, K. FORTUNIAK, S. HANNA, P. KLEIN, L.S. KALKSTEIN, C.H. LIU, A. NICKSON, D. PEARLMUTTER, D. SAILOR, J. VOOGT, 2010: Climate and More Sustainable Cities: Climate Information for Improved Planning and Management of Cities (Producers/Capabilities Perspective). – Proc. Env. Sci. **1**, 247–274.
- HARTMANN, D.L., 1994: Global Physical Climatology. – Academic Press, 411 pp.
- HUTTER, H. P., H. MOSHAMMER, P. WALLNER, B. LEITNER, M. KUNDI, 2007: Heatwaves in Vienna: effects on mortality. – Wien Klin. Wochenschr. **119**, 223–227.
- IPCC, 2013: The Physical Science Basis, Contribution of Working Group I to the Fifth Assessment Report of the Intergovernmental Panel on Climate Change. – In: Climate Change 2013, Stocker, T.F., D. Qin, G-K. Plattner, M.M.B. Tignor, S.K. Allen, J. Boschung, A. Nauels, Y. Xia, V. Bex, P.M. Midgley, Cambridge University Press, Cambridge, United Kingdom and New York, NY, USA, 1535 pp.
- JACOB, D., J. PETERSEN, B. EGGERT, A. ALIAS, O.B. CHRISTENSEN, L.M. BOUWER, A. BRAUN, A. COLETTE, M. DÉQUÉ, G. GEORGIEVSKI, E. GEORGOPOULOU, A. GOBIET, L. MENUT, G. NIKULIN, A. HAENSLER, N. HEMPELMANN, C. JONES, K. KEULER, S. KOVATS, N. KRÖNER, S. KOTLARSKI, A. KRIEGSMANN, E. MARTIN, E. V. MEIJGAARD, C. MOSELEY, S. PFEIFER, S. PREUSCHMANN, C. RADERMACHER, K. RADTKE, D. RECHID, M. ROUNSEVELL, P. SAMUELSSON, S. SOMOT, J. -F. SOUSSANA, C. TEICHMANN, R. VALENTINI, R. VAUTARD, B. WEBER, P. YIOU, 2014: EURO-CORDEX: new high-resolution climate change projections for European impact research. – Reg. Env. Change. **14**, 2, 563–578 DOI:10.1007/s10113-013-0499-2.
- JASPER, K., P. CALANCA, J. FUHRER, 2006: Changes in summertime soil water patterns in complex terrain due to climatic change. – J. Hydrol. **327**, 3–4, 550–563 DOI:10.1016/j.jhydrol.2005.11.061.
- JENDRITZKY, G., R. DE DEAR, G. HAVENITH, 2012: UTCI – Why another thermal index? – Int. J. Biometeorol. **56**, 421–428.
- JONES, R., J. MURPHY, D. HASSELL, R. TAYLOR, 2001: Ensemble mean changes in a simulation of the European climate of 2071–2100 using the new Hadley Centre regional modelling system HadAM3H/HadRM3H. – Hadley Centre, Met Office, Bracknell, UK. http://prudence.dmi.dk/public/publications/hadley_200208.pdf (last access: 06.06.2019).
- KALISA, E., S. FADLALLAH, M. AMANI, L. NAHAYO, G. HABIYAREMYE, 2018: Temperature and air pollution relationship during heatwaves in Birmingham, UK. – Sustain. Cities Soc. **43**, 111–120.
- KENNEDY, C., J. STEINBERGER, B. GASSON, Y. HANSEN, T. HILLMAN, M. HAVRÁNEK, D. PATAKI, A. PHDUNGSILP, A. RAMASWAMI, G.V. MENDEZ, 2009: Greenhouse Gas Emissions from Global Cities. – Environmental Science & Technology **43**, 7297–7302. DOI:10.1021/es900213p.
- KETTERER, C., A. MATZARAKIS, 2015: Comparison of Different Methods for the Assessment of the Urban Heat Island in Stuttgart, Germany. – Int. J. Biometeorol. **59**, 1299–1309 DOI:10.1007/s00484-014-0940-3.
- KETTERER, C., M. GANGWISCH, D. FRÖHLICH, A. MATZARAKIS, 2017: Comparison of Selected Approaches for Urban Roughness Determination Based on Voronoi Cells. – Int. J. Biometeorol. **61**, 1, 189–98. DOI:10.1007/s00484-016-1203-2.
- KIM, J., J. KYSELÝ, 2009: Mortality during heat waves in South Korea, 1991 to 2005: How exceptional was the 1994 heat wave? – Climate Res. **38**, 105–116. DOI:10.3354/cr00775.
- KOHLER, M., C. TANNIER, N. BLOND, R. AGUEJDAD, A. CLAPIER, 2017: Impacts of several urban-sprawl countermeasures on building (space heating) energy demands and urban heat island intensities. A case study. – Urban Climate **19**, 92–121. DOI:10.1016/j.uclim.2016.12.006.
- KORNHUBER, K., V. PETOUKHOV, S. PETRI, S. RAHMSTORF, D. COUMOU, 2017: Evidence for wave resonance as a key mechanism for generating high-amplitude quasi-stationary waves in boreal summer. – Climate Dynamics, **49**, 5–6, 1961–1979 DOI:10.1007/s00382-016-3399-6.
- KRISPEL, S., M. PEYERL, P. WEIHS, G. MAIER, 2017: Reduction of Urban Heat Islands with Whitetopping. – Bauphysik. **39**, 1, 33–39.
- KUTTNER, W., S. WEBER, J. SCHONNEFELD, A. HESSEL-SCHWERDT, 2007: Urban/rural atmospheric water vapour pressure differences and urban moisture excess in Krefeld, Germany. – International Journal of Climatology, **27**, 14, 2005–2015. DOI:10.1002/joc.1558.

- KYSELÝ, J., J. KALVOVÁ, V. KVETON, 2000: Heat waves in the South Moravian region during the period 1961–1995. – *Studia Geophys Geodaet.* **44**, 57–72.
- LANDSBERG, H.E., 1981: *The Urban Climate*. – Academic Press, 275 pp.
- LEE, H., H. MAYER, 2018: Thermal comfort of pedestrians in an urban street canyon is affected by increasing albedo of building walls. – *Int. J. Biometeorol.* **62**, 1199–1209. DOI: [10.1007/s00484-018-1523-5](https://doi.org/10.1007/s00484-018-1523-5).
- LEMONSU, A., C.S.B. GRIMMOND, V. MASSON, 2004: Modeling the surface energy balance of the core of an old Mediterranean City: Marseille. – *J. Appl. Meteor. Climatol.* **43**, 312–327.
- LEMONSU, A., V. MASSON, L. SHASHUA-BAR, E. ERELL, D. PEARLMUTTER, 2012: Inclusion of vegetation in the Town Energy Balance model for modelling urban green areas. – *Geosci. Model Develop.* **5**, 1377–1393.
- LEMONSU, A., R. KOUNKOU-ARNAUD, J. DESPLAT, J.L. SALAGNAC, V. MASSON, 2013: Evolution of the Parisian urban climate under a global changing climate. – *Climatic Change* **116**, 679–692.
- LEUPRECHT, A., B. CHIMANI, M. HOFSTÄTTER, M. KERSCHBAUMER, S. KIENBERGER, M. KOTTEK, H. TRUHETZ, A. LEXER, S. PESSENTEINER, 2017: ÖKS15 bias corrected Euro-Cordex models, version 2. – <https://data.ccca.ac.at/group/oks15> (last access: 05.09.2019).
- LI, Y., R. BABCOCK, 2014: Green roofs against pollution and climate change. A review. – *Agro. Sustain. Develop.* **34**, 695–705. DOI: [10.1007/s13593-014-0230-9](https://doi.org/10.1007/s13593-014-0230-9).
- MA (Magistratsabteilung) 18 – Stadtentwicklung und Stadtplanung, 2005: Urban Development Plan Vienna 2005 – STEP05, <https://www.wien.gv.at/stadtentwicklung/strategien/step/step05/download/pdf/step-gesamt.pdf> (in German), <https://www.wien.gv.at/stadtentwicklung/strategien/step/step05/download/pdf/step05kurz-en.pdf> (last access: 05.08.2019).
- MA (Magistratsabteilung) 18 – Stadtentwicklung und Stadtplanung, 2011: Patterns for new urban developments. – *Werkstattberichte der Stadtentwicklung Wien Nr. 116*, <https://www.wien.gv.at/stadtentwicklung/studien/b008197.html> (last access: 05.08.2019).
- MA (Magistratsabteilung) 18 – Stadtentwicklung und Stadtplanung, 2014a: Smart City Wien – Framework Strategy, <https://www.wien.gv.at/stadtentwicklung/studien/pdf/b008384b.pdf> (last access: 05.08.2019).
- MA (Magistratsabteilung) 18 – Stadtentwicklung und Stadtplanung, 2014b: Urban Development Plan Vienna 2015 – STEP 2025 (in German), www.step.wien.at (last access: 05.08.2019).
- MA (Magistratsabteilung) 22 – Umweltschutz, 2018: Urban Heat Island Strategy, Vienna. – <https://www.wien.gv.at/umweltschutz/raum/pdf/uhi-strategieplan-englisch.pdf> (last access: 2019.04.12).
- MAHMOOD, R., K.G. HUBBARD, R.D. LEEPER, S.A. FOSTER, 2008: Increase in Near-Surface Atmospheric Moisture Content due to Land Use Changes: Evidence from the Observed Dewpoint Temperature Data. – *Mon. Wea. Rev.* **136**, 1554–1561 DOI: [10.1175/2007MWR2040.1](https://doi.org/10.1175/2007MWR2040.1).
- MASSON, V., 2000: A physically-based scheme for the urban energy budget in atmospheric models. – *Bound-Layer Meteorol.* **94**, 357–397 DOI: [10.1023/A:1002463829265](https://doi.org/10.1023/A:1002463829265).
- MASSON, V., C.S.B. GRIMMOND, T.R. OKE, 2002: Evaluation of the Town Energy Balance (TEB) scheme with direct measurements from dry districts in two cities. – *J. Appl. Meteor.* **41**, 1011–1026.
- MASSON, V., M. BONHOMME, J.-L. SALAGNAC, X. BRIOTTET, A. LEMONSU, 2014: Solar panels reduce both global warming and urban heat island. – *Front. Environ. Sci.* **2**, published online. DOI: [10.3389/fenvs.2014.00014](https://doi.org/10.3389/fenvs.2014.00014).
- MATZARAKIS, A., C. ENDLER, 2010: Climate change and thermal bioclimate in cities: Impacts and options for adaptation in Freiburg, Germany. – *Int. J. Biometeorol.* **54**, 479–83. DOI: [10.1007/s00484-009-0296-2](https://doi.org/10.1007/s00484-009-0296-2).
- MATZARAKIS, A., S. MUTERS, E. KOCH, 2011: Human biometeorological evaluation of heat-related mortality in Vienna. – *Theor. Appl. Climatol.* **105**, 1–10. DOI: [10.1007/s00704-010-0372-x](https://doi.org/10.1007/s00704-010-0372-x).
- MCMICHAEL, A.J., R. WOODRUFF, K. WHETTON, N. HENNESSY, N. NICHOLLS N., S. HALES, A. WOODWARD, T. KJELLSTROM, 2003: Human Health and Climate Change in Oceania: Risk Assessment Canberra. – Commonwealth Department of Health and Ageing, <http://citeseerx.ist.psu.edu/viewdoc/download?doi=10.1.1.183.6422&rep=rep1&type=pdf> (last access: 05.08.2019).
- MAYER, H., P. HÖPPE, 1987: Thermal comfort of man in different urban environments. – *Theor. Appl. Climatol.* **38**, 43–49 DOI: [10.1007/BF00866252](https://doi.org/10.1007/BF00866252).
- MICHALAKES, J., S. CHEN, J. DUDHIA, L. HART, J. KLEMP, J. MIDDLECOFF, W. SKAMAROCK, 2001: Development of a next-generation regional weather research and forecast model. – In: World Scientific (Pub.): *Developments in Teracomputing*. 269–276.
- MICHELOZZI, P., F. DE DONATO, G. ACCETTA, F. FORASTIERE, M. D’OVIDIO, C.A. PERUCCI, 2004: Impact of heatwaves on mortality – Rome, Italy – June–August 2003. – *JAMA.* **291**, 2537–2538. DOI: [10.1001/jama.291.21.2537](https://doi.org/10.1001/jama.291.21.2537).
- MORECROFT, M.D., M.E. TAYLOR, H.R. OLIVER, 1998: Air and Soil Microclimates of Deciduous Woodland Compared to an Open Site. – *Agricult. Forest Meteorol.* **90**, 141–56. DOI: [10.1016/S0168-1923\(97\)00070-1](https://doi.org/10.1016/S0168-1923(97)00070-1).
- MORINI, E., A. TOUCHAEI, B. CASTELLANI, F. ROSSI, F. COTANA, 2016: The Impact of Albedo Increase to Mitigate the Urban Heat Island in Terni (Italy) Using the WRF Model. – *Sustainability* **8**, 999. DOI: [10.3390/su8100999](https://doi.org/10.3390/su8100999).
- MUTERS, S., A. MATZARAKIS, E. KOCH, 2010: Climate change and mortality in Vienna – a human biometeorological analysis based on regional climate modeling. – *Int. J. Environ. Res. Public Health.* **7**, 2965–2977. DOI: [10.3390/ijerph7072965](https://doi.org/10.3390/ijerph7072965).
- NEUWIRTH, C., 2015: Effects of climate on Urban Trees in Vienna. – Master Thesis (in German) at the Institute of Soil Bioengineering and Landscape Construction, University of Natural Resources and Life Sciences, Vienna, https://zidapps.boku.ac.at/abstracts/download.php?dataset_id=11754&property_id=107 (last access: 11.10.2019).
- OFFERLE, B., P. JONSSON, I. ELIASSON, C.S.B. GRIMMOND, 2005: Urban modification of the surface energy balance in the West African Sahel: Ouagadougou, Burkina Faso. – *J. Climate* **18**, 3983–3995.
- OKE, T. R., 1982: The energetic basis of the urban heat island. – *Quart. J. Roy. Meteor. Soc.* **108**, 1–24. DOI: [10.1002/qj.49710845502](https://doi.org/10.1002/qj.49710845502).
- OKE, T. R., 1987: *Boundary Layer Climates*. – Routledge, Taylor&Francis Group, 464 pp.
- ÖROK, 2017: ÖROK Atlas (in German), <https://www.oerok-atlas.at/#indicator/65> (last access: 05.08.2019).
- OTANI, H., G. TAKAYUKI, G. HEITA, S. MINAYUKI, 2017: Time-of-day effects of exposure to solar radiation on thermoregulation during outdoor exercise in the heat. – *Chronobiol. Int.* **34**, 1224–1238.
- PEARLMUTTER, D., P. BERLINER, E. SHAVIV, 2005: Evaluation of urban surface energy fluxes using an open-air scale model. – *Bound-Layer Meteorol.* **44**, 532–545.
- PIGEON, G., K. ZIBOUCHE, B. BUENO, J. LE BRAS, V. MASSON, 2014: Improving the capabilities of the Town Energy Balance model with up-to-date building energy simulation algorithms:

- an application to a set of representative buildings in Paris. – *Energy Build.* **76**, 1–14.
- PINEDA, N., O. JORBA, J. JORGE, J. BALDASANO, 2004: Using NOAAAVHR Rand SPOT VGT data to estimate surface parameters: application to a mesoscale meteorological model. – *Int. J. Remote Sens.* **25**, 129–143.
- PGO (Planungsgemeinschaft Ost), 2011: stadregion+ (in German), Planungskoooperation zur räumlichen Entwicklung der Stadtregion Wien Niederösterreich Burgenland, http://www.planungsgemeinschaft-ost.at/fileadmin/root_pgo/Studien/Raumordnung/Zwischenbericht_Stadregion.pdf (last access: 05.08.2019).
- RAD, H.R., M. RAFIEIAN, H. SOZER, 2017: Evaluating the effects of increasing of building height on land surface temperature. – *Int. J. Urban Manage Energy Sustain.* **1**, 11–16. DOI:10.2034/ijumes.2017.01.01.002.
- RAFAEL, S., H. MARTINS, E. SÁ, D. CARVALHO, C. BORREGO, M. LOPES, 2016: Influence of urban resilience measures in the magnitude and behaviour of energy fluxes in the city of Porto (Portugal) under a climate change scenario. – *Sci. Total Environ.* **566–567**, 1500–1510, DOI: 10.1016/j.scitotenv.2016.06.037.
- RAMAMURTHY, P., T. SUN, K. RULE, E. BOU-ZEID, 2015: The Joint Influence of Albedo and Insulation on Roof Performance: A Modeling Study. – *Energy Build.* **102**, 317–27. DOI: 10.1016/j.enbuild.2015.06.005.
- REDON, E.C., A. LEMONSU, V. MASSON, B. MORILLE, M. MUSY, 2017: Implementation of street trees within the solar radiative exchange parameterization of TEB in SURFEX v8.0. – *Geosci. Model Develop.* **10**, 385–411. DOI: 10.5194/gmd-10-385-2017.
- ROMAN, K.K., T. O'BRIEN, J.B. ALVEY, O. WOO, 2016: Simulating the Effects of Cool Roof and PCM (Phase Change Materials) Based Roof to Mitigate UHI (Urban Heat Island) in Prominent US Cities. – *Energ.* **96**, 103–17, DOI:10.1016/j.energy.2015.11.082.
- SALAMANCA, F., A. MARTILLI, C. YAGÜE, 2012: A Numerical Study of the Urban Heat Island over Madrid during the DESIREX, 2008: Campaign with WRF and an Evaluation of Simple Mitigation Strategies. – *Int. J. Climatol.* **32**, 2372–2386. DOI:10.1002/joc.3398.
- SCHICKER, I., D. ARNOLD ARIAS, P. SEIBERT, 2016: Influences of updated land-use datasets on WRF simulations for two Austrian regions. – *Meteor. Atmos. Phys.* **128**, 279–301 DOI: 10.1007/s00703-015-0416-y.
- SCHIMANN, J., 2015: The effect of climate on trees in streets of Vienna. – Bachelor Thesis (in German) at the Institute of Soil Bioengineering and Landscape Construction, University of Natural Resources and Life Sciences, Vienna.
- SCHNELL, J.L., M.J. PRATHER, 2017: Co-occurrence of extremes in surface ozone, particulate matter, and temperature over eastern North America. – *Proc. Natl. Acad. Sci. USA.* **114**, 2854–2859 DOI:10.1073/pnas.1614453114.
- SCHREIER, S., I. SUOMI, P. BRÖDE, H. FORMAYER, H.E. RIEDER, I. NADEEM, G. JENDRITZKY, E. BATCHVAROVA, P. WEIHS, 2013: The uncertainty of UTCI due to uncertainties in the determination of radiation fluxes derived from numerical weather prediction and regional climate model simulations. – *Int. J. Biometeorol.* **57**, 2, 207–223.
- SCHRIJVERS, P.J.C., H.J.J. JONKER, S.R. DE ROODE, S. KENJEREŠ, 2016: The Effect of Using a High-Albedo Material on the Universal Temperature Climate Index within a Street Canyon. – *Urban Climate* **17**, DOI:10.1016/j.uclim.2016.02.005.
- SENEVIRATNE, S.I., R. WARTENBURGER, B.P. GUILLOD, A.L. HIRSCH, M.M. VOGEL, V. BROVKIN, D.P. VAN VUUREN, N. SCHALLER, L. BOYSEN, K.V. CALVIN, J. DOELMAN, P. GREVE, P. HAVLIK, F. HUMPENÖDER, T. KRISZTIN, D. MITCHELL, A. POPP, K. RIAHI, J. ROGELJ, C.-F. SCHLEUSSER, J. SILLMANN, E. STEHFEST, 2018: Climate extremes, land–climate feedbacks and land-use forcing at 1.5 °C. – *Philosophical Transactions of the Royal Society A: Mathematical, Physical and Engineering Sciences* **376**, 2119, DOI:10.1098/rsta.2016.0450.
- SHARIFI, A., Y. YAMAGATA, 2018: Resilience-Oriented Urban Planning. – In: YAMAGATA, Y., A. SHARIFI (Eds.): *Resilience-Oriented Urban Planning*. – Lecture Notes in Energy **65**, 3–27. DOI:10.1007/978-3-319-75798-8_1.
- SKAMAROCK, W.C., J.B. KLEMP, J. DUDHIA, D.O. GILL, D.M. BARKER, M.G. DUDA, X.-Y. HUANG, W. WANG, J.G. POWERS, 2008: A Description of the Advanced Research WRF Version 3. – NCAR. Tech. Note NCAR/TN-475+STR, 113 pp.
- STEADMAN, R.G., 1979a: The Assessment of Sultriness. Part I: A Temperature-Humidity Index Based on Human Physiology and Clothing Science. – *J. Appl. Meteor.* **18**, 861–873. DOI: 10.1175/1520-0450(1979)018<0861:TAOSPI>2.0.CO;2.
- STEADMAN, R. G., 1979b: The Assessment of Sultriness. Part II: Effects of Wind, Extra Radiation and Barometric Pressure on Apparent Temperature. – *J. Appl. Meteor.* **18**, 874–885 DOI: 10.1175/1520-0450(1979)018<0874:TAOSPI>2.0.CO;2.
- STEWART, I.D., T.R., OKE, 2012: Local climate zones for urban temperature studies. – *Bull. Amer. Meteor. Soc.* **93**, 1879–1900.
- STULL, R. B., 1988: An Introduction to Boundary Layer Meteorology. – Kluwer academic Publishers, Dordrecht-Boston-London.
- SWITANEK, M.B., P.A. TROCH, C.L. CASTRO, A. LEUPRECHT, H.-I. CHANG, R. MUKHERJEE, E.M.C. DEMARIA, 2017: Scaled distribution mapping: a bias correction method that preserves raw climate model projected changes. – *Hydrol. Earth Syst. Sci.* **21**, 2649–2666. DOI:10.5194/hess-21-2649-2017.
- TAHA, H., S. DOUGLAS, J. HANEY, 1997: Mesoscale meteorological and air quality impacts of increased urban albedo and vegetation. – *Energy Build.* **25**, 169–177. DOI:10.1016/S0378-7788(96)01006-7.
- TAN, J., Y. ZHENG, G. SONG, L. KALKSTEIN, A. KALKSTEIN, X. TANG, 2007: Heatwave Impacts on Mortality in Shanghai: 1998 to 2003. – *Int. J. Biometeorol.* **51**, 193.
- TAYLOR, K.E., R.J. STOUFFER, G.A. MEEHL, 2012: An Overview of CMIP5 and the Experiment Design. – *Bull. Am. Meteorol. Soc.* **93**, 4, 485–498 DOI:10.1175/BAMS-D-11-00094.1.
- URBAN, A., J. KYSELÝ, 2014: Comparison of UTCI with Other Thermal Indices in the Assessment of Heat and Cold Effects on Cardiovascular Mortality in the Czech Republic. – *Int. J. Env. Res.Public Health* **11**, 952–67. DOI:10.3390/ijerph110100952.
- ÜRGE-VORSATZ, D., C. ROSENZWEIG, R.J. DAWSON, R.S. RODRIGUEZ, X. BAI, A.S. BARAU, K.C. SETO, S. DHAKAL, 2018: Locking in Positive Climate Responses in Cities. – *Nature Climate Change* **8**, 174–77. DOI:10.1038/s41558-018-0100-6.
- VALLERON, A.J., A. BOUMENDIL, 2004: Epidemiology and heat waves: Analysis of the 2003 episode in France. – *C.R. Biology* **327**, 1125–41.
- VIDALE, P.L., D. LÜTHI, R. WEGMANN, C. SCHÄR, 2007: European summer climate variability in a heterogeneous multi-model ensemble. – *Climatic Change* **81**, S1, 209–232. DOI: 10.1007/s10584-006-9218-z.
- VOGEL, M.-M., 2018: Temperature extremes in a changing climate – Processes, emergent constraints and impacts. – Doctoral Thesis at ETH Zürich, DOI:10.3929/ethz-b-000323120.
- WANG, C., Z.-H. WANG, J. YANG, 2018: Cooling Effect of Urban Trees on the Built Environment of Contiguous United States. – *Earth's Future* **6**, 1066–1081. DOI:10.1029/2018EF000891.

- WEIHS, P., H. STAIGER, B. TINZ, E. BATCHVAROVA, H. RIEDER, L. VUILLEUMIER, M. MATURILLI, G. JENDRITZKY, 2012: The uncertainty of UTCI due to uncertainties in the determination of radiation fluxes derived from measured and observed meteorological data. – *Int. J. Biometeorol.* **56**, 537–555.
- WEIHS, P., S. ZAMINI, S. KRISPEL, S. OSWALD, M. PEYERL, M. REVESZ, A. SCHNEIDER, H. TRIMMEL, 2018: Optimierung reflektierender Materialien und Photovoltaik im Stadtraum bezüglich Strahlungsbilanz und Bioklimatik (PVOPTI-Ray). (in German), Berichte aus Energie- und Umweltforschung 18/2018 Nachhaltig wirtschaften, Bundesministerium für Verkehr, Innovation und Technologie, Wien, https://nachhaltigwirtschaften.at/resources/sdz_pdf/schriftenreihe_2018-18_pvoptiray.pdf (last access: 05.08.2019).
- ZAMPIERI, M., F. D'ANDREA, R. VAUTARD, P. CIAIS, N. DE NOBLET-DUCOUDRÉ, P. YIOU, 2009: Hot European Summers and the Role of Soil Moisture in the Propagation of Mediterranean Drought. – *J. Climate* **22**, 4747–4758. DOI: [10.1175/2009JCLI2568.1](https://doi.org/10.1175/2009JCLI2568.1).
- ZARE, S., N. HASHEMINEJAD, H.E. SHIRVAN, R. HEMMATJO, K. SAREBANZADEH, S. AHMADI, 2018: Comparing Universal Thermal Climate Index (UTCI) with selected thermal indices/environmental parameters during 12 months of the year. – *Wea. Climate Extremes* **19**, 49–57. DOI: [10.1016/j.wace.2018.01.004](https://doi.org/10.1016/j.wace.2018.01.004).
- ZEILER, S., 2015: Auswirkungen des Klimas auf Stadtbäume im Bezirk Korneuburg/Niederösterreich. – Master Thesis (in German), Institute of Soil Bioengineering and Landscape Construction, University of Natural Resources and Life Sciences, Vienna, 231 pp, https://zidapps.boku.ac.at/abstracts/download.php?dataset_id=12169&property_id=107 (last access: 11.10.2019).
- ZHANG, H., Y. WANG, T. PARK, Y. DENG, 2017: Quantifying the relationship between extreme air pollution events and extreme weather events. – *Atmos. Res.* **188**, 64–79.
- ZOMMERS, Z., K. ALVERSON, 2018: Resilience – The Science of Adaptation to Climate Change. – Elsevier, Amsterdam, Oxford, Cambridge, 354 pp.
- ŽUVELA-ALOISE, M., K. ANDRE, K., H. SCHWAIGER, D.N. BIRD, H. GALLAUN, 2018: Modelling reduction of urban heat load in Vienna by modifying surface properties of roofs. – *Theor. Appl. Climatol.* **131**, 1005–1018. DOI: [10.1007/s00704-016-2024-2](https://doi.org/10.1007/s00704-016-2024-2).

The pdf version (Adobe Java Script must be enabled) of this paper includes an electronic supplement:
Table of content – Electronic Supplementary Material (ESM)

Figure A-1

Bibliography

- [1] Arnold, D., Schicker, I., Seibert, P.: Towards high-resolution environmental modelling in the Alpine region, p. 269–273. Springer (2011)
- [2] Bhumralkar, C.M.: Numerical experiments on the computation of ground surface temperature in an atmospheric general circulation model. *J. Appl. Meteor.* **14**, 1246–1258 (1975)
- [3] Blackadar, A.K.: Modeling the nocturnal boundary layer. In: *Third Symp. on Atmospheric Turbulence, Diffusion and Air Quality*, p. 46–49. Amer. Meteor. Soc (1976)
- [4] Boone, A., Samuelsson, P., Gollvik, S., Napoly, A., Jarlan, L., Brun, E., Decharme, B.: The interactions between soil–biosphere–atmosphere land surface model with a multi-energy balance (ISBA-MEB) option in SURFEXv8 – Part 1: Model description. *Geosci. Model Dev.* **10**, 843–872 (2017). DOI 10.5194/gmd-10-843-2017
- [5] Boyd, M., Kasper, B.: Analytical methods for dynamic open channel heat and mass transfer: Methodology for heat source model Version 7.0 (2003)
- [6] Bröde, P., Fiala, D., Blazejczyk, K., Holmér, I., Jendritzky, G., Kampmann, B., Tinz, B., Havenith, G.: Deriving the operational procedure for the universal thermal climate index (utci) **56**, 481–494 (2012)
- [7] Bueno, B., Pigeon, G., Norford, L., Zibouche, K., Marachadier, C.: Development and evaluation of a building energy model integrated in the teb scheme. *Geosci. Model Develop.* **5**, 433–448 (2012). DOI 10.5194/gmd-5-433-2012
- [8] Cattiaux, J., Douville, H., Schoetter, R., Parey, S., Yiou, P.: Projected increase in diurnal and interdiurnal variations of European summer temperatures **42**(3), 899–907. DOI 10.1002/2014GL062531. URL <http://doi.wiley.com/10.1002/2014GL062531>
- [9] Cook, G.C.: Effect of global warming on the distribution of parasitic and other infectious diseases: a review. *Journal of Royal Society of Medicine* **85**, 688 – 691 (1992)
- [10] De Munck, C., Lemonsu, A., Masson, V., LeBras, K., Bonhome, M.: Evaluating the impacts of greening scenarios on thermal comfort and energy and water consumptions for adapting

- Paris city to climate change. *Urban Climate* **23**, 260–286 (2018). DOI 10.1016/j.uclim.2017.01.003
- [11] Déqué, M.: Frequency of precipitation and temperature extremes over France in an anthropogenic scenario: model results and statistical correction according to observed values. *Glob Planet Change* **57**(1-2), 16–26 (2007)
- [12] Déqué, M., Drevet, C., Braun, A., Carilolle, D.: The ARPEGE/IFS atmosphere model: a contribution to the French community climate modelling **10**, 249–266 (1994). DOI <https://doi.org/10.1007/BF00208992>
- [13] Donner, L.J., Wyman, B.L., Hemler, R.S., Horowitz, L.W., Ming, Y., Zhao, M., Golaz, J.C., Ginoux, P., Lin, S.J., Schwarzkopf, M.D., Austin, J., Alaka, G., Cooke, W.F., Delworth, T.L., Freidenreich, S.M., Gordon, C.T., Griffies, S.M., Held, I.M., Hurlin, W.J., Klein, S.A., Knutson, T.R., Langenhorst, A.R., Lee, H.C., Lin, Y., Magi, B.I., Malyshev, S.L., Milly, P.C.D., Naik, V., Nath, M.J., Pincus, R., Ploshay, J.J., Ramaswamy, V., Seman, C.J., Shevliakova, E., Sirutis, J.J., Stern, W.F., Stouffer, R.J., Wilson, R.J., Winton, M., Wittenberg, A.T., Zeng, F.: The dynamical core, physical parameterizations, and basic simulation characteristics of the atmospheric component AM3 of the GFDL global coupled model CM3 **24**(13), 3484–3519. DOI 10.1175/2011JCLI3955.1. URL <http://journals.ametsoc.org/doi/abs/10.1175/2011JCLI3955.1>
- [14] Duchez, A., Frajka-Williams, E., Josey, S.A., Evans, D.G., Grist, J.P., Marsh, R., McCarthy, G.D., Sinha, B., Berry, D.I., Hirschi, J.J.M.: Drivers of exceptionally cold North Atlantic Ocean temperatures and their link to the 2015 European heat wave. *Environmental Research Letters* **11**(7), 074,004 (2016). DOI 10.1088/1748-9326/11/7/074004. URL <http://stacks.iop.org/1748-9326/11/i=7/a=074004?key=crossref.f57a5f42ff74f02a1f629c6583ace1c7>
- [15] Dullinger, S., Gattringer, A., Thuiller, W., Moser, D., Zimmermann, N.E., Guisan, A., Willner, W., Plutzer, C., Leitner, M., Mang, T., Caccianiga, M., Dirnböck, T., Ertl, S., Fischer, A., Lenoir, J., Svenning, J.C., Psomas, A., Schmatz, D.R., Silc, U., Vittoz, P., Hülber, K.: Extinction debt of high-mountain plants under twenty-first-century climate change. *Nature Climate Change* **2**(8), 619–622 (2012). DOI 10.1038/nclimate1514. URL <http://www.nature.com/articles/nclimate1514>
- [16] Emberson, L., Simpson, D., Tuovinen, J.P., Ashmore, M., Cambridge, H.: Towards a model of ozone deposition and stomatal uptake over Europe. Tech. Rep. EMEP/MSC-W Note 6/00, The Norwegian Meteorological Institute (2000)
- [17] Fanger, P.: *Thermal Comfort, Analysis and Applications in Environmental Engineering*. McGraw-Hill Company, US (1970)

- [18] Fiala, D., Loma, K., Stohrer, M.: Computer prediction of human thermoregulatory and temperature responses to a wide range of environmental conditions **45**, 143–159 (2001)
- [19] Fischer, E.M., Seneviratne, S.I., Vidale, P.L., Lüthi, D., Schär, C.: Soil moisture–atmosphere interactions during the 2003 european summer heat wave **20**(20), 5081–5099. DOI 10.1175/JCLI4288.1. URL <http://journals.ametsoc.org/doi/abs/10.1175/JCLI4288.1>
- [20] Fishman, J., Creilson, J., Parker, P., Ainsworth, E., Vining, G., Szarka, J., Booker, F., Xiaojing, X.: An investigation of widespread ozone damage to the soybean crop in the upper midwest determined from ground-based and satellite measurements. *Atmospheric Environment* **44**, 2248–2256 (2010)
- [21] Formayer, H., Haas, P., Hofstätter, M., Radanovics, S., Kromp-Kolb, H.: Räumlich und zeitlich hochaufgelöste Temperaturszenarien für Wien und ausgewählte Analysen bezüglich Adaptionstrategien (2007)
- [22] Francis, J.A., Vavrus, S.J.: Evidence for a wavier jet stream in response to rapid Arctic warming. *Environmental Research Letters* **10**(1), 014,005 (2015). DOI 10.1088/1748-9326/10/1/014005. URL <https://doi.org/10.1088/1748-9326/10/1/014005>
- [23] Gobiet, A., Kotlarski, S., Beniston, M., Heinrich, G., Rajczak, J., Stoffel, M.: 21st century climate change in the European Alps—A review **493**, 1138–1151. DOI 10.1016/j.scitotenv.2013.07.050. URL <http://linkinghub.elsevier.com/retrieve/pii/S0048969713008188>
- [24] Goler, R., Formayer, H.: Temporal disaggregation of daily meteorological data to 15-minute intervals for use in hydrological models. In: EMS Annual Meeting Abstracts, no. Vol. 9 in EMS2012-174-1. URL <http://meetingorganizer.copernicus.org/EMS2012/EMS2012-174-1.pdf>
- [25] Grimmond, C., Roth, M., Oke, T., Au, Y., Best, M., Betts, R., Carmichael, G., Cleugh, H., Dabberdt, W., Emmanuel, R., Freitas, E., Fortuniak, K., Hanna, S., Klein, P., Kalkstein, L., Liu, C., Nickson, A., Pearlmutter, D., Sailor, D., Voogt, J.: Climate and more sustainable cities: Climate information for improved planning and management of cities (producers/capabilities perspective) **1**, 247–274. DOI 10.1016/j.proenv.2010.09.016. URL <https://linkinghub.elsevier.com/retrieve/pii/S1878029610000174>
- [26] Guenther, A., Monson, R., Fall, R.: Isoprene and monoterpene emission rate variability: Observations with eucalyptus and emission rate algorithm development. *Journal of Geophysical Research* **96/D6**, 10,799–10,808 (199)
- [27] Guldenschuh, M.: Longitudinal zonation of habitat parameters and fish species assemblages in the austrian lowland rivers lafnitz and pinka

- [28] Hagen, K., Gasiénica-Wawrythko, B., Loibl, W., Pauleit, S., Stiles, R., Tötzer, T., Trimmel, H., Köstl, M., Feilmayer, W.: Smart environment for cities: Assessing Urban Fabric Types and Microclimate Responses for Improved Urban Living Conditions. In: M. Schrenk, V.V. Popovich, P. Zeile, P. Elisei (eds.) Proceedings REAL CORP 2014 (2014)
- [29] Haiden, T., Kann, A., Wittmann, C., Pistotnik, G., Bica, B., Gruber, C.: The Integrated Nowcasting through Comprehensive Analysis (INCA) System and Its Validation over the Eastern Alpine Region **26**(2), 166–183. DOI 10.1175/2010WAF2222451.1. URL <http://journals.ametsoc.org/doi/abs/10.1175/2010WAF2222451.1>
- [30] Hartmann, D.: Global Physical Climatology. Academic Press (1994)
- [31] Haylock, M.R., Hofstra, N., Klein Tank, A.M.G., Klok, E.J., Jones, P.D., New, M.: A European daily high-resolution gridded data set of surface temperature and precipitation for 1950–2006. *Journal of Geophysical Research* **113**(D20) (2008). DOI 10.1029/2008JD010201. URL <http://doi.wiley.com/10.1029/2008JD010201>
- [32] Heino, J., Virkkala, R., Toivonen, H.: Climate change and freshwater biodiversity: detected patterns, future trends and adaptations in northern regions **84**(1), 39–54. DOI 10.1111/j.1469-185X.2008.00060.x. URL <http://doi.wiley.com/10.1111/j.1469-185X.2008.00060.x>
- [33] Hillinger, S.: Unterschiedliche Fassaden und deren jeweilige Auswirkung auf angrenzende Rasenfläche (2017)
- [34] Höpfe, P.: Heat balance modelling. *Experimentia* **49**, 741 – 746 (1993)
- [35] IPCC: Climate Change 2007 - Impacts, Adaptation and Vulnerability - Contribution of Working Group II to the Fourth Assessment Report of the IPCC. Cambridge University Press (2007)
- [36] IPCC: Climate Change 2013 - The Physical Science Basis. Contribution of Working Group I to the Fifth Assessment Report of the Intergovernmental Panel on Climate Change. Cambridge University Press, Cambridge, United Kingdom and New York, NY, USA (2013). Doi:10.1017/CBO9781107415324
- [37] Jasper, K., Calanca, P., Fuhrer, J.: Changes in summertime soil water patterns in complex terrain due to climatic change **327**(3), 550–563. DOI 10.1016/j.jhydrol.2005.11.061. URL <https://linkinghub.elsevier.com/retrieve/pii/S0022169405006530>
- [38] Jendritzky, G., Dear, R.D., Havenith, G.: Utci – why another thermal index? *Int. J. Biometeorol* **56**, 421–428 (2012)

- [39] Jendritzky, G., Menz, G., Schirmer H. and Schmidt-Kessen, W.: Methodik zur raumbezogenen Bewertung der thermischen Komponente im Bioklima des Menschen (Fortgeschriebenes Klima-Michel-Modell), Beitrge der Akademie fr Raumforschung und Landesplanung 114, Hannover. Akademie fr Raumforschung und Landesplanung 114, Hannover (1990)
- [40] Kalny, G., Laaha, G., Melcher, A., Trimmel, H., Weihs, P., Rauch, H.P.: The influence of riparian vegetation shading on water temperature during low flow conditions in a medium sized river. *Knowl. Manag. Aquat. Ecosyst.* **418**(5) (2017). DOI 10.1051/kmae/2016037
- [41] Kornhuber, K., Petoukhov, V., Petri, S., Rahmstorf, S., Coumou, D.: Evidence for wave resonance as a key mechanism for generating high-amplitude quasi-stationary waves in boreal summer. *Climate Dynamics* **49**(5-6), 1961–1979 (2017). DOI 10.1007/s00382-016-3399-6. URL <http://link.springer.com/10.1007/s00382-016-3399-6>
- [42] Koutsoyiannis, D.: *Rainfall disaggregation methods: Theory and applications* (2003)
- [43] Kyselý, J., Kalvová, J., Květoň, V.: Heat waves in the south Moravian region during the period 1961-1995 **44**(1), 57–72. URL <http://link.springer.com/article/10.1023/A:1022009924435>
- [44] Kyselý, J., Kim, J.: Mortality during heat waves in South Korea, 1991 to 2005: How exceptional was the 1994 heat wave? **38**, 105–116. DOI 10.3354/cr00775. URL <http://www.int-res.com/abstracts/cr/v38/n2/p105-116/>
- [45] Lahoz A. Khattatov B., M.R.: *Data Assimilation – Making Sense of Observations*. Springer-Verlag, Berlin-Heidelberg (2010). DOI 10.1007/978-3-540-74703-1
- [46] Larcher, W.: *Physiological Plant Ecology: ecophysiology and stress physiology of functional groups*. Springer-Verlag, Berlin, Heidelberg, New York (2001)
- [47] LeMoigne, P.: *Surfex scientific documentation* (2018)
- [48] Lemonsu, A., Koukoku-Arnaud, R., Desplat, J., Salagnac, J., Masson, V.: Evolution of the parisian urban climate under a global changing climate. *Climatic Change* **116**, 679–692 (2013)
- [49] Lin, M., Horowitz, L.W., Xie, Y., Paulot, F., Malyshev, S., Shevliakova, E., Finco, A., Gerosa, G., Kubistin, D., Pilegaard, K.: Vegetation feedbacks during drought exacerbate ozone air pollution extremes in Europe. *Nature Climate Change* **10**(5), 444–451 (2020). DOI 10.1038/s41558-020-0743-y. URL <http://www.nature.com/articles/s41558-020-0743-y>
- [50] Lindberg, F., Grimmond, C., Gabey, A., Huang, B., Kent, C.W., Sun, T., Theeuwes, N.E., Järvi, L., Ward, H.C., Capel-Timms, I., Chang, Y., Jonsson, P., Krave, N., Liu, D., Meyer, D.,

- Olofson, K.F.G., Tan, J., Wästberg, D., Xue, L., Zhang, Z.: Urban multi-scale environmental predictor (UMEP): An integrated tool for city-based climate services **99**, 70–87. DOI 10.1016/j.envsoft.2017.09.020. URL <http://linkinghub.elsevier.com/retrieve/pii/S1364815217304140>
- [51] Lindberg, F., Holmer, B., Thorsson, S.: SOLWEIG 1.0 – modelling spatial variations of 3d radiant fluxes and mean radiant temperature in complex urban settings **52(7)**, 697–713. DOI 10.1007/s00484-008-0162-7. URL <http://link.springer.com/10.1007/s00484-008-0162-7>
- [52] Loibl, W., Stiles, R., Pauleit, S., Hagen, K., Gasienica, B., Tötzer, T., Trimmel, H., Köstl, M., Feilmayr, W.: Improving Open Space Design to Cope Better with Urban Heat Island Effects. *GAIA* **13/1**, 64–66. DOI 10.14512/gaia.23.1.17
- [53] Mahfouf, F., Noilhan, J.: Inclusion of gravitational drainage in a land surface scheme based on the force-restore method. *J. Appl. Meteorol.*
- [54] Mann, M.E., Rahmstorf, S., Kornhuber, K., Steinman, B.A., Miller, S.K., Coumou, D.: Influence of Anthropogenic Climate Change on Planetary Wave Resonance and Extreme Weather Events. *Scientific Reports* **7(1)**, 45,242 (2017). DOI 10.1038/srep45242. URL <http://www.nature.com/articles/srep45242>
- [55] Masson, V.: A physically-based scheme for the urban energy budget in atmospheric models. *Bound-Layer Meteor.* **94**, 357–397 (2000)
- [56] Masson, V., Grimmond, C.S.B., Oke, T.R.: Evaluation of the Town Energy Balance (TEB) scheme with direct measurements from dry districts in two cities **41(10)**, 1011–1026. URL [http://journals.ametsoc.org/doi/abs/10.1175/1520-0450\(2002\)041%3C1011:EOTTEB%3E2.0.CO;2](http://journals.ametsoc.org/doi/abs/10.1175/1520-0450(2002)041%3C1011:EOTTEB%3E2.0.CO;2)
- [57] Matulla, C., Schmutz, A., Melcher, A., Gerersdorfer, T., Haas, P.: Assessing the impact of a downscaled climate change simulation on the fish fauna in an Inner-Alpine River **52(2)**, 127–137
- [58] Matzarakis, A., Endler, C.: Climate change and thermal bioclimate in cities: impacts and options for adaptation in freiburg, germany **54(4)**, 479–483. DOI 10.1007/s00484-009-0296-2. URL <http://link.springer.com/10.1007/s00484-009-0296-2>
- [59] Melcher, A., Dossi, F., Graf, W., Pletterbauer, F., Schaufler, K., Kalny, G., Rauch, H.P., Formayer, H., Trimmel, H., Weihs, P.: Effects of riparian vegetation to mitigate water temperature effects on benthic invertebrates and fish shown at the rivers lafnitz and pinka. *Österreichische Wasser- und Abfallwirtschaft* **68**, 308–323 (2016)

- [60] Melcher, A., Dossi, F., Wolfram Graf, Guldenschuh, M., Holzappel, G., Lautsch, E., Leitner, P., Schaufler, K., Seebacher, M., Trimmel, H., Weihs, P., Rauch, H.P.: Assessment of aquatic habitat availability and climate change effects in medium sized rivers. 10th ISE Trondheim, Norway
- [61] Melcher, A., Pletterbauer, F., Guldenschuh, M., Rauch, P., Schaufler, K., Seebacher, M., Schmutz, S.: Der Einfluss der Wassertemperatur auf die Habitatpräferenz von Fischen in mittelgroßen Flüssen. *Mitteilungsblatt für die Mitglieder des Vereins für Ingenieurbioogie, Ingenieurbioogie: Neue Entwicklungen an Fließgewässern, Hängen und Böschungen* **1**, 15–21 (2015)
- [62] Muthers, S., Matzarakis, A., Koch, E.: Climate Change and Mortality in Vienna—A Human Biometeorological Analysis Based on Regional Climate Modeling *7*(7), 2965–2977. DOI 10.3390/ijerph7072965. URL <http://www.mdpi.com/1660-4601/7/7/2965>
- [63] Niu, S., Luo, Y., Li, D., Cao, S., Xia, J., Li, J., Smith, M.D.: Plant growth and mortality under climatic extremes: An overview. *Environmental and Experimental Botany* **98**, 13–19 (2014). DOI 10.1016/j.envexpbot.2013.10.004. URL <https://linkinghub.elsevier.com/retrieve/pii/S0098847213001482>
- [64] Noilhan, J., Planton, S.: A simple parameterization of land surface processes for meteorological models. *Mon. Weather Rev.*, **117**(3), 536–549 (1989)
- [65] Oke, T.: *Boundary Layer Climates*. Routledge (1987)
- [66] Oswald, S.M., Revesz, M., Trimmel, H., Weihs, P., Zamini, S., Schneider, A., Peyerl, M., Lindberg, F.: Coupling of urban energy balance model with 3-d radiation model to derive human thermal (dis)comfort. *International Journal of Climatology* (2018)
- [67] Otani, H., Goto, T., Goto, H., Shirato, M.: Time-of-day effects of exposure to solar radiation on thermoregulation during outdoor exercise in the heat **34**(9), 1224–1238. DOI 10.1080/07420528.2017.1358735. URL <https://doi.org/10.1080/07420528.2017.1358735>
- [68] Peñuelas, J., Rutishauser T. and Filella, I.: Phenology feedbacks on climate change. *Science* **324**, 887 – 888 (2009)
- [69] Petoukhov, V., Rahmstorf, S., Petri, S., Schellnhuber, H.J.: Quasiresonant amplification of planetary waves and recent Northern Hemisphere weather extremes. *Proceedings of the National Academy of Sciences* **110**(14), 5336–5341 (2013). DOI 10.1073/pnas.1222000110. URL <http://www.pnas.org/cgi/doi/10.1073/pnas.1222000110>
- [70] Pletterbauer, F., Melcher, A.H., Ferreira, T., Schmutz, S.: Impact of climate change on the structure of fish assemblages in European rivers **744**(1), 235–254. DOI 10.1007/s10750-014-2079-y. URL <http://link.springer.com/10.1007/s10750-014-2079-y>

- [71] Revesz, M., Oswald, S.M., Trimmel, H., Weihs, P., Zamini, S.: Potential increase of Solar Irradiation and its influence on PV-Facades inside an Urban Canyon by increasing the Ground Albedo. *Solar Energy* (2018)
- [72] Revesz, M., Zamini, S., Oswald, S., Trimmel, H., Weihs, P.: SEBEpv – New digital surface model based method for estimating the ground reflected irradiance in an urban environment. *Solar Energy* **199**, 400–410 (2020). DOI doi.org/10.1016/j.solener.2020.01.075
- [73] Scharf, B., Pitha, U., Trimmel, H.: Thermal performance of green roofs. In: *World Green Roof Congress - Copenhagen* (2012)
- [74] Schaufler, K.: Water temperature effects on fish in pre-alpine, medium-sized rivers
- [75] Schnell, J.L., Prather, M.J.: Co-occurrence of extremes in surface ozone, particulate matter, and temperature over eastern north america **114**(11), 2854–2859. DOI [10.1073/pnas.1614453114](https://doi.org/10.1073/pnas.1614453114). URL <http://www.pnas.org/lookup/doi/10.1073/pnas.1614453114>
- [76] Schreier, S.F., Suomi, I., Bröde, P., Formayer, H., Rieder, H.E., Nadeem, I., Jendritzky, G., Batchvarova, E., Weihs, P.: The uncertainty of UTCI due to uncertainties in the determination of radiation fluxes derived from numerical weather prediction and regional climate model simulations **57**(2), 207–223. DOI [10.1007/s00484-012-0525-y](https://doi.org/10.1007/s00484-012-0525-y). URL <http://link.springer.com/10.1007/s00484-012-0525-y>
- [77] Steadman, R.G.: The Assessment of Sultriness. Part I: A Temperature-Humidity Index Based on Human Physiology **7**(18), 861–873. DOI [https://doi.org/10.1175/1520-0450\(1979\)018<0861:TAOSPI>2.0.CO;2](https://doi.org/10.1175/1520-0450(1979)018<0861:TAOSPI>2.0.CO;2)
- [78] Steadman, R.G.: The Assessment of Sultriness. Part II: Effects of Wind, Extra Radiation and Barometric Pressure on Apparent Temperature. *J. Appl. Meteor* **18**, 874–885 (1979). DOI [https://doi.org/10.1175/1520-0450\(1979\)018<0874:TAOSPI>2.0.CO;2](https://doi.org/10.1175/1520-0450(1979)018<0874:TAOSPI>2.0.CO;2).
- [79] Stull, R.B.: *An Introduction to Boundary Layer Meteorology*. Kluwer Academic Publishers (1988)
- [80] Teng, H., Branstator, G., Tawfik, A.B., Callaghan, P.: Circumglobal Response to Prescribed Soil Moisture over North America. *Journal of Climate* **32**(14), 4525–4545 (2019). DOI [10.1175/JCLI-D-18-0823.1](https://doi.org/10.1175/JCLI-D-18-0823.1). URL <https://doi.org/10.1175/JCLI-D-18-0823.1>
- [81] Terzi, L., Wotawa, G., Schoepner, M., Kalinowski, M., Saey, P.R.J., Steinmann, P., Luan, L., Staten, P.W.: Radioisotopes demonstrate changes in global atmospheric circulation possibly caused by global warming. *Scientific Reports* **10**(1) (2020). DOI [10.1038/s41598-020-66541-5](https://doi.org/10.1038/s41598-020-66541-5). URL <http://www.nature.com/articles/s41598-020-66541-5>

- [82] Teskey, R., Wertin T. and Bauweraerts, I., Ameye, M., McGuire, M., Steppe, K.: Responses of tree species to heat waves and extreme heat events. *Plant, Cell and Environment* **38**, 1699–1712 (2015). DOI 10.1111/pce.12417,2015
- [83] Trimmel, H., Formayer, H., Gützer, C., Nadeem, I., Oswald, S., Weihs, P., Faroux, S., Lemonsu, A., Masson, V., Schoetter, R.: Evolution of the Viennese Urban Heat Island caused by expected Reduction of Vegetation Fraction in favour of Built-Up Land until 2030/2050, EGU2018-7927-3. In: EGU General Assembly 2018, Geophysical Research Abstracts, vol. 20 (2018). Oral
- [84] Trimmel, H., Formayer, H., Masson, V., Mursch-Radlgruber, E., Nadeem, I., Oswald, S., Schoetter, R., Weihs, P.: Entwicklung der Urbanen Wärmeinsel Wiens bis 2030/2050 bei Berücksichtigung der Erweiterung der Stadt Wien. In: Tagungsband, 19. Österreichischer Klimatag (2018)
- [85] Trimmel, H., Formayer, H., Mursch-Radlgruber, E., Nadeem, I., Oswald, S., Weihs, P., Faroux, S., Lemonsu, A., Masson, V., Schoetter, R.: Evolution of the Viennese Urban Heat Island and Mitigation Strategies in the Context of Urban Growth, Compacting and Climate Change by optimizing the Urban Surface Energy Balance. In: ICUC-10 (2018). Oral
- [86] Trimmel, H., Gangneux, C., Kalny, G., Weihs, P.: Application of the model 'Heat Source' to assess the influence of meteorological components on stream temperature and simulation accuracy under heat wave conditions. *METEOROL Z* **25(4)**, 389–406 (2016). DOI 10.1127/metz/2016/0695
- [87] Trimmel, H., Gasienica-Wawrytko, B., Hagen, K., Köstl, M., Loibl, W., Pauleit, S., Stiles, R., Tötzer, T.: Freiraumstrukturelle Effekte auf das städtische Mikroklima - eine Simulationssstudie für Wien. In: Tagungsband, 15. Österreichischer Klimatag. Universität Innsbruck, Campus Innrain 52, 6020 Innsbruck (2014). Oral
- [88] Trimmel, H., Hagen, K., Mursch-Radlgruber, E., Scharf, B., Weihs, P.: The influence of vegetation on the energy balance within urban settlements. In: Tagungsband, 13. Österreichischer Klimatag: Klima, Klimawandel, Auswirkungen und Anpassungen sowie Klimaschutz in Österreich. Klimaforschungsinitiative AustroClim, Climate Change Center Austria CCCA, Klima -und Energiefonds, joint with Universität für Bodenkultur Wien (2012). Poster
- [89] Trimmel, H., Kalny, G., Dossi, F., Formayer, H., Graf, W., Leitner, P., Leidinger, D., Nadeem, I., Rauch, H.P., Weihs, P., Melcher, A.: Abiotic and biotic data of the rivers Pinka and Lafnitz 2012 - 2014 pp. 1–12 (2017). DOI 10.15504/fmj.2017.22. URL http://data.freshwaterbiodiversity.eu/metadb/showfmjarticle.php?dbcode=FWM_8

- [90] Trimmel, H., Weihs, P., Faroux, S., Formayer, H., Gützer, C., Hasel, K., Leidinger, D., Lemnosu, A., Masson, V., Nadeem, I., Oswald, S., Revesz, M., Schoetter, R.: Influence of urban growth of the city Vienna on the thermal comfort of its inhabitants. In: EGU General Assembly 2019, Geophysical Research Abstracts, vol. 21
- [91] Trimmel, H., Weihs, P., Faroux, S., Formayer, H., Gützer, C., Hasel, K., Leidinger, D., Lemnosu, A., Masson, V., Nadeem, I., Oswald, S., Revesz, M., Schoetter, R.: Influence of urban growth of the city Vienna on the thermal comfort of its inhabitants. In: EGU General Assembly 2019, Geophysical Research Abstracts
- [92] Trimmel, H., Weihs, P., Faroux, S., Formayer, H., Hamer, P., Hasel, K., Laimighofer, J., Leidinger, D., Masson, V., Nadeem, I., Oswald, S., Revesz, M., Schoetter, R.: Thermal conditions during heat waves of a mid-European metropolis under consideration of climate change, urban development scenarios and resilience measures for the mid-21st century. *CONTRIB ATM SCI* (2019). DOI 10.1127/metz/2019/0966
- [93] Trimmel, H., Weihs, P., Formayer, H., Holzapfel: Methods of modeling the energy fluxes of low land rivers including the shading effect of river geometry and riparian vegetation. In: European River Restoration Conference 2013. European Centre for River Restoration (2013). Poster
- [94] Trimmel, H., Weihs, P., Formayer, H., Holzapfel, G.: Methods of modeling the energy fluxes of low land rivers including the shading effect of river geometry and riparian vegetation
- [95] Trimmel, H., Weihs, P., Leidinger, D., Formayer, H., Kalny, G., Melcher, A.: Can riparian vegetation shade mitigate the expected rise in stream temperatures due to climate change during heat waves in a human-impacted pre-alpine river? *HYDROL EARTH SYST SC* **22(1)**, 437–461 (2018). DOI 10.5194/hess-22-437-2018
- [96] Trimmel, H., Weihs, P., Oswald, S.M., Masson, V., Schoetter, R., Hammerberg, K., Bechtel, B.: Land use and urban morphology parameters for Vienna required for initialisation of the urban canopy model TEB derived via the concept of “local climate zones”. In: EGU General Assembly 2017, Geophysical Research Abstracts, vol. 19, pp. 7226–7226
- [97] Valleron, A., Boumendil, A.: Epidemiology and heat waves: Analysis of the 2003 episode in france. *C.R. Biology* **327**, 1125–41 (2004)
- [98] Vautard R. and Honoré, C.B.M.R.L.: Simulation of ozone during the August 2003 heat wave and emission control scenarios. *Atmospheric Environment* **39**, 2857–2967 (2005)
- [99] Wang, C., Wang, Z.H., Yang, J.: Cooling Effect of Urban Trees on the Built Environment of Contiguous United States

- [100] Weihs, P., Staiger, H., Tinz, B., Batchvarova, E., Rieder, H., Vuilleumier, L., Maturilli, M., Jendritzky, G.: The uncertainty of UTCI due to uncertainties in the determination of radiation fluxes derived from measured and observed meteorological data. *Int. J. Biometeorol.* **56**, 537–555 (2012)
- [101] Weihs, P., Zamini, S., Krispel, S., Oswald, S., Peyerl, M., Revesz, M., Schneider, A., Trimmel, H.: Optimierung reflektierender Materialien und Photovoltaik im Stadtraum bezüglich Strahlungsbilanz und Bioklimatik (PVOPTI-Ray). *Berichte aus Energie- und Umweltforschung 18/2018*, Bundesministerium für Verkehr, Innovation und Technologie, Wien (2018). URL https://nachhaltigwirtschaften.at/resources/sdz_pdf/schriftenreihe2018-18_pvoptiray.pdf
- [102] WHO: Particulate matter, ozone, nitrogen dioxide and sulfur dioxide, pp. 307–326. WHO (2006)
- [103] Zampieri, M., D’Andrea, F., Vautard, R., Ciais, P., de Noblet-Ducoudré, N., Yiou, P.: Hot European Summers and the Role of Soil Moisture in the Propagation of Mediterranean Drought **22**(18), 4747–4758. DOI 10.1175/2009JCLI2568.1. URL <http://journals.ametsoc.org/doi/abs/10.1175/2009JCLI2568.1>
- [104] Zsiborács, H., Pintér, G., Bai, A., Popp, J., Gabnai, Z., Pályi, B., Farkas, I., Baranyai, N., Gützer, C., Trimmel, H., Oswald, S., Weihs, P.: Comparison of Thermal Models for Ground-Mounted South-Facing Photovoltaic Technologies: A Practical Case Study **11**(5), 1114. DOI 10.3390/en11051114. URL <http://www.mdpi.com/1996-1073/11/5/1114>
- [105] Žuvela-Aloise, M., Andre, K., Schwaiger, H., Bird, D.N., Gallaun, H.: Modelling reduction of urban heat load in Vienna by modifying surface properties of roofs. *Theoretical and Applied Climatology* **131**(3-4), 1005–1018 (2018). DOI 10.1007/s00704-016-2024-2. URL <http://link.springer.com/10.1007/s00704-016-2024-2>

B. Abbreviations

BVOC	Biogenic Volatile Organic Compounds
DFS	Distance from Source
ECMWF	European Centre for Medium-Range Weather Forecasts
LAI	Leaf Area Index
GIS	Geoinformation System
HVAC	Heating Ventilation and Cooling (system)
INCA	Integrated Nowcasting through Comprehensive Analysis
MLF	Mean Low Flow conditions
MRT	Mean Radiant Temperature
SVF	Sky View Factor
RMSE	Root Mean Square Error
RCM	Regional Climate Model
UHI	Urban Heat Island

B. Abbreviations

Global models

ARPEGE	Action de Recherche Petite Echelle Grande Echelle
GFPL-CM3 model	Geophysical Fluid Dynamics Laboratory - Coupled Physical Model

Regional models

ALADIN	Aire Limitée Adaptation dynamique Développement InterNational
WRF	Weather Research and Forecast

Microscale models

BEM	Building Energy Model
ISBA	Interactions between the Soil Biosphere and Atmosphere
MEGAN	Model of Emissions of Gases and Aerosols from Nature
SOLWEIG	SOLar Long Wave Environmental Irradiance Geometry
SURFEX	Surface Externalisée
TEB	Town and Energy Balance
UTCI	Universal Thermal Climate Index

Emissions scenarios

RCP8.5	Representative Concentration Pathway, radiative forcing value 2100: 8.5 W/m^2
A1B	Rapid economic growth, "Balanced" approach regarding alternative energy supply technologies

Vegetation scenarios

STQ, V0, V100
VH100, VH50, VD90, VD70, VD50

Urban development scenarios

R, S, O
